FUNDAMENTAL STUDIES OF THE WAKE STRUCTURE FOR SURFACE-MOUNTED FINITE-HEIGHT CYLINDERS AND PRISMS

A Thesis Submitted

to the College of Graduate Studies and Research

in Partial Fulfillment of the Requirements

for the Degree of Doctor of Philosophy

in the Department of Mechanical Engineering

University of Saskatchewan

Saskatoon, Saskatchewan, Canada

by

Noorallah Rostamy

Permission to Use

In presenting this thesis in partial fulfillment of the requirements for a Postgraduate degree from the University of Saskatchewan, I agree that the Libraries of this University may make it freely available for inspection. Permission for copying of my thesis in any manner, in whole or in part, for scholarly purposes may be granted by my supervisors (Professors David Sumner and Donald J. Bergstrom) or, in their absence, by the Head of the Department of Mechanical Engineering or the Dean of the College of Graduate Studies and Research at the University of Saskatchewan. Any copying, publication, or use of this thesis, or parts thereof, for financial gain without my written permission is strictly prohibited. Proper recognition shall be given to me and to the University of Saskatchewan in any scholarly use which may be made of any material in my thesis.

Request for permission to copy or to make any other use of material in this thesis in whole or in part should be addressed to:

Head of the Department of Mechanical Engineering

University of Saskatchewan

57 Campus Drive

Saskatoon, Saskatchewan, Canada

S7N 5A9

Acknowledgments

I would like to appreciate my supervisors, Professors David Sumner and Donald J. Bergstrom. Thank you for your advice, support, guidance, and insight. You were more than supervisors to me. My sincere thanks to you and your lovely families.

My thanks also go to my advisory committee members, Professors J. D. Bugg, D. A. Torvi, and K. A. Mazurek, as well as my external examiner Professor P. Oshkai, for their useful comments and suggestions. Special thanks to Dave Deutscher for his technical assistance and for his support and encouragement during my Ph.D. program. Working with you was a pleasure for me. My appreciation also goes to the secretaries in the Department of Mechanical Engineering (Kelley Neale, Sherri Haberman, and Janai Simonson) for their help and support.

It is my pleasure to show my sincere thanks to my friends Cameron and Jozie Janzen, Gerry and Shirley Falk, and Esther Magnus for their love and kindness to me and my wife since I came to Saskatoon.

I want to acknowledge the support and encouragements received from my wife, Mom and Dad, and my siblings that helped me in many ways to make my Ph.D. program a success.

Financial support from the Natural Sciences and Engineering Research Council of Canada (NSERC), the University of Saskatchewan Graduate Scholarship, and the donor of the Douglas Patton Hogg Memorial Award are acknowledged and appreciated.

Abstract

Surface-mounted finite-height circular cylinders and square prisms can be found in many industrial and engineering applications. The local flow fields around these bluff bodies are not yet well understood due to lack of experimental and numerical data close to the cylinder and prism. The aim of this thesis was therefore to gain an improved physical description of the flow field above the free end surface and around the cylinders and prisms. In the present experimental study, the particle image velocimetry (PIV) technique was used to measure the flow field very close to these bluff bodies in the test section of a low-speed wind tunnel. Four finite circular cylinders and square prisms of aspect ratios AR = 9, 7, 5 and 3 were tested at a Reynolds number of $Re_D = 4.2\times10^4$. At the location of the cylinder or prism, the boundary layer thickness relative to the cylinder diameter or prism width (D) was $\delta/D = 1.6$. PIV velocity field measurements in the near-wake region were made in a vertical plane parallel to the mean flow direction on the flow centreline (the symmetry plane), within 2D upstream and 5D downstream of the cylinder or prism. Additional PIV measurements were carried out in three orthogonal x-z, x-y, and y-z planes above the free end surface of the models.

In the near-wake region of the finite circular cylinders, the large recirculation zone contained a vortex immediately behind and below the free end; this vortex was found for all four aspect ratios. A second vortex was found behind the cylinder near the cylinder-wall junction; this vortex was not observed for the cylinder of AR = 3, indicating a distinct wake structure for this cylinder. Similar to the circular cylinder case, in the near-wake region of the square prisms, a vortex was observed immediately behind and below the free end in the recirculation zone. The size and strength of this vortex increased as the aspect ratio of the prism decreased. Also, a second vortex was found near the prism-wall junction downstream of the prisms of AR = 9 and 7, while this vortex was not observed for the prisms of AR = 5 and 3. The PIV results in the near-wake regions of the circular cylinders and square prisms show that the effect of the bluff body shape (circular or square cross-section) is evident in the maximum length of the mean recirculation zone. A considerable difference was seen between the maximum length of the mean recirculation zones of the circular cylinder and square prism of AR = 9, while the shape of the

bluff body does not considerably affect the length of the recirculation zones for the bodies of AR = 7, 5, and 3.

The present PIV results also provided insight into the separated flow above the free ends, including the effects of AR and body shape. Above the free end of the cylinders, flow separation from the leading edge led to the formation of a mean recirculation zone on the free-end surface. The point of reattachment of the flow onto the free-end surface moved towards the trailing edge as the cylinder aspect ratio was decreased. Large regions of elevated turbulence intensity and Reynolds shear stress were found above the free end. For the finite circular cylinders, the flow pattern above the free end was similar in all three *x*-*z* planes for all aspect ratios, consisting of a cross-stream vortex at approximately $x/D = 0$. According to the PIV results in the *x*-*y* planes, one of the main characteristics of the flow over the free end surface of the circular cylinders was a pair of focal points at $x/D \approx 0$ and near the edge of the free end. As the cylinder aspect ratio increased, the size and strength of these vortices decreased. Also, the centers of the vortices moved downstream as the aspect ratio increased.

For the finite square prism, the large, separated, recirculating flow region extended into the near wake. For the square prism of AR = 3, considerable difference was seen in the free-end flow pattern compared to the more slender prisms of AR = 9, 7 and 5. In particular, a cross-stream vortex formed due to interaction between the separated flow from the leading edge of the prism and the reverse flow over the trailing edge of the free end. This vortex was seen in all three planes at different cross-stream locations for AR = 3 but only in the symmetry plane for AR = 9. Hence, the present PIV results in the *x*-*z* planes revealed the effect of the near-wake flow on the flow above the prism free end. The results also showed a considerable effect of the aspect ratio on the mean velocity field as well as the Reynolds stress fields. The results in the *x*-*y* planes showed different flow patterns for the prism of AR = 3 including wall-normal vortices close to the free end at the sides of the prism as well as two saddle points close to the corners of the trailing edge and one node downstream of the trailing edge, while for AR = 9, no vortices and node were observed. Two streamwise vortices with opposite sign of rotation were seen in the *y*-*z* plane at $x/D = 0.2$ for all aspect ratios. The present results illustrate in-plane vorticities originating from the vertices of the leading edge of the prism for all aspect ratios.

Table of Contents

List of Tables

List of Figures

List of Symbols and Abbreviations

English Symbols

AR	Aspect ratio, H/D
C_D	Mean drag coefficient
c_τ	Uncertainty in particle image location relative to d_τ
D	Cylinder diameter or prism width [m]
D_I	Linear dimension of interrogation area [m^2]
d_p	Outer diameter of the Pitot tube [m]
d_{pix}	Diameter of pixel or pixel pitch [m]
d_τ	Particle image diameter [m]
E	Voltage [V]
H	Cylinder or prism height [m]
H_δ	Shape factor, δ^*/θ
L_{max}	Maximum longitudinal length the recirculation region [m]
N	Number of samples
N_I	Image density
P_∞	Freestream static pressure [N/m^2]
q_∞	Freestream dynamic pressure [N/m^2]
R	Gas constant for air [J/kgK]
Re_D	Reynolds number based on the cylinder diameter or prism width
Re_x	Reynolds number based on the distance from the leading edge of the ground plane
Re_θ	Ground plane Reynolds number based on the momentum thickness
T	Temperature [K]

U	Local velocity vector [m/s]
$\overline{U}$	Mean streamwise velocity component [m/s]
U_∞	Freestream velocity [m/s]
u'	Streamwise root-mean-square velocity [m/s]
$-\overline{u'v'}, -\overline{u'w'}, -\overline{v'w'}$	Reynolds shear stress components [m^2/s^2]
$\overline{V}$	Mean cross-stream velocity component [m/s]
v'	Cross-stream root-mean-square velocity [m/s]
$\overline{W}$	Mean wall-normal velocity component [m/s]
w'	Wall-normal root-mean-square velocity [m/s]
x	Streamwise distance from the cylinder/prism center [m]
y	Cross-stream distance from the cylinder/prism center [m]
z	Wall-normal distance from the ground plane [m]

Greek Symbols

α	Yaw angle [Degrees]
δ	Boundary layer thickness [m]
$\delta_{\Delta x}$	Error in the measurement of displacement vector in image domain [m]
δ^*	Boundary layer displacement thickness [m]
ϵ_X	Random error in estimated particle image location [m]
η	Random fluctuations associated with the film grain [m^2]
ν_∞	Freestream kinematic viscosity [m^2/s]
ρ_∞	Freestream density [kg/m^3]
τ_{00}	Total particle image density per unit illumination [m^2]
$\overline{\omega}_x$	Streamwise vorticity component [s^{-1}}

$\overline{\omega}_y$	Cross-stream vorticity component [s^{-1}]
$\overline{\omega}_z$	Wall-normal vorticity component [s^{-1}]

Abbreviations

CBC	Correlation based correction
CCD	Charge-coupled device
CCW	Counter clockwise
CFD	Computational fluid dynamics
CNN	Cellular neural network
CTA	Constant temperature anemometer
CW	Clockwise
FFT	Fast Fourier Transform
HWA	Hot-wire anemometry
LDA	Laser Doppler anemometry
LES	Large eddy simulation
Nd:YAG	Neodymium-doped yttrium aluminum garnet
PIV	Particle image velocimetry
POD	Proper orthogonal decomposition
SNR	Signal-to-noise ratio

1. Introduction

1.1 Background

The flow around a bluff body at a sufficiently high Reynolds number is characterized by a large region of separated flow which leads to the formation of a sizeable wake downstream. The classical example of a two-dimensional bluff body is the "infinite" circular cylinder, which has been the subject of a number of review articles (e.g., Coutanceau and Defaye, 1991; Williamson, 1996) and monographs (e.g., Sumer and Fredsoe, 1997; Zdravkovich, 1997). For a wide range of Reynolds numbers, the flow field is characterized by the periodic, alternate formation and shedding of vortices from opposite sides of the circular cylinder and a regular pattern of vortices in its wake known as the von Karman vortex street. Flow around an infinite cylinder has been studied extensively due to the common occurrence of cylinder-like structures in engineering applications and the potential for vortex-induced vibration. The alternating vortex shedding causes large fluctuating pressure forces which can lead to noise, vibration, and even structural failure when the frequency of the vortex shedding coincides with the natural frequency of the body. Bluff bodies experience high drag forces due to the high pressure forces from the upstream flow acting on the leading surface of the body. This corresponds to the high wind loading on cylindrical or prismatic structures in engineering applications.

Many of the cylinder-like structures encountered in engineering applications are better approximated as "finite" circular cylinders (e.g., Sakamoto and Arie, 1983; Okamoto and Sunabashiri, 1992; Tanaka and Murata, 1999; Park and Lee, 2000; Sumner et al., 2004; Adaramola et al., 2006; Wang et al., 2009; Krajnović, 2011). Surface-mounted finite-height circular cylinders are found in many engineering applications, such as buildings, cooling towers, fuel and gas storage tanks, bridge piers, and rooftop chimney stacks.

A schematic of the flow around a surface-mounted finite circular cylinder is shown in Figure 1.1, for a cylinder of diameter, *D*, and height, *H*, where *x* is the streamwise coordinate, *y* is the cross-stream coordinate, and *z* is the wall-normal coordinate. Here, the cylinder is mounted normal to a ground plane and is partially immersed in a flat-plate boundary layer, where $\overline{U}(z)$ is the incoming mean velocity profile, U_∞ is the freestream velocity outside the boundary layer on the ground plane, and δ is the thickness of the boundary layer. Flow over the circular cylinder's free end and flow around the cylinder-wall junction cause the local flow field and the cylinder's wake to become strongly three-dimensional. In addition to the familiar Kármán vortex shedding from the sides of the cylinder, the horseshoe vortex forming upstream at the cylinder-wall junction, and two sets of streamwise counter-rotating vortex structures within the wake, one near the free end (the tip vortices) and the other near the ground plane (the base vortices), highlight the increased complexity of the flow behavior in the wake.

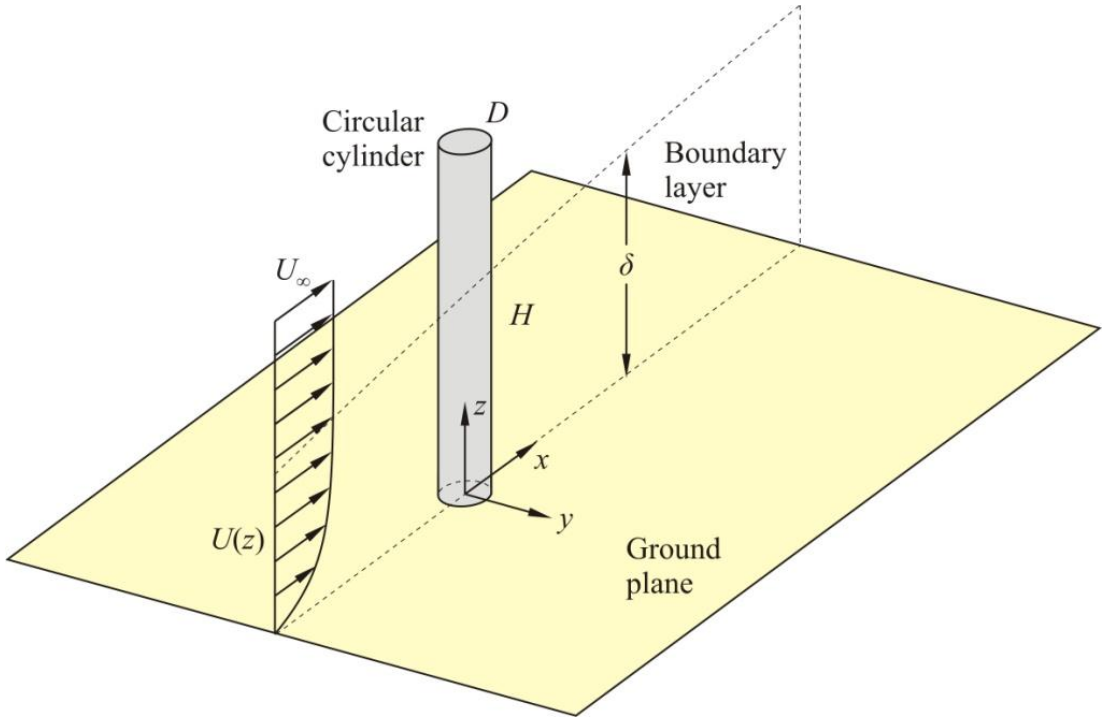

Figure 1.1: A schematic representation of flow past a finite circular cylinder mounted normal to a ground plane and partially immersed in a flat-plate boundary layer.

Apart from the Reynolds number, $\mathrm{Re}_D = U_\infty D/\nu$ (where ν is the kinematic viscosity), the wake of the finite circular cylinder is strongly influenced by several other parameters, including the cylinder aspect ratio (or slenderness ratio) AR = *H/D*, the approach velocity profile on the ground plane, $\overline{U}(z)/U_\infty$, and the relative thickness of the boundary layer on the ground plane, i.e., the ratios δ/D or δ/H. Many studies in the literature (e.g., Okamoto and Yagita, 1973; Sakamoto and Arie, 1983; Sumner et al., 2004; Adaramola et al., 2006) have shown the existence of a critical aspect ratio below which the cylinder has a distinct wake structure (sometimes referred to as symmetric "arch vortex shedding" as distinct from the more familiar antisymmetric Kármán

vortex shedding). The critical aspect ratio ranges from AR = 1 to 7 depending on the study, and is sensitive to the thickness of the boundary layer on the ground plane among other parameters.

Similar to the finite-height circular cylinders, surface-mounted prismatic structures are found in many engineering applications, such as the flow past high-rise buildings, chimneys and cooling towers. For these bluff bodies, the flow field is strongly influenced by the flow around the free end and the flow around the junction between the prism and the surface. The flow around the prism-wall junction (at the ground plane) and over the free end cause the local flow field to become strongly three-dimensional. A schematic of the base vortices, tip vortices and the shed Kármán vortices are shown in Figure 1.2 to better illustrate the influence of vortices on the three-dimensional near-wake flow.

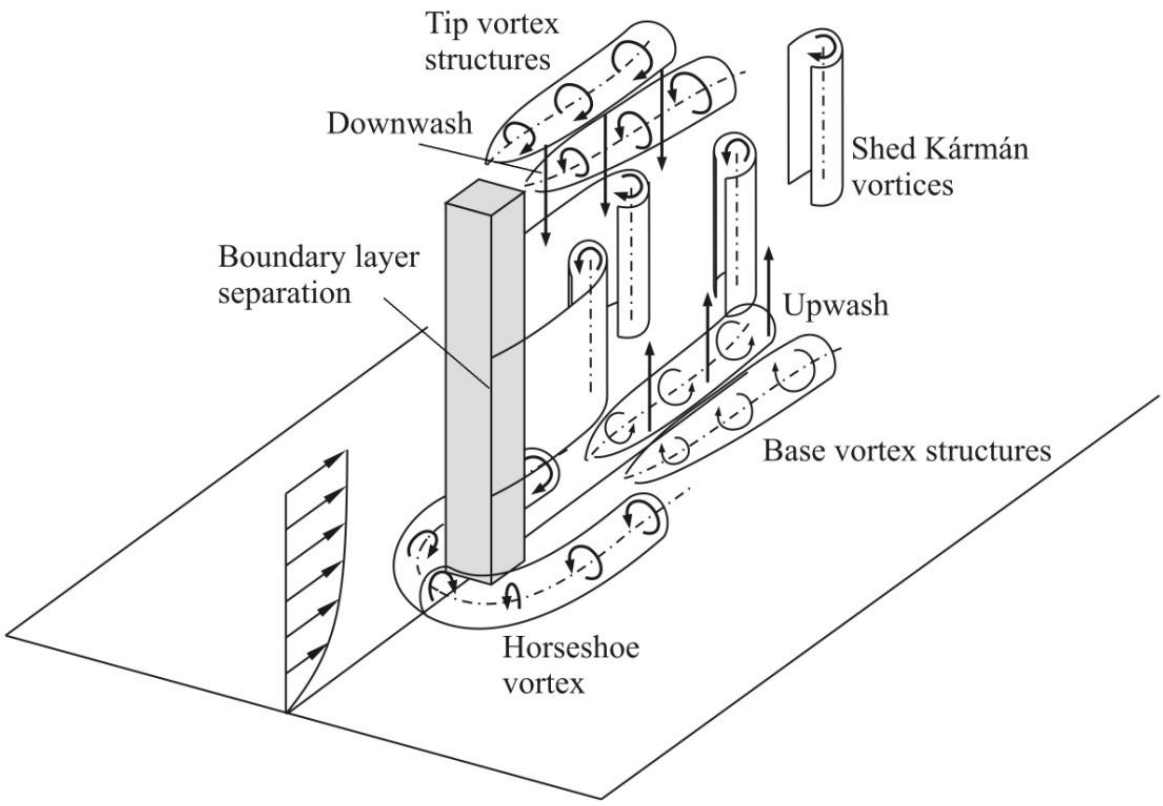

Figure 1.2: A schematic representation of the vortices around a finite square prism.

The main difference between the finite-height circular cylinders and square prisms is the separation location of the shear layers from the bluff bodies. Due to the sharp edges and corners of the square prisms, the approaching flow separates from the leading edges meaning that there are fixed separation points/lines in the square prism case. The separation lines are straight for the square prism case, whereas, in the circular cylinder case, the separation occurs on the sides of the cylinder but its exact location depends on the Reynolds number as well as the surface roughness. The separation location can also vary in angular position along the height of the cylinder. Furthermore, the separation of the flow from the free end surface, which leads to the formation of tip vortices, is different in the circular cylinder and square prism cases due to the difference in

the shape of the leading edge of the free end surfaces of the bodies. The approaching flow separates from the circumference of the free end surface of the finite-height circular cylinders, while it separates from the leading edge and side edges of the free end surface of the square prism.

Although the near-wake region of a finite circular cylinder and square prism has been studied by several researchers, not much attention has been paid to the flow over and above the free end of the finite circular cylinders and more specifically finite square prisms. Studies of finite circular cylinders by Okamoto and Yagita (1973) and Kawamura et al. (1984) have shown that the tip vortices originate near the point of side wall boundary layer separation a short distance below the free end. On the other hand, Etzold and Fiedler (1976) and Park and Lee (2000) have reported that the tip vortices for a finite circular cylinder originate from separation at the circumferential leading edge of the free end, while Roh and Park (2003) indicated that the tip vortices originate on the upper surface of the circular cylinder's free end.

The tip vortices are associated with a downward-directed local velocity field near the free end, known as “downwash” which is a problem for stacks operating at low exhaust-to-wind velocity ratios, since pollutants can be brought toward the ground. This “downwash” flow interacts with the regular Kármán vortex shedding from the sides of the cylinder or prism. As mentioned above, a critical aspect ratio exists below which the familiar antisymmetric Kármán vortex shedding is replaced by symmetric “arch vortex shedding”. Vortex shedding from the sides of the body is also affected by the local flow field of the cylinder-wall junction and, if the cylinder exceeds the critical AR, the formation of a second pair of streamwise vortices in the wake known as the base vortex pair (Sumner et al., 2004).

Flow separation occurs not only from the sides of the cylinder or prism but also from the free end. A few studies have examined the reattachment of the separated flow on the free end (e.g., Kawamura et al. (1984); Leder (2003); Roh and Park (2003); Park and Lee (2004); Pattenden et al. (2005); Krajnović (2011)). Since the flow field above the free end of a finite-height cylinder or prism influences the flow pattern in the near-wake region, and is directly related to the downwash flow field, further study of this local flow field is of interest in order to obtain a more complete understanding of the flow around finite-height surface-mounted bluff bodies. Because of the complexity of the flow field around the finite circular cylinder or square prism, and the many influencing parameters, further study is also needed to obtain a complete physical understanding of the wake behavior, especially very close to the cylinder/prism (i.e., the local flow field or the near-wake region) where the flow is strongly three-dimensional and recirculating. In this study, the flow fields above the free end surfaces of surface-mounted, finite-height circular cylinders and square prisms were investigated in a wind tunnel using particle image velocimetry (PIV).

The research described in this thesis is focused on understanding the complex flow field around surface-mounted finite-height circular cylinders and square prisms.

1.2 Scope and Objectives

Surface-mounted finite-height bluff bodies are found in many engineering applications. The purpose of the present study is to measure the mean and fluctuating velocity fields, and vorticity fields in the near-wake region of finite-height circular cylinders and square prisms. This study specifically focuses on measurement of the flow characteristics above the free end surfaces of these bluff bodies. The velocity fields are presented as mean velocity vectors, mean streamlines,

and contour lines of the mean and fluctuating components, while the turbulence intensities are shown as contour lines.

Like other experimental works, there were limitations in the present study that restricted the scope. All the present measurements were carried out at a single flow speed of the wind tunnel and a single diameter of the circular cylinder, resulting in a single Reynolds number of $Re_D = 4.2\times10^4$. According to Countanceau and Defaye (1991), for the range of $350 < Re_D < 2\times10^5$, a subcritical regime is defined for infinite circular cylinders that is characterized by a laminar boundary layer before separation and a quasi-constant separation angle of approximately 80 degrees measured from the front stagnation point of the cylinder. Therefore, the present results are constrained to a single Reynolds number and a subcritical flow regime. In the present measurements, the circular cylinders and the square prisms were immersed in a relatively thick boundary layer. The boundary layer thickness compared to the diameter or width of the cylinder or prism was kept constant, so that the boundary layer thickness relative to the height of the bodies is in the range of 18% to 54% indicating a thick boundary layer compared to other studies (e.g., Leder (2003); Krajnović (2011)). The present experimental set-up including the wind tunnel facilities and the models were similar to previous work by Adaramola (2008) and Heseltine (2003). However, the velocity measurement technique and the regions of interest in the present study were different from these works. A low-frame-rate PIV system used in this study provided time-averaged and instantaneous PIV data, but not phase-averaged data. Although a single boundary layer thickness and Reynolds number were used, the aspect ratio of the cylinder and prism were varied. The present experimental data were collected in different fields of view in the near wake of the bodies, each at different time, so that no temporal information was

obtained from the near-wake measurements. The present PIV data were also collected in a limited number of planes due to challenges in positioning the camera and light sheet optics.

The overall objective of the present study is to advance the fundamental understanding of finite circular cylinder and square prism flows. Of particular interest are the effects of the aspect ratio (AR) and the bluff body shape (circular or square cross-section) on the flow characteristics in the near-wake region, and above and around the free end surfaces.

1.3 Outline of the Thesis

The main part of this thesis is made up of eight chapters. Reviews of the flow around the finite-height cylinders and prisms as well as the flow above the free end surfaces of the bodies are presented in Chapter 2. Chapter 3 describes the instrumentation, physical models, and experimental set-up used for this study.

Results and discussions are presented in Chapters 4 to 7. In Chapter 4, the effects of aspect ratio on the near-wake structure of a finite-height circular cylinder are presented and discussed. Flow characteristics in the near wake of cylinders of AR = 9, 7, 5, and 3 are discussed in this chapter. The near wake of finite square prisms of AR = 9, 7, 5, and 3 are presented in Chapter 5. In this chapter, the flow field behind the prisms is studied and a comparison is made between the near-wake flows of the finite circular cylinders (studied in Chapter 4) and the finite square prisms.

In Chapter 6, the flow above the free end of the circular cylinders of AR = 9, 7, 5, and 3 are studied. The PIV measurements in different vertical *x*-*z* planes and different horizontal *x*-*y* planes are presented in this chapter.

The flow above the free end of the finite square prisms of AR = 9, 7, 5, and 3 are presented in Chapter 7. The PIV measurements are carried out in three orthogonal planes, i.e. the *x*-*z*, *x*-*y*, and *y*-*z* planes.

A summary of the findings, the conclusions, and contributions and some recommendations for future work, are presented in Chapter 8.

2. Literature Review

2.1 Introduction

In this chapter, a review of recent work investigating the local flow fields around surface-mounted finite circular cylinders and square prisms is presented. Also, a review of studies on the flow above the free end surface of a finite circular cylinder as well as a square prism is presented. In the literature, the results of different studies are typically compared based on the cylinder or prism's aspect ratio (AR), Reynolds number (Re_D), and the ratio of the flat-plate boundary layer thickness to either the diameter/width of the cylinder or prism (δ/D) or the height of the cylinder or prism (δ/H). The main flow features in the near wake of the cylinder and prism, and above the free end surfaces of the bodies, are described in the following sections. The vortices formed around a finite surface-mounted square prism immersed in a boundary layer were schematically shown in Figure 1.2.

2.2 Flow around a Finite-height Circular Cylinder

The flow around a two-dimensional infinite circular cylinder immersed in a cross-flow is a classical problem in fluid mechanics. The behavior of this well-studied flow is presented by Countanceau and Defaye (1991), Williamson (1996), Zdravkovich (1997), and others. In the infinite cylinder case, the wake is not affected by the ends of the cylinder so that the wake structures and the velocity fields do not change along the cylinder span. Although there is neither perfectly two-dimensional flow nor any infinitely long cylinders in real-world applications, the study of the flow around these models can be useful since the flow around a finite-height circular cylinder found in real-world engineering applications exhibits some of the flow features around an infinite cylinder.

Vortex shedding is one of the main characteristics of the flow downstream of an infinite circular cylinder. The vortex shedding occurs for a wide range of Reynolds number. According to Countanceau and Defaye (1991), for $Re_D > 40$, the shear layers separating from the cylinder roll up alternately into vortices. These vortices are then shed into the cylinder wake forming two rows of vortices with an opposite sense of rotation known as the Kármán vortex street.

The three-dimensional local flow field of a surface-mounted finite circular cylinder is much less well-understood than the classical case of the infinite cylinder. This can in part be attributed to the challenges it poses for visualization, measurement, and modeling, owing to the complex fluid behavior immediately upstream and downstream of the cylinder, and around the free-end and cylinder-wall junction. The free end of the finite cylinder is exposed to the approaching freestream while the base of the cylinder (cylinder-wall junction) is exposed to the ground plane boundary layer flow. The flow in the region of the cylinder-wall junction is important in applications such as bridge piers. This flow has been studied by Agui and Andreopoulos (1992), Graf et al. (1998), and others for the circular cylinder geometry case. Due to the no-slip condition at the ground plane, the incoming flow has a lower velocity close to the wall resulting in flow recirculation upstream and at the leading edge of the cylinder. This recirculating flow is then swept around the cylinder base, rotating and rolling up into the so called “horseshoe vortex”. Downstream of the cylinder base, the boundary layer tends to separate from the cylinder due to the adverse pressure gradient. This three-dimensional separation of the wall boundary layer causes the horseshoe vortex to be lifted away from the ground plane. The behavior of the horseshoe vortex and cylinder wall-junction flow field has been well-documented in the literature (e.g., Baker, 1979, 1980). A schematic of the horseshoe vortex at the base of a finite square prism is shown in Figure 2.1.

There are different theories proposed for the flow around and above the free end of a finite cylinder or prism. Kitagawa et al. (1997, 2001, and 2002) proposed that a pair of counter-rotating trailing vortices exists near the tip of the cylinder. According to their studies, the vortex structure near the tip is responsible for the end-cell induced vibration which occurs at higher Reynolds number.

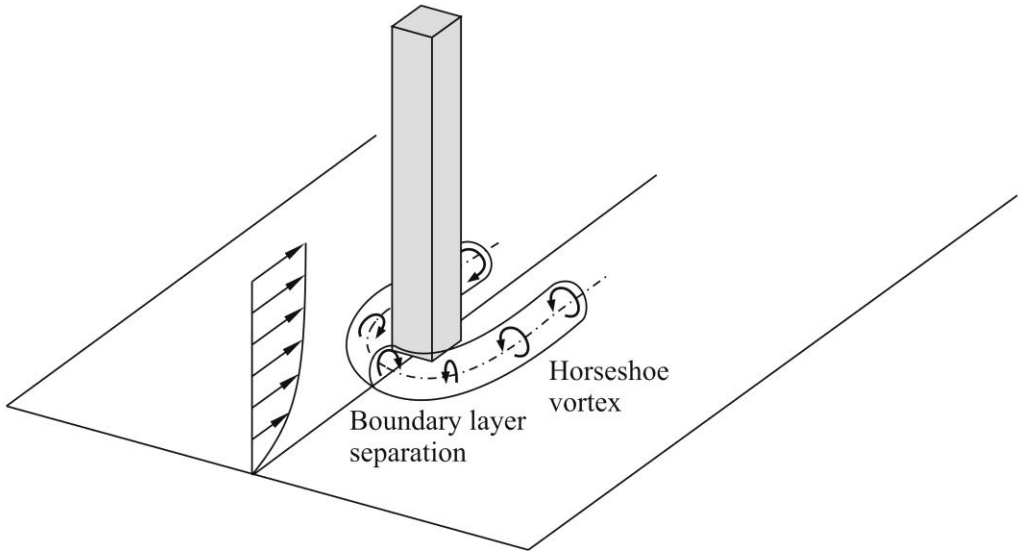

Figure 2.1: Horseshoe vortex in the wake of prism-wall junction.

The formation of the counter-rotating trailing vortices begins upstream of the cylinder tip as the approaching flow inclines towards the flow over the free end forming the “upwash” flow. As the flow passes over the free end of the cylinder, it is brought down to the low-pressure wake region forming a “downwash” flow. According to Kitagawa et al. (1997, 2001, 2002), the combination of the upwash flow on the sides and the downwash flow in the centre rolls up into two counter-

rotating trailing vortices. The transaction between the alternating Kármán vortex shedding with the tip vortex structure still remains challenging for researchers to describe.

There is another proposal for the flow behavior around and above the free end of a finite cylinder or prism. Okamoto and Yagita (1973), Sakamoto and Arie (1983), Okamoto (1991), Lee and Wang (1987), and Johnston et al. (1998) suggested that there is no trailing tip vortices above the free end of a finite cylinder; instead, an arch vortex forms behind the cylinder due to the delay in the formation of Kármán vortices near the tip of the cylinder. Therefore, the Kármán vortices are inclined and attached to the cylinder near the free end of the cylinder. According to Okamoto and Yagita (1973), one end of the vortex attaches onto the cylinder side wall near the cylinder tip, while the other end attaches to the ground plane. According to Lee and Wang (1997), for cylinders of shorter aspect ratio (AR < 4), the shear layer from the free end plays an important role as the shear layers from all sides of the cylinder roll up to form an arch structure.

Downstream of the cylinder, the wake is characterized by a pair of counter-rotating streamwise vortex structures extending from the free end, i.e., the tip vortices (e.g., Etzold and Fiedler, 1976; Kawamura et al., 1984; Lee, 1997; Park and Lee, 2000, 2002, 2004; Sumner et al., 2004). Okamoto and Yagita (1973) and Kawamura et al. (1984) proposed that the tip vortices originate near the point of side wall boundary layer separation a short distance below the free end. On the other hand, Etzold and Fiedler (1976) and Park and Lee (2000) reported that the tip vortices originate from separation at the circumferential leading edge of the free end, while Roh and Park (2003) indicated that the tip vortices originate on the upper surface of the free end.

The tip vortices are associated with a downward-directed local velocity field near the free end known as downwash, which is a serious problem for stacks operating at low exhaust-to-wind

velocity ratios, since pollutants can be brought toward the ground (e.g., Johnston and Wilson, 1997; Adaramola et al., 2010). This downwash flow interacts with the regular Kármán vortex shedding from the two sides of the cylinder, resulting in weakened or suppressed vortex shedding and a three-dimensional flow structure near the free end of the cylinder. In addition, the regular vortex shedding near the cylinder-wall junction is affected by the flat-plate boundary layer and the steady horseshoe vortex structure in this region.

In addition to the tip vortex structures, a pair of weaker base vortex structures (distinct from the horseshoe vortex) may be found in the lower part of the wake close to the cylinder-wall junction and within the boundary layer developed on the wall (Tanaka and Murata, 1999; Sumner et al., 2004). These are associated with a weak upward-directed local velocity field, known as upwash. Sumner et al. (2004) showed that below the critical aspect ratio, the base vortex structures are absent within the wake of the finite circular cylinder. Wang et al. (2006) investigated the effect of initial conditions on the interaction between a boundary layer and the flow around a finite-height cylinder of AR = 5. In their study, three different boundary layer thicknesses were used. According to their results, initial boundary layer conditions have a significant effect on the near wake as well as on the flow near the cylinder free end. Their results also showed that as the boundary layer thickness increases, the base vortex pair is enhanced, inducing a stronger upwash flow from the cylinder base. This weakens the downwash free-end shear layer and the tip vortex. Therefore, the spanwise vortices become stronger near the free end, and weaker near the wall. This causes the Reynolds stresses to increase significantly in magnitude near the free end and to decrease near the wall.

Flow separation occurs not only from the sides of the cylinder but also from the free end. A few studies have examined the reattachment of the separated flow on the free end of the

cylinder. Kawamura et al. (1984) studied the flow pattern on the free ends of finite circular cylinders of AR = 8, 4 and 1 with δ/D = 1 at Re_D = 1.07 × 10^4 to 3.2×10^4. According to their flow visualization results (shown in Figure 2.2), reattachment of the separated flow on the free end was sensitive to both AR and δ/H: reattachment occurred for the most slender and least slender cylinders (for AR = 8 and δ/H = 0.125 and AR = 1 and

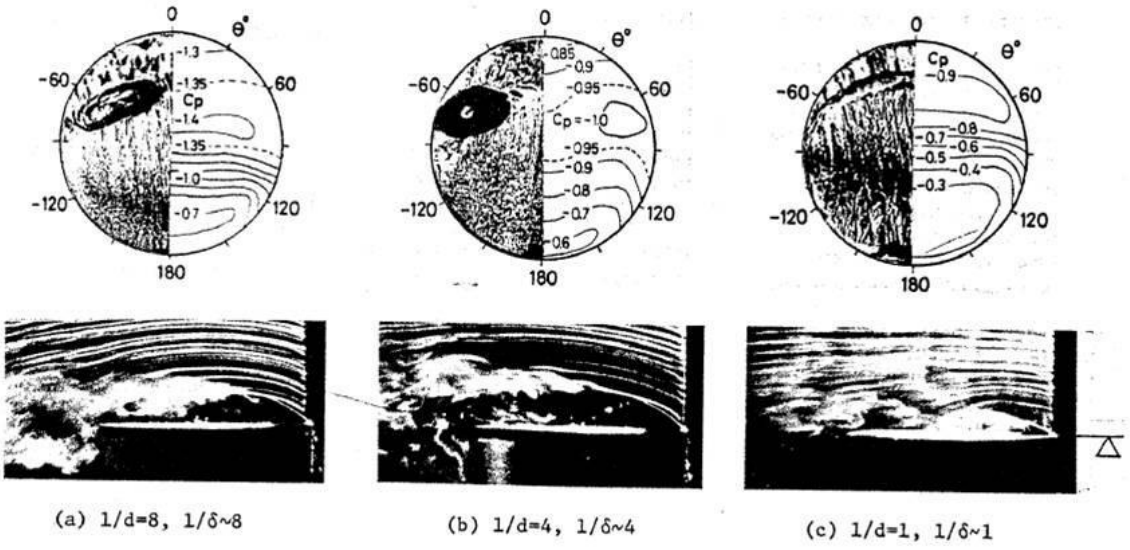

Figure 2.2: Flow pattern on the free end of a circular cylinder (Kawamura et al. 1984).

Upper row: Oil-film photographs and iso-mean pressure coefficient diagrams, Re_D = 3.2×10^4

Lower row: Smoke-wire photographs at the symmetric plane, Re_D = 1.07×10^4

δ/H = 1) but not for the intermediate cylinder (for AR = 4 and δ/H = 0.25). They attributed this difference to a more negative minimum base pressure at the tip when the aspect ratio increases. They also found that when the cylinder is fully immersed in the boundary layer, reattachment occurs due to the mixing effects of turbulence revealing the effect of δ/D or δ/H on the flow

above the free end surface. Leder (2003) studied the flow past a finite circular cylinder of AR = 2 at $Re_D = 2\times10^5$ and with $\delta/D = 0.008$ using laser Doppler velocimetry (LDV). On the central vertical plane, flow separated at the leading edge of the free-end surface and reattached close to the trailing edge, at $x/D = 0.34$ (measured from the centre of the cylinder). Weak recirculating flow was seen inside the time-mean separation bubble. Park and Lee (2004) studied the flow around the free end of a finite circular cylinder of AR = 6 at $Re_D = 7500$ using flow visualization, thermal anemometry, and PIV. On the flow centreline, reattachment of the separated flow on the free-end surface was observed. Pattenden et al. (2005) experimentally investigated the flow over a small-aspect-ratio surface-mounted finite circular cylinder of AR = 1 (well below the critical aspect ratio), using PIV, surface flow visualization, and surface pressure measurements. Their results showed flow separation at the leading edge of the free-end surface and, along the centreline, reattachment on the top of the cylinder at $x/D = 0.17$ (measured from the centre of the cylinder). Palau-Salvador et al. (2010) presented numerical and experimental results for the flow around finite circular cylinders of AR = 2.5 and 5. They also investigated the flow behavior above the free end of the cylinder of AR = 2.5 using flow visualization. According to their results, the flow separates at the leading edge and reattaches at $x/D = 0.38$ (measured from the center of the cylinder). Roh and Park (2003) used oil flow visualization within the separation zone on the free end surface to show two spiral nodes as well as vortical flow patterns.

Recently, Krajnović (2011) used large eddy simulation (LES) to study the flow around a finite circular cylinder with AR = 6 ($Re_D = 2 \times 10^4$), and reported that the flow on the top surface of the cylinder includes a large primary recirculation region and a secondary recirculation region. He showed that the large recirculation region originates at the leading edge of the cylinder and reattaches at approximately $0.82D$ from the leading edge (i.e., at $x/D = 0.32$, as measured from

the center of the cylinder) in the streamwise direction and in the symmetry plane (y = 0). The results of his simulations disagreed with the tip flow structure suggested by Roh and Park (2003) but were in general agreement with the proposals of Pattenden et al. (2005) and Kawamura et al. (1984). Figures 2.3 and 2.4 show the flow behavior above the free end surface of a circular cylinder proposed by Krajnović (2011).

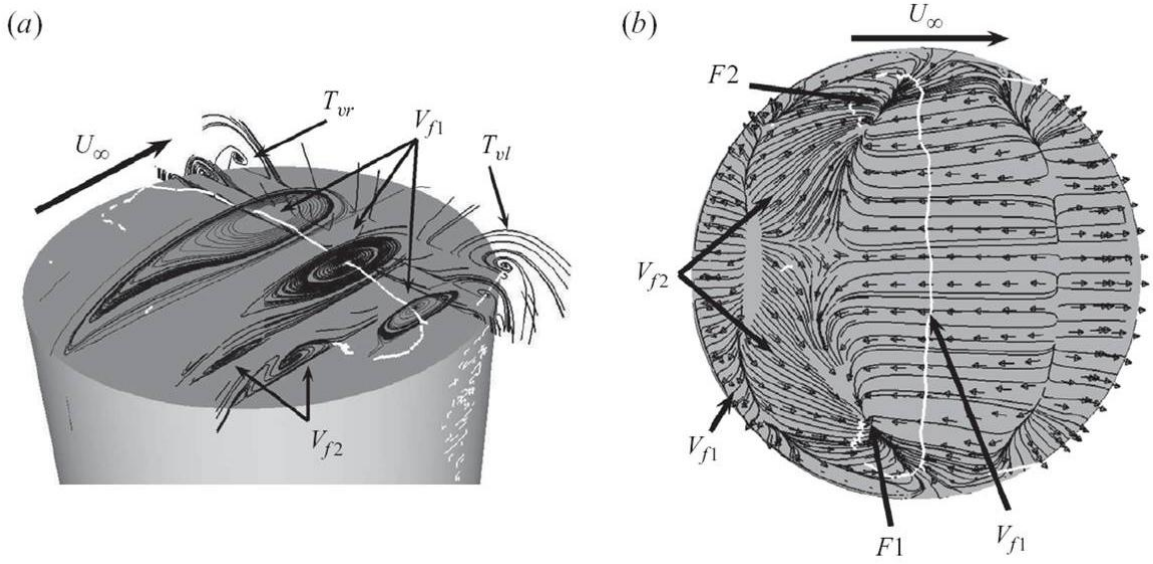

Figure 2.3: Flow pattern on the free end of a circular cylinder (Krajnović, 2011); (a): Projected streamlines on several x-y planes; T_{vr} and T_{vl} are tip vortices; (b): Particle traces and velocity vectors; V_{f1} and V_{f2} are recirculating region; F represents focal point.

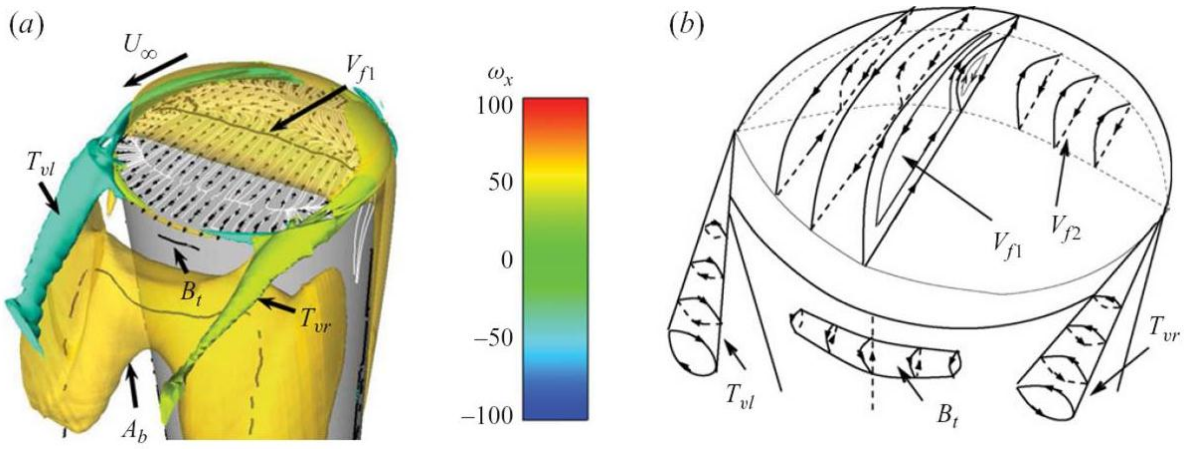

Figure 2.4: Schematic of the flow above the free end surface of a circular cylinder (Krajnović, 2011). (a): Iso-surface streamwise component of vorticity; (b): Time-averaged vortex system on and around the free end.

In terms of the wake velocity field of the finite circular cylinder, several studies have presented mean velocity, turbulence intensity and Reynolds shear stress profiles at selected locations in the wake (e.g., Okamoto and Yagita, 1973; Kawamura et al., 1984; Okamoto, 1991; Park and Lee, 2002; Frederich et al., 2007; Mahjoub Said et al., 2008; Palau-Salvador et al., 2010), often restricted to the mid-height ($z = H/2$) position. Other studies have presented whole-field measurements of the mean velocity field and turbulence fields (e.g., Tanaka and Murata, 1999; Park and Lee, 2004; Sumner et al., 2004; Pattenden et al., 2005; Adaramola et al., 2006; Hain et al., 2008; Mahjoub Said et al., 2008; Palau-Salvador et al., 2010). These studies have shown the existence of a time-averaged attached recirculation zone behind the cylinder that varies in length along the cylinder height (Tanaka and Murata, 1999; Sumner et al., 2004). The mean velocity, turbulence intensity, and Reynolds shear stress fields are similar for cylinders greater than the critical aspect ratio but have unique properties for cylinders smaller than the critical aspect ratio (Sumner et al., 2004; Adaramola et al., 2006). More recent studies have

begun to focus on instantaneous and phase-averaged representations of the wake flow field (e.g., Pattenden et al., 2005; Hain et al., 2008; Bourgeois et al., 2010; Sattari et al., 2010).

Effects of the aspect ratio of the circular cylinder on the drag of the cylinder have been recently studied by Wang et al. (2012). They showed that the values of drag and Strouhal number for a finite-height circular cylinder reduce monotonically as the aspect ratio decreases. According to their results, the dependence of the drag and Strouhal number become less significant for cylinders of AR < 3.

Recently, a number of numerical studies on the flow around a finite circular cylinder (e.g., Frohlich and Rodi, 2004; Liu et al., 2005; Afgan et al., 2007; Frederich et al., 2007; Lee et al., 2007; Pattenden et al., 2007; Mahjoub Said et al., 2008; Palau-Salvador et al., 2010; Frederich and Thiele, 2011; Frederich et al., 2011; Krajnović, 2011) have appeared in the literature. Many of these studies have focused on cylinders and prisms with aspect ratios below the critical aspect ratio.

In the present study, the effect of aspect ratio for four cylinders and prisms of AR = 9, 7, 5, and 3, as well as the effect of the cross-sectional shape (circular cylinder or square prism) on the flow structure in the near-wake region and above the free end surface of the bodies are investigated.

2.3 Flow around a Finite-height Square Prism

The flow around the prism-wall junction (at the ground plane) and over the free end of a finite-height square prism causes the local flow field to become strongly three-dimensional, such that the flow field over and above the free end of the finite-height prism influences the flow pattern in

the near-wake region, including the formation of a pair of mean streamwise trailing vortex structures in the upper wake and the downwash (downward-directed) flow associated with it. Few studies of finite circular cylinders have examined, in detail, the flow separation on the free end and its potential for reattachment. For the finite square prism, on the other hand, recent studies have focused mostly on the wake dynamics (e.g., Wang et al. (2006, 2009), Wang and Zhou (2009), Bourgeois et al. (2010, 2011), and Einian (2012)), but without considering in depth the flow above the free end of the square prism.

Some of the most extensive insight into the wake vortex dynamics (vortex shedding, streamwise vortex structures) of the finite square prism comes from recent experimental studies by Wang et al. (2006, 2009), Wang and Zhou (2009), and Bourgeois et al. (2010, 2011). These studies used a variety of experimental techniques, including flow visualization, thermal anemometry, laser Doppler velocimetry (LDV), and particle image velocimetry (PIV). Because of the complexity of the flow field around the surface-mounted finite-height square prism, and the many influencing parameters, further study is needed to obtain a complete physical understanding of the wake behavior, especially very close to the prism, i.e., the local flow field.

A comprehensive experimental investigation on the near wake of a finite square-prism immersed in a boundary layer was reported by Wang and Zhou (2009). In their study, the PIV technique was used for measurements of velocity fields in the near-wake region of the prism. LDV was used for the velocity measurements in the x-z plane at $y/D = 0$ in order to show the boundary layer characteristics as well as the time-averaged velocity fields in the near-wake region. Furthermore, hot-wire anemometry (HWA) was used to measure the streamwise velocity fluctuations in order to determine the vortex shedding frequency of the prism. All three of the above-mentioned techniques were used for obtaining quantitative information of the flow field

near the prism with different aspect ratios of AR = 3, 5, 7, 9, and 11. Flow visualization was also performed simultaneously in two orthogonal planes of *x*-*y* at *z*/*D* = 6 for AR = 7, and *x*-*z* at *y*/*D* = 0 in order to capture the three-dimensional (3-D) aspects of the vortical structures and the interaction between the free end and the spanwise shear layers. Flow visualization was also performed at different spanwise locations of *z*/*D* = 1 and *z*/*D* = 3.5 for the prism with AR = 7. They focused on the wake of the finite-height square prism which is characterized by three vortical structures: longitudinal tip and base vortices, and the spanwise Kármán vortex shedding. The interaction between these three types of vortices makes the near wake of the prism highly three-dimensional. According to their PIV measurements of the instantaneous velocity field, two distinct types of instantaneous streamlines were observed. The first type, which is topologically similar to the time-averaged streamlines, is characterized by meeting of the downwash flow from the free end and the upwash flow from the wall. Also, a saddle point is observed in this case due to the interaction between upwash and downwash flows. The second type, which seems more complicated, shows more critical points including two saddle points, three foci and one node. Two saddle points result from the interaction between the upwash flow or downwash flow and the spanwise shear flow. The counter-rotating foci are associated with the mushroom-like longitudinal rib structures which are inherently associated with spanwise vortex rolls. This means that the flow topology of the second type of the instantaneous streamlines is linked to the occurrence of the spanwise vortex shedding. In the second type of instantaneous streamlines, the presence of the node is ascribed to the roll up of the spanwise shear layer which sweeps across the *x*-*z* plane at *y*/*D* = 0. In the first type of streamlines, the upwash and downwash flows are dominant due to absence of spanwise vortex shedding at that instant. Also, the resemblance of this type of instantaneous streamlines with the time-averaged streamlines is due to the fact that

the rib structures and hence the foci and nodes occur rather randomly in time and also in the streamwise and spanwise locations. Consequently these critical points are averaged out.

According to the PIV measurements in *y-z* planes at different *x/D* locations, Wang and Zhou (2009) reported two distinct flow patterns which are consistent with their observations in the *x-z* planes. In the first flow pattern, the vortical structures can only be observed on one side of the prism over most of the cylinder span. This corresponds to the roll up of the spanwise shear layer sweeping across the *x-z* plane at $y/D = 0$, resulting in the antisymmetrically arranged spanwise vortices. The second type of flow pattern in the *y-z* planes is characterized by two pairs of counter rotating vortical structures which are symmetrically arranged about the prism. One pair is located near the free end of the prism while the second pair is located near the wall. A physical model was proposed by Wang and Zhou (2009) for the near wake of a finite square prism based on their PIV, LDA, and HWA measurements. Their proposed model is shown in Figure 2.5. According to this model, the spanwise vortices from both sides of the prism are connected with each other near the free end causing the formation of an arch-type vortex. The arch-type vortex has two legs which are partially immersed in the wall boundary layer.

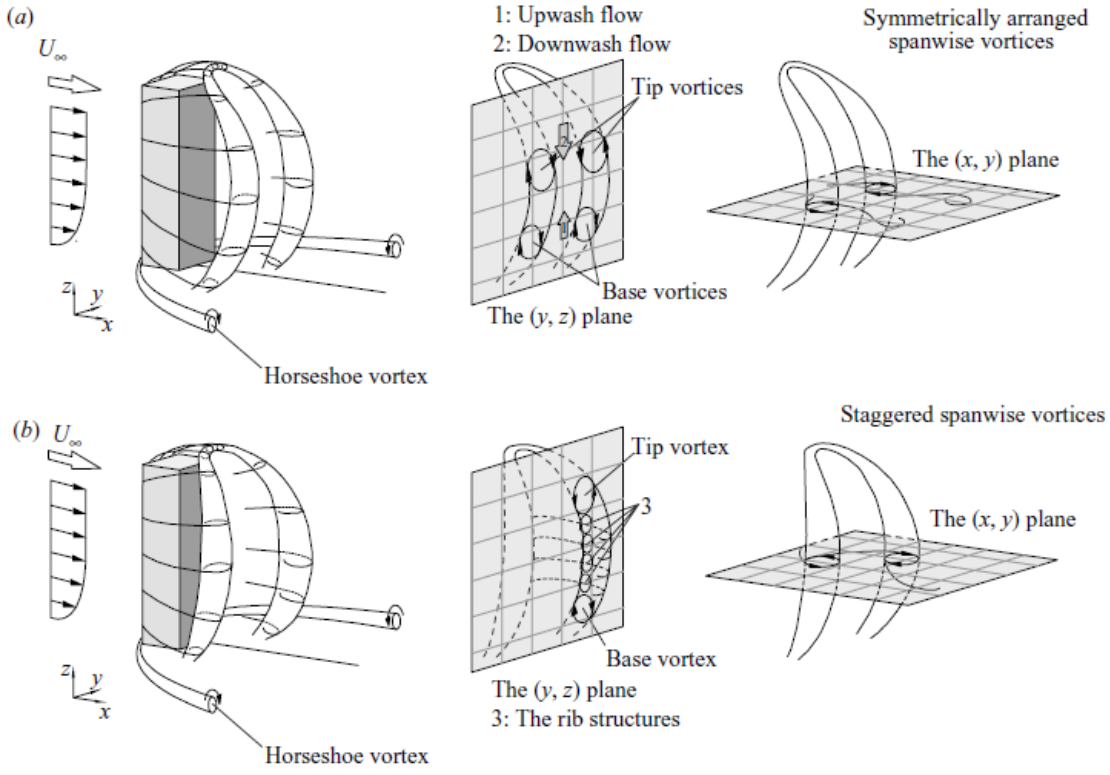

Figure 2.5: A schematic model of the flow structure around a surface-mounted finite square prism (Wang and Zhou, 2009). (a): Symmetrically arranged two spanwise vortex roll; (b): Staggered arranged spanwise vortex roll.

These legs join each other near the free end of the prism. Because of the downwash flow from the free end and the boundary layer of the wall, both upper and lower parts of the arch-type vortex structure are inclined upstream and towards the prism. According to their proposal, there are two configurations of the instantaneous near wake flow structure: one with spanwise vortices symmetrically arranged and the other with two staggered spanwise vortex rolls. In the first case, when the symmetrically arranged spanwise vortices join each other near the free end, the two

spanwise vortex rolls are inclined upstream forming a pair of symmetrical tip vortices in the *y-z* plane close to the prism. There is another pair of vortices (base vortices) in the *y-z* plane near the wall due to the incline of the spanwise vortex rolls upstream. In this case, where the spanwise vortices are symmetrically arranged, the spanwise shear flow does not sweep across the *x-z* plane at $y/D = 0$ and hence the downwash and upwash flows are predominant in the *x-z* planes. In the second type of near wake structure, the corresponding spanwise vortices are antisymmetrically arranged in the *x-y* plane. In this case, the longitudinal rib structure occurs on one side of the prism in the *y-z* plane. According to Wang and Zhou (2009), both antisymmetrical and symmetrical configurations were observed along the cylinder span. The probability of antisymmetrically arranged vortices is large at the middle of the prism span, reducing towards the prism free end or the ground plane. According to their Reynolds stress measurements, the antisymmetrical vortices are associated with larger Reynolds stresses than the symmetrical vortices. The spanwise variation of Reynolds stresses in the near wake correlates with the probability of the vortex configurations and that is why the stresses are stronger about the mid span of the prism and weaker close to the free end.

The near wake of a finite square prism of AR = 4 was experimentally investigated by Bourgeois et al. (2011). They used PIV to measure phase-averaged data in *x-y* and *x-z* planes. According to their planar data, the three-dimensional large scale structure of the near wake of the prism was educed. In order to phase-align the PIV planar measurements, simultaneous measurements of the surface pressure difference on either side of the prism were used. According to the topological analysis presented in their study, they proposed a physical model for the vortex structure in the near wake of the prism. Furthermore, they offered a contrasting interpretation of the mean streamwise vorticity which has been presumed to originate from

structures generated at the leading edge of the free end. In their work, they studied the mean streamwise vorticity distribution which was of either quadruple type (four patches of alternating sense of rotation for prisms with aspect ratios larger than the critical aspect ratio) or dipole type (two patches of vorticity of alternating sense for prisms with aspect ratios less than the critical aspect ratio). According to the literature, as the aspect ratio of the prism is reduced, the changes occur in topology from antisymmetric "Karman-type" to symmetric "arch-type" vortex shedding. However, Bourgeois et al. (2011) showed that the vortex topology remains anti-symmetric despite a dipole-type mean streamwise vorticity.

Bourgeois et al. (2011) presented a vortex skeleton model with a vertical arch structure in the recirculating region interlaced with a streamwise hairpin at the top of the wake consistent with the rotational flow field. Their proposed model is shown in Figure 2.6.

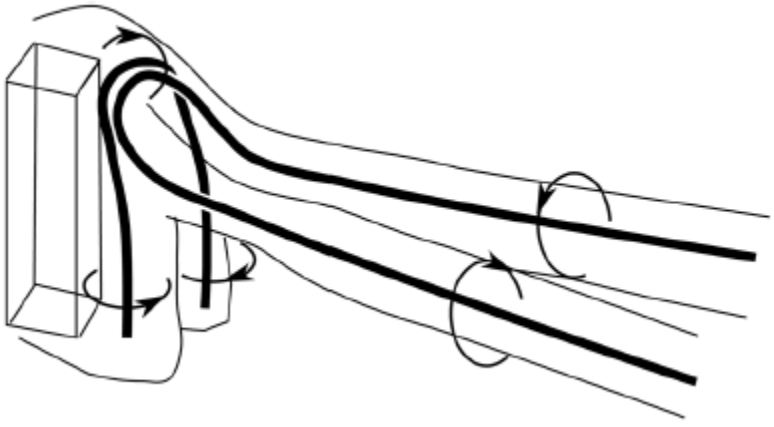

Figure 2.6: Model of the educed mean vortex structure proposed by Bourgeois et al. (2011).

Bourgeois et al. (2011) also proposed a model (shown in Figure 2.7) based on their results of the phased-averaged flow structure. The topology educed was that of alternating half-loop structures which have a leading principal core which is nearly vertical at the ground plane where the vortex lines are deflected horizontally outwards at the ground plane surface and the shed vortices interact with boundary layer vorticity. In their half-loop shed structure proposal, there are streamwise connector strands due to the Biot-Savart induction of the crosswise vorticity, ω_y , by the free-end shear layer on the vertical columnar vortex formed by the rollup of the side-face shear layer and its own self induction. Bourgeois et al. (2011) also presented a phase-averaged wake with strong interaction between the prism free end and the ground plane end-conditions as alternately shedding initially vertical vortices. These vortices are then deformed by the free-end shear layer vorticity. The vortex structures will then have a vertical principal core near the wall due to this deformation while the upper portion of the vortex structure is reoriented upstream and then connects to the preceding structure, which is shedding on the opposite side of the wake. The streamwise vorticity of the connector strands provides an explanation for the mean streamwise vorticity which is in contrast to the explanation about tip vortices in the previous studies.

2.3 Summary

As mentioned above, relatively few studies have focused on the turbulent near wake of a finite-height circular cylinder or square prism. Also, there are a few studies of the flow above the free ends of finite circular cylinders (mentioned in Section 2.1), while there are no studies on the flow above the free end of square prisms with, perhaps, the exception of cubes. Hence, comprehensive information about the flow behavior including velocity fields as well as turbulence characteristics of the near wake and of the flow above the free end surface are not

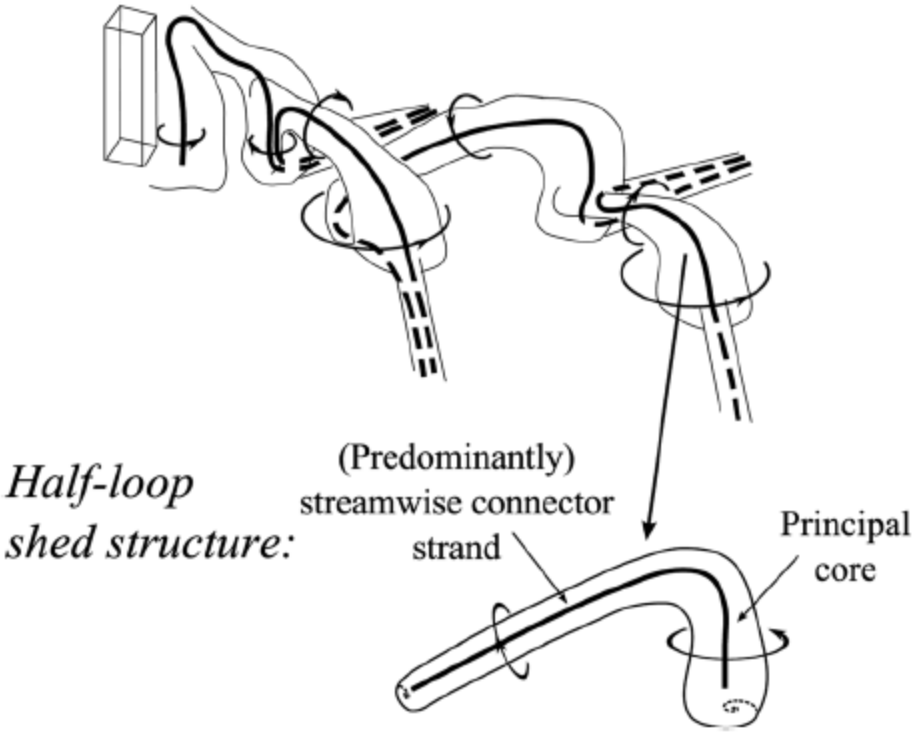

Figure 2.7: Model of educed phase-averaged vortex structure (Bourgeois et al., 2011).

available in the literature perhaps due to the lack of experimental data and numerical simulations on the near-wake flow and the flow above the free end. Therefore, further study of these local flow fields is of interest in order to obtain a complete understanding of the flow behavior around and above the free end surface of the circular cylinders and square prisms. The effect of cylinder/prism aspect ratio on these local flow fields, and the influence of bluff body shape (circular or square cross-section), have not yet been extensively addressed. Hence, the focus in this research is to address important characteristics of the flow in the near-wake region and above the free end surface of surface-mounted finite-height circular cylinders and square prisms of different aspect ratios.

3. Experimental Set-up and Instrumentation

3.1 Introduction

In this chapter, the experimental set-up and the instrumentation used for the thesis research are described and explained. The wind tunnel facility as well as the PIV set-up and the associated instrumentation are described in Sections 3.2 to 3.8.

3.2 Wind Tunnel

The wind tunnel used in the thesis research is a low-speed and closed-return type. This wind tunnel is located in the Department of Mechanical Engineering, University of Saskatchewan. Airflow inside the wind tunnel is supplied by a constant-speed variable-pitch fan powered by a 100-hp electric motor. This fan can provide freestream velocities up to U_∞ = 50 m/s within the test section. A schematic representation of the wind tunnel is shown in Figure 3.1. As shown in this figure, the airflow passes through a diffuser downstream of the fan. The flow expands while passing through the diffuser and then passes through two sets of turning vanes located at the top and bottom corners to smooth out the velocity profiles and reduce losses of the flow being redirected by 180°. The flow then passes through a pair of turbulence reduction screens located at the exit of the turning vanes. These screens reduce the turbulence intensity of the airflow. The flow then enters a large settling chamber with dimensions of 2.97 m (height) × 2.4 m (width) × 7.0 m (length). A contraction section with a 7:1 contraction ratio is located downstream of the settling chamber to increase the freestream velocity. After the contraction section, the airflow enters the test section of the wind tunnel. The dimensions of the test section are 0.91 m (height) × 1.13 m (width) × 1.96 m (length). The streamwise freestream turbulence intensity inside the test section is less than 0.6% over the range of freestream velocities, and the mean velocity non-

uniformity outside the test section wall boundary layers is less than 0.5%. Note that the exact values of these parameters depend on the operating speed of the wind tunnel. The test section is fitted with an aluminum ground plane which contains a turntable controlled by computer for mounting test models. A fully-developed turbulent flat-plate boundary layer is produced on the ground plane at the location of the test models.

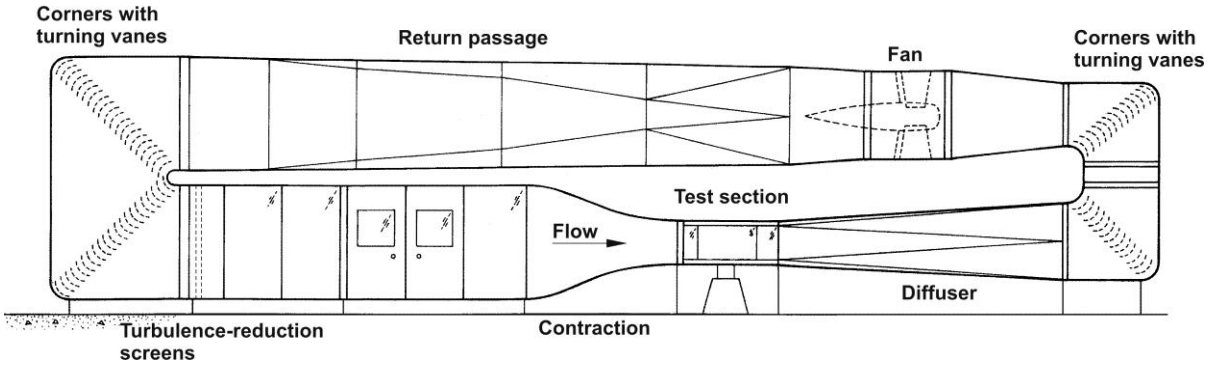

Figure 3.1: Schematic of the low-speed wind tunnel.

Inside the test section, there is also a three-axis, computer-controlled traversing system for positioning hot-wire probes, pressure probes, etc., in order to have automated flow measurements at different positions. The traversing wing is positioned by three stepper motors to move in the three coordinate directions of *x*, *y*, and *z*. The stepper motors are controlled by computer using LabVIEW software, an NI PCI7344 motor controller card in the computer, and IMS 1007 microstep drivers. The traversing wing is also equipped with limit switches in all three directions in order to avoid contacting the measuring probe mounted on the wing with the ground plane, test section walls, and test models. The positioning precision of the traversing system is

0.006 mm, 0.012 mm, and 0.013 mm in the *x*, *y*, and *z* direction, respectively. However, there may be larger errors in the movements of the traverse due to slip, particularly for the *y* and *z* directions.

The wind tunnel data are acquired using a computer with a 1.8-GHz Intel Pentium 4 processor, a National Instruments SCXI 1140 signal conditioner module connected to a PCIe-6259 16-bit 1.25 MS/s (mega samples per second) data acquisition board, and LabVIEW software.

3.3 Pressure Probes

The freestream conditions were obtained using a United Sensor, 3.2-mm-diameter Pitot-static probe, a 600A-1000T-513-H21X-4 Datametrics Barocell absolute pressure transducer, a 590D-10W-2QB-VIX-4D Datametrics Barocell differential pressure transducer, and an Analog Devices AD590 integrated circuit temperature transducer. To measure the freestream temperature, T_∞, the temperature sensor was located downstream of the test section and connected to the wind tunnel data acquisition system. However, recently, the temperature inside the test section is being measured using a thermocouple mounted in the Pitot-static probe mounted on the test section's side wall. The absolute pressure transducer was used to measure the absolute freestream static pressure, P_∞, and the differential pressure transducer was used to measure the freestream dynamic pressure, q_∞. The Pitot-static probe was mounted on the side wall of the test section 400 mm above the ground plane, 400 mm downstream of the test section entrance, and extending 160 mm into the test section. This location of the probe eliminated the wall-proximity effects on the probe.

As mentioned in Section 3.2, a turbulent flat-plate boundary layer is produced on the ground plane at the location of the models inside the test section of the wind tunnel. To characterize the boundary layer on the ground plane, a United Sensor boundary layer Pitot tube of model BA-0.025-12-C-11-0.650 with an outer diameter of d_p = 0.6 mm was used to measure the mean velocity profile of the boundary layer. The probe was mounted to the traversing wing and was connected to a Validyne Model P55D differential pressure transducer. To examine the development of the boundary layer mean velocity profile, boundary layer Pitot tube measurements were taken at five locations of $x/D = -10, -5, 0, 5$, and 10, where D is the model diameter (31.5 mm), and $x/D = 0$ is the location of the test models which is approximately 900 mm from the leading edge of the ground plane. At each location, the Pitot tube was traversed from the ground plane up to the boundary layer edge where the local velocity is 99% of the freestream velocity. The sampling frequency for the pressure measurements was 5 kHz.

The density of the air (ρ_∞) was calculated using the ideal gas equation,

$$\rho_\infty = \frac{P_\infty}{RT_\infty}, \tag{3.1}$$

where R is the gas constant for air (287 J/kgK), T_∞(K) is the freestream temperature, and P_∞ (Pa) is the absolute freestream static pressure. The kinematic viscosity of the air, ν_∞, is calculated using the Sutherland correlation as given below (White, 2003):

$$\nu_\infty = 1.453 \times 10^{-6} \frac{{T_\infty}^{1.5}}{\rho_\infty (T_\infty + 110.4)}. \tag{3.2}$$

3.4 Hot-wire Anemometry Probe

In addition to the boundary layer Pitot tube (Section 3.3), an X-wire boundary layer probe was used to measure the mean velocity profile as well as the turbulence intensity profiles of the boundary layer. In this research, a constant temperature anemometer (CTA) type of thermal anemometry was employed. For this type of anemometry, the heat is transferred between the heated wire sensor and the flow. Due to the heat transfer, the resistance of the sensor changes which results in changes in the voltage from the anemometer output. This output voltage is then applied to the circuit in order to have a constant wire temperature. The velocity of the flow is then determined from the output voltage.

The X-wire probes have the ability to measure both the mean and fluctuating components of the velocity in a flow. The probe used was a TSI model 1243-20 boundary layer cross-wire (X) probe. The sensors of this probe were made of platinum wire of diameter 50.8 μm, and a sensing length of 1.02 mm. The distance between the supports of this probe is 1.65 mm. This probe was oriented in a way that it measured the streamwise, u, and wall-normal, w, components of the velocity field of the boundary layer. The probe was traversed to different measurement points using the wind tunnel traversing system. Measurements were taken at a sampling frequency of 1 kHz.

Variable-angle calibration of the X-wire probe was performed using a Dantec Dynamics 90H02 Flow Unit calibrator fitted with a yaw-roll manipulator. Pressurized air was supplied to the unit from an external source, and was filtered and regulated before entering the calibrator unit. An MKS model 1559A mass flow controller was added upstream of the calibrator to improve the accuracy and steadiness of the flow rate during the calibration. The calibrator creates a free jet with a uniform, low-turbulence velocity profile, in which the probe is immersed.

The velocity magnitude set-points are controlled from the Dantec StreamWare software and the yaw angle (α) set points of the probe were set manually. For each velocity-yaw angle pair (U, α), a unique voltage pair (E_1, E_2) was obtained. The probe was positioned in a way that the velocity component, v, perpendicular to both wires had a magnitude of zero. During the calibration, the reference ambient temperature was kept constant at 22°C. The signal from each sensor was offset and filtered, and then sampled at a sampling frequency of 2.5 kHz for 30,000 samples. The calibration was performed at eight velocity magnitudes (ranging from 5 m/s < U < 40 m/s in increments of 5 m/s), and nine values of yaw angle (ranging from -35° < α < +35° in increments of 10°), for a total of 72 calibration set points. For each individual calibration set point, comprising U, and α, two mean voltages were acquired, E_1, and E_2, each corresponding to one of the two wires. The calibration data reduction method used for the present data was the one proposed by Oster and Wygnanski (1982) as:

$$U = a_1E_1^3 + a_2E_1^2 E_2 + a_3E_1 E_2^2 + a_4 E_2^3 + a_5E_1^2 + a_6E_2^2 + a_7 E_1E_2 + a_8E_1 + a_9E_2 + a_{10} \quad (3.3)$$

$$\alpha = b_1E_1^3 + b_2E_1^2 E_2 + b_3E_1 E_2^2 + b_4 E_2^3 + b_5E_1^2 + b_6E_2^2 + b_7 E_1E_2 + b_8E_1 + b_9E_2 + b_{10} \quad (3.4)$$

where a_1 to a_{10} and b_1 to b_{10} are constant coefficients which were obtained using the TableCurve 3D Software.

The uncertainties in the velocity magnitude, and yaw angle of the calibration data set, were estimated as ±0.2 m/s, and ±1°, respectively.

3.5 Characteristics of the Ground Plane Boundary Layer

A set of experiments was carried out to investigate the characteristics of the boundary layer that forms on the ground plane and partially covers the models inside the test section of the wind tunnel. Two freestream velocities of U_∞ = 20 m/s and 30 m/s were used for the boundary layer investigation. These experiments were performed with the cylinder or prism removed, and the velocity measurements were taken using the boundary layer Pitot tube and the X-wire boundary layer probe.

Tables 3.1 and 3.2 present a summary of the turbulent boundary layer characteristics for freestream velocities of U_∞ = 20 m/s and 30 m/s, respectively. In these tables, the distance of 900 mm from the leading edge of the ground plane (x/D = 0) is the location of the models inside the test section. The Reynolds number, Re_x, is based on the distance measured from the leading edge of the ground plane, and the Reynolds number, Re_θ, is based on the momentum thickness (θ) obtained by numerical integration of the experimental velocity data. According to Table 3.1, the boundary layer thickness is δ = 51 mm at the location of the cylinders and prisms.

To check whether the boundary layer was fully developed, the velocity profiles were measured at different streamwise locations of 600 mm, 750 mm, 900 mm (location of the model), 1050 mm, and 1200 mm from the leading edge of the flat plate. Figure 3.2 shows the time-averaged streamwise velocity profiles of the ground plane boundary layer at three locations for U_∞ = 20 m/s. According to this figure, the mean velocity profiles collapse onto a common curve. No tripping device was used for the boundary layer; rather, the boundary layer was allowed to naturally develop from the leading edge of the ground plane.

Table 3.1: Characteristics of the turbulent flat-plate boundary layer used in the wind tunnel, U_∞ = 20 m/s. δ, δ^*, and θ are the boundary layer thickness, displacement thickness, and momentum thickness, respectively, and $H_\delta = \delta^* / \theta$ is the shape factor.

x/D	δ (mm)	δ^* (mm)	θ (mm)	H_δ	$Re_x \times 10^{-6}$	Re_θ
-10	41	4.6	3.76	1.22	0.826	5179
-5	46	5.16	4.19	1.23	1.015	5670
0	51	5.72	4.59	1.25	1.162	5927
5	54	6.07	4.88	1.24	1.415	6573
10	56	6.27	5.04	1.24	1.620	6804

Table 3.2: Characteristics of the turbulent flat-plate boundary layer used in the wind tunnel, U_∞ = 30 m/s.

x/D	δ (mm)	δ^* (mm)	θ (mm)	H_δ	$Re_x \times 10^{-6}$	Re_θ
-10	42	4.46	3.68	1.21	1.211	7430
-5	46	4.94	4.05	1.22	1.487	8030
0	50	5.44	4.44	1.23	1.819	8972
5	54	5.68	4.63	1.23	2.123	9362
10	56	5.89	4.80	1.23	2.426	9706

Figures 3.3 and 3.4, respectively, show the time-averaged streamwise and wall-normal turbulence intensity profiles measured at three locations of 600 mm, 900 mm (location of the model), and 1200 mm from the leading edge of the flat plate. In these figures, the turbulence intensities, u' and w', were normalized by the freestream velocity, and the normal distance from the ground plane was normalized by the boundary layer thickness at the corresponding streamwise distance. These figures indicate that at the location of the model (x/D = 0), the flat-plate boundary layer is not yet fully developed, despite the fact that the mean velocity profiles at different streamwise locations collapsed to each other showing a self-similar behavior.

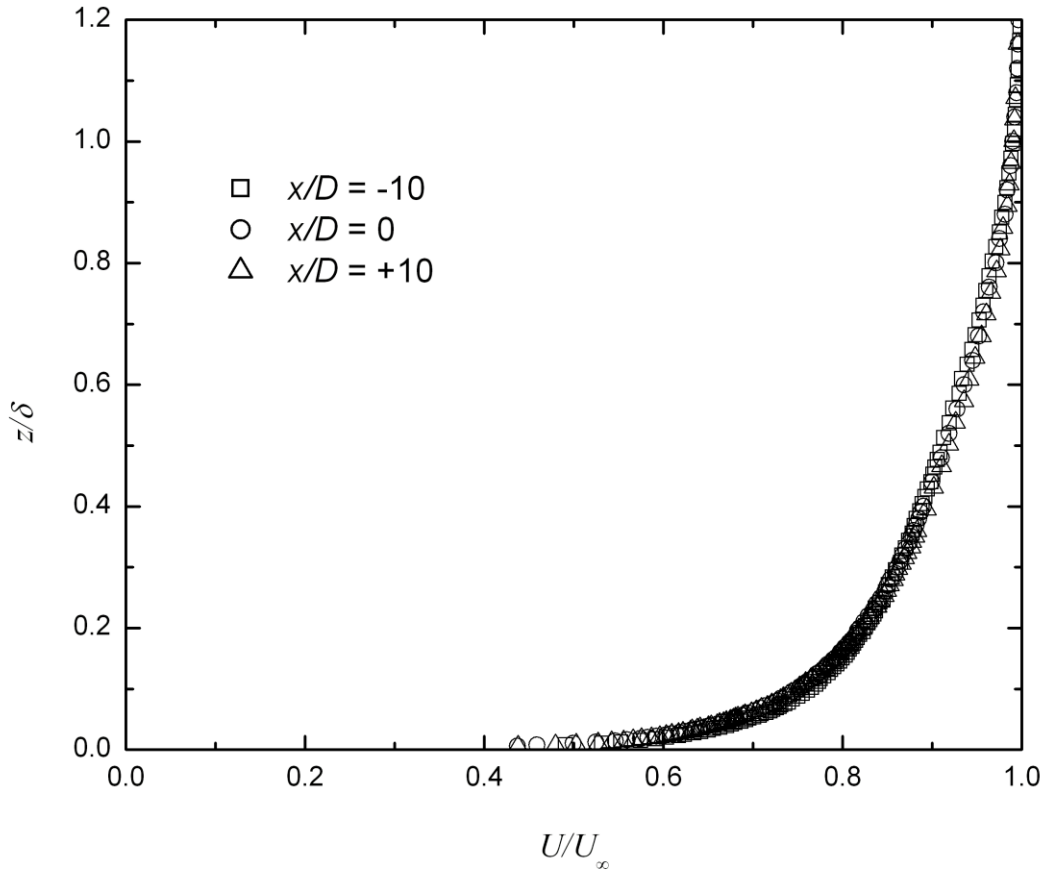

Figure 3.2: Mean streamwise velocity profiles of the turbulent boundary layer on the ground plane (with the cylinder/prism removed) at different streamwise locations in a freestream velocity of U_∞ = 20 m/s.

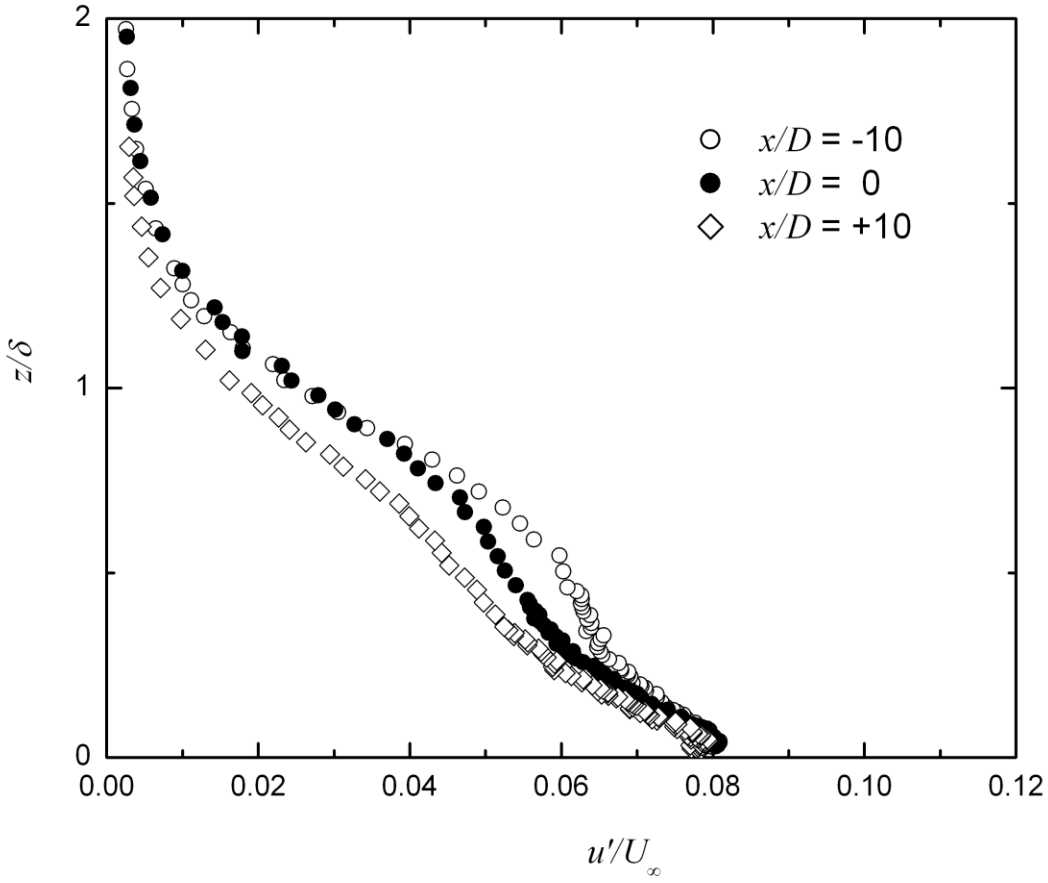

Figure 3.3: Streamwise turbulence intensity profiles of the boundary layer on the ground plane at three streamwise locations in a freestream velocity of U_∞ = 30 m/s.

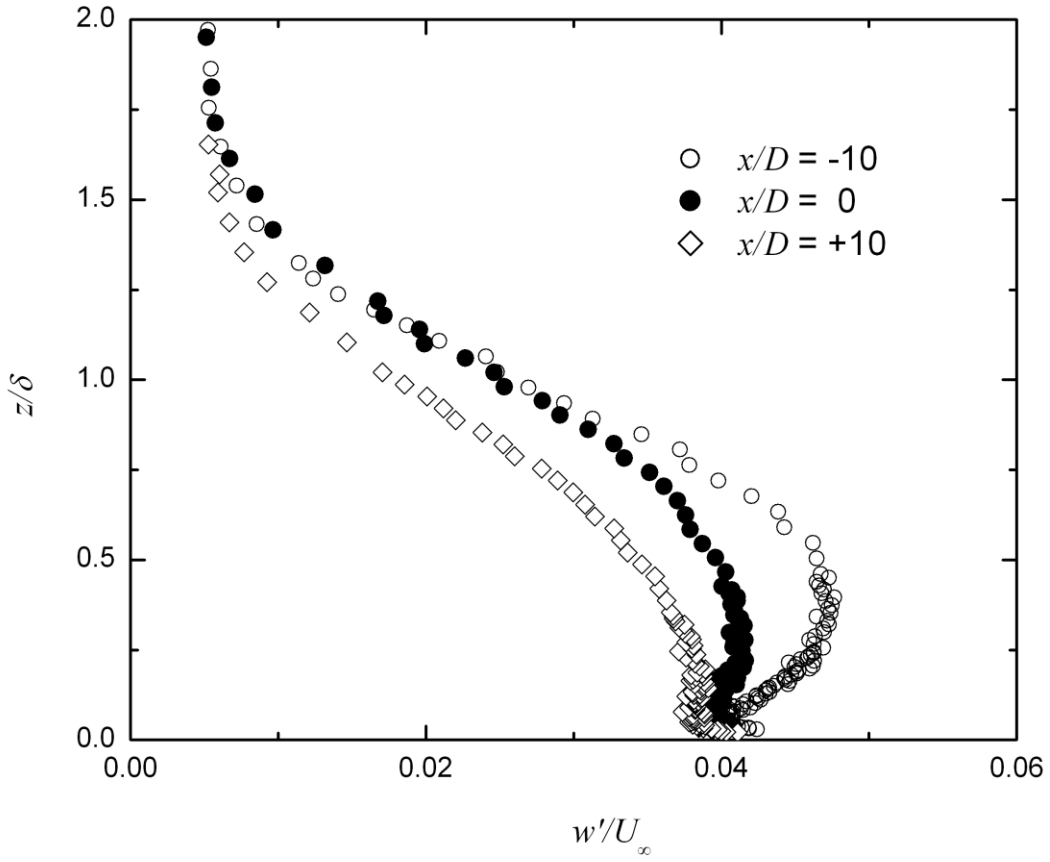

Figure 3.4: Wall-normal turbulence intensity profiles of the boundary layer on the ground plane at three streamwise locations in a freestream velocity of U_∞ = 30 m/s.

Figure 3.5 shows a comparison between the boundary layer velocity profiles measured in the wind tunnel. The present boundary layer profile measured by the Pitot tube probe is in good agreement with the Pitot tube data of Igbalajobi (2011) and the PIV data measured by Akon (2012). The present data are also compared to the familiar 1/7th power law in Figure 3.5 showing that the present flat-plate boundary layer can be considered a typical turbulent flat-plate boundary layer.

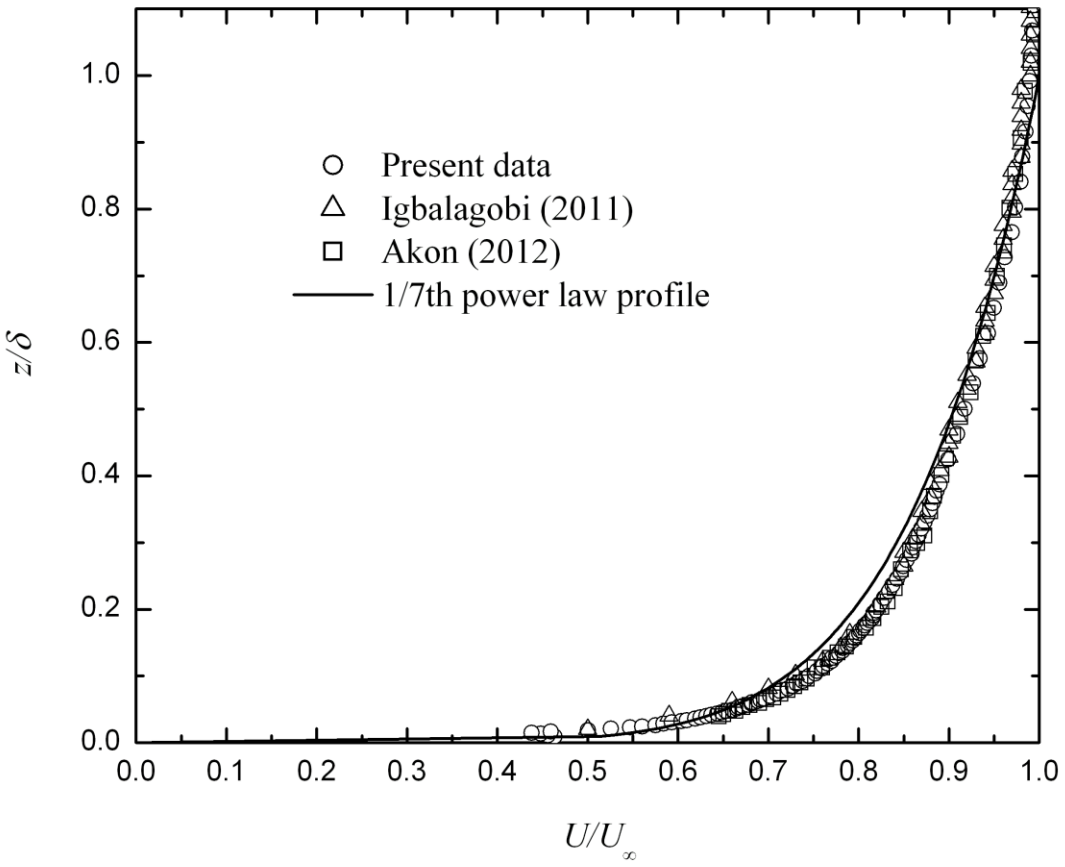

Figure 3.5: Comparison of the boundary layer mean velocity profiles at the location of the model (900 mm from the leading edge of the ground plane) and at a freestream velocity of U_∞ = 20 m/s.

3.6 Experimental Models

3.6.1 Finite-height Circular Cylinder Models

Four different, smooth, aluminum circular cylinder models, all of the same diameter, D = 31.5 mm, were used for the finite-height circular cylinder experiments. The free end of each cylinder was a flat surface with sharp circumferential edge. Each cylinder had a different height, giving cylinders with aspect ratios of AR = 9, 7, 5, and 3 (shown in Figure 3.6), similar to the experiments of Sumner et al. (2004) and Adaramola et al. (2006). The cylinders were anodized flat black to minimize unwanted reflections from the laser light sheet used for the PIV measurements. The cylinder model being tested was mounted to a six-component force balance below the test section at a distance of 900 mm from the leading edge of the ground plane. The cylinder extended vertically into the test section through a hole in the ground plane, with a circumferential gap of about 1 mm around the cylinder, and was partially immersed in the turbulent boundary layer on the ground plane. The solid blockage ratio was at most 0.9% and no wall interference corrections were made. The experiments were conducted at a freestream velocity of U_∞ = 20 m/s, giving a Reynolds number, based on cylinder diameter, of Re_D = 4.2 $\times 10^4$. These models were used to show the effect of AR of the cylinder and the prism on the flow structure in the near-wake region and above the free end surface of the bodies. In addition, as the AR changes, the ratio of the boundary layer thickness to the diameter/width of the cylinder/prism changes. So that the effect of AR and boundary layer thickness on the flow structure are investigated at the same time.

Figure 3.6: Finite-height circular cylinder models.

3.6.2 Finite-height Square Prism Models

Four smooth, aluminum square prism models of the same side length of D = 31.5 mm, were tested for the finite-height square prism experiments. Similar to the circular cylinder models, each square prism had a different height, giving prisms with aspect ratios of AR = 9, 7, 5, and 3 (shown in Figure 3.7). The square prisms had sharp edges on all sides causing the approaching flow to be separated from the leading edges and resulting in a different flow pattern around the prisms compared to the circular cylinders. The experiments performed for the square prisms were the same as those used for circular cylinders described in Subsection 3.6.1. However, the prisms were mounted to the six-component force balance below the test section in a way that

there was a small vertical gap (less than 1 mm) between the bottom of the prisms and the ground plane.

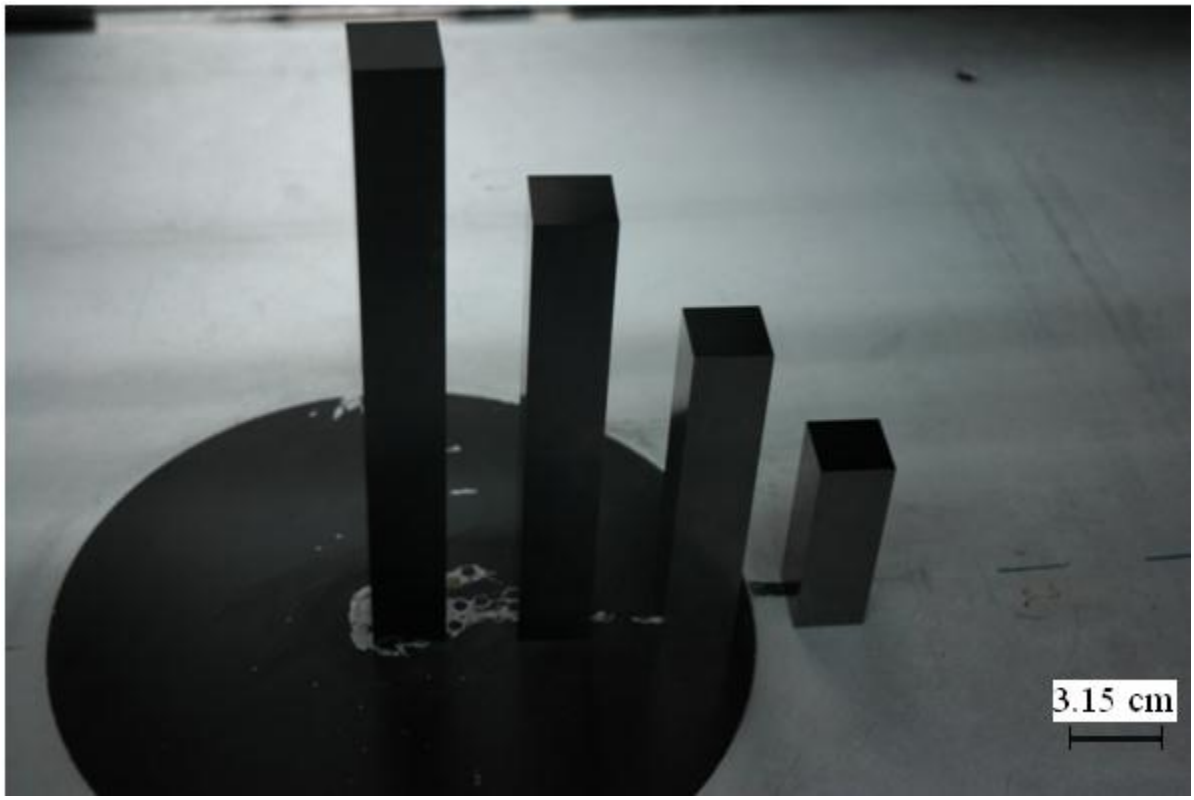

Figure 3.7: Finite-height square prism models.

3.7 PIV Measurement System

3.7.1 PIV Measurements of the Near-wake Flow in *x*-*z* Planes

Velocity field measurements in the vicinity of the finite cylinders and prisms were made with a two-dimensional PIV system. A 532-nm laser light was supplied by a 200-mJ/pulse dual Nd:YAG Gemini PIV 15 laser from New Wave Research, which had a maximum pulse frequency of 15 Hz. A TSI light arm was used to deliver the laser beam from the laser to the light sheet optics. The light sheet optics included a -50-mm or -25-mm cylindrical lens and a 500-mm, 750-mm, or 1000-mm spherical lens, depending on the location of the field of view. Images were acquired with a CCD camera (MegaPlus ES4020, double frames, 2048 × 2048 pixels) and captured by a 64-bit EDT PCI DV C-Link frame grabber on a computer workstation. The lens used for the imaging of the particles was an AF Micro Nikkor 200-mm f/4 fixed-focal-length lens. The timing of the laser, camera, and frame grabber was controlled by a Berkeley Nucleonics 505-8C digital delay generator synchronizer. PIV measurements were made in vertical (*x*-*z*) planes (refer to Figures 1.1 and 2.1 for the coordinate system) located on the centreline of the test section ($y = 0$). The light sheet optics were located above the wind tunnel test section and the laser light was directed through a small aperture in the test section roof and towards the ground plane. Great care was taken to ensure the light sheet was aligned with the flow centreline. The camera was located outside the wind tunnel test section's side wall. The field of view was 61 mm × 61 mm (1.9*D* × 1.9*D*) yielding an image resolution of about 30 μm/pixel. For the tallest cylinder or prism (of AR = 9), more than 25 fields of view were used to build a composite picture of the flow field upstream and downstream of the cylinder. Figure 3.8 shows the position of the 25 fields of view in the wake region of a cylinder or prism of AR = 9. In this figure, the number of each field of view is placed at the center of the field of view. For

each field of view, an ensemble of 1,000 sample images was acquired from which the mean velocity vector field was determined. Image pairs were processed with a half-padded FFT cross-correlation algorithm, a relative maxima peak detection algorithm, and a Gaussian sub-pixel interpolation algorithm. A Hart correlation-based (CBC) validation method (Hart, 2000) with 50% overlap was used for reducing the sub-pixel errors and eliminating spurious vectors from the PIV results. The cellular neural network (CNN) method (Shinneeb et al., 2004) together with dynamic threshold outlier identification was used as a post-interrogation algorithm to detect spurious vectors in the PIV measurements. According to the used outlier identification method, the fraction of the rejected vectors in most cases was varied in the range of 5% - 8% indicating acceptable results from the present data. Most fields of view were analyzed with initial interrogation areas of 32 × 32 pixels. Owing to large pixel displacements in some limited regions of the flow, initial interrogation sizes of 64 × 64 pixels were used in the remaining fields of view. In all cases a two-level analysis technique was used that halved the interrogation area size during the second pass. In addition, a 50% interrogation area overlap was used in all cases. The resulting velocity vector fields contained approximately 127 × 127 and 63 × 63 velocity vectors with a vector spacing (spatial resolution) of approximately 0.015D and 0.03D, respectively. This spatial resolution is significantly greater than the seven-hole probe experiments of Sumner et al. (2004), the X-probe measurements of Adaramola et al. (2006), and the PIV studies of Wang and Zhou (2009) and Park and Lee (2004) in the literature.

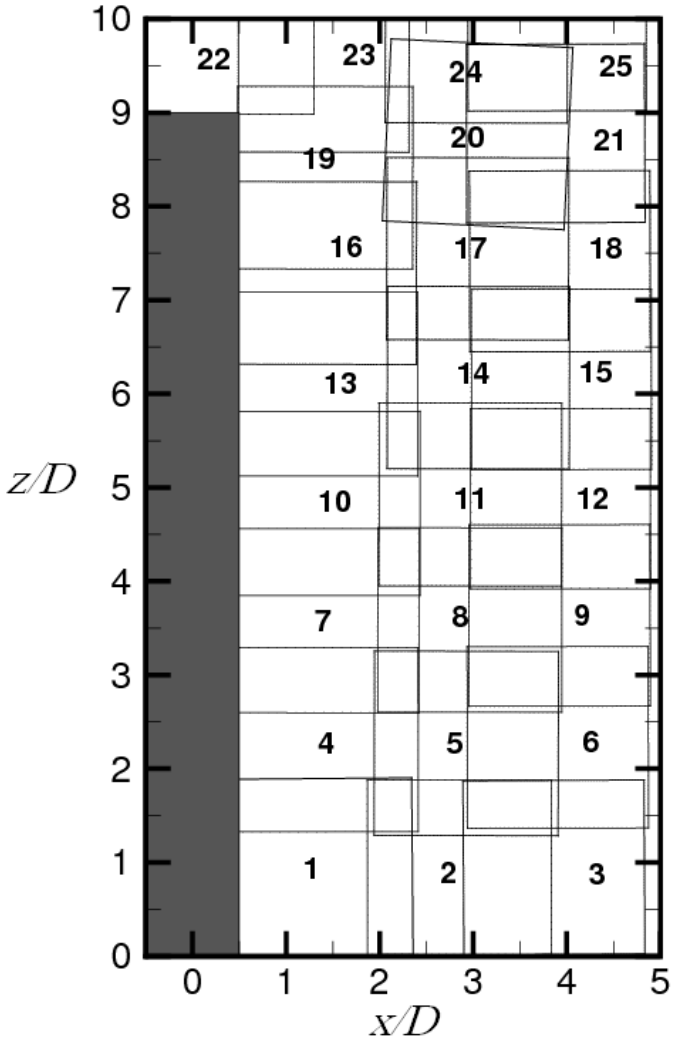

Figure 3.8: Combination of different fields of view for PIV measurements behind the model of AR = 9.

3.7.2 PIV Measurements of the Flow above the Free End in *x-z* Planes

To take PIV measurements above the free end of the cylinder or prism in *x-z* planes, the same experimental apparatus described in Subsection 3.7.1 was used. For each cylinder and prism, the light sheet was located at three cross-stream locations of y/D = 0, 0.25, and 0.375. A 750-mm spherical lens and a -50-mm cylindrical lens were included in the light sheet optics for the models of AR = 3 and 5, while for models of AR = 7 and 9, a 500-mm spherical lens was used. It should be noted that in order to have brighter particles in the PIV images, the distance between the centers of the field of view to the light sheet optics should be as close as possible to the focal length of the spherical lens used in the light sheet optics. Figures 3.9 and 3.10, respectively, show the side view and top view of the positioning of the camera and the laser optics for the PIV measurements in *x-z* plane above the free end surface of the models.

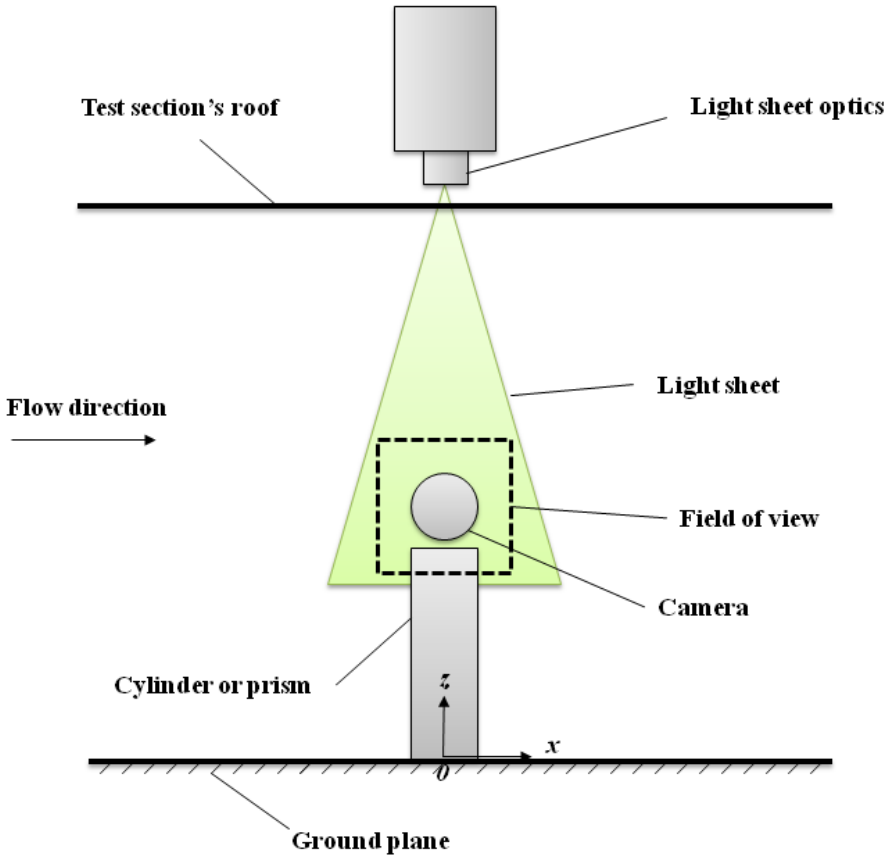

Figure 3.9: Side-view sketch of the experimental setup for the measurements in the vertical *x*-*z* planes.

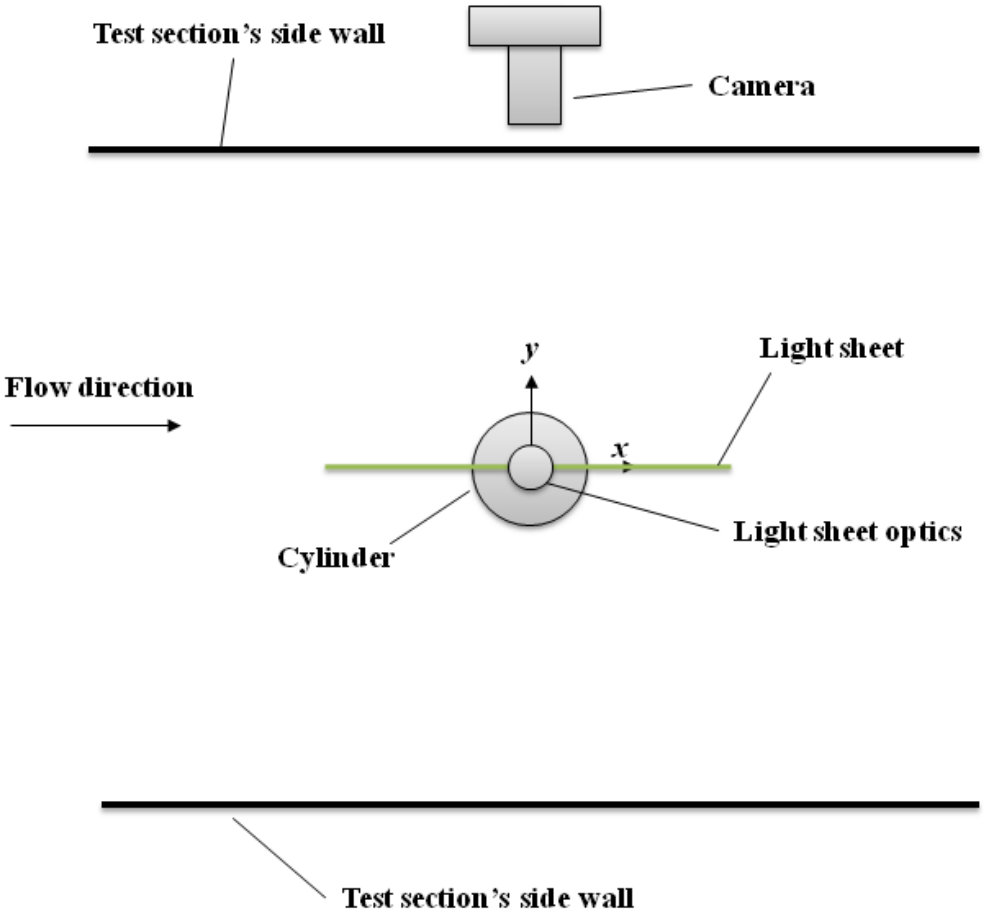

Figure 3.10: Top-view sketch of the experimental setup for the measurements in the vertical *x*-*z* planes.

3.7.3 PIV Measurements of the Flow above the Free End in *x-y* Planes

For the measurements in the *x-y* planes, the same PIV system described in Subsection 3.7.1 was used. In this experiment, the CCD camera was mounted on a solid aluminum bar at the top of the test section of the wind tunnel. PIV images were taken by this camera through a hole with a diameter of 60 mm. Good care was taken to make sure the camera lens was normal to the horizontal light sheet. The light sheet optics were located outside the wind tunnel test section's side wall. A 750-mm spherical lens was used in the light sheet optics together with a -25-mm cylindrical lens. The distance between the light sheet optics and the centre of the models was kept at approximately 750 mm in order to have proper PIV images. The location of the camera changed as the aspect ratio of the cylinder or prism changed in order to have a same size for the field of view for all PIV measurements in *x-y* planes above the free end of the models. The measurements were taken in six different wall-normal (*z*) distances of 0.016*D*, 0.032*D*, 0.048*D*, 0.08*D*, 0.11*D*, and 0.16*D* above the free end of cylinders and prism. For the square prism case, measurements were also taken in two additional wall-normal distances of 0.2*D* and 0.25*D* above the free end due to the thicker recirculation region above the prisms compared to circular cylinders. The laser sheet optics were mounted on a Dantec Dynamics traverse system and were controlled by a computer. This traverse was able to move in three orthogonal directions with a movement accuracy of about 0.05 mm. In these measurements, the field of view was 56 mm × 56 mm (1.8*D* × 1.8*D*) yielding an image resolution of about 35 μm/pixel.

Figures 3.11 and 3.12, respectively, show the side view and top view of the positioning of the camera and the light sheet optics for the PIV measurements in horizontal *x-y* planes above the free end surface of the models.

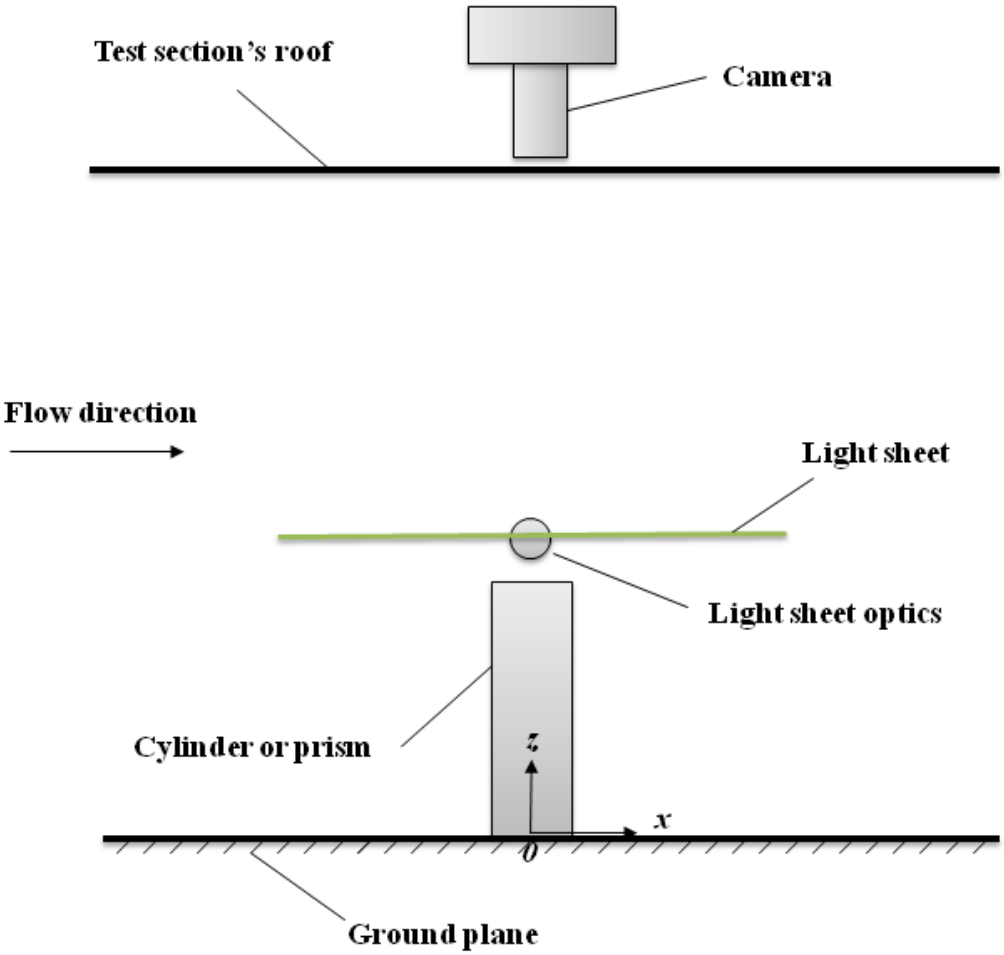

Figure 3.11: Side-view sketch of the experimental setup for the measurements in the vertical *x-y* planes.

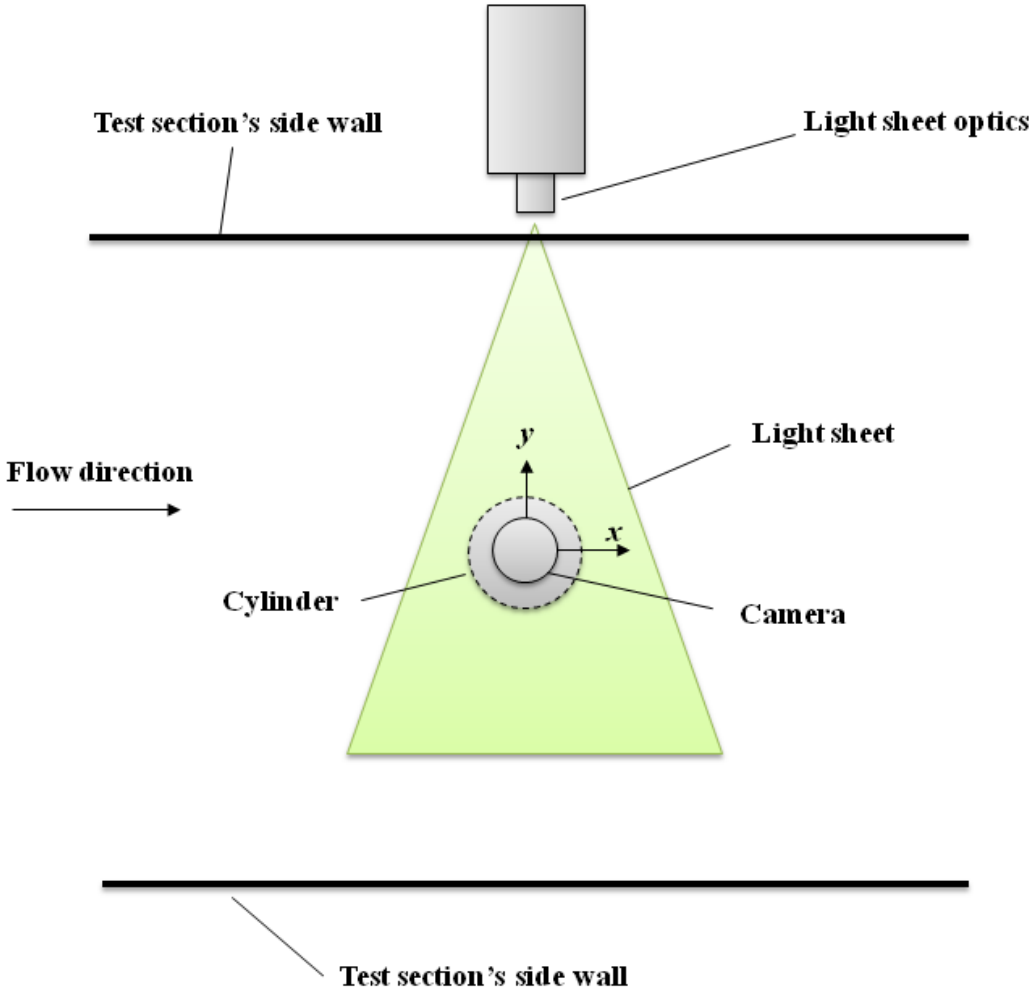

Figure 3.12: Top-view sketch of the experimental setup for the measurements in the vertical *x*-*y* planes.

3.7.4 PIV Measurements of the Flow above the Free End in *y-z* Planes

For the measurements in *y-z* planes, the same PIV system described in Subsection 3.7.1 was used. For these measurements, the light sheet optics were located outside the wind tunnel test section's side wall. The light sheet optics were mounted on the traversing system, so that the laser sheet was placed at different streamwise locations from upstream of the leading edge of the model's free end to downstream of the trailing edge of the free end. The CCD camera was mounted on the traversing wing (see Section 3.3) inside the test section and normal to the flow facing upstream toward the test section entrance. Movement of the camera was controlled by a computer. In these measurements, the distance between the camera and the laser sheet was kept constant in order to have same size of field of view for each set of data.

Figures 3.13 and 3.14, respectively, show the side view and top view of the positioning of the camera and the laser optics for the PIV measurements in *y-z* plane above the free end surface of the models.

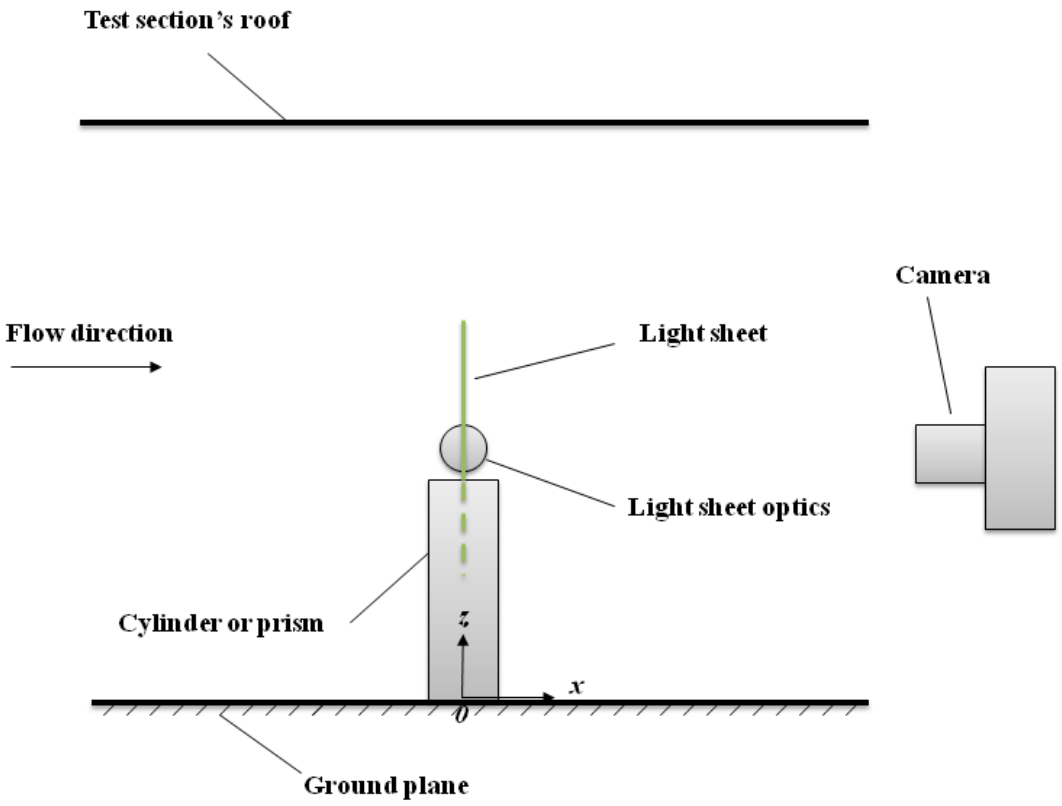

Figure 3.13: Side-view sketch of the experimental setup for the measurements in the vertical *y-z* planes.

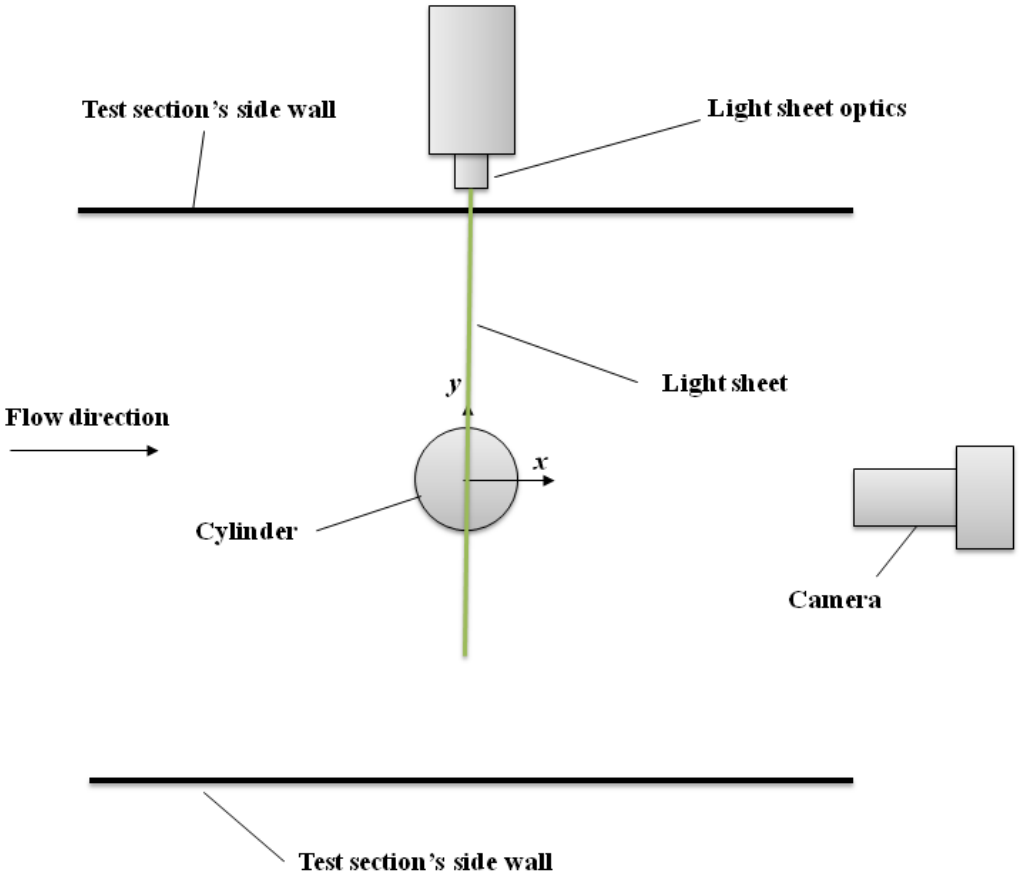

Figure 3.14: Top-view sketch of the experimental setup for the measurements in the vertical *y*-*z* planes.

3.8 Seeding the Flow

The flow was seeded by atomized propylene glycol droplets produced by a 700-W theatrical RadioShack fog machine (see Figure 3.15). The generator was located in the wind tunnel's settling chamber upstream of the contraction and test section (Figure 3.1). Fog fluid was manually poured in the fog machine for flow seeding. Droplets with approximate diameter of 1 μm were generated by the fog machine and were seeded to the flow inside the wind tunnel. After seeding the flow, the raw images were taken by the CCD camera. In order to have appropriate images for PIV image processing, the image pairs were checked based on the particles' diameter during the measurements to minimize the possible error in PIV measurements. Errors in PIV are discussed in Section 3.9. The concentration of the particles in the flow was adjusted manually looking at the raw images during the measurements. Figures 3.16 and 3.17 show two sample raw images taken for the flow above the free end of circular cylinder and square prism, respectively. In these figures, reflection of the laser sheet from the models is seen as a bright line above the free end surface of the cylinder or prism. These reflections indicate that the uncertainty in the PIV measurements close to the solid surfaces is large and hence the results in those regions cannot be used.

Figure 3.15: Fog generator machine.

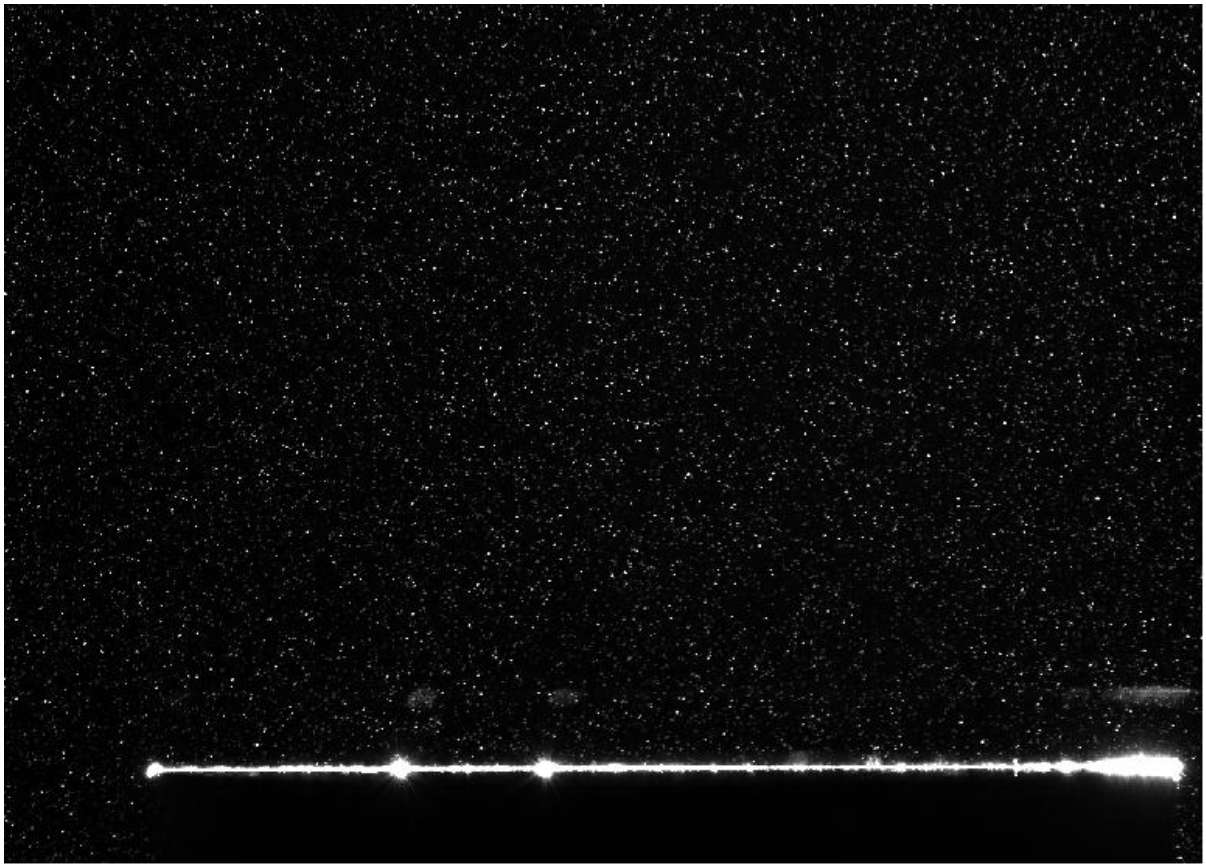

Figure 3.16: Illuminated particles in a raw image taken by the CCD camera for the flow around a finite-height circular cylinder.

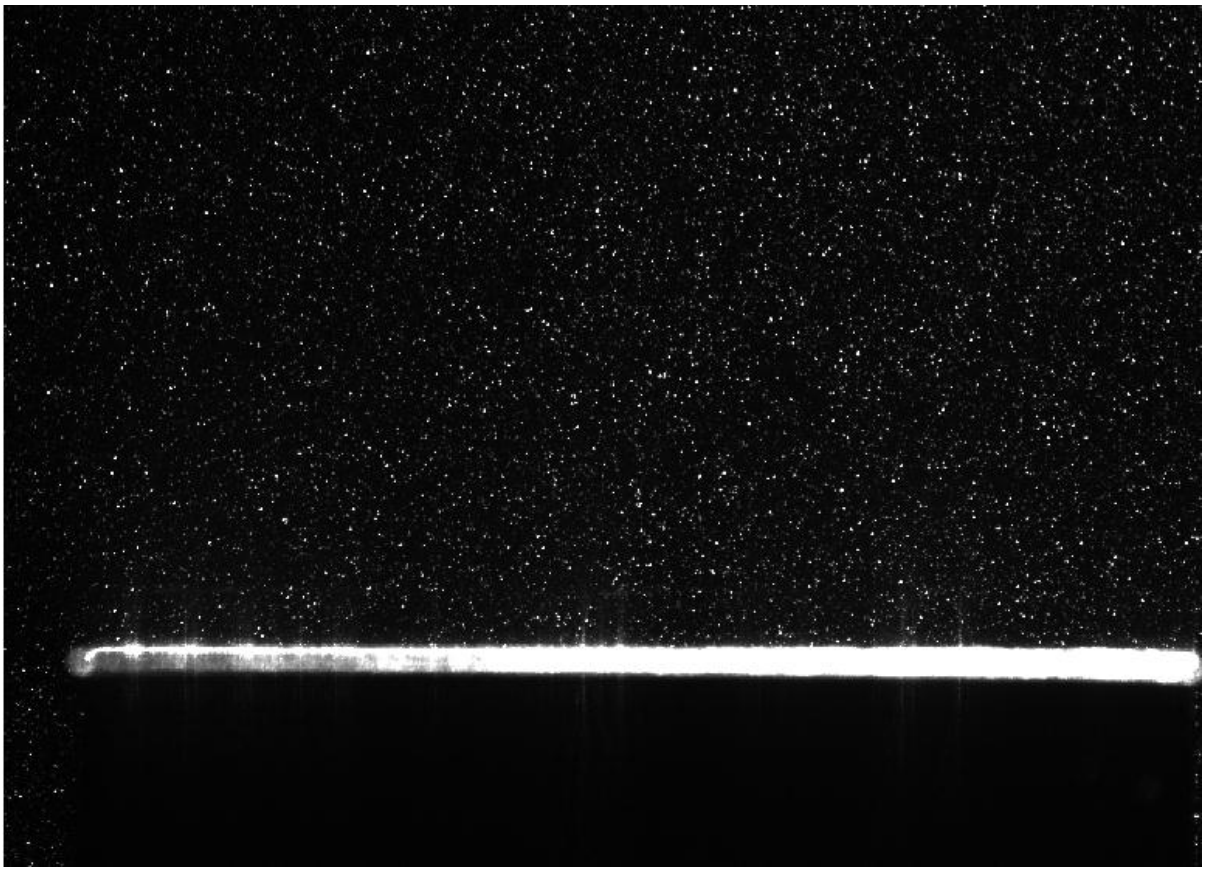

Figure 3.17: Illuminated particles in a raw image taken by the CCD camera for the flow around a finite-height square prism.

3.9 Estimate of Uncertainty in the PIV Data

The overall measurement accuracy in PIV measurements is defined as the combination of systematic (bias) errors and random (precision) errors. In the evaluation of a PIV recording, if the cross-correlation method is inadequate, systematic errors will arise (Adrian and Westerweel, 2011). In PIV measurements, each displacement vector can be associated with a certain degree of bias error and some degree of random error. The bias error is defined as the mean difference between the measured and actual displacement. On the other hand, when the pixel resolution is not adequate, there will be a discrepancy between the actual position of the particle image and the position calculated from the pixel array data. When the particle images become very small, or

the particle image diameter is much smaller than the pixel resolution, the displacements tend to be biased towards integral values. In this case, regardless of the location of the particle image on a given pixel, the bias is always towards the center of the pixel. Hence, the maximum possible bias error for the location of a particle image would be half of the pixel spacing (Adrian and Westerweel, 2011). This error is caused by improper sub-pixel displacement estimation made by the sub-pixel peak estimator as the signal peak is poorly resolved. This effect is called "peak locking" which is used to describe a displacement bias error which has a periodic pattern on pixel intervals. The peak locking effect causes a bias in most of PIV data analysis done by cross-correlation algorithms. This locking effect is inherent to the smooth curve fitting through discrete correlation values used to obtain the sub-pixel part of the displacement (Chen and Katz, 2005). The peak locking effect can be detected by plotting a displacement histogram of actual PIV displacement data. The peak locking associated with too small particle image size can be detected as distorted histograms with peaks at integer displacement values indicating that the systematic errors due to the algorithm used for peak fit are larger than the random noise in the estimation of the displacement. According to Raffel et al. (2006) there are some alternatives in order to decrease this effect. First the particle image diameter can be increased ($d_\tau > 2$ pixels) during the recording process by increasing the sampling rate (adding more tracers) or by defocusing the particle image. The second choice is to choose a different peak estimator which is better suited for smaller particle image diameters. A third approach is to pre-process the images using filters which optimize the particle image diameter with respect to the peak estimator. Finally, another technique was reported by Roth and Katz (2001) which applies an equalization transfer function to the peak-locked data.

The total error in PIV measurements is the combination of the bias error and random error. Bias errors are generally associated with resolution effects. That means when the pixel size becomes large with respect to the particle image diameter, the bias error becomes important. The random errors are associated with the random fluctuations in the measured particle image intensity. The error for the centroid estimate is zero when particle images are symmetric (Adrian and Westerweel, 2011). But, in practical situations the particle images are not perfectly symmetric. So there is always rms error amplitude ($\sigma_{\Delta x}$) for the particle image displacement, which is defined as: $\sigma_{\Delta x} \approx c_\tau \, d_\tau$ where d_τ is the particle image diameter and c_τ is a constant which is a function of the following (Prasad et al., 1994):

- Choice of peak location technique: centroiding or curve fitting;
- Irregularity of particle images, pixel readout noise and other practical limitations on obtaining ideal particle images;
- Number of particle images or image density.

According to Adrian and Westerweel (2011), $1/c_\tau$ can be interpreted as a signal-to-noise ratio. For low image density PIV images, it was found that $c_\tau \approx 0.09$-0.13. The bias estimation error, ϵ_X, for the centroid is given as $\epsilon_X \approx c_e \, d_\tau$, where c_e is a constant determined by the random fluctuations in the particle image intensity. According to the above explanations, the total estimation error can be calculated as $\sqrt{\langle \epsilon_X \rangle^2 + \sigma \Delta x^2}$. The total error is dominated by the bias error (peak locking effect) for

$d_\tau / d_{pix} < 1$ where d_{pix} is the diameter of pixel or pixel separation, while the total error is dominated by the random error for $d_\tau / d_{pix} > 2$. When the particle image diameter is too small, d_τ

$/d_{pix} \approx 0$, the total estimation error, which is the rms bias error for centroid estimation, approaches 0.29 d_{pix}.

It is obvious that the minimum total error would be the optimum particle image diameter. According to Prasad et al. (1992), the optimal image diameter occurs at $d_\tau / d_{pix} \approx 2$ (see Figure 3.18). Considering Figure 3.18, the value of the minimum total error seems to be insensitive to the value of c_τ. The optimal particle image diameter ranges from 2 to 4 according to empirical estimates in the literature (Adrian and Westerweel, 2011). It should be mentioned that the signal-to-noise ratio (SNR) is the ratio of the height of the signal peak (i.e., highest peak) to the second-highest peak (i.e., highest noise peak) on the correlation plane.

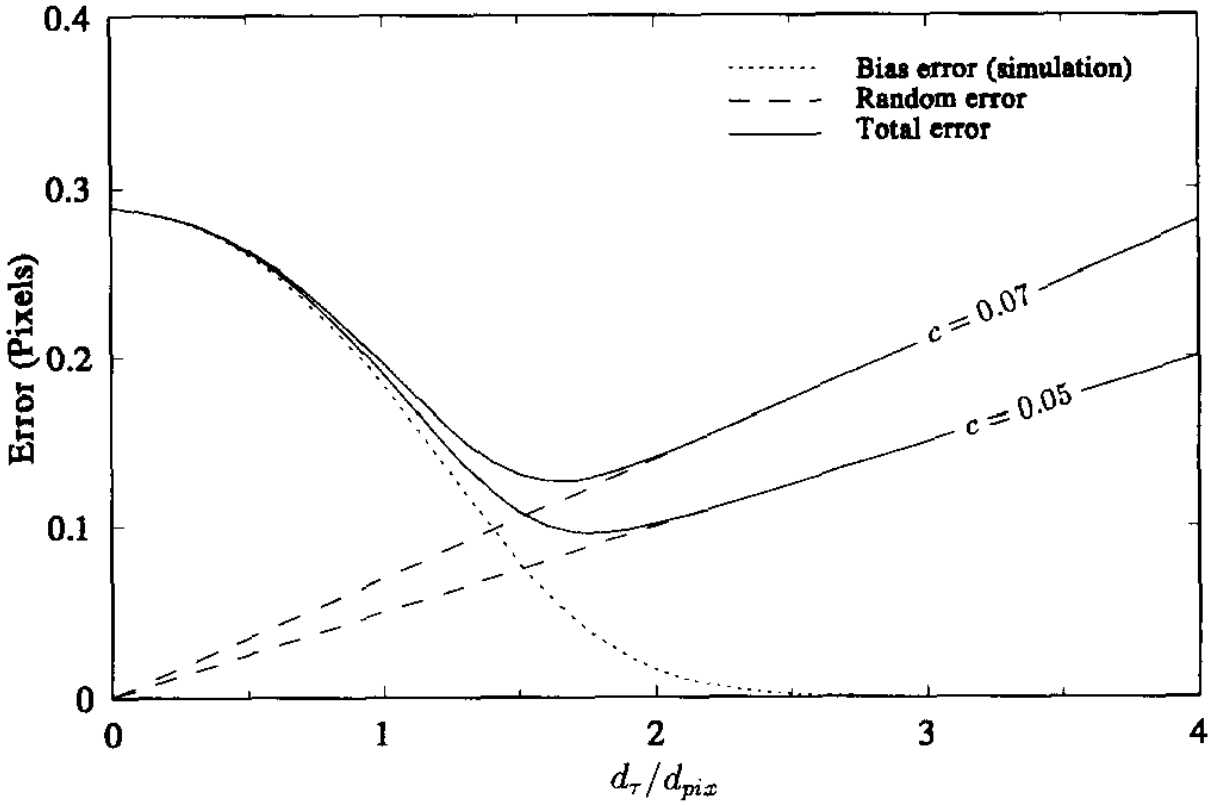

Figure 3.18: Variation of PIV bias and random errors with d_τ / d_{pix} (Prasad et al. 1992).

The peak locking which is associated with too small particle image size is detected as distorted histograms with several peaks on the signal and noise correlation plane. The ratio of the highest peak in the histogram to the nearest peak can be related to signal-to-noise ratio which can be interpreted from the inverse of c_τ value. This peak locking effect indicates that the systematic errors due to the peak fit algorithm are larger than the random noise in the estimation of the displacement (Adrian and Westerweel, 2011). Figures 3.19 and 3.20 show a section of the typical histograms of the particle displacements from the present PIV data for circular cylinder and

square prism, respectively. According to these figures, there is one outstanding peak in the particle displacement histograms meaning that many velocities are near zero. One can also infer from these figures that no peak locking is expected. Note that, in a displacement histogram, the secondary peaks at integer displacement values are an indication of peak locking.

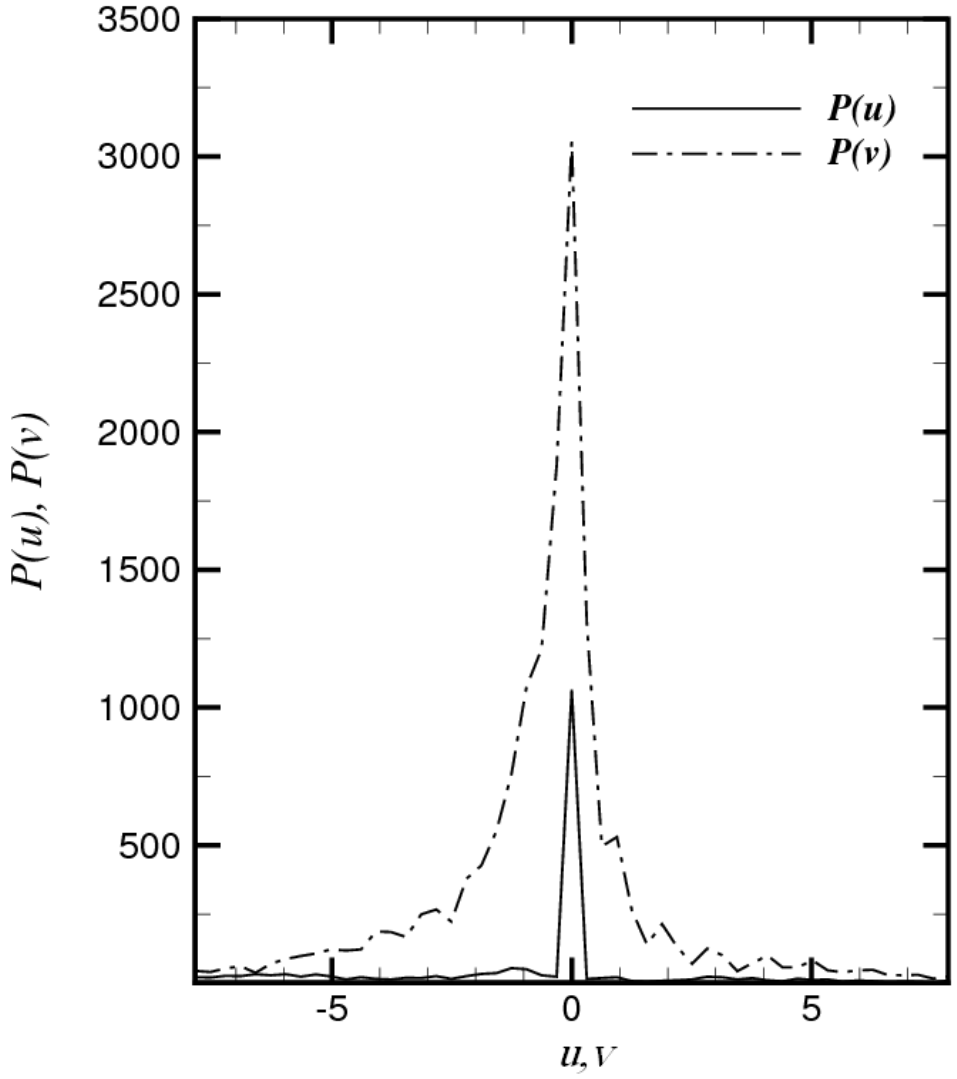

Figure 3.19: Displacement histogram of streamwise (u) and wall-normal velocity (v) components of a random image pair taken for the flow above the free end surface of a circular cylinder.

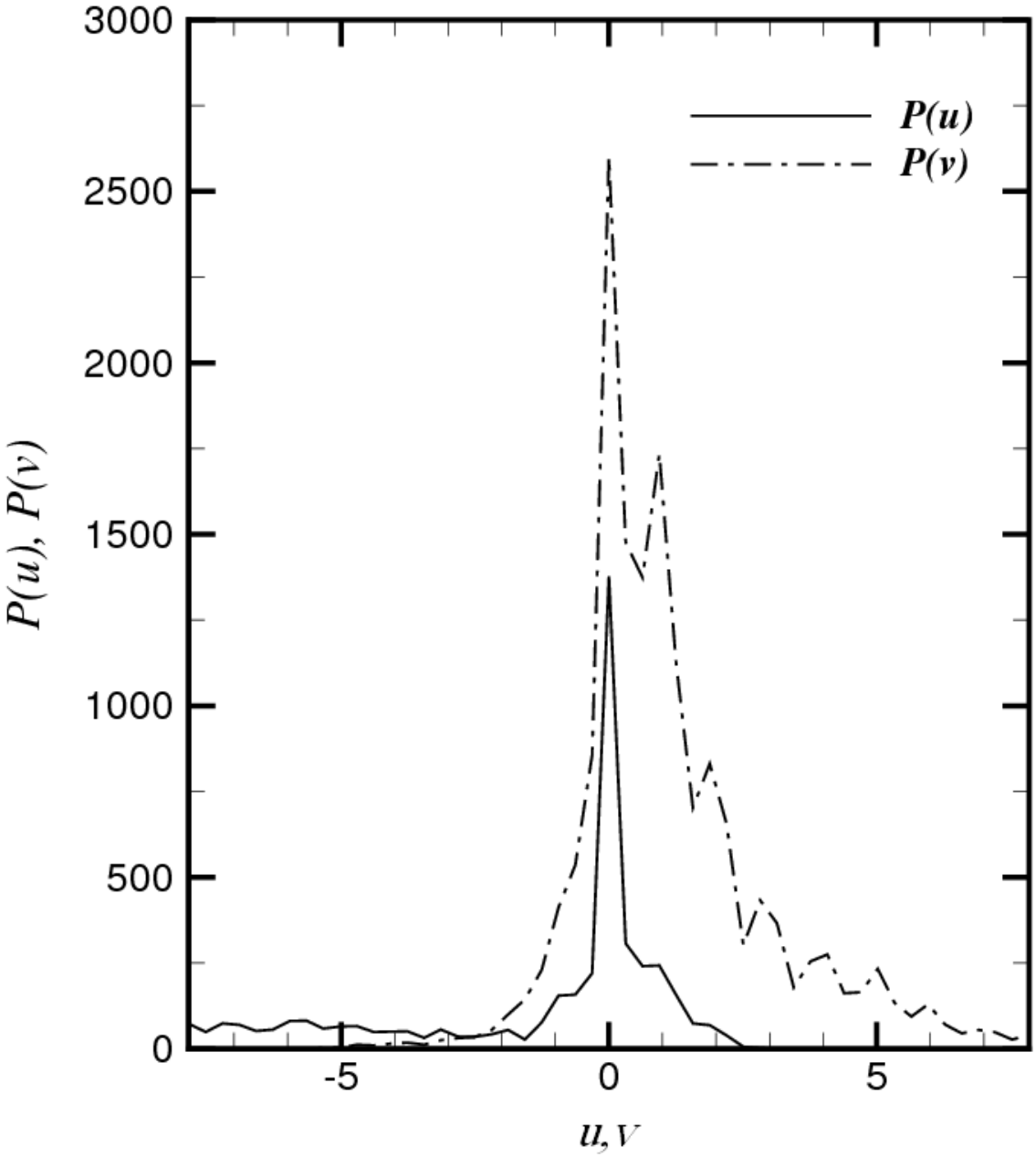

Figure 3.20: Displacement histogram of streamwise (u) and wall-normal velocity (v) components of a random image pair taken for the flow above the free end surface of a square prism.

In order to assess the peak locking effect in a PIV data set, the value of c_τ needs to be calculated according to the experimental setup used in the experiment. According to Adrian and Westerweel (2011), the value of c_τ can be estimated as

$$c_\tau = \frac{1}{\sqrt{2}\,\tau_{00}/\eta}\frac{D_I/d_{pix}}{{N_I}^{1/2}} \tag{3.5}$$

where τ_{00} is the mean normalized exposure, η represents the random fluctuations associated with the film grain, N_I is the number of particle images or the image intensity, and D_I is the dimension of the interrogation domain. After calculation of c_τ, Figure 3.18 can be used to estimate the bias error (in pixels) due to the peak locking effect.

In order to estimate the uncertainty in the present PIV data, the present Pitot-tube boundary layer profile were compared to the PIV data of Akon (2012) who used the same PIV set up for boundary layer measurements inside the test section of the wind tunnel. Figure 3.21 shows that the PIV data are in good agreement with the Pitot-tube data collected at the location of the models. According to this figure, the uncertainty in the mean velocity measurements was estimated to be about 2.7%. It should be noted that, in the present PIV data, d_pix has a value of approximately 28 μm.

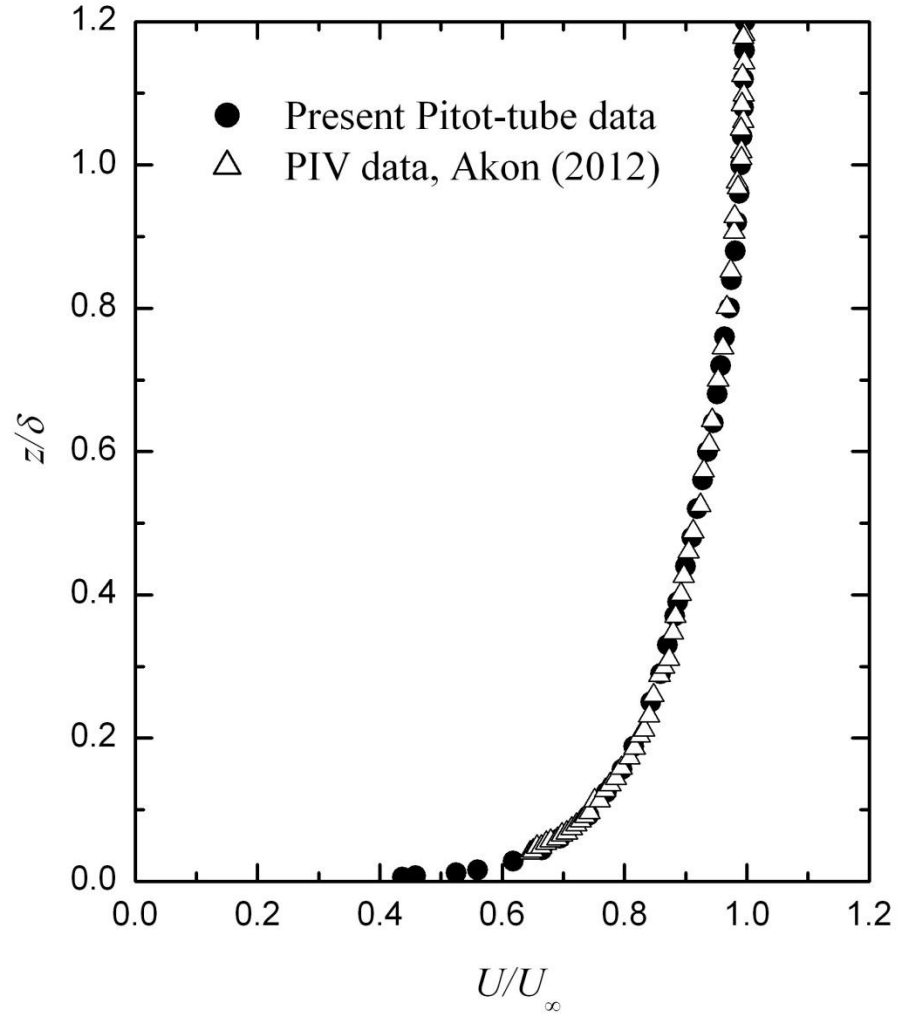

Figure 3.21: Comparison of the PIV and the Pitot-tube results for the mean velocity profiles of a boundary layer at a freestream velocity of U_∞ = 20 m/s.

Since different PIV setups were used for the measurements in *x*-*z*, *x*-*y*, and *y*-*z* planes, the results at some intersection lines of the planes were compared to each other in order to check whether different PIV setups give the same results. One example of the comparisons is shown in Figure 3.22. This figure shows the mean normalized velocity profiles measured in both *x*-*z* and *x*-

y planes along the centerline of *y/D* = 0 and at a wall-normal distance of *z/D* = 0.11 above the free end surface of a square prism of AR = 3. According to Figure 3.22, the profiles are close to each other indicating that the uncertainty in PIV data due to the change of setup can be ignored. According to this figure, the difference between the mean velocity data in the *x*-*z* and *x*-*y* planes at the intersection line is within the uncertainty of 2.7% indicating acceptable PIV results for the present study.

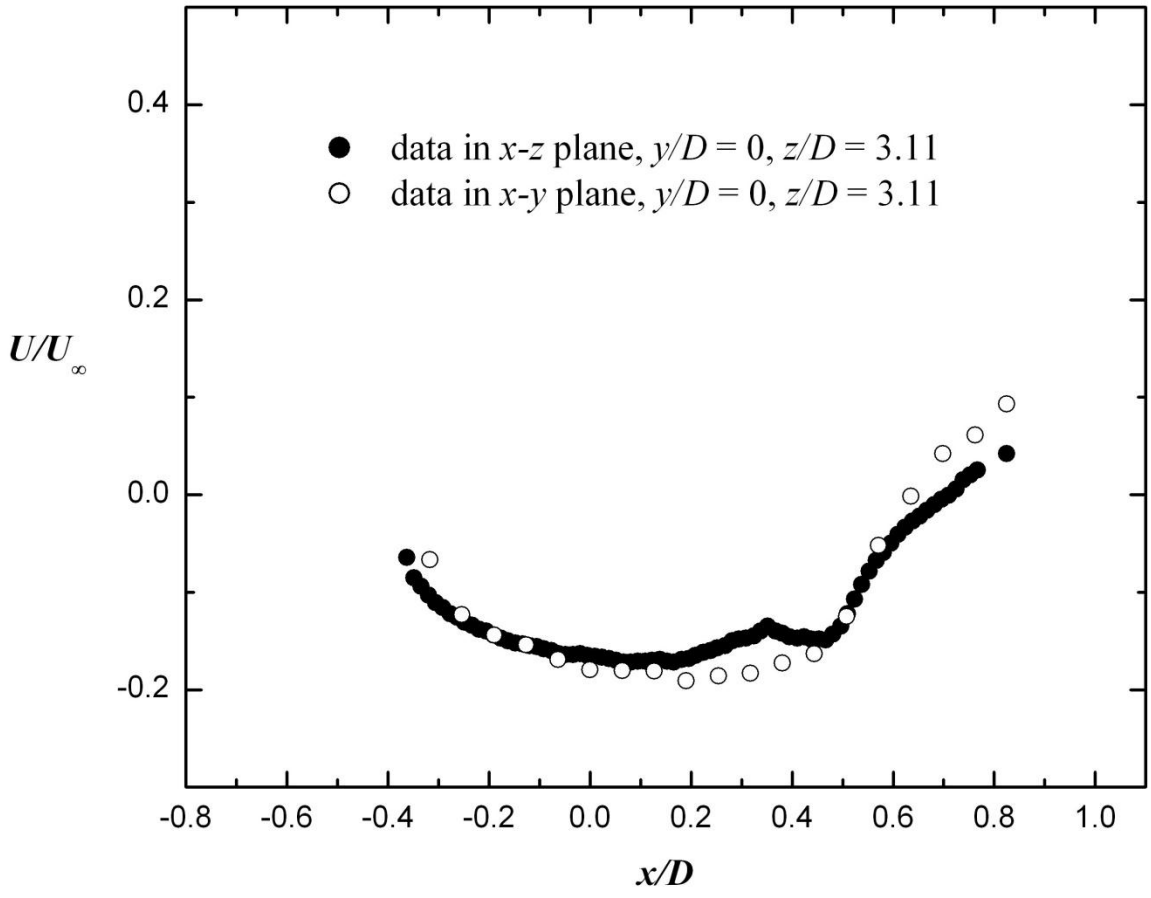

Figure 3.22: Comparison of the PIV results at the intersection line of two planes of *x*-*z* and *x*-*y*.

4. Turbulent Near Wake of Surface-mounted Finite Circular Cylinders

4.1 Introduction

The near-wake region of a surface-mounted finite-height circular cylinder contains fundamental flows such as the ground plane boundary layer, separated shear layers from the cylinder, and the low-pressure wake region behind the cylinder. There is limited information about the flow pattern of the local flow field of a surface-mounted finite-height circular cylinder. In order to understand the near wake of the circular cylinders, it was investigated using the PIV measurement technique. This chapter provides information on the mean velocity distribution, turbulence quantities, Reynolds shear stress, and mean vorticity field in the near wake of surface-mounted finite-height circular cylinders of AR = 9, 7, 5, and 3 in order to investigate the effect of AR and the boundary layer thickness on the flow structure around the cylinders. In order to have appropriate PIV results, the field of view for the PIV measurements in the *x*-*z* plane was set to be 61 mm × 61 mm (1.9*D* × 1.9*D*). Hence, the measurements were taken in different fields of view within the *x*-*z* plane to cover the whole near wake of the cylinders. In all of the present experiments, the Reynolds number was $Re_D = 4.2\times10^4$ and the ratio of the flat-plate boundary layer thickness to the diameter of the cylinders was approximately $\delta/D = 1.6$.

4.2 Mean Velocity Distribution

The local mean velocity fields on the wake centerline (y/D = 0) for the four cylinders (of AR = 9, 7, 5, and 3) are shown and discussed in this section. In this section, the in-plane mean velocity components ($\overline{U}$,$\overline{W}$) are made dimensionless with the freestream velocity, U_∞, and the mean field is calculated from an ensemble of 1000 instantaneous PIV velocity fields.

4.2.1 Streamwise Velocity

Figure 4.1 shows the local mean velocity vector field for each of the four cylinders of AR = 9, 7, 5, and 3. The corresponding mean flow streamlines of the near-wake regions of the cylinders are shown in Figure 4.2.

Behind the cylinder, in the near-wake region, a strong downwash flow (downward-directed velocity vectors in Figure 4.1) is observed immediately downstream of the free end in the near wake of the cylinder. The downwash originates near the free end, persists in the streamwise direction and descends into the central portion of the wake. In the streamlines shown in Figure 4.2, some part of the flow is directed towards the ground plane and stagnates onto the rear surface of the cylinder, where a large recirculation zone is located, while the other part of the flow moves away from the cylinder into the far wake.

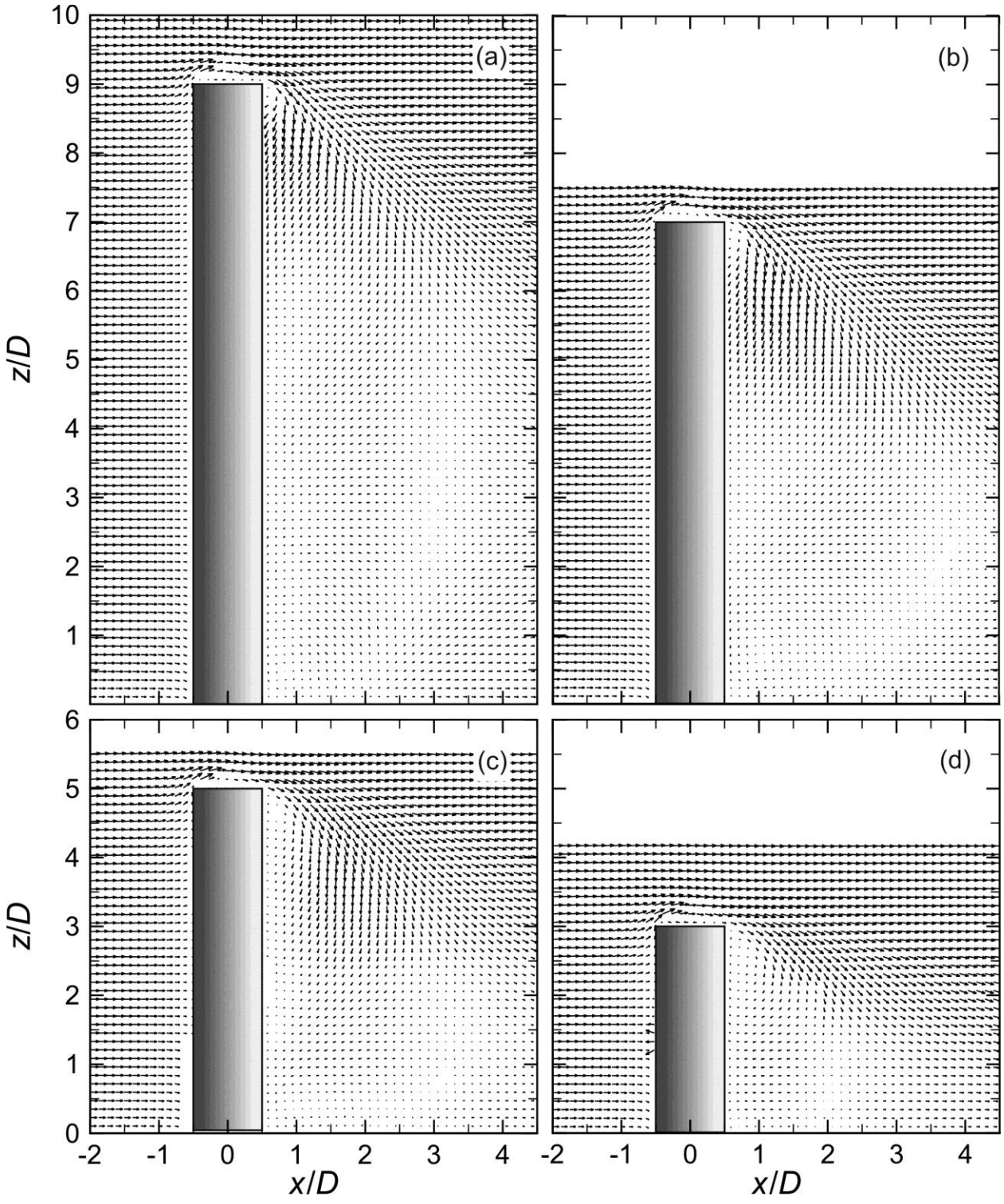

Figure 4.1: Mean velocity vector field ($\overline{U}/U_\infty$, $\overline{W}/U_\infty$ components) in a vertical plane on the wake centerline (y/D = 0, the symmetry plane) of a finite-height circular cylinder: (a) AR = 9; (b) AR = 7; (c) AR = 5; (d) AR = 3. $\mathrm{Re}_D = 4.2 \times 10^4$ and δ/D = 1.6. Half of the vectors were skipped.

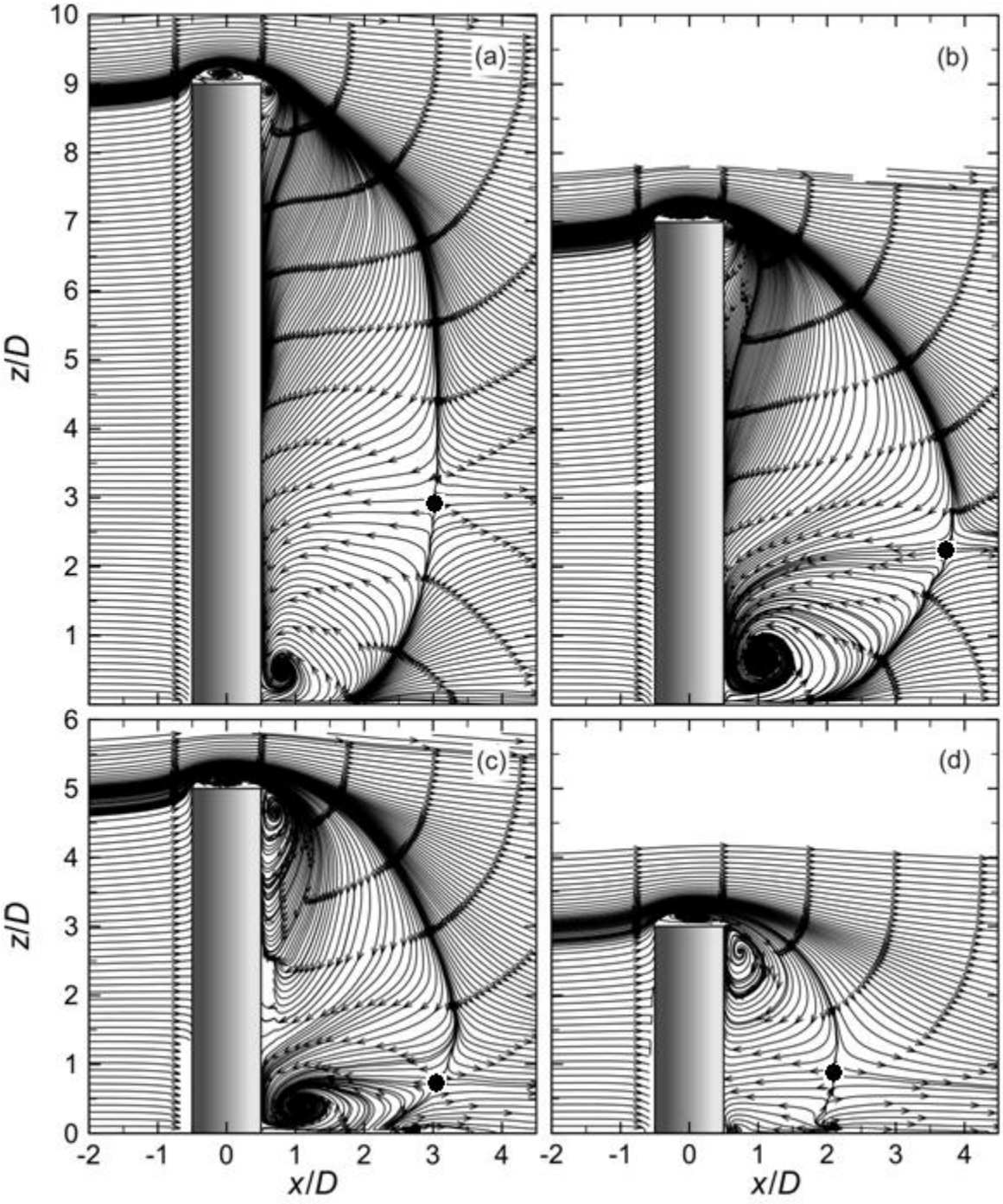

Figure 4.2: Mean streamlines in a vertical plane on the wake centerline (y/D = 0, the symmetry plane) corresponding to the mean velocity vector field in Figure 4.1: (a) AR = 9; (b) AR = 7; (c) AR = 5; (d) AR = 3. Saddle points are indicated as black circles.

A small clockwise (CW) vortex also forms immediately downstream of the free end and is centered just below the free end. This vortex is present for all four aspect ratios and can be seen in both the velocity vector fields (Figure 4.1) and streamlines (Figure 4.2). The size of the vortex appears to be a function of aspect ratio, with the largest vortex occurring for the smallest aspect ratio (AR = 3, Figures 4.1 (d) and 4.2 (d)). This vortex might be related to the flow direction along the height of the cylinder. It should be noted that, the mean streamlines are not the best indicator for the strength and size of the vortices. The mean in-plane vorticity field of a region of interest can also be shown in order to verify the location, size, and strength of a vortex. According to Figures 4.2 (a, b), for AR = 9 and 7, some of the downwash flow is directed along the cylinder wall toward the ground plane, whereas for AR = 5 and 3 (Figures 4.2 (c, d)), flow moves upwards along the cylinder wall toward the free end, resulting in larger vortices just below the free end. This vortex also corresponds to vortex B_t identified in the LES simulations of Krajnović (2011) for $Re_D = 2\times10^4$, AR = 6, and $\delta/D = 0.07$ (see Figure 2.5).

For the three most slender cylinders (AR = 9, 7, and 5, Figures 4.1 (a, b, c)), a weak upwash flow (upward-directed velocity vectors) can be discerned, originating near the ground plane and moving towards the central region of the wake. A vortex with CCW sense of rotation can also be found immediately behind the cylinder, near the cylinder-wall junction, for AR = 9, 7 and 5 (Figures 4.2 (a, b, c)). This vortex corresponds to vortex N_w identified in the LES simulations of Krajnović (2011). Notably, however, this upwash flow and vortex are absent for the shortest cylinder (AR = 3, Figure 4.2 (d)), signifying that this cylinder has a different wake structure. This different wake structure for AR = 3 is consistent with the earlier results of Sumner et al. (2004) and Adaramola et al. (2006) and suggests the critical aspect ratio lies between AR = 5 and AR = 3 in the present experiments.

The streamlines in Figure 4.2 also show a saddle point that corresponds to the streamwise extent of the main recirculation zone. For the three shortest cylinders, the saddle point moves farther downstream as AR increases, at *x/D* = 3.8, 3.0, and 2.2 for AR = 7, 5, and 3 respectively. For the tallest cylinder considered (AR = 9), the saddle point moves closer to the cylinder, at *x/D* = 3.0. According to Figure 4.2, the locations of the saddle points seem to be related to the two vortices identified and described above, one immediately below the free end and the other near the cylinder-wall junction: as mentioned above, the size and the location of these vortices are functions of cylinder aspect ratio, AR.

To further illustrate the fluid behavior in the near wake of the finite circular cylinder, contour plots are presented in Figure 4.3 showing the mean streamwise velocity component. A similar approach was adopted by Adaramola et al. (2006, 2010).

The mean streamwise velocity component contours in Figure 4.3 (contours of $\overline{U}/U_\infty$) show a region of negative streamwise velocity immediately behind each of the four cylinders, which broadly denotes the mean recirculation zone. For the cylinders of AR = 9, 7 and 5 (Figures 4.3 (a, b, c)), the region of negative velocity extends to almost the free end of the cylinder, whereas this is not the case for AR = 3 (Figure 4.3(d)). From the contour lines in Figure 4.3, it can be concluded that the largest value of negative mean velocity is approximately $\overline{U}/U_\infty$ = - 0.3 which occurs for AR = 3.

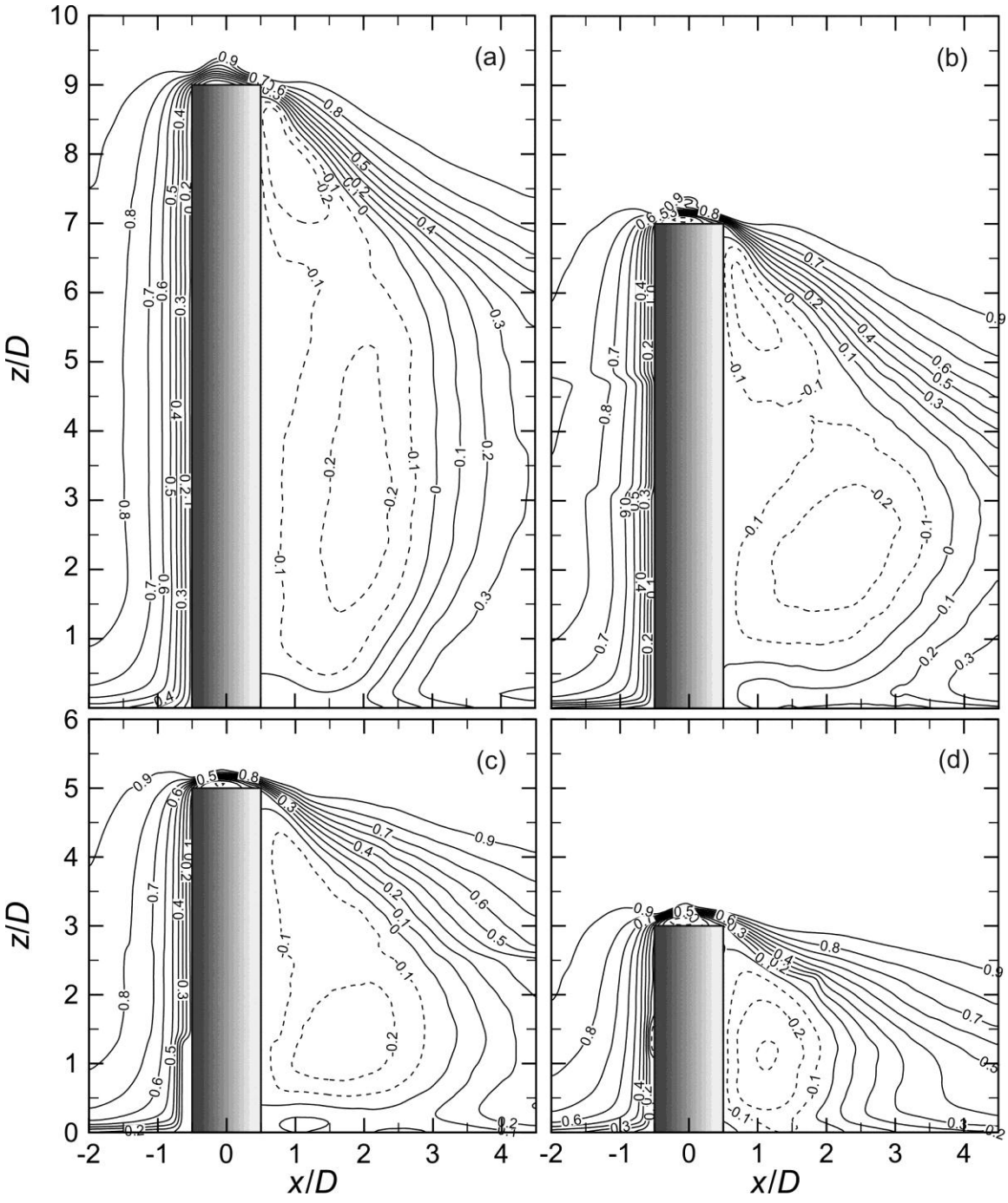

Figure 4.3: Streamwise mean velocity field (contours of $\overline{U}/U_\infty$) in a vertical plane on the wake centerline (y/D = 0, the symmetry plane): (a) AR = 9; (b) AR = 7; (c) AR = 5; (d) AR = 3. Solid contour lines represent positive streamwise velocity, dashed contour lines represent negative streamwise velocity.

Figure 4.4 shows the dependence of the maximum reverse flow (recirculation) zone on the cylinder aspect ratio. According to this figure, the maximum length of the recirculation zone increases from 2.09D for AR = 3 to 3.76D for AR = 7, and then decreases to 2.94D for AR = 9. The maximum length of the region of recirculating flow, L_{max}/D, typically occurs at the location close to the saddle points observed in Figure 4.2. In Figure 4.4, the present data are compared to the square prism LDV data of Wang and Zhou (2009) at $Re_D = 9.3\times10^3$, and to the square prism PIV data of Bourgeois et al. (2011) at $Re_D = 1.2\times10^4$. According to this comparison a good agreement is demonstrated. In particular, the maximum length occurs for an intermediate aspect ratio (AR = 7). A similar behavior for the maximum length of the recirculation zone was also noticed by Tanaka and Murata (1999) for circular cylinders of AR = 10, 5, 2.5, and 1.25 at $Re_D = 3.7\times10^4$ and $\delta/D = 0.1$, where the maximum length was observed for the case of AR = 5. According to Figure 4.4, Wang and Zhou (2009) showed a constant value for L_{max}/D for prisms of AR > 9 indicating that the maximum length of the recirculation region for finite cylinders of AR > 9 approaches the value of L_{max}/D of infinite cylinder.

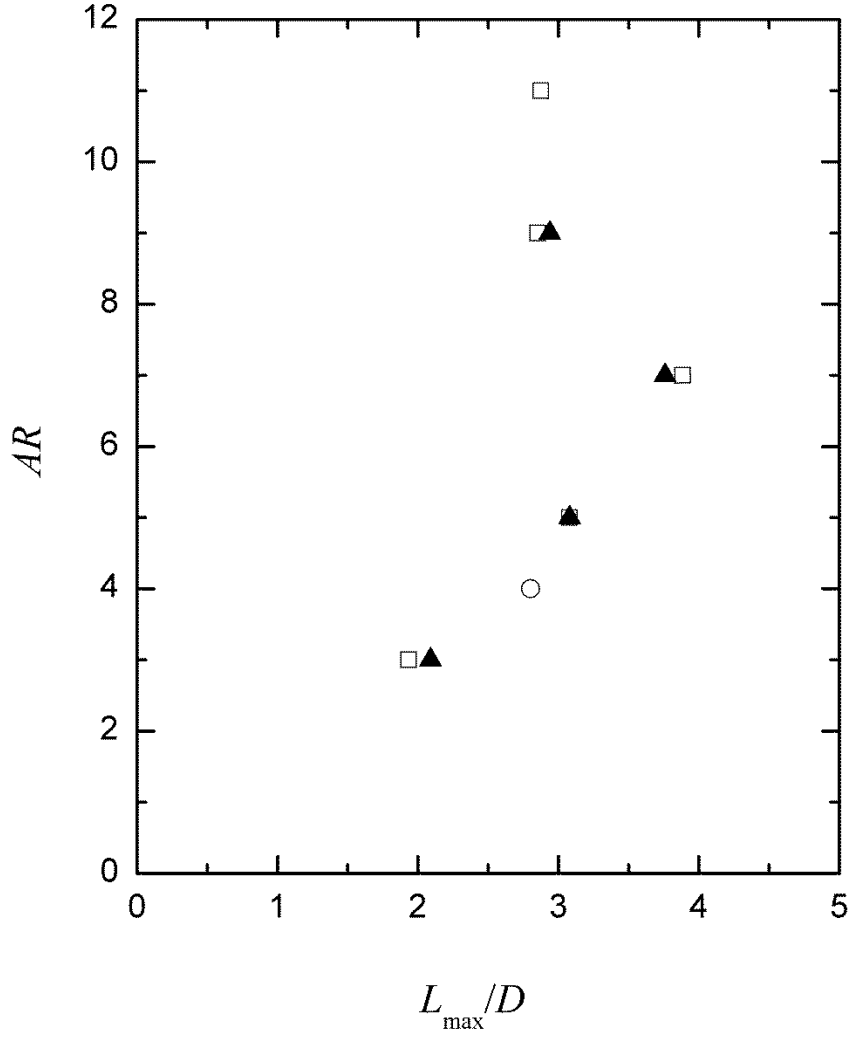

Figure 4.4: Maximum longitudinal length of the mean recirculation zone for different aspect ratios. ▲, Present study, circular cylinder, $Re_D = 4.2\times10^4$; □, Wang and Zhou (2009), square prism, $Re_D = 9.3\times10^3$; ○, Bourgeois et al. (2011), square prism, $Re_D = 1.2\times10^4$.

.

Figure 4.5 shows an enlargement (with increased spatial resolution) of the region close to the ground plane behind the cylinder at the cylinder-wall junction, showing the vortex located in this region (seen earlier in the streamline fields in Figure 4.2). Both vectors and streamlines are shown in this figure to better illustrate the location of the vortex in the cylinder-wall junction region. The vortex appears for AR = 9, 7, and 5 (Figures 4.5 (a, b, c)) only. The vortex centers for AR = 9, 7 and 5 seem to be dependent on AR, located at approximately (x/D, z/D) = (0.75, 0.5), (1.05, 0.65), and (1.05, 0.4) for AR = 9, 7, and 5, respectively. As mentioned earlier, this vortex corresponds to vortex N_w identified by Krajnović (2011), and is considered to be a time-averaged representation of the base vortex pair. The absence of this vortex for AR = 3 (Figure 4.5 (d)) is evidence of the distinct flow behavior for this cylinder (it is smaller than the critical aspect ratio) where no base vortex pair is observed (Sumner et al., 2004). In the present experiments, vortex B_f identified by Krajnović (2011), which rotates in the opposite sense and is much smaller in size than vortex N_w, was not observed.

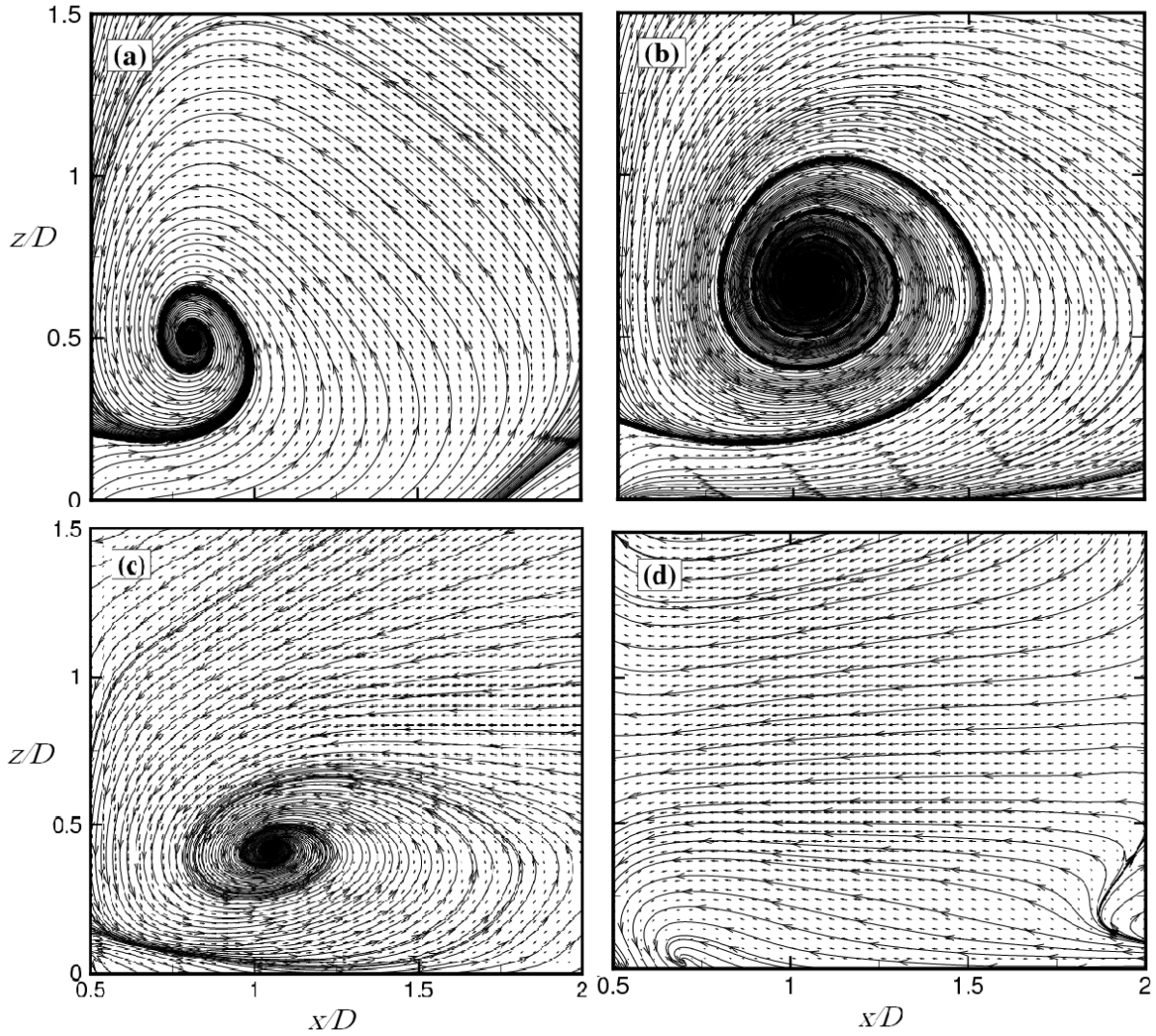

Figure 4.5: Enlarged view of mean velocity vector field (($\overline{U}/U_\infty$, $\overline{W}/U_\infty$ components) and corresponding streamlines in a vertical plane on the wake centerline (y/D = 0, the symmetry plane) behind the cylinder close to the cylinder-wall junction: (a) AR = 9; (b) AR = 7; (c) AR = 5; (d) AR = 3.

4.2.2 Wall-Normal Velocity

The time-averaged wall-normal velocity fields ($\overline{W}/U_\infty$) in the *x*-*z* plane, for the circular cylinders of AR = 9, 7, 5, and 3 are shown in Figure 4.6. The wall-normal velocity component contours in Figure 4.6 illustrate regions of upward-directed and downward-directed flow within the local flow field of the cylinders. According to this figure, there are upwash flows at the front of cylinder free end for all four aspect ratios, and at the region close to the ground plane downstream of the cylinders for larger aspect ratios, i.e. AR = 9 and 7. The extent and predominance of the strong downwash flow field is clearly evident for all four cylinders; the upwash flow field behind the cylinders near the ground plane is much weaker, and weakens as the aspect ratio decreases. According to Figure 4.6, the downwash flow stretches along the cylinder height towards the junction of the cylinder and the ground plane for AR = 9, 7, and 5 (Figures 4.6 (a, b, c)), while there is no evidence of this stretch for the cylinder of AR = 3 (Figure 4.6 (d)). Furthermore, a small region of upwash flow just below the cylinder free end can be seen for the cylinder of AR = 3 (Figure 4.6 (d)).

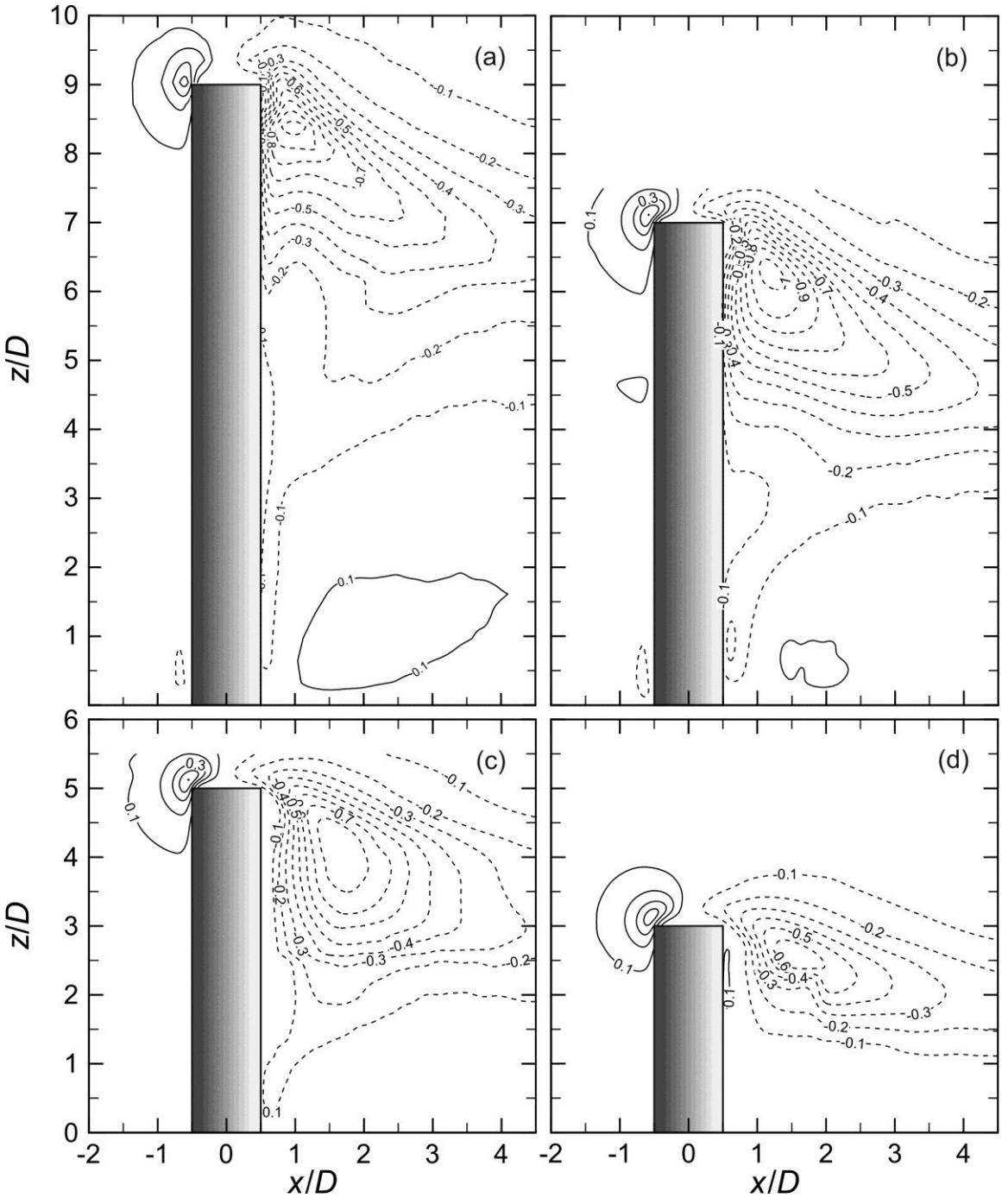

Figure 4.6: Wall-normal mean velocity field (contours of $\overline{W}/U_\infty$) in a vertical plane on the wake centerline (y/D = 0, the symmetry plane): (a) AR = 9; (b) AR = 7; (c) AR = 5; (d) AR = 3. Solid contour lines represent positive wall-normal velocity, dashed contour lines represent negative wall-normal velocity.

4.3 Turbulence Structure

Contour plots of the streamwise turbulence intensity (u'/U_∞), wall-normal turbulence intensity (w'/U_∞), and Reynolds shear stress ($-\overline{u'w'}/{U_\infty}^2$), on the wake centreline for the four circular cylinders of AR = 9, 7, 5, and 3, are shown and discussed in this section. It should be noted that the enlarged regions of turbulence above the free end of the cylinders are shown and discussed later in Chapter 6. In this section, the main focus is on the turbulence characteristics of the flow in the near-wake region behind the circular cylinders.

4.3.1 Turbulence Intensity Distribution

For all four cylinders, the highest values of streamwise (Figure 4.7) and wall-normal (Figure 4.8) turbulence intensity are encountered above the free end of the cylinder where a region of separated flow is located. Park and Lee (2004) showed similar results for a cylinder of AR = 6 at Re_D = 7500, with the highest levels of turbulent kinetic energy found above the free end. This region of elevated turbulence intensity then extends into the region of downwash flow within the near wake. Elevated freestream turbulence is also encountered within the recirculation zones of the cylinders. From Figures 4.7 and 4.8, there is little within the turbulence fields to distinguish the cylinder of AR = 3 from the three more slender cylinders. This is in contrast to the wake turbulence structure farther downstream and away from the wake centreline, which is found to have a distinct structure for AR = 3 (Adaramola et al., 2006). According to Figure 4.8, the location of highest wall-normal turbulence intensity in the near-wake region moves downward and in the streamwise direction compared to the tip of the cylinder as the aspect ratio of the cylinder decreases.

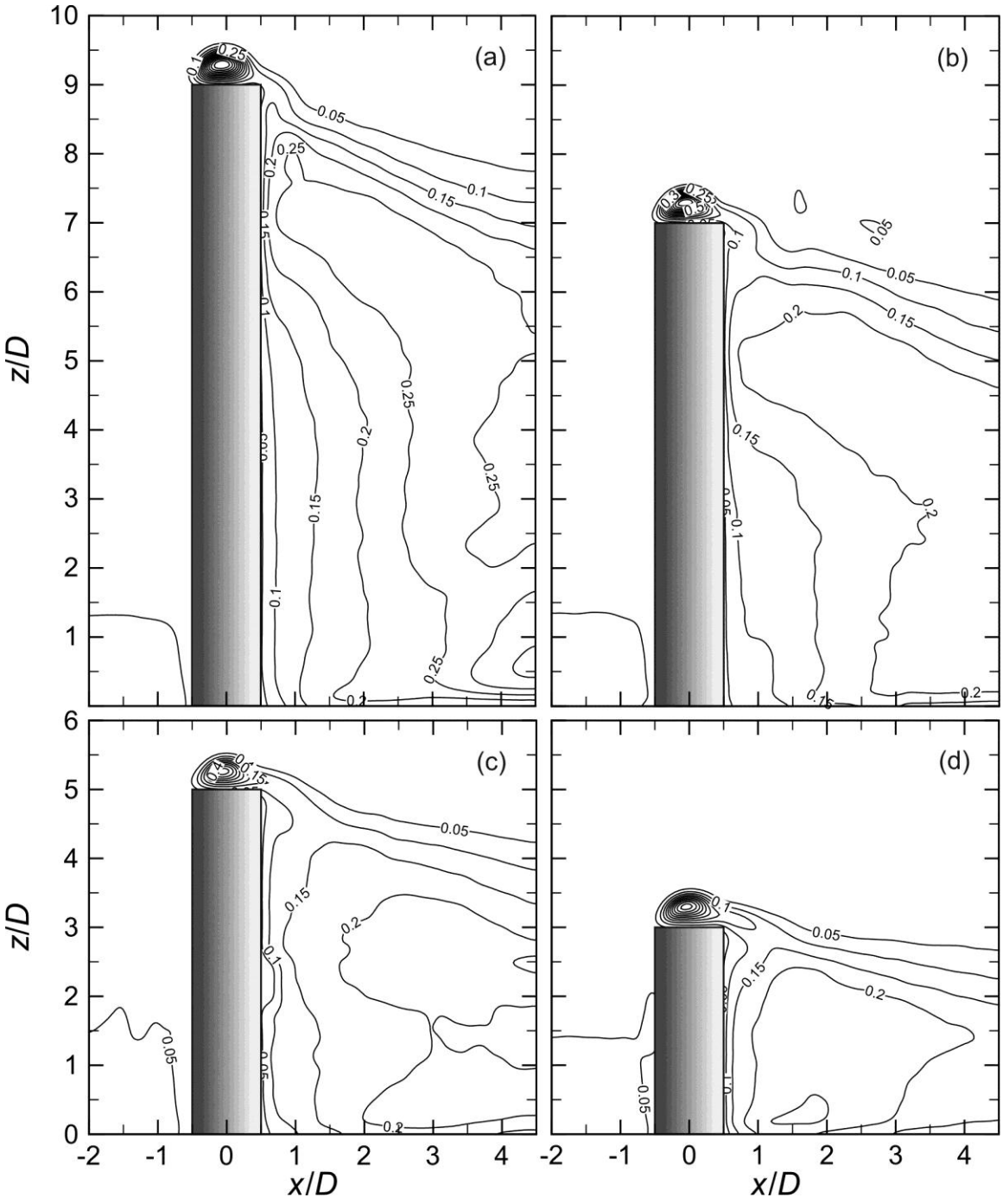

Figure 4.7: Streamwise turbulence intensity field (contours of u'/U_∞) in a vertical plane on the wake centerline (y/D = 0, the symmetry plane): (a) AR = 9; (b) AR = 7; (c) AR = 5; (d) AR = 3.

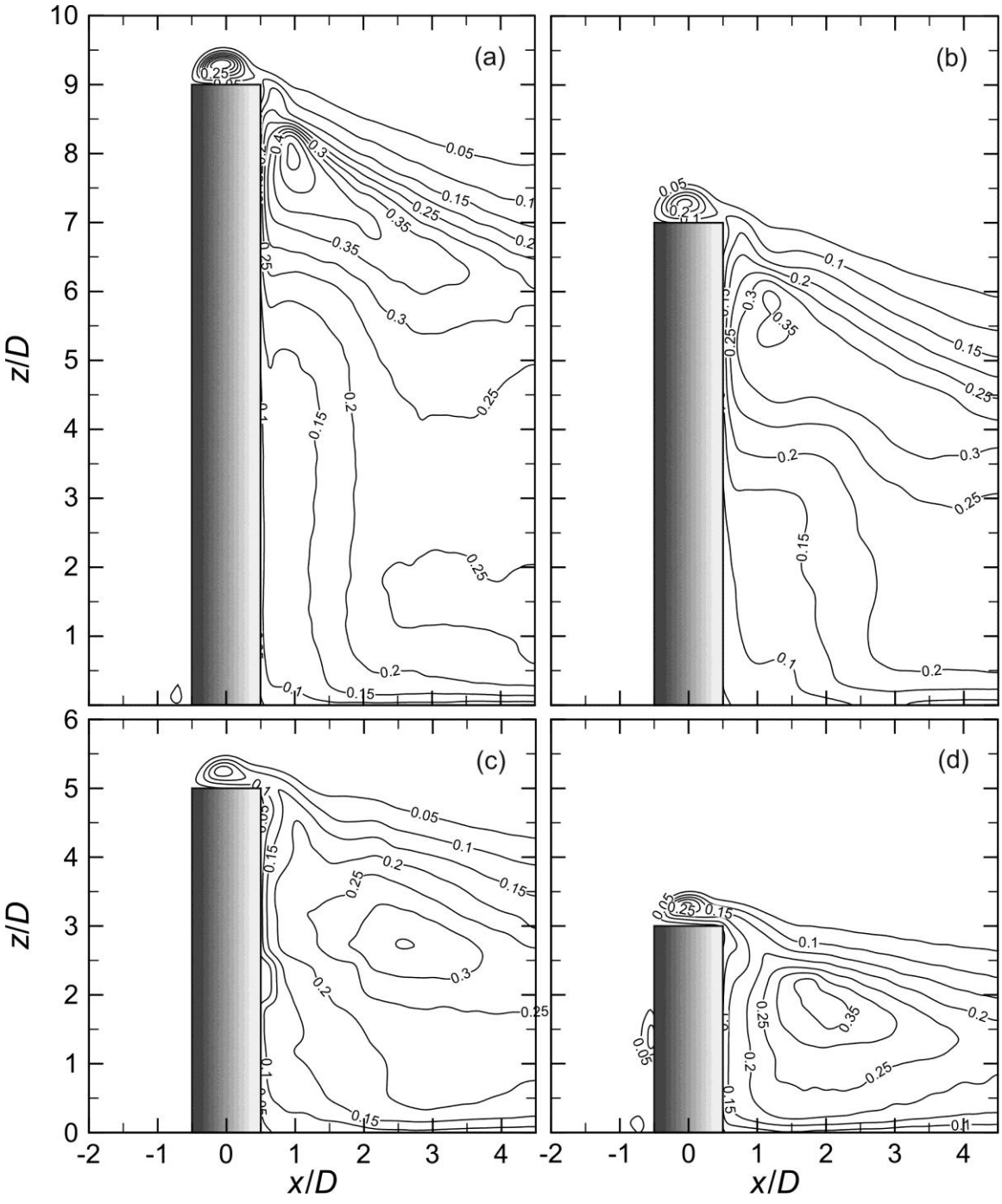

Figure 4.8: Wall-normal turbulence intensity field (contours of w'/U_∞) in a vertical plane on the wake centerline (y/D = 0, the symmetry plane): (a) AR = 9; (b) AR = 7; (c) AR = 5; (d) AR = 3.

4.3.2 Reynolds Shear Stress

The Reynolds shear stresses on the wake centreline for the four circular cylinders of AR = 9, 7, 5, and 3 are shown in Figure 4.9. According to this figure, the Reynolds shear stress for the cylinder of AR = 3 (Figure 4.9 (d)) is distinct from those for AR = 9, 7, and 5 (Figures 4.9 (a, b, c)). For the three most slender cylinders, the near-wake region is characterized by two regions of elevated Reynolds shear stress, a region of negative shear stress at the top of the wake and a region of positive shear stress closer to the ground plane (in the flat-plate boundary layer and localized with the upwash flow field). For AR = 3 (Figure 4.9 (d)), however, the region of positive shear stress below the free end is almost absent, showing a distinct wake structure for this cylinder. A similar result was found by Adaramola et al. (2006). Furthermore, the positive Reynolds shear stress just below the cylinder free end decreases in size and level as the aspect ratio of the cylinder decreases and it disappears for AR = 3. Considering the behavior of the mean recirculation zone on the free end, and the relationship between cylinder aspect ratio and the reattachment point (discussed later in Chapter 6), it seems that when the reattachment point moves towards the trailing edge there are changes to the local Reynolds shear stress in the region of downwash flow.

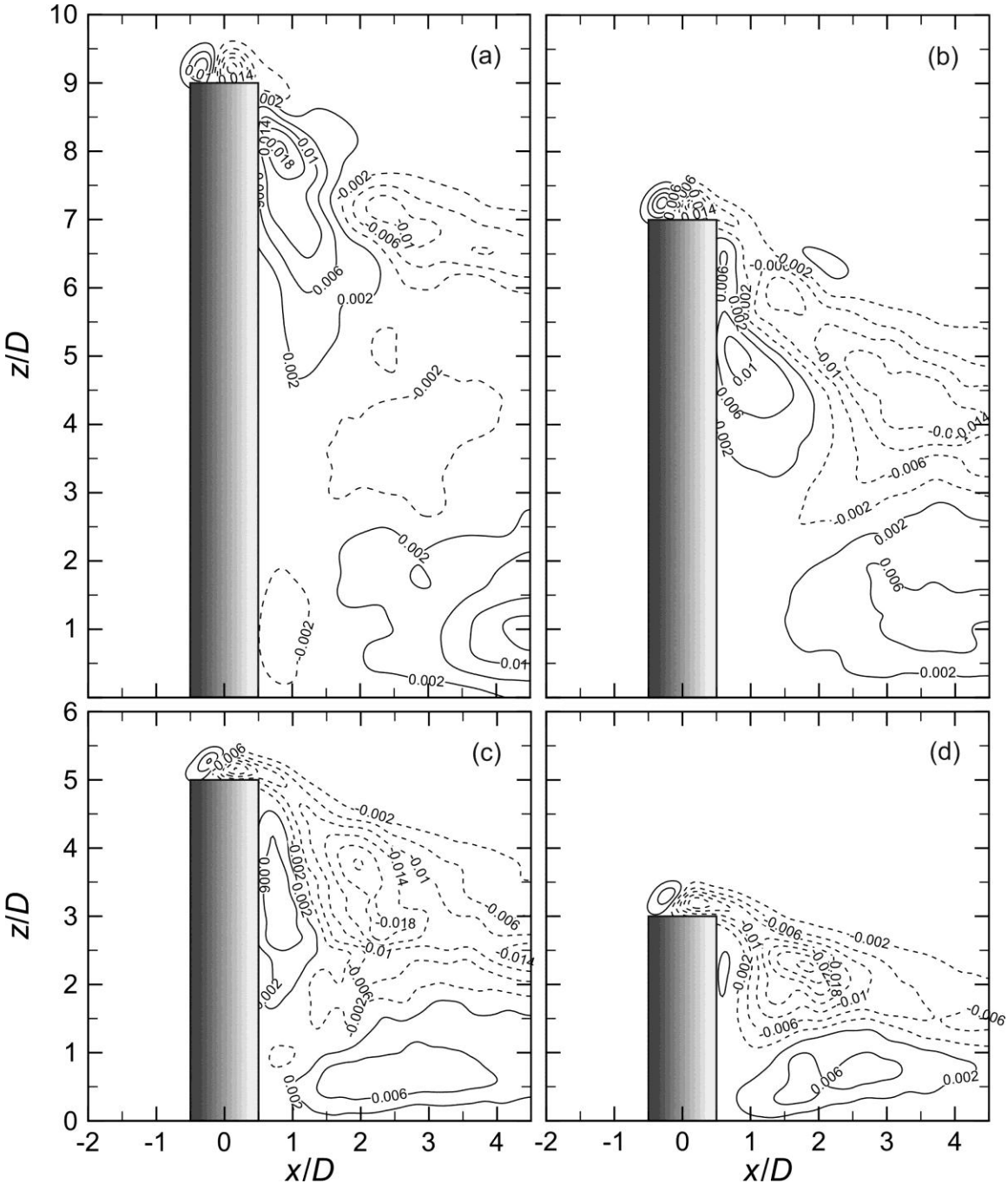

Figure 4.9: Reynolds shear stress field (contours of $-\overline{u'w'}/{U_\infty}^2$) in a vertical plane on the wake centerline (*y/D* = 0, the symmetry plane): (a) AR = 9; (b) AR = 7; (c) AR = 5; (d) AR = 3. Solid contour lines represent positive Reynolds shear stress; dashed contour lines represent negative Reynolds shear stress.

4.4 Mean In-plane Vorticity Field

The mean cross-stream vorticity ($\overline{\omega_y}D/U_\infty$) fields for the four finite circular cylinders are shown in Figure 4.10. Upstream of the cylinder, the negative vorticity near the ground plane reveals the presence of the boundary layer and horseshoe vortex. For all four aspect ratios, negative (CW) vorticity is generated as the flow moves around the free end and downward into the near wake of the cylinder. For the cylinders of AR = 9 and 7 (Figures 4.10 (a, b)), this region of mean vorticity remains close to the trailing edge of the free end but also extends downwards along the base of the cylinder, approaching the mid-height point. For the cylinder of AR = 5 (Figure 4.10 (c)), this vorticity is spread over a larger region behind the cylinder, extending to $x/D \approx 2$. This pattern is similar for the cylinder of AR = 3 (Figure 4.10 (d)) with this concentration of vorticity extending farther downstream (for $x/D > 2$) than the other cylinders. It is apparent that as the reattachment point on the free end surface moves closer to the trailing edge, the region of mean cross-stream vorticity behind the cylinder becomes larger in area and extends farther downstream.

Close to the cylinder-wall junction, and immediately behind the cylinder, a small region of positive (CCW) vorticity is found for the cylinders of AR = 9, 7 and 5 (Figures 4.10 (a, b, c)). This corresponds to the small recirculating region seen earlier in the mean velocity vector field (Figures 4.1 (a, b, c)) and mean streamlines (Figures 4.2 (a, b, c)). Compared to AR = 9, 7, and 5, no isolated region of positive vorticity is found in the region immediately behind the cylinder at its junction with the wall for the cylinder of AR = 3 (Figure 4.10 (d)). This is consistent with the absence of vortex N_w in this region for the cylinder of AR = 3 (see Figure 4.5).

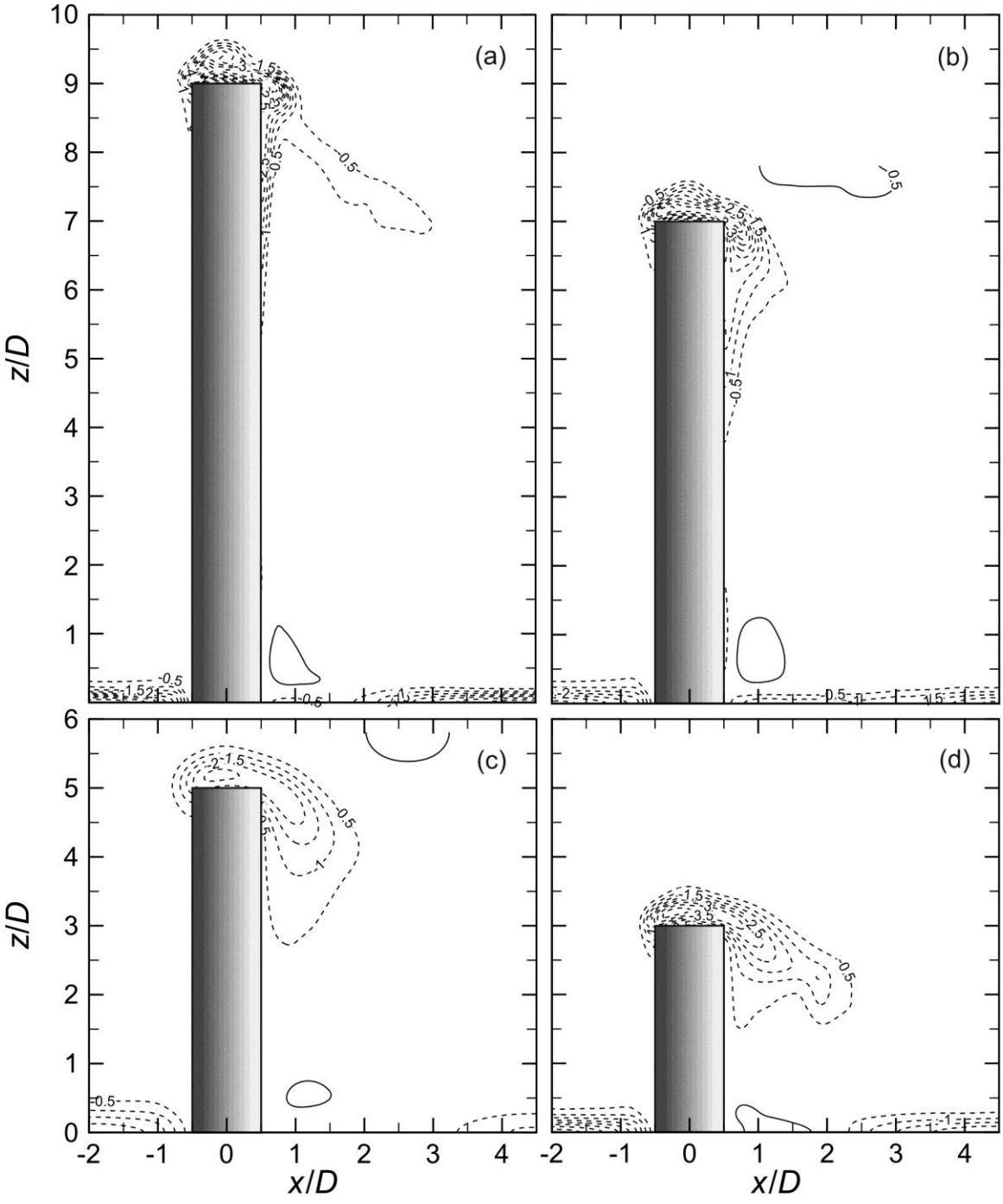

Figure 4.10: Mean in-plane vorticity field (contours of $\overline{\omega_y}D/U_\infty$) in a vertical plane on the wake centerline (*y/D* = 0, the symmetry plane): (a) AR = 9; (b) AR = 7; (c) AR = 5; (d) AR = 3. Solid contour lines represent positive (CCW) vorticity; dashed contour lines represent negative (CW) vorticity.

5. Turbulent Near Wake of a Surface-mounted Finite Square Prism

5.1 Introduction

Similar to the circular cylinder case discussed in Chapter 4, there is limited information about the flow pattern of the local flow field of a finite-height square prism. The near wake of square prisms of four different aspect ratios of AR = 9, 7, 5, and 3 was investigated using the PIV technique in order to understand this region of interest. This chapter provides information on the mean velocity distribution, turbulence quantities, Reynolds shear stress, and mean vorticity field in the near wake of the square prisms of AR = 9, 7, 5, and 3. Similar to the circular cylinder case, the field of view for the PIV measurements in the *x*-*z* plane was set to be 61 mm × 61 mm (1.9*D* × 1.9*D*). Different fields of view were then combined to examine the whole near-wake region of the square prisms.

5.2 Mean Velocity Distribution

The local mean velocity vector fields on the wake centerline (*y/D* = 0) for each of the four square prisms (of AR = 9, 7, 5, and 3) are shown in Figure 5.1. The corresponding mean flow streamlines are shown in Figure 5.2. In these figures, the in-plane mean velocity components are made dimensionless with the freestream velocity ($\overline{U}/U_\infty$, $\overline{W}/U_\infty$). The mean fields are calculated from an ensemble of 1,000 instantaneous PIV velocity fields.

5.2.1 Mean Streamwise Velocity

In order to show the mean flow behavior in the near-wake region of the finite square prisms, the mean velocity vector fields and streamlines together with the contours of mean streamwise velocity are presented and discussed.

According to Figures 5.1 and 5.2, upstream of the prism, for all four aspect ratios, part of the approach flow moves up and over the tip and separates from the leading edge of the free end. Unlike the finite circular cylinder case (discussed in Chapter 4), no flow reattachment occurs on the free end of the finite square prisms. The other part of the approach flow, closer to the ground plane, moves downwards as it nears the prism and recirculates upstream of the prism-wall junction. It is in this region where the familiar horseshoe vortex is located. Although the horseshoe vortex cannot be discerned in the velocity vectors (Figure 5.1), a small horseshoe vortex can be seen in the streamlines in Figure 5.2 for the different aspect ratios.

In the near-wake region, a strong downwash flow (downward-directed velocity vectors in Figure 5.1) is observed immediately downstream of the free end in the near wake of the prism. The downwash originates downstream of the free-end recirculation zone, persists in the streamwise direction and descends into the central portion of the wake. In the mean streamlines shown in Figure 5.2, part of the downwash flow is directed towards the ground plane and returns upstream to stagnate onto the rear surface of the prism; a large recirculation zone forms behind the prism. The rest of the downwash flow moves away from the prism into the far wake. As seen in Figure 5.2, a small vortex forms immediately downstream of the trailing edge of the free end. The size of the vortex is a function of the prism aspect ratio, such that the largest vortex occurs for the smallest aspect ratio (AR = 3, Figure 5.2 (d)). According to Figures 5.2 (a, b, c), for AR = 9, 7 and 5, respectively, some of the downwash flow is directed along the prism rear surface

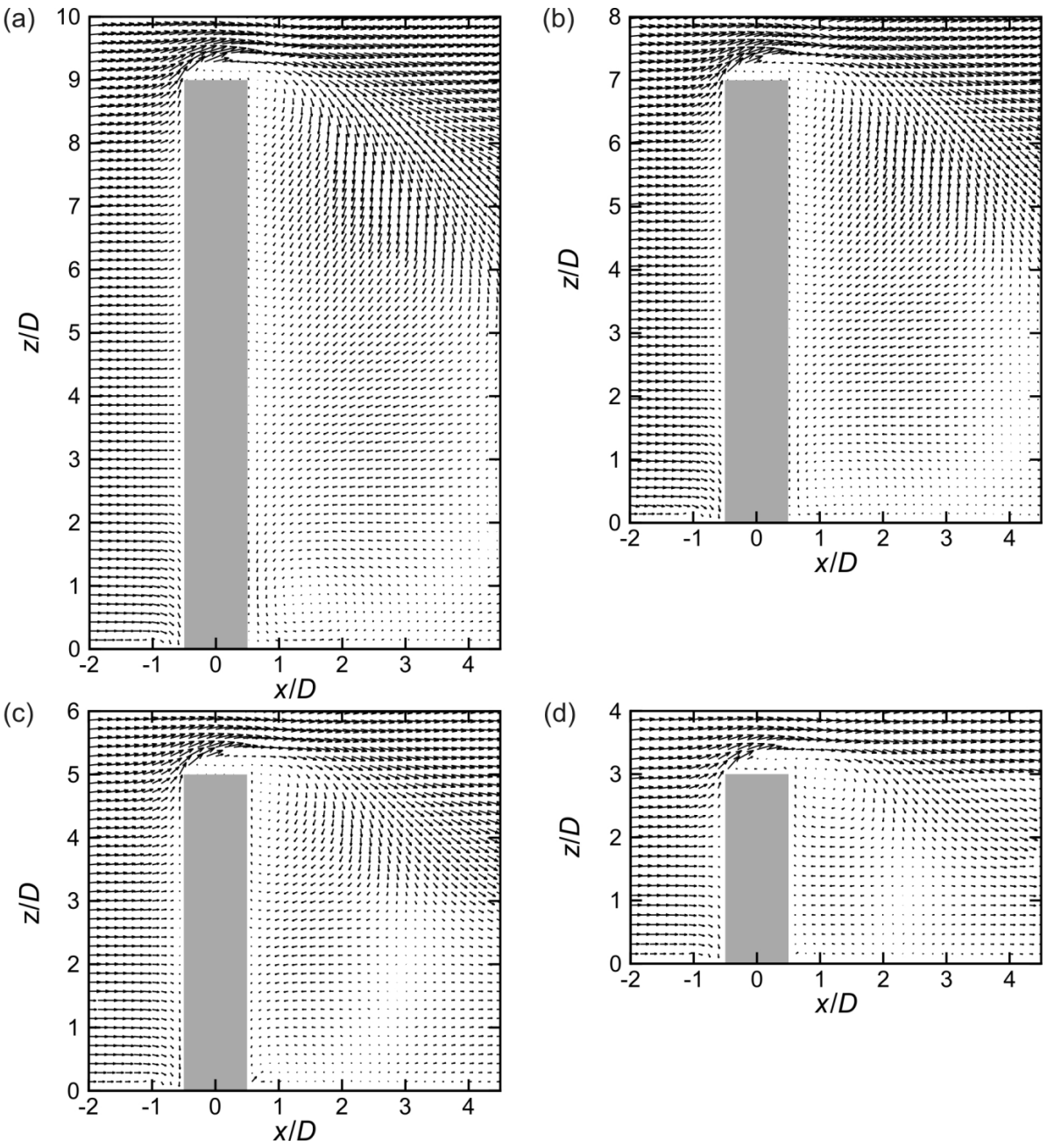

Figure 5.1: Mean velocity vector field ($\overline{U}/U_\infty$, $\overline{W}/U_\infty$ components) in a vertical plane on the wake centerline (y/D = 0, the symmetry plane) of a finite-height square prism: (a) AR = 9; (b) AR = 7; (c) AR = 5; (d) AR = 3. $\mathrm{Re}_D = 4.2 \times 10^4$ and δ/D = 1.6. Half of the vectors were skipped.

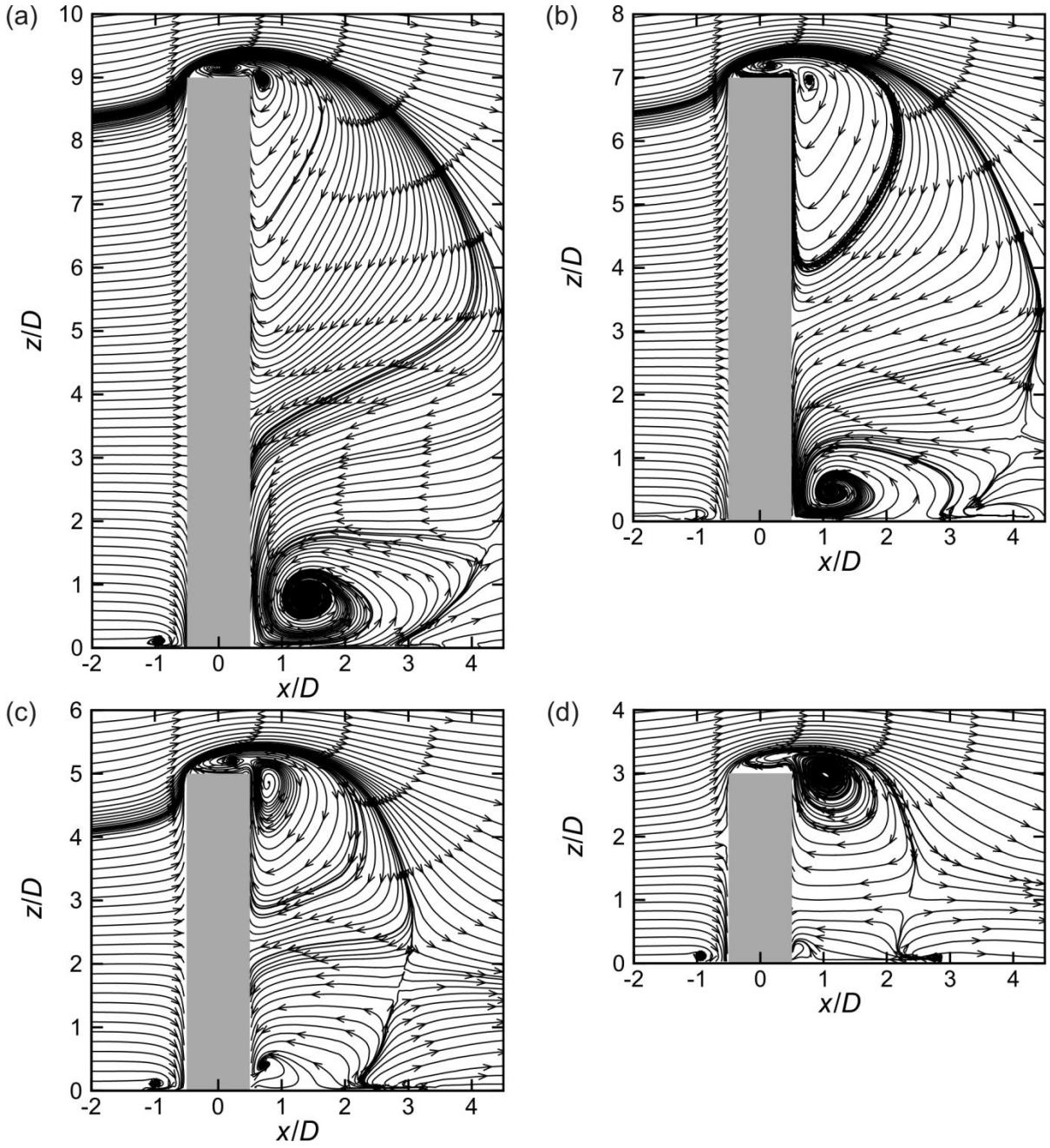

Figure 5.2: Mean streamlines in a vertical plane on the wake centerline (y/D = 0, the symmetry plane) corresponding to the mean velocity vector field in Figure 5.1: (a) AR = 9; (b) AR = 7; (c) AR = 5; (d) AR = 3.

toward the ground plane, whereas for AR = 3 (Figure 5.2 (d)) the flow moves upwards along the prism rear surface toward the free end, resulting in a larger vortex just below the free end.

According to Figure 5.2, another vortex, with CCW sense of rotation, can be found immediately behind the prism, near the prism-wall junction, for AR = 9 and 7 (Figures 5.2 (a, b)); enlargements of these vortices are shown in Figure 5.3. This vortex is much weaker and nearly absent for the prisms of AR = 5 and 3 (Figures 5.3 (c, d)). The distinct near-wake structure for AR = 3, and to some extent for AR = 5, suggest the critical aspect ratio for these prisms is between AR = 5 and AR = 3, similar to the circular cylinder. This is consistent with the results of McClean and Sumner (2012) who investigated the mean drag coefficient as well as the Strouhal number for finite-height square prisms of different aspect ratios. They showed that the critical aspect ratio for the square prisms is between AR = 5 and AR = 3.

The mean streamwise velocity component contours shown in Figure 5.4 (contours of $\overline{U}/U_\infty$) indicate a region of negative streamwise velocity immediately behind each of the four prisms, which broadly denotes the mean recirculation zone. For the prisms of AR = 9, 7 and 5 (Figures 5.4 (a, b, c)), the region of negative velocity extends to almost the free end of the prism, whereas this is not the case for AR = 3 (Figure 5.4 (d)). According to the contour lines in Figure 5.4, the largest value of negative mean velocity is approximately $\overline{U}/U_\infty$ = - 0.3 for all AR.

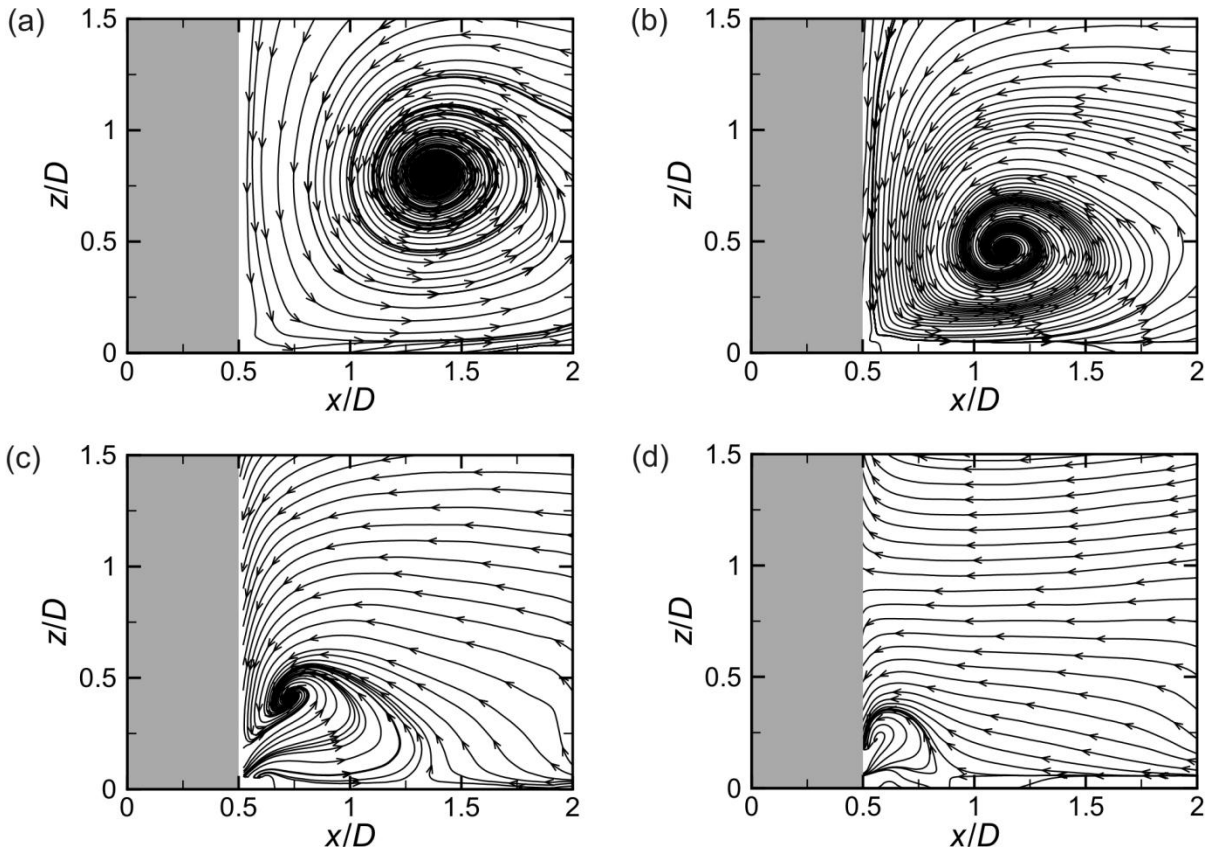

Figure 5.3: Enlarged view of mean streamlines (($\overline{U}/U_\infty$, $\overline{W}/U_\infty$ components) in a vertical plane on the wake centerline (*y/D* = 0, the symmetry plane) behind the prism close to the prism-wall junction: (a) AR = 9; (b) AR = 7; (c) AR = 5; (d) AR = 3.

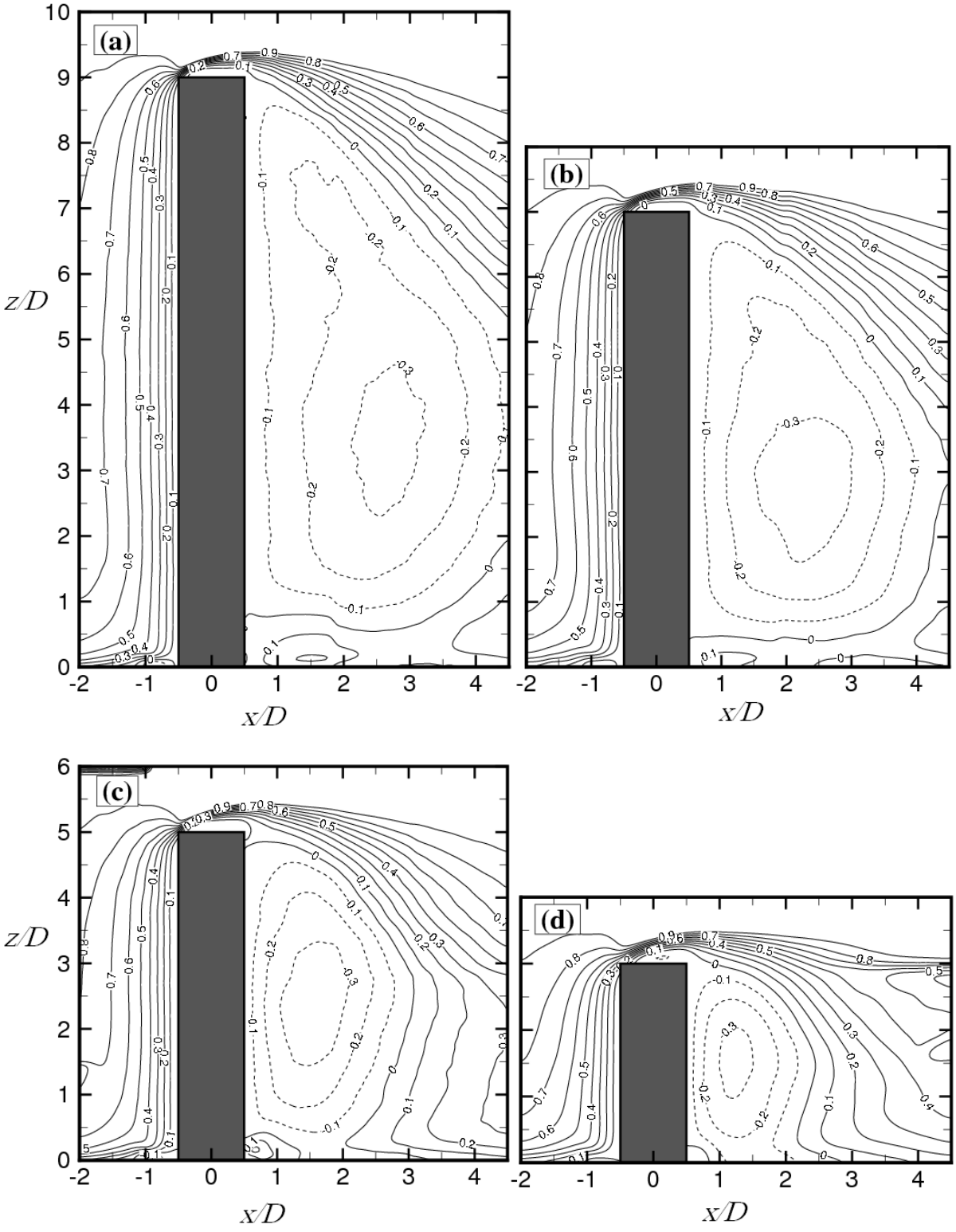

Figure 5.4: Streamwise mean velocity field (contours of $\overline{U}/U_\infty$) in a vertical plane on the wake centerline (y/D = 0, the symmetry plane): (a) AR = 9; (b) AR = 7; (c) AR = 5; (d) AR = 3. Solid

contour lines represent positive streamwise velocity; dashed contour lines represent negative streamwise velocity.

Figure 5.5 shows how the maximum length of the recirculation zone is dependent on the square prism's aspect ratio. According to this figure, the maximum length of the recirculation zone increases from L_{max}/D = 2.3 for AR = 3 to L_{max}/D = 4.2 for AR = 9. In Figure 5.5, the present data are compared to the square prism data of Wang and Zhou (2009) at $Re_D = 9.3 \times 10^3$, and Bourgeois et al. (2010) at $Re_D = 1.2 \times 10^4$. Good agreement can be seen between the present data and the other studies for prisms of AR = 3, 5, and 7. However, there is a considerable difference between the maximum length of the recirculation zone from the present results to the one reported by Wang and Zhou (2009). This discrepancy might be related to the difference in Reynolds number or δ/D.

5.2.2 Mean Wall-normal Velocity

The time-averaged wall-normal velocity fields ($\overline{W}/U_\infty$) in the *x*-*z* plane, for the square prisms of AR = 9, 7, 5, and 3 are shown in Figure 5.6. The wall-normal velocity component contours in Figure 5.6 illustrate regions of upward-directed and downward-directed flow within the local flow field of the prisms. According to this figure, there are upwash flows at the front of prism free end for all four aspect ratios. The extent and predominance of the strong downwash flow field is clearly evident for all four prisms. According to Figure 5.6, the downwash flow stretches along the prism height towards the junction of the prism and the ground plane for AR = 9, and 7 (Figures 5.6 (a, b)), while there is no evidence of this stretch for the prisms of AR = 5 and 3 (Figures 5.6 (c, d)). Furthermore, a small region of upwash flow just below the prism free end can be seen for the prism of AR = 3 (Figure 5.6 (d)).

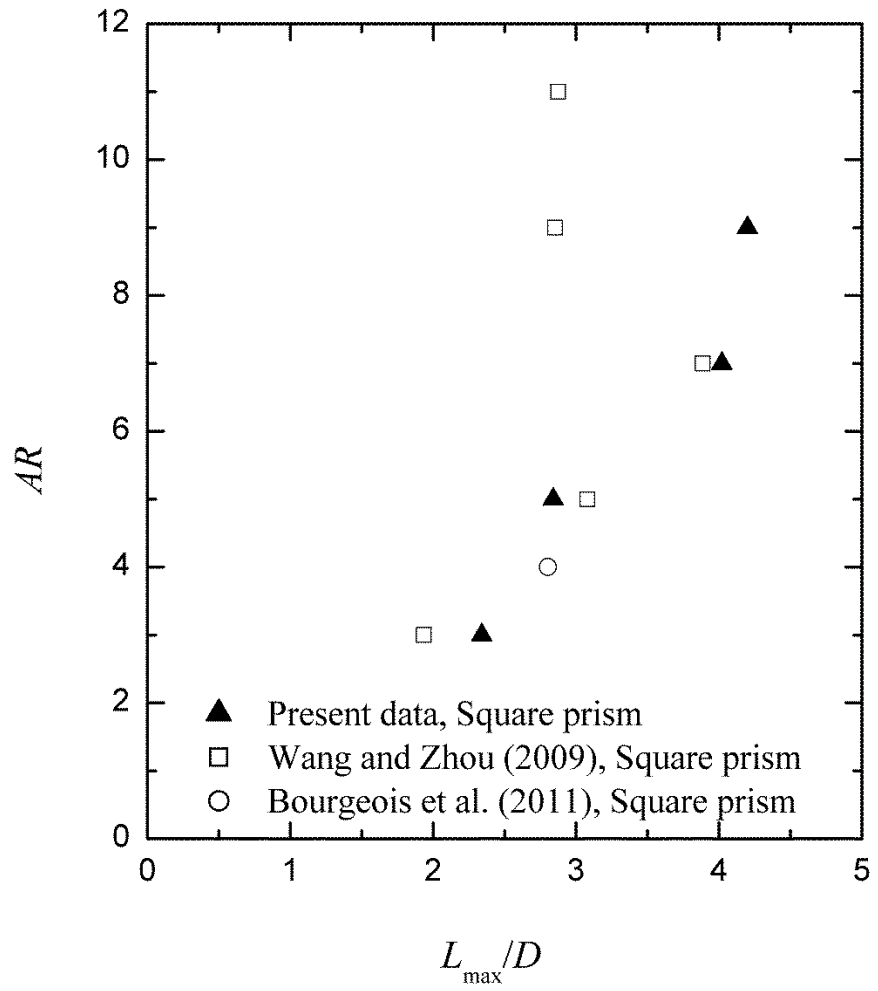

Figure 5.5: Maximum longitudinal length of the mean recirculation zone for square prisms of different aspect ratios. ▲, Present study, $Re_D = 4.2\times10^4$; □, Wang and Zhou (2009), $Re_D = 9.3\times10^3$; ○, Bourgeois et al. (2011), $Re_D = 1.2\times10^4$.

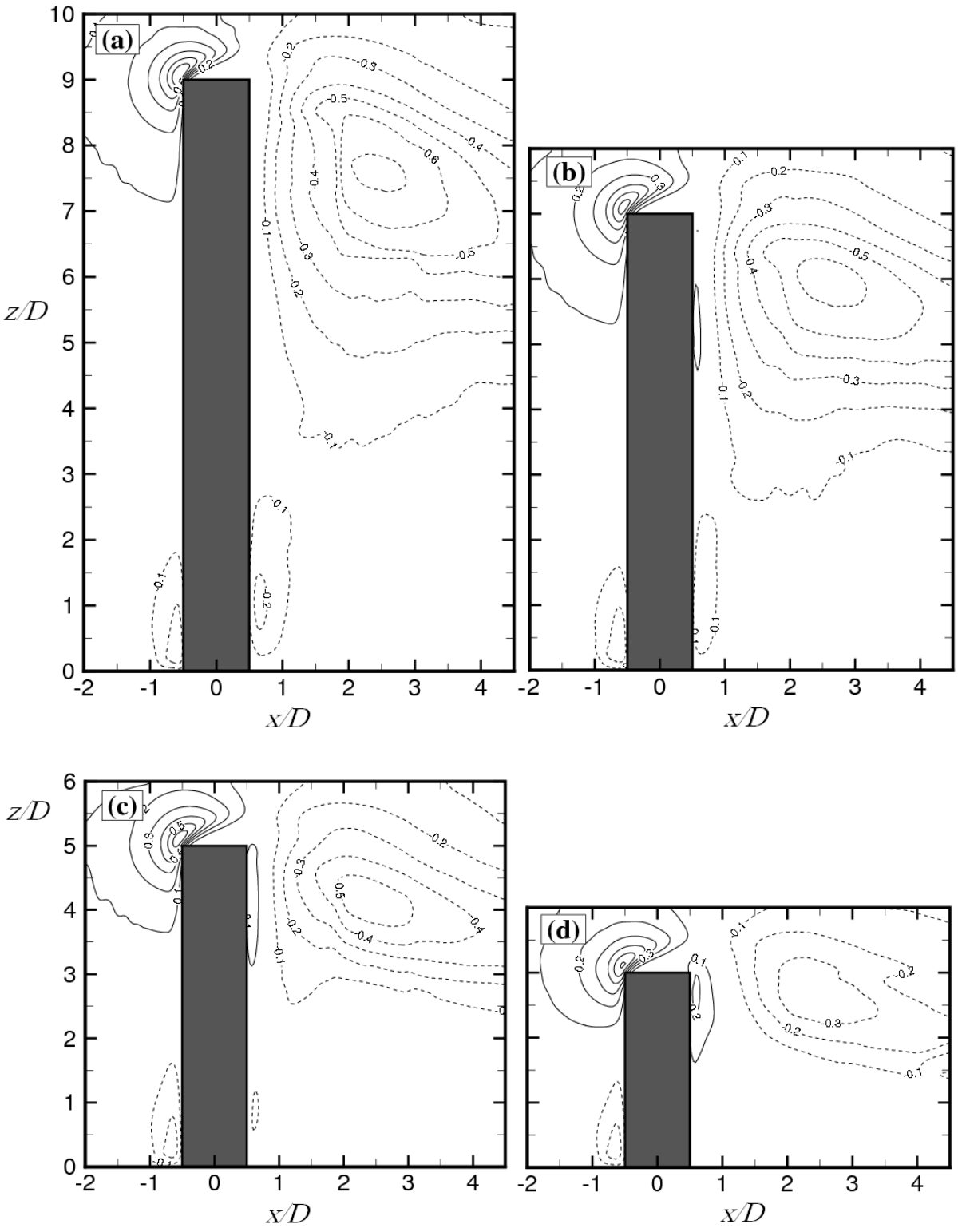

Figure 5.6: Wall-normal mean velocity field (contours of $\overline{W}/U_\infty$) in a vertical plane on the wake centerline (y/D = 0, the symmetry plane): (a) AR = 9; (b) AR = 7; (c) AR = 5; (d) AR = 3.

5.3 Turbulence Structure

Contour plots of the streamwise turbulence intensity (u'/U_∞), wall-normal turbulence intensity (w'/U_∞), and Reynolds shear stress ($-\overline{u'w'}/{U_\infty}^2$), on the wake centreline for the four square prisms of AR = 9, 7, 5, and 3, are shown and discussed in this section.

5.3.1 Turbulence Intensity Distribution

A contour plot of the streamwise turbulence intensity (u'/U_∞), on the wake centreline, is shown in Figure 5.7. The highest values of streamwise turbulence intensity are encountered above the free end of the prisms of AR = 9, 7, and 5 (Figures 5.7 (a, b, c)), while the highest value of u'/U_∞ for AR = 3 (Figure 5.7 (d)) occurs farther downstream, showing a distinct turbulence structure for AR = 3.

For all four prisms, the highest values of wall-normal turbulence intensity, w'/U_∞, (shown in Figure 5.8) are encountered within the recirculation zones of the prisms. According to Figure 5.8, the location of highest wall-normal turbulence intensity in the near-wake region tends to move downward and towards the prism as the aspect ratio of the prism decreases.

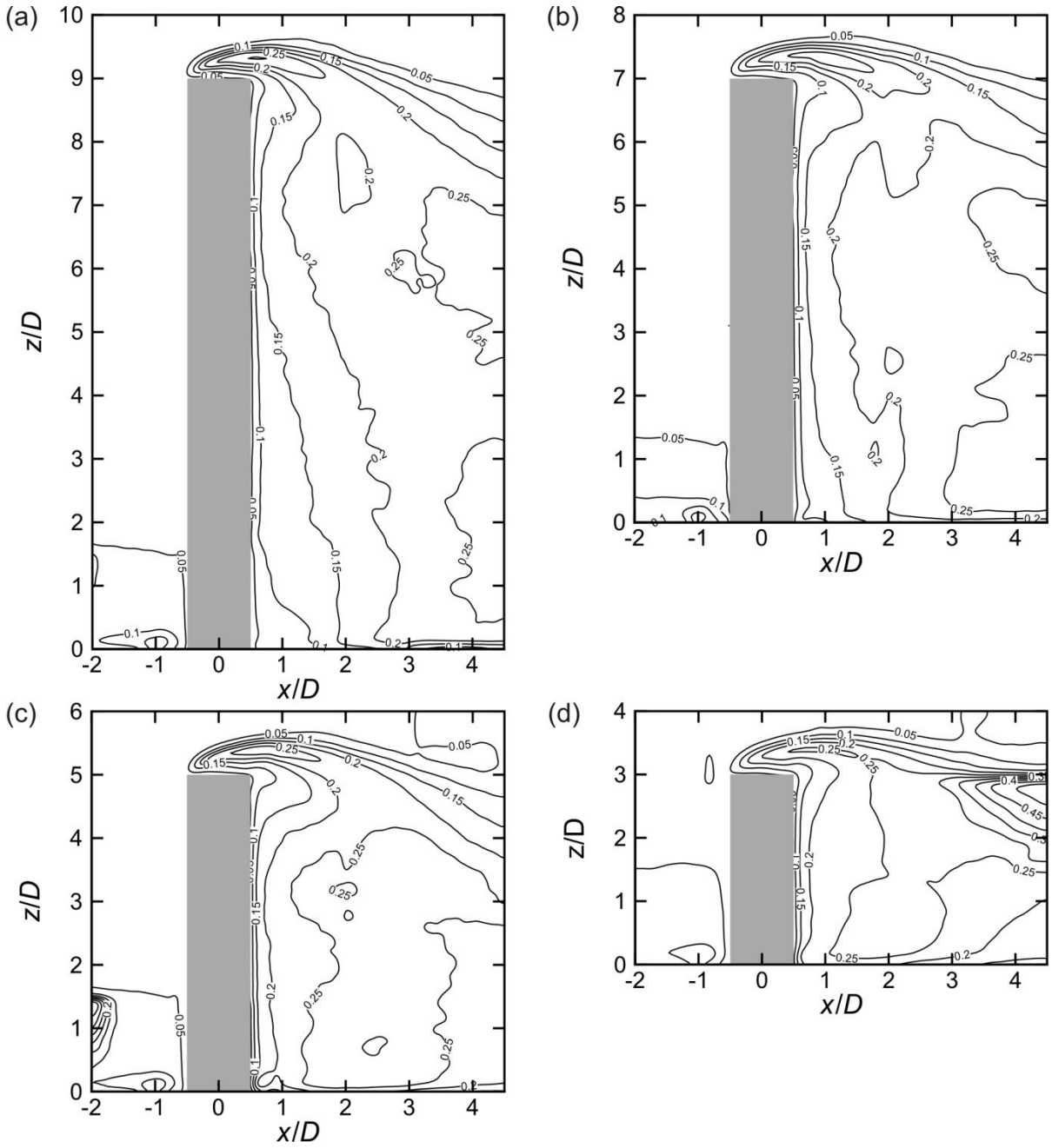

Figure 5.7: Streamwise turbulence intensity field (contours of u'/U_∞) in a vertical plane on the wake centerline ($y/D = 0$, the symmetry plane): (a) AR = 9; (b) AR = 7; (c) AR = 5; (d) AR = 3.

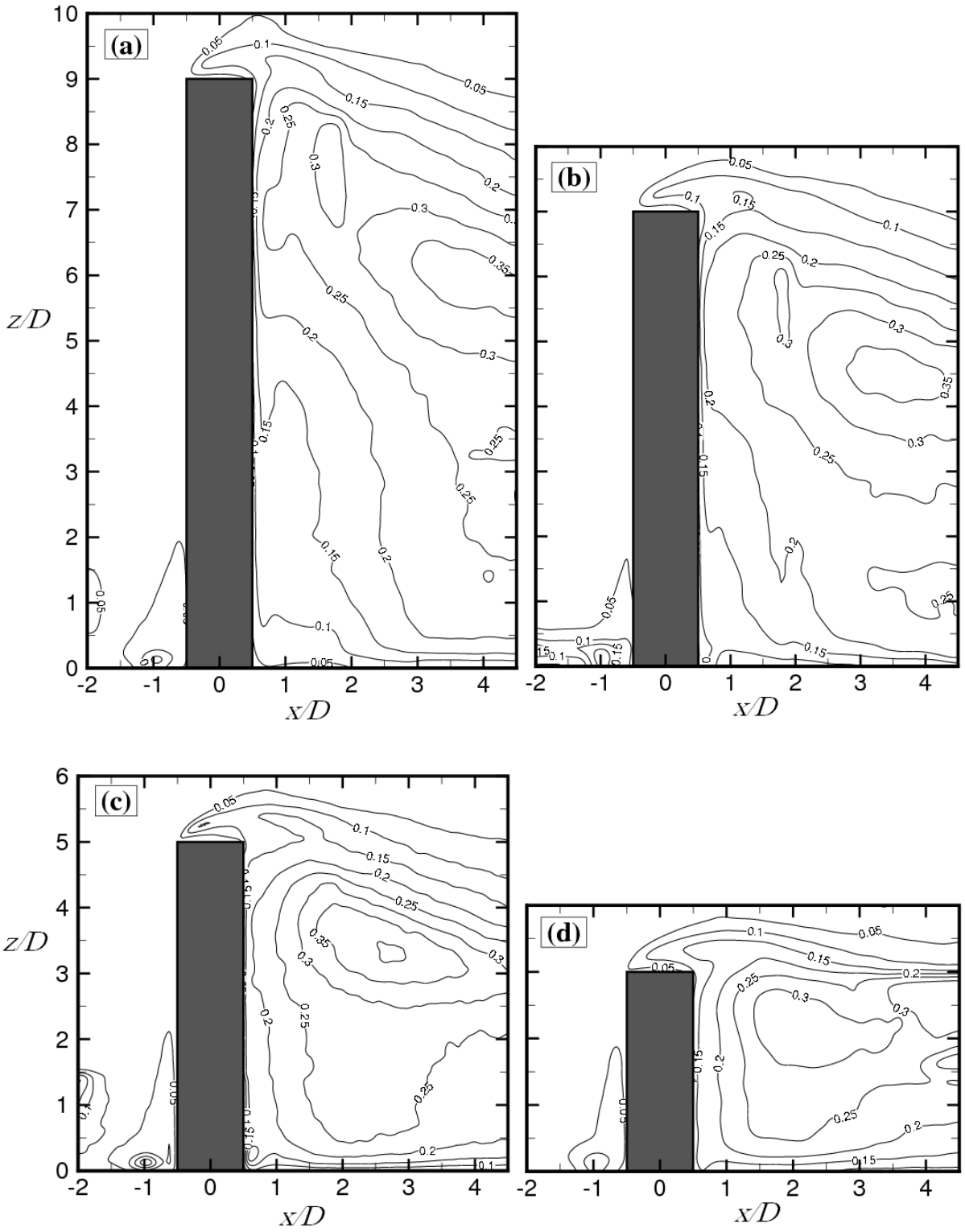

Figure 5.8: Wall-normal turbulence intensity field (contours of w'/U_∞) in a vertical plane on the wake centerline ($y/D = 0$, the symmetry plane): (a) AR = 9; (b) AR = 7; (c) AR = 5; (d) AR = 3.

5.3.2 Reynolds Shear Stress

The Reynolds shear stresses on the wake centreline for four square prisms of AR = 9, 7, 5, and 3 are shown in Figure 5.9. According to this figure, the Reynolds shear stress field on the wake centreline for AR = 3 (Figure 5.9 (d)) is distinct from those for AR = 9, 7, and 5 (Figures 5.9 (a, b, c)). For the three most slender prisms, the near-wake region is characterized by two regions of elevated Reynolds shear stress: a region of negative shear stress at the top of the wake and a region of positive shear stress closer to the ground plane. For AR = 3 (Figure 5.9 (d)), however, the region of positive shear stress below the free end is almost absent, showing a distinct wake structure for this prism. Furthermore, the positive Reynolds shear stress just below the prism free end decreases in size and level as the aspect ratio of the prism decreases; it disappears for AR = 3.

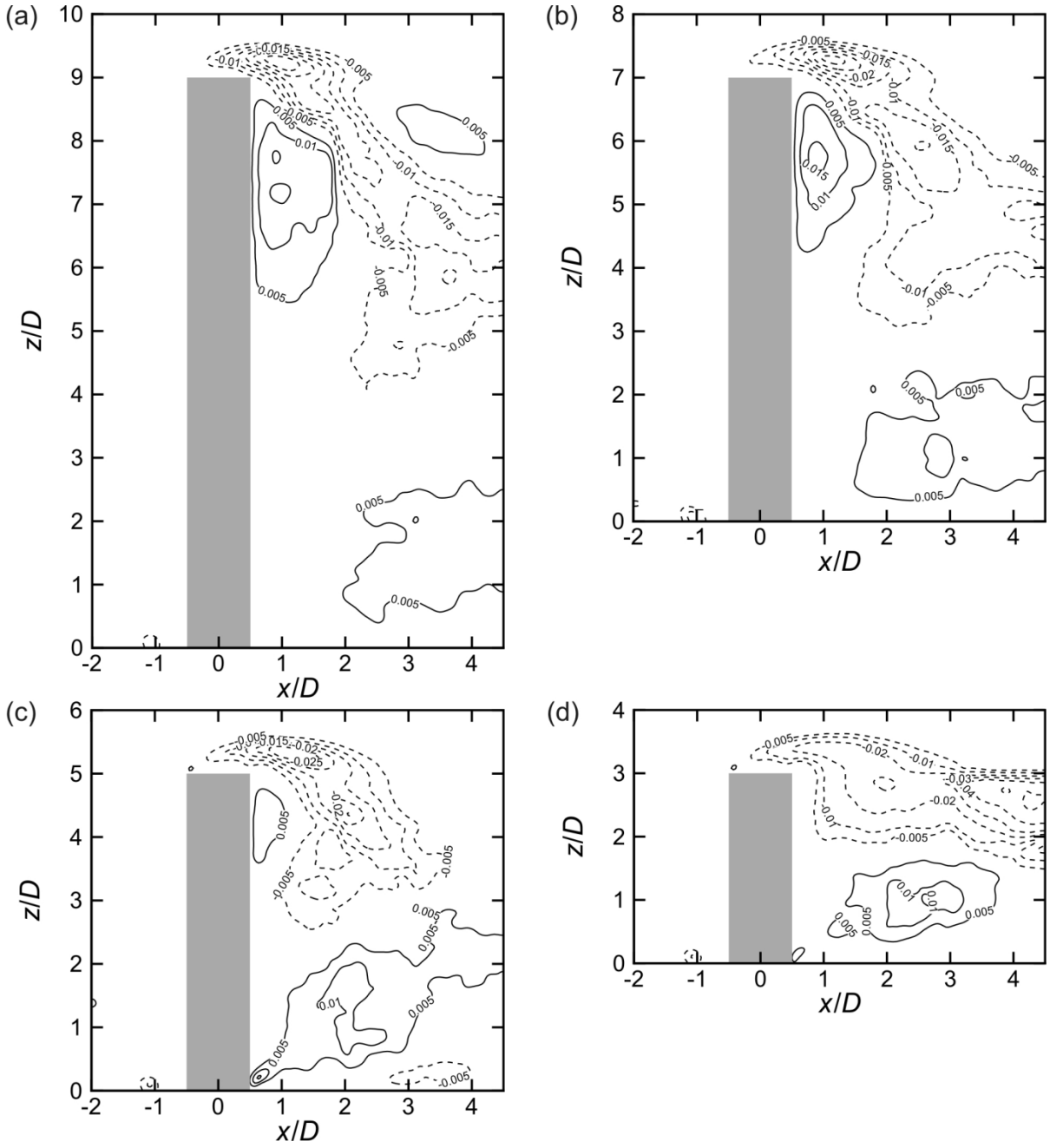

Figure 5.9: Reynolds shear stress field (contours of $-\overline{u'w'}/U_\infty^2$) in a vertical plane on the wake centerline (*y/D* = 0, the symmetry plane): (a) AR = 9; (b) AR = 7; (c) AR = 5; (d) AR = 3. Solid contour lines represent positive Reynolds shear stress; dashed contour lines represent negative Reynolds shear stress.

5.4 Mean In-plane Vorticity Field

The mean cross-stream vorticity ($\overline{\omega_y}D/U_\infty$) fields for the four finite square prisms are shown in Figure 5.10. Upstream of the prism, the negative (CW) vorticity near the ground plane reveals the presence of the boundary layer and horseshoe vortex. For finite square prisms, this vortex is more obvious compared to that of the finite circular cylinders (see Figures 4.2 and 4.10). This may be related to the shape of the cross-section of the bluff body (circular or square cross-section), as the square prism is considered more bluff than the circular cylinder. Sumer and Fredsoe (1997) showed a smaller size of the horseshoe vortex for a finite circular cylinder compared to finite square prism of same diameter, Reynolds number, and boundary layer thickness. They reported that the adverse pressure gradient upstream of the square prism is larger than the circular cylinder resulting in an early separation of the flow in this region for the square prism.

For all four aspect ratios, negative vorticity is generated as the flow moves around the free end and downward into the near wake of the prism. It is apparent that as the square prism aspect ratio decreases, the region of mean cross-stream vorticity behind the prism becomes larger in area and extends farther downstream. Close to the prism-wall junction, and immediately behind the prism, a small region of positive (CCW) vorticity is found for the prisms of AR = 9, 7 and 5 (Figures 5.10 (a, b, c)). This corresponds to the small recirculation shown earlier (Figures 5.3). Compared to AR = 9, 7, and 5, no region of positive vorticity is found in the region immediately behind the prism at its junction with the wall for the prism of AR = 3 (Figure 5.10 (d)).

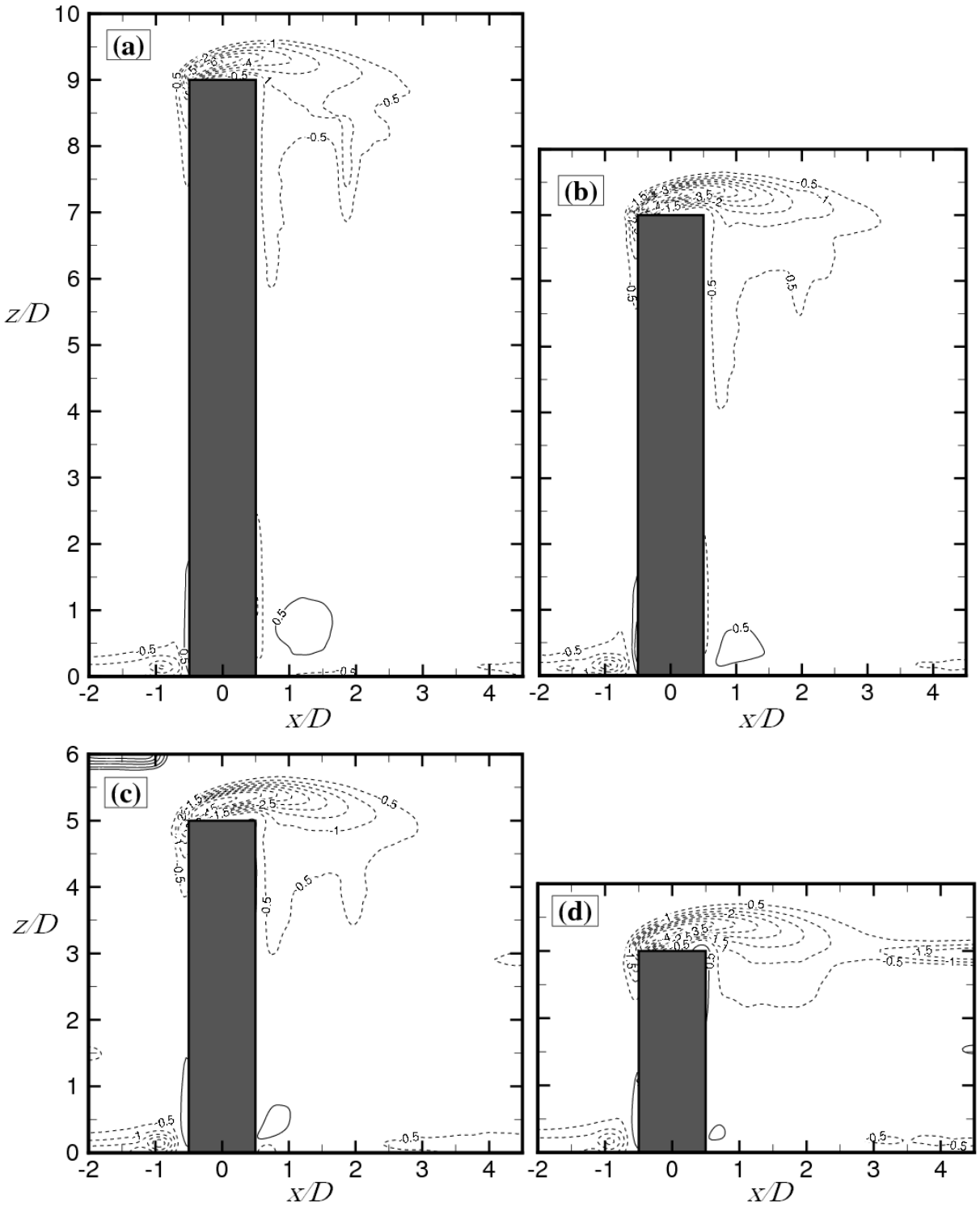

Figure 5.10: Mean in-plane vorticity field (contours of $\overline{\omega_y}D/U_\infty$) in a vertical plane on the wake centerline (y/D = 0, the symmetry plane): (a) AR = 9; (b) AR = 7; (c) AR = 5; (d) AR = 3. Solid contour lines represent positive (CCW) vorticity; dashed contour lines represent negative (CW) vorticity.

5.5 Comparison between the Near-wake Regions of Circular Cylinders and Square Prisms

According to the results discussed in Chapters 4 and 5, there are some similarities and differences between the flow characteristics of the near-wake regions of circular cylinders and square prisms, showing the effects of bluff body shape (circular or square cross-section) on the near-wake regions. A schematic of the flow separation from the circular cylinder and the square prism is shown in Figure 5.11. According to this figure, the upstream flow separates from the edges of the leading surface of the prism, while for the circular cylinder case, the flow separation location changes depending on the Reynolds number and other parameters.

A comparison of the mean streamlines shown in Figures 4.2 and 5.2 shows larger cross-stream vortices just downstream of the free end surface of the square prisms compared to the circular cylinders. This is observed for all aspect ratios and is related to the difference in the behavior of the shear flow separated from the leading edge of the free end and directed toward the near-wake regions. According to Figures 4.5 and 5.3, for square prisms of AR = 9 and 7 (Figures 5.3(a, b)), the vortices close to the prism-wall junction are larger than those of circular cylinders (Figures 4.5(a, b)), while for the square prism of AR = 5 (Figure 5.3(c)), the vortex is much smaller than that of the circular cylinder of AR = 5 (Figure 4.5(c)). For the case of AR = 3, no vortices are observed close to the model-wall junction for both circular cylinders and square prisms (Figures 4.5(d) and 5.3(d)).

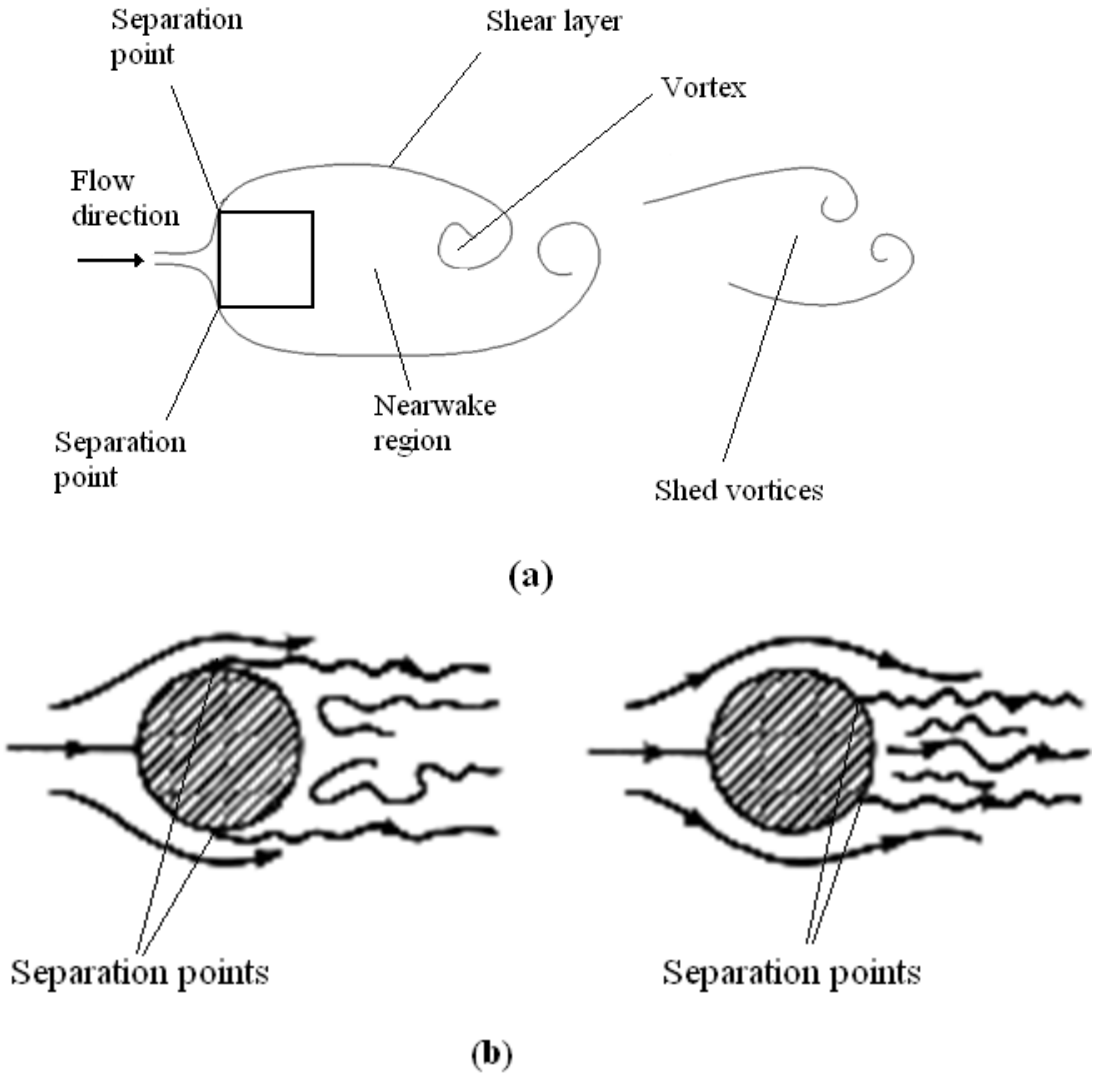

Figure 5.11: Schematic representation of the flow separation from the bluff bodies: (a) square prism, fixed separation points; (b) circular cylinder, variable separation locations.

The effect of the bluff body shape (circular or square cross-section) is also evident in the maximum length of the mean recirculation zone shown in Figures 4.4 and 5.5. According to these figures, a considerable difference is seen between the maximum length of the mean recirculation zones of a circular cylinder and square prism of AR = 9, while the shape of the

bluff body does not considerably affect the length of the recirculation zones of models of AR = 7, 5, and 3.

Comparison between the wall-normal mean velocity components of circular cylinder and square prisms (shown in Figures 4.6 and 5.6) shows that the downwash flow in the near-wake region of circular cylinders is stronger than that of square prisms. The minimum wall-normal mean velocity ($\overline{W}/U_\infty$) has a value of -0.9 and -0.6 for circular cylinder of AR = 9 and 3, respectively, while it reaches -0.7 and -0.3 for square prisms of AR = 9 and 3, respectively. It is also concluded that the shape of the bluff bodies does not considerably affect the levels of turbulence characteristics of the flow in the near-wake regions of finite circular cylinders and square prisms.

There are a few studies about the effect of the cross-section of the cylinders on the flow structure around the cylinder. Ozgoren (2006) found that the values of Strouhal number, as well as the wake patterns, are functions of the cross-sectional shape (profile) of the cylinders and Reynolds number. According to his results, Strouhal numbers for the circular cylinder and square prism were found to be around 0.21, and 0.13, respectively. His results also showed larger length scales for the square prism, not only in the cross-stream direction but also in the streamwise direction compared to the circular cylinder. Owing to the fixed separation points of the square prism, the flow separation and the recirculation regions have an increasing effect on the wake region. This is consistent with the present results in terms of the size of the mean recirculating zone behind the circular cylinder and square prism. Hu et al. (2006) investigated the effect of corner radius on the near wake of a square prism. According to their results, the mean drag coefficient (C_D) increases from 1.182 for the circular cylinder to 1.951 for a square prism at Re_D = 2,600. The Strouhal number for the circular cylinder case decreases from 0.272 to 0.207 for the

square prism case. This is due to the increase in the vortex “wavelength”. According to Hu et al. (2006), the vortex formation length and the wake closure length for the circular cylinder is almost twice of those for the square prism, which is consistent with the results of the turbulence intensities of the present study.

Okamoto and Uemura (1991) investigated the effect of rounding side corners on the wake structure of a surface-mounted cube. Their study looked at the flow past a sphere, hemisphere-cylinder, circular cylinder, square plate and cube. According to their results, the drag for a cube is larger than that of a circular cylinder of the same length due to the round side-corners. Okamoto and Uemura (1991) also showed that the effect of rounding side-corners on the turbulent wake is weakened by the downwash from the free end of the cylinder.

6. Flow Above the Free End of the Finite Circular Cylinder

6.1 Introduction

As discussed in Chapters 1 and 2, the flow around surface-mounted cylinders of finite height is more complex than the more familiar case of the flow around an infinite cylinder. The flows around cylinder-like structures are strongly influenced by the finite height of the structure and the fact that the structure is mounted normal to a flat surface. The flow over the free end of the cylinder and around the cylinder-wall junction causes the overall flow field and near-wake region to become strongly three-dimensional. Since the flow field above the free end of a finite-height cylinder influences the flow pattern in the near-wake region, and is directly related to the downwash flow field (discussed in Chapter 4), further study of this local flow field is of interest in order to obtain a more complete understanding of the flow around finite-height surface-mounted bluff bodies. In this thesis, the flow fields above the free end surfaces of surface-mounted, finite-height circular cylinders and square prisms were investigated. Of particular interest were the effects of bluff body shape (circular or square cross-section) and aspect ratio on the flow pattern above the free end surface.

In this chapter, the PIV results in orthogonal planes (*x*-*z* and *x*-*y*) above the free end surface of four finite circular cylinders of AR = 9, 7, 5, and 3 are presented and discussed. The mean velocity fields, turbulence intensities, Reynolds shear stress, and vorticity fields for the flow above the free end of the cylinders are presented here.

6.2 Measurements in *x-z* Planes

PIV measurements were taken in *x-z* vertical planes above the free ends of the cylinders at three cross-stream locations of y/D = 0, 0.25, and 0.375. In this Section, the effect of the cylinder aspect ratio on the flow field above the free end in the symmetry plane (y/D = 0) is investigated. In addition, the free-end flow field away from the symmetry plane is presented and discussed here for circular cylinders.

6.2.1 Free-end Flow Field in the Symmetry Plane (y/D = 0)

Figures 6.1 and 6.2 show, respectively, the mean velocity vectors and streamlines in the symmetry plane above the free end of the circular cylinders. This region is of interest since it is directly related to the downwash flow behind the cylinder. According to Figures 6.1 and 6.2, the approaching flow separates from the leading edge of the free end surface and an attached region of recirculating flow forms on the free end surface. The attached region of recirculating flow corresponds to recirculating region V_{f1} shown in Figures 2.4 and 2.5. The results in these figures show that the flow above the cylinder reattaches onto the free end surface before reaching the trailing edge; this is consistent with the results of Leder (2003), Park and Lee (2004), Hain et al. (2008), Palau-Salvador et al. (2010), and Krajnović (2011).

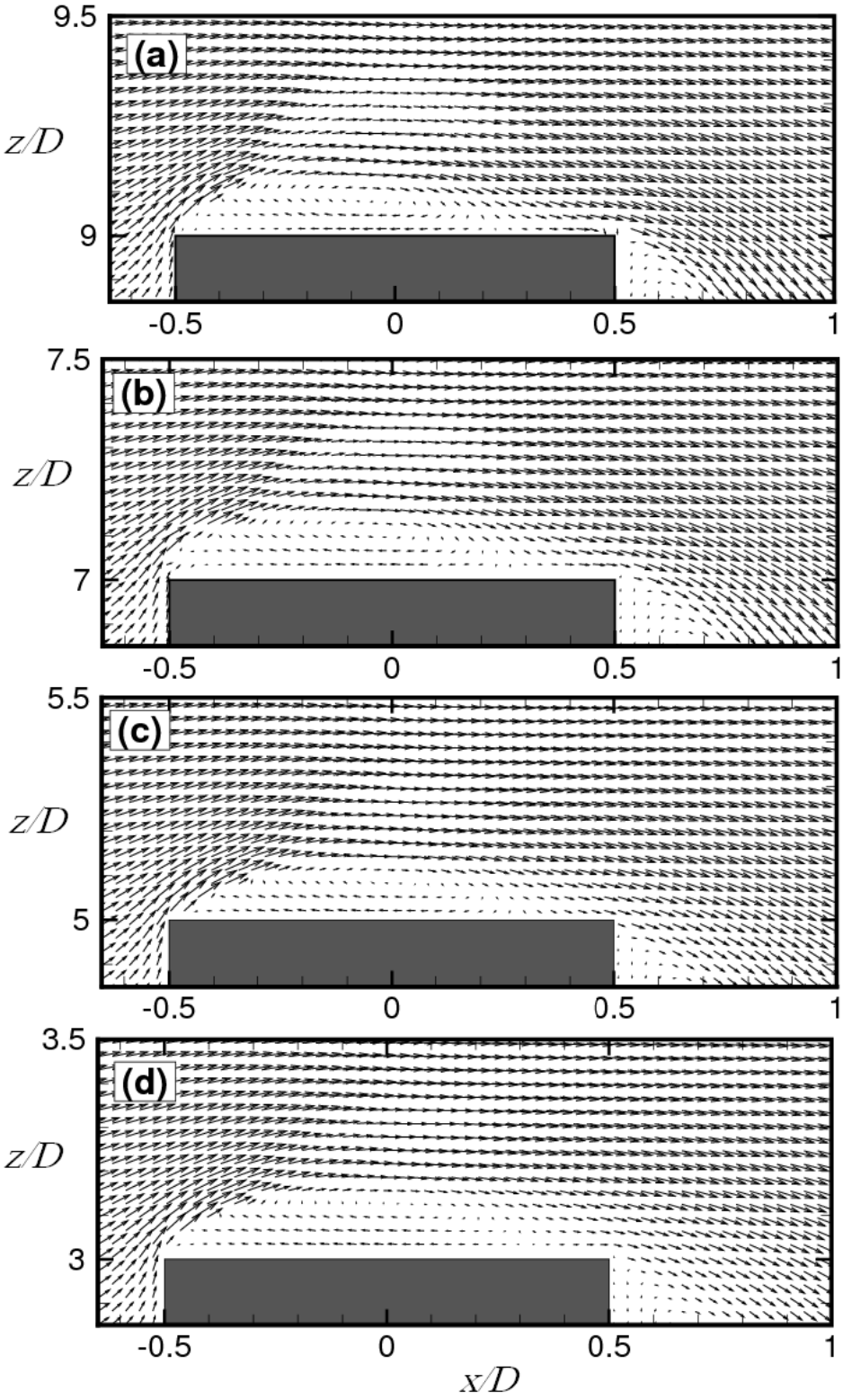

Figure 6.1: Mean velocity vector field in the symmetry plane (y/D = 0) above the free end surface of finite-height circular cylinders: (a) AR = 9; (b) AR = 7; (c) AR = 5; (d) AR = 3.

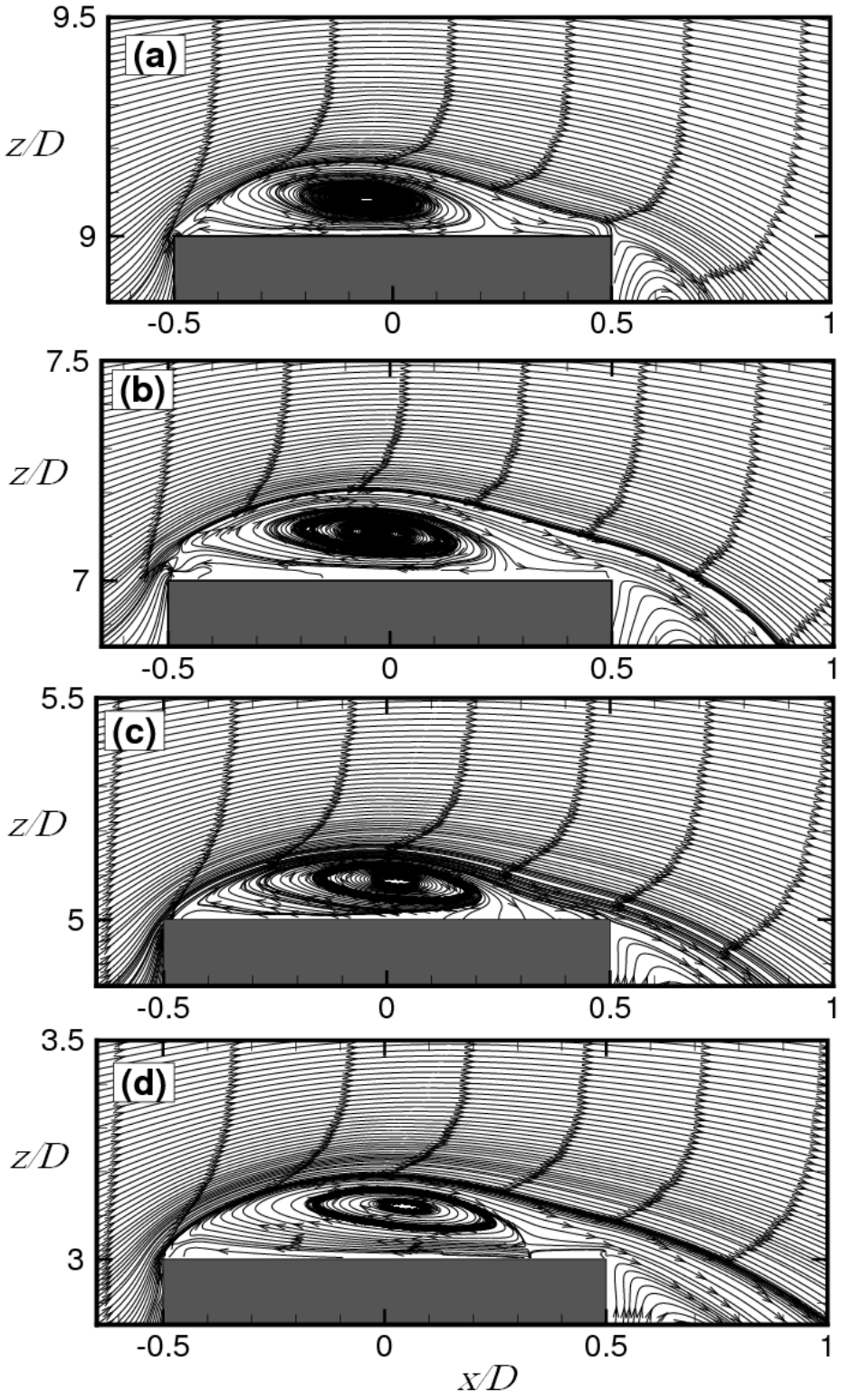

Figure 6.2: Mean streamlines in the symmetry plane (y/D = 0) above the free end surface of finite-height circular cylinders: (a) AR = 9; (b) AR = 7; (c) AR = 5; (d) AR = 3.

Contours of the wall-normal components of the mean velocity for the flow above the free end surface of circular cylinders of AR = 9, 7, 5, and 3 are shown in Figure 6.3. Regions of upward and downward flows are seen above the free end surface for all four aspect ratios. According to the contours of negative wall-normal velocity, the separated flow tends to move downward earlier for the cases of AR = 9 and 7 (Figures 6.3 (a, b)), while for cylinders of AR = 5 and 3 (Figures 6.3 (c, d)) the downward flow tends to move towards the trailing edge of the free end surface. This is consistent with the results shown in Figures 6.1 and 6.2.

The streamwise and wall-normal turbulence intensity fields above the free end are shown in Figures 6.4 and 6.5, respectively. These figures show large regions of elevated streamwise and wall-normal turbulence intensities above the free ends. Also, the core of higher streamwise turbulence intensities decreases in strength as the cylinder aspect ratio decreases. According to Figures 6.4 and 6.5, downstream of the free end, the region of elevated turbulence intensities extends farther above the cylinder as the aspect ratio of the cylinder decreases; this may have to do with the reattachment flow pattern on the free end described earlier.

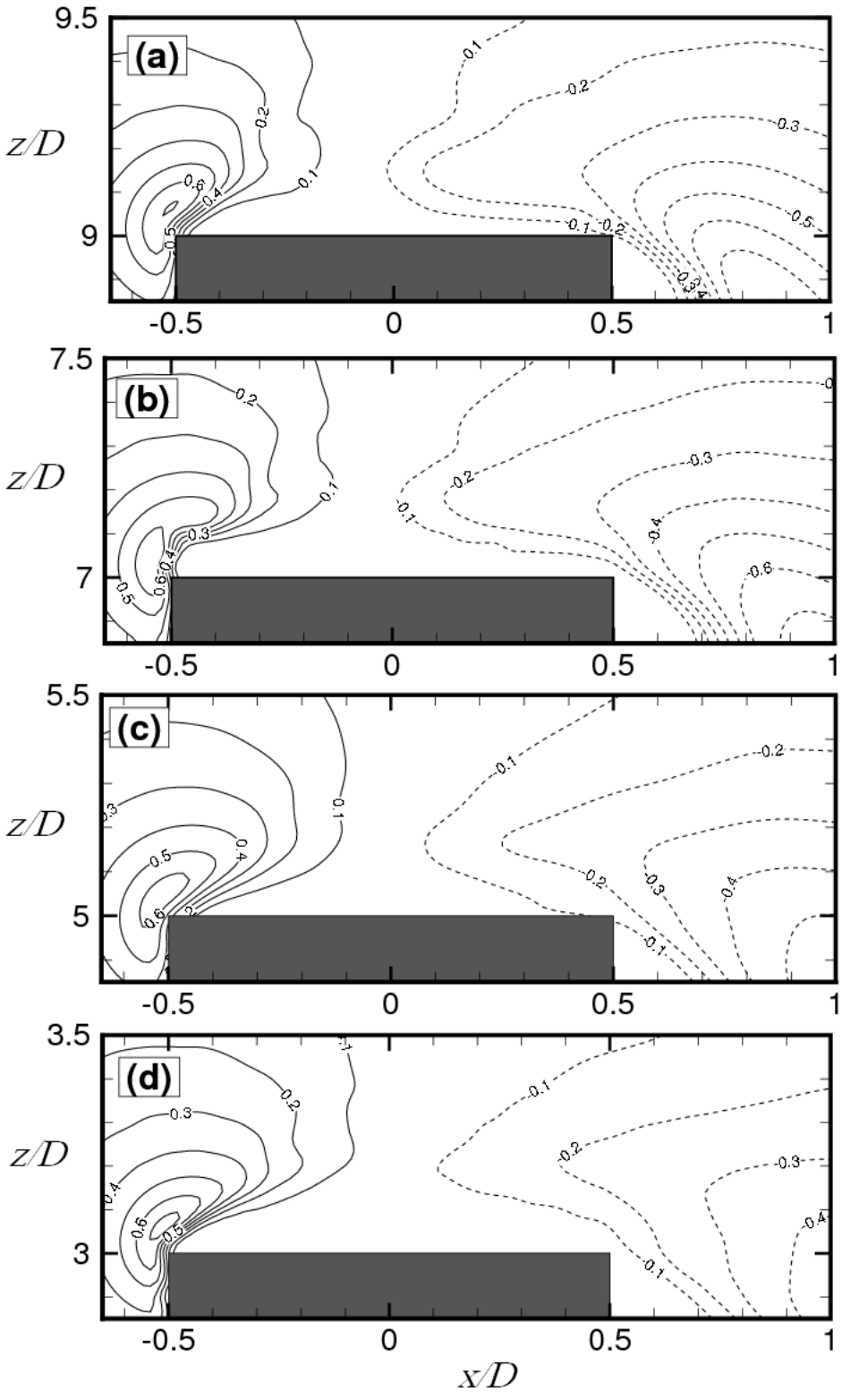

Figure 6.3: Wall-normal mean velocity fields (contours of $\overline{W}/U_\infty$) above the free end surface of finite-height circular cylinders: (a) AR = 9; (b) AR = 7; (c) AR = 5; (d) AR = 3.

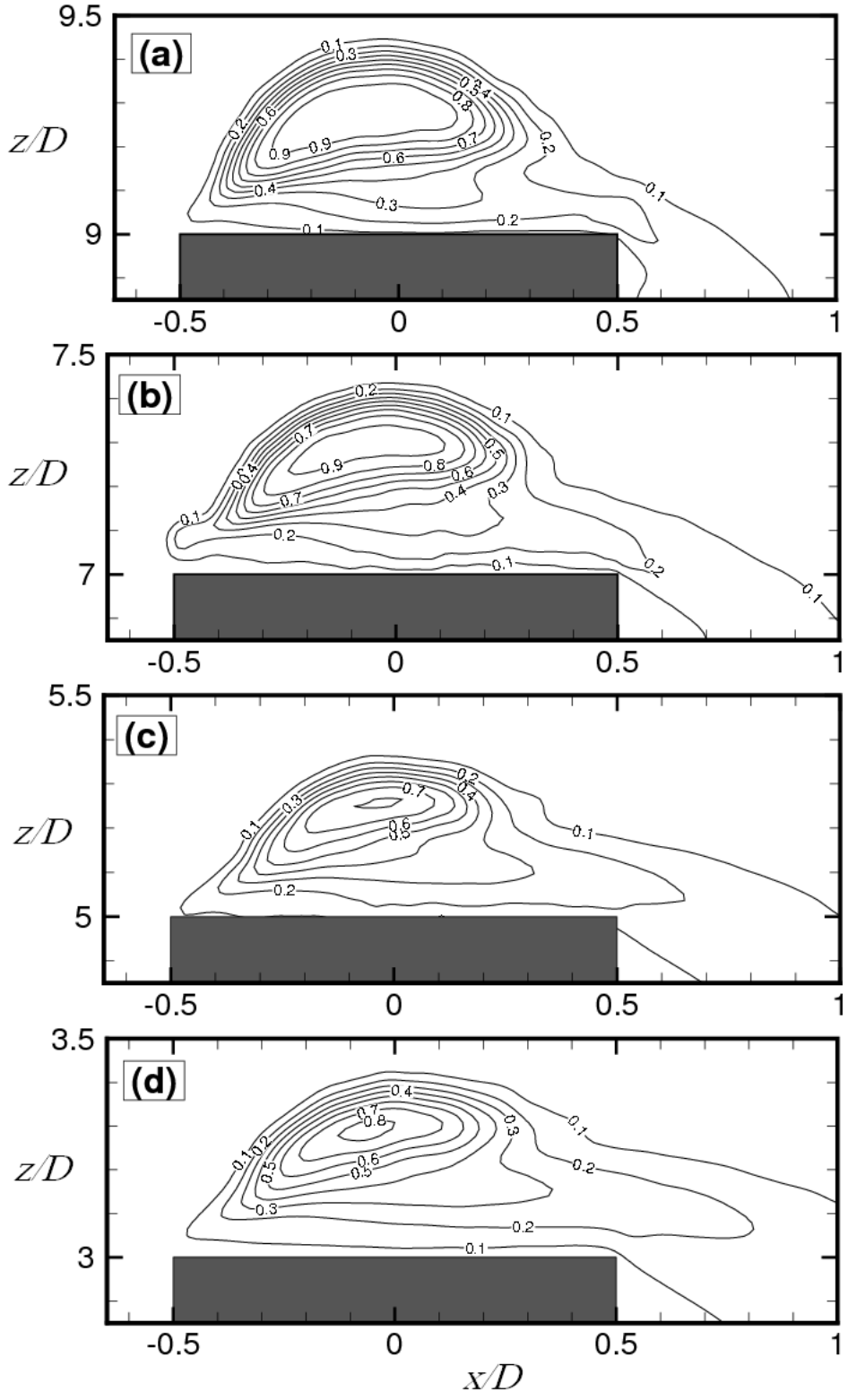

Figure 6.4: Streamwise turbulence intensity field (contours of u'/U_∞) above the free end surface of finite-height circular cylinders: (a) AR = 9; (b) AR = 7; (c) AR = 5; (d) AR = 3.

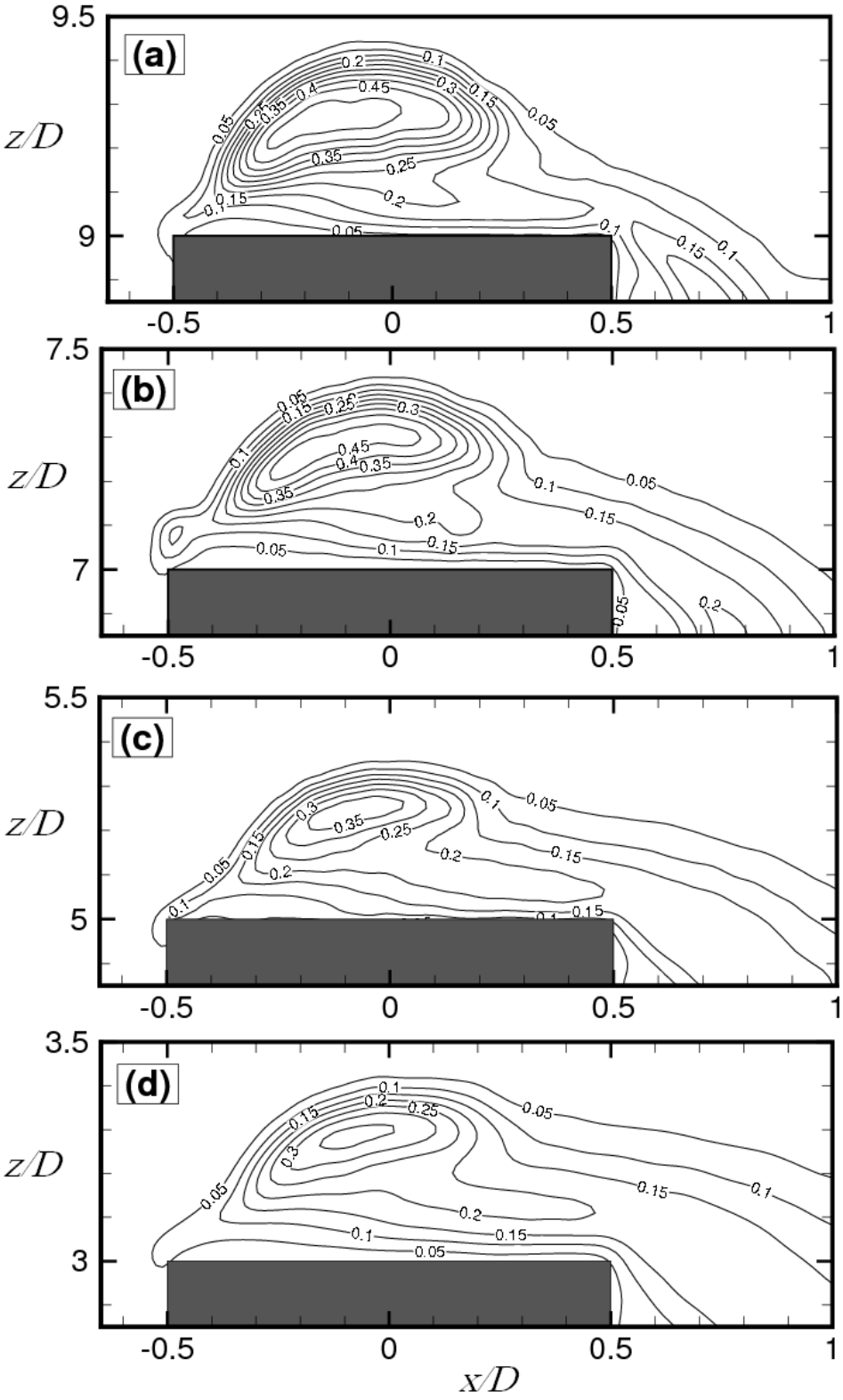

Figure 6.5: Wall-normal turbulence intensity field (contours of w'/U_∞) above the free end surface of finite-height circular cylinders: (a) AR = 9; (b) AR = 7; (c) AR = 5; (d) AR = 3.

The Reynolds shear stress fields above the free end of circular cylinders of AR = 9, 7, 5, and 3 are shown in Figure 6.6. Here, the highest Reynolds shear stresses are found for AR = 9 (Figure 6.6 (a)). According to Figure 6.6, regions with positive Reynolds shear stress are formed at the leading edge of the cylinder and extend towards the location of maximum streamwise turbulence intensity due to the separation of the shear layer. Regions with negative values of Reynolds shear stress also occur above the free end of the circular cylinders extending from the near-wake region up to the location x/D = -0.25 for all aspect ratios. At the trailing edge of the free end, the region of elevated Reynolds shear stress extends farther above the circular cylinder as the aspect ratio is decreased; this may be related to the reattachment flow pattern on the free end described earlier.

6.2.2 Free-end Flow Field Away From the Symmetry Plane

Figures 6.7 and 6.8 show the mean streamlines in vertical (x-z) planes above the free ends for different cross-stream positions (y/D = 0, 0.25, and 0.375); results for AR = 9 are given in Figure 6.7 and results for AR = 3 are given in Figure 6.8.

For the finite circular cylinders of AR = 9 (Figure 6.7) and AR = 3 (Figure 6.8), the mean flow pattern above the free end does not change significantly as the cross-stream position from the centreline (y/D) increases. For all three cross-stream positions, the cross-stream vortex is visible. However, the strength and size of this vortex decreases away from the symmetry plane. This may be attributed to the separation of the approach flow from the

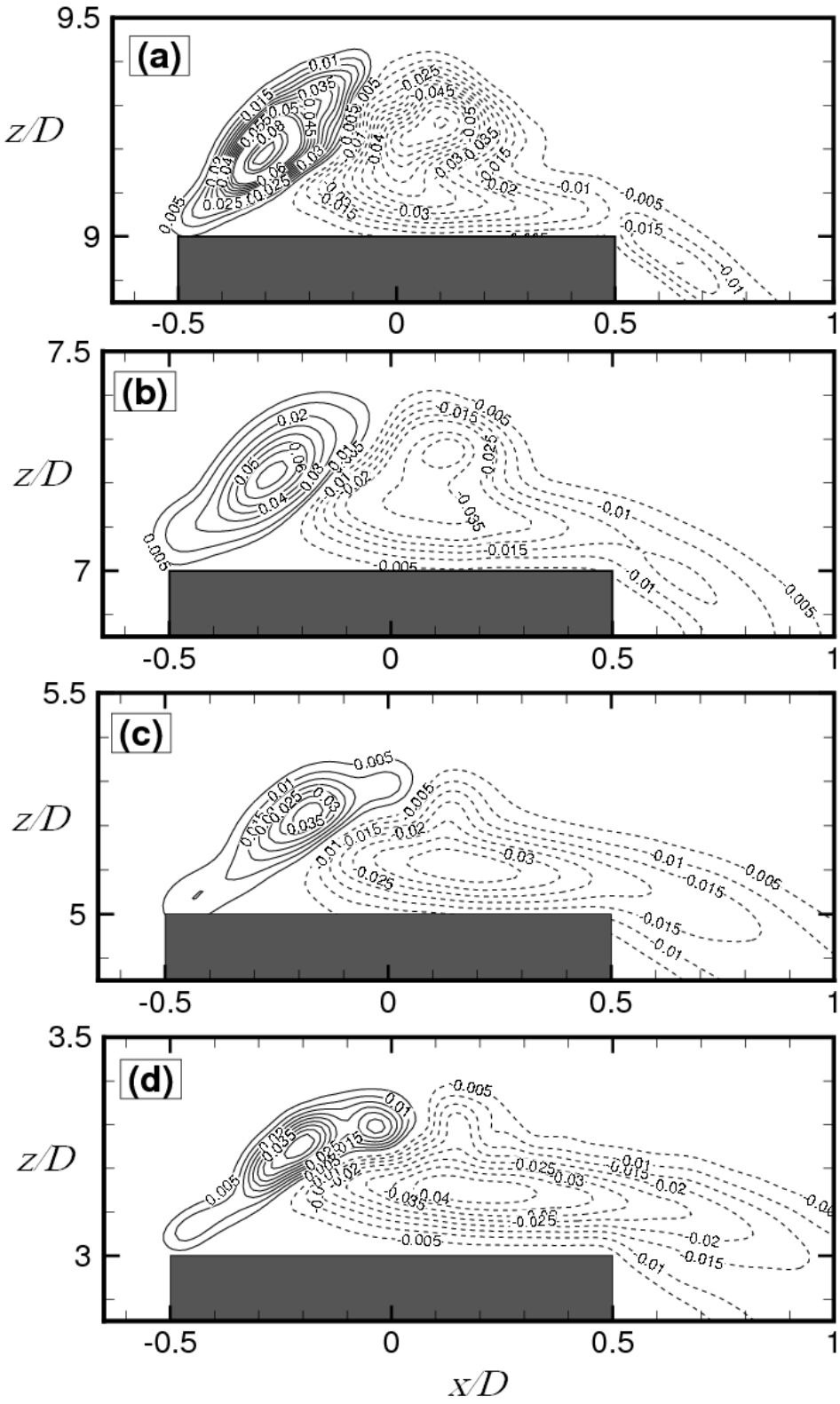

Figure 6.6: Reynolds shear stress field (contours of $-\overline{u'w'}/U_\infty^2$) above the free end surface of finite-height circular cylinders: (a) AR = 9; (b) AR = 7; (c) AR = 5; (d) AR = 3.

circumference of the leading edge of the free end surface suppressing the cross-stream vortex at larger *y/D*. This means that, the curved separation line at the leading edge of the cylinder's free end surface produces both cross-stream ($\overline{\omega}_y$) and streamwise vorticity ($\overline{\omega}_x$) vector components which results a weaker cross-stream vorticity farther from the centerline. A general observation for the finite circular cylinder, by comparing the results in Figures 6.7 and 6.8 for AR = 9 and 3, respectively, is that the aspect ratio is not a strong influencing parameter for the flow pattern above the free end.

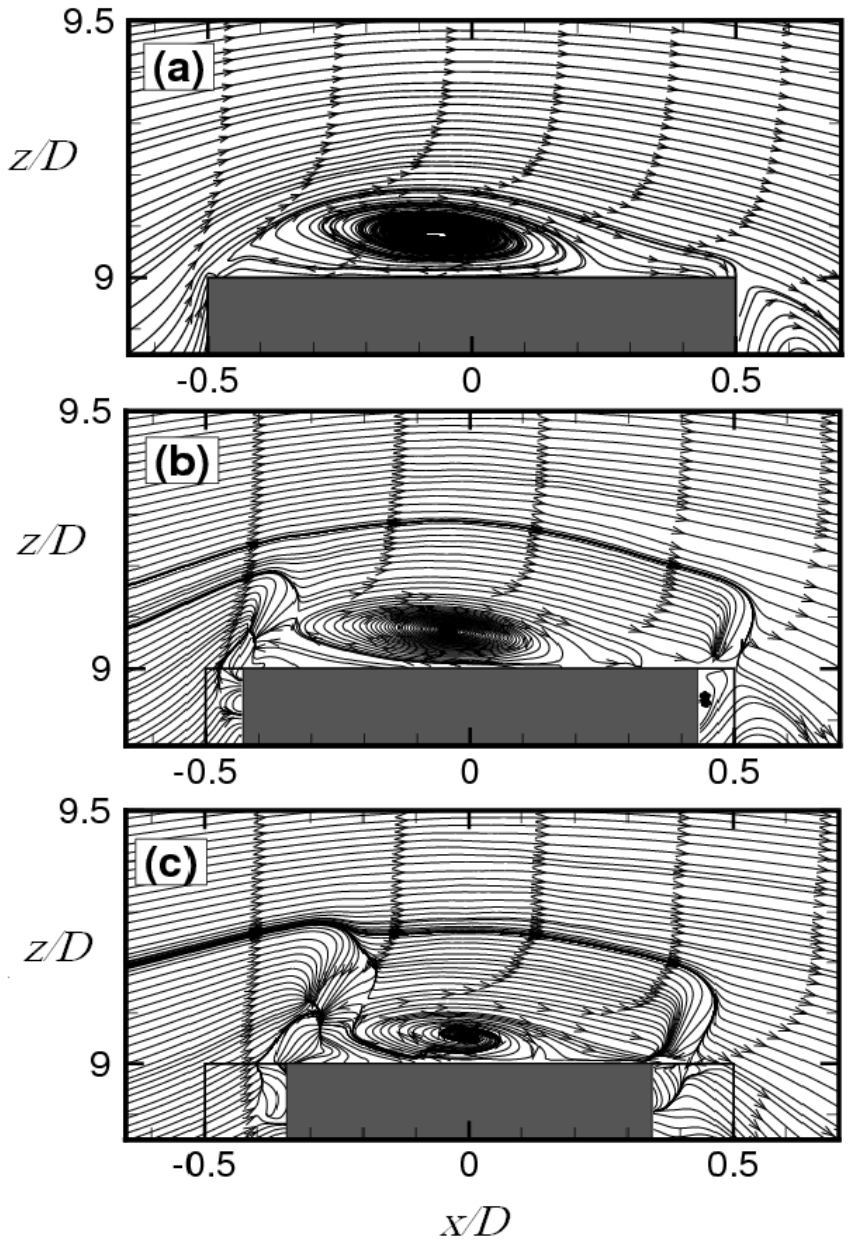

Figure 6.7: Mean streamlines for the flow over the free ends of surface-mounted finite-height circular cylinders of AR = 9; measurements made in vertical planes at: (a) $y/D = 0$; (b) $y/D = 0.25$; (c) $y/D = 0.375$.

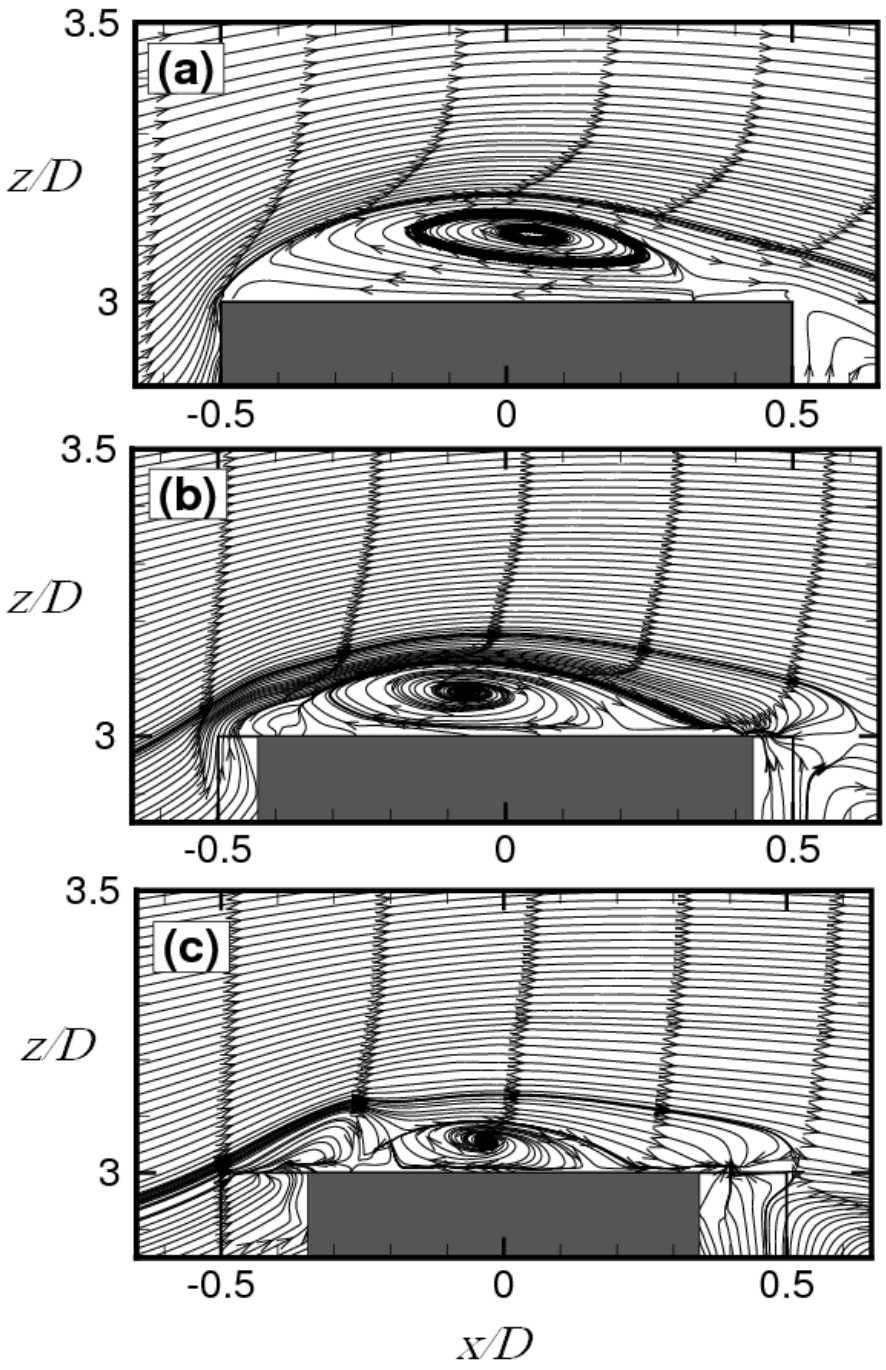

Figure 6.8: Mean streamlines for the flow over the free ends of surface-mounted finite-height circular cylinders of AR = 3; measurements made in vertical planes at: (a) $y/D = 0$; (b) $y/D = 0.25$; (c) $y/D = 0.375$.

6.3 Measurements in *x-y* Planes

6.3.1 Flow Behavior on the Free End Surface

PIV measurements were carried out in horizontal *x-y* planes at three wall-normal distances of *z/D* = 0.016, 0.048, and 0.08 above the free end surfaces of the circular cylinders of AR = 9, 7, 5, and 3.

Figure 6.9 shows the flow pattern very close to the free end surface of finite-height circular cylinders of AR = 9, 7, 5, and 3. One of the main characteristics of the flow over the free end surface are two foci located near the side edges of the free end. This is consistent with the "owl-face" behavior reported by Palau-Salvador et al. (2010). Also, as the cylinder aspect ratio increases, the size and strength of these vortices (denoted by pair of foci) decrease. Furthermore, the center of these vortices moves downstream as the aspect ratio increases. For the cylinder of AR = 9 (Figure 6.9(a)), the centers of the foci are located at (*x/D*, *y/D*) = (0, ± 0.45) at the wall-normal distance of *z/D* = 0.016, while for the shortest cylinder of AR = 3 (Figure 6.9(d)), those centers are located at (*x/D*, *y/D*) = (-0.1, ± 0.4). Considerable difference between the flow behavior above the free end of the cylinder of AR = 9 (Figure 6.9(a)) and the other aspect ratios (Figures 6.9(b, c, d)) is observed. This difference in flow patterns can be related to the effects of the side flow and the ground plane boundary layer on the approach flow separated from the leading edge of the free end surface of the circular cylinders. This is consistent with the results of Kawamura et al. (1984) who showed that in the free end region of the cylinder, the flow inclines toward the free end producing a bended separation line along the sides of the cylinder approaching the free end. Einian (2012) showed the flow pattern along the span of a finite height square prism. According to her results, the ground plane boundary layer thickness has a

considerable effect on the flow pattern along the span and close to the free end surface of the square prism.

According to Figure 6.9, the approach flow separates from the leading edge, forming a recirculation region and then reattaches at approximately x/D = 0.21, 0.25, 0.3 and 0.29 for the cylinder of AR = 9, 7, 5 and 3, respectively. This corresponds to the reattachment of the separated flow discussed in Subsection 6.2.1. A summary of the flow reattachment details from the present study and other works is shown in Table 6.1.

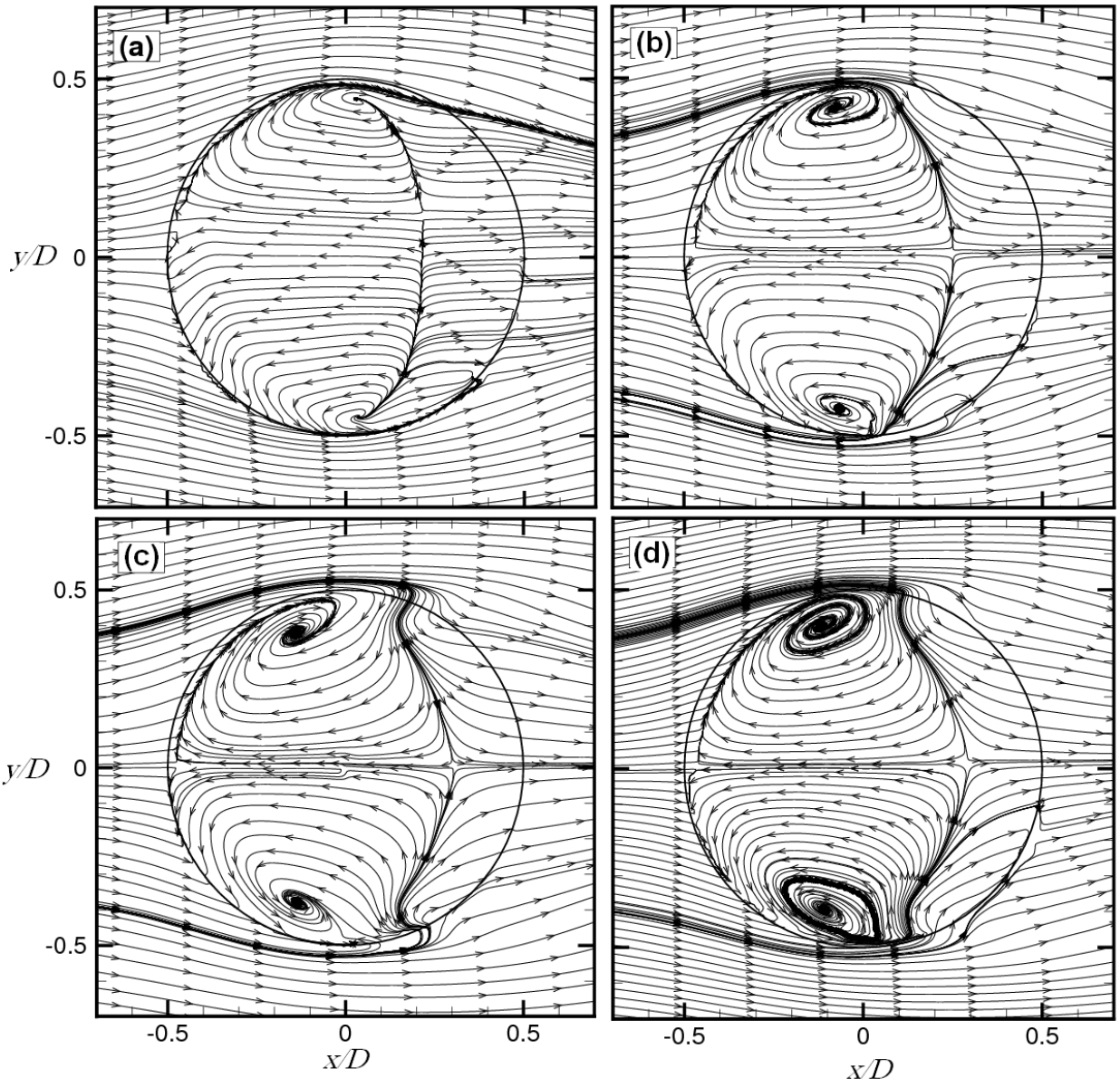

Figure 6.9: Mean velocity fields above the free end surface of a finite circular cylinder of different aspect ratios at the wall-normal location of z/D = 0.016 (at the vicinity of the free end surface): (a) AR = 9, (b) AR = 7, (c) AR = 5. (d) AR = 3.

Table 6.1: Experiments on the flow above the free end of a finite-height circular cylinder and the variation in the reattachment location.

Study	Re_D	δ/H	δ/D	AR	Reattachment (x/D)
Krajnović (2011)	2.0×10^4	0.012	0.7	6	0.32
Park and Lee (2004)	7.5×10^3	-	-	6	0.30
Palau Salvador et al. (2010)	4.3×10^4	0.1	0.25	2.5	0.38
Hain et al. (2008)	1.0×10^5	0.115	0.25	2.167	0.28
Leder (2003)	2.0×10^5	0.004	0.008	2	0.34
Present study	4.2×10^4	0.18	1.62	9	0.21
Present study	4.2×10^4	0.23	1.62	7	0.25
Present study	4.2×10^4	0.32	1.62	5	0.30
Present study	4.2×10^4	0.54	1.62	3	0.29

According to Table 6.1, the location of reattachment can be influenced by different parameters, such as AR and δ/D. Although the available data are limited, the reattachment of the separated flow seems to occur closer to the trailing edge as the cylinder aspect ratio decreases. This tendency is consistent with the result of Kawamura et al. (1984) who observed reattachment for AR = 8, but found no reattachment occurred for a cylinder of AR = 4 and δ/D = 1. From Figures 6.2 and 6.9, reattachment occurs at approximately x/D = 0.21 and x/D = 0.25 (measured from the centre of the cylinder) for AR = 9 and 7, respectively. However, for AR = 5 and 3 (Figures 6.9 (c, d)) in the present study, the outer flow field seems to reattach at locations closer to trailing edge of the cylinders ($x/D \approx 0.3$). These results are further evidence of a distinct wake structure for the least slender cylinder in the present study. According to Table 6.1, the reattachment location (x/D) for the present cylinder of AR = 3 is consistent with those of cylinders with AR below the critical aspect ratio in the studies such as Leder (2003), Palau-Salvador et al. (2010), and Hain et al. (2008). Apart from the influence of aspect ratio, the limited data in Table 6.1 also

suggest there may be an influence of the plane wall boundary layer thickness on the tendency towards reattachment. However, additional data are required in order to draw any firm conclusions. The location of reattachment on the free end also influences the mean angle of the downwash in the symmetry plane. Looking at the streamlines behind the cylinder in Figures 6.2 and 4.2, as the reattachment point moves towards the trailing edge of the free end surface, the downwash angle reduces, the flow over the free end becoming more horizontal.

6.3.2 Flow Behavior above the Free End Surface

The flow behavior above the free end surface of the circular cylinders at three different wall-normal distances (z/D) is presented here to show how the flow field changes as (z) increases. Due to space constraints, only the results for cylinders of AR = 9 (above critical AR) and 3 (below critical AR) are shown and discussed in this section. The present PIV results in the x-y planes are ensemble averages of 526 instantaneous fields.

Figures 6.10 and 6.11 show the mean velocity vector field and the mean streamlines for the flow above the free end of circular cylinders of AR = 9 and 3 at three wall-normal distances. For the cylinder of AR = 9 (left column in Figures 6.10 and 6.11), two weak foci are seen near the side edges of the free end (Figures 6.10(a) and 6.11(a)). As the wall-normal distance increases, at z/D = 0.048, the foci move away from the outer edges of the free end (Figures 6.10(b) and 6.11(b)). At farther distance from the free end (z/D = 0.08, Figures 6.10(c) and 6.11(c)), there is no evidence of the focal points, while a node can be observed at this location (Figure 6.11(c)).

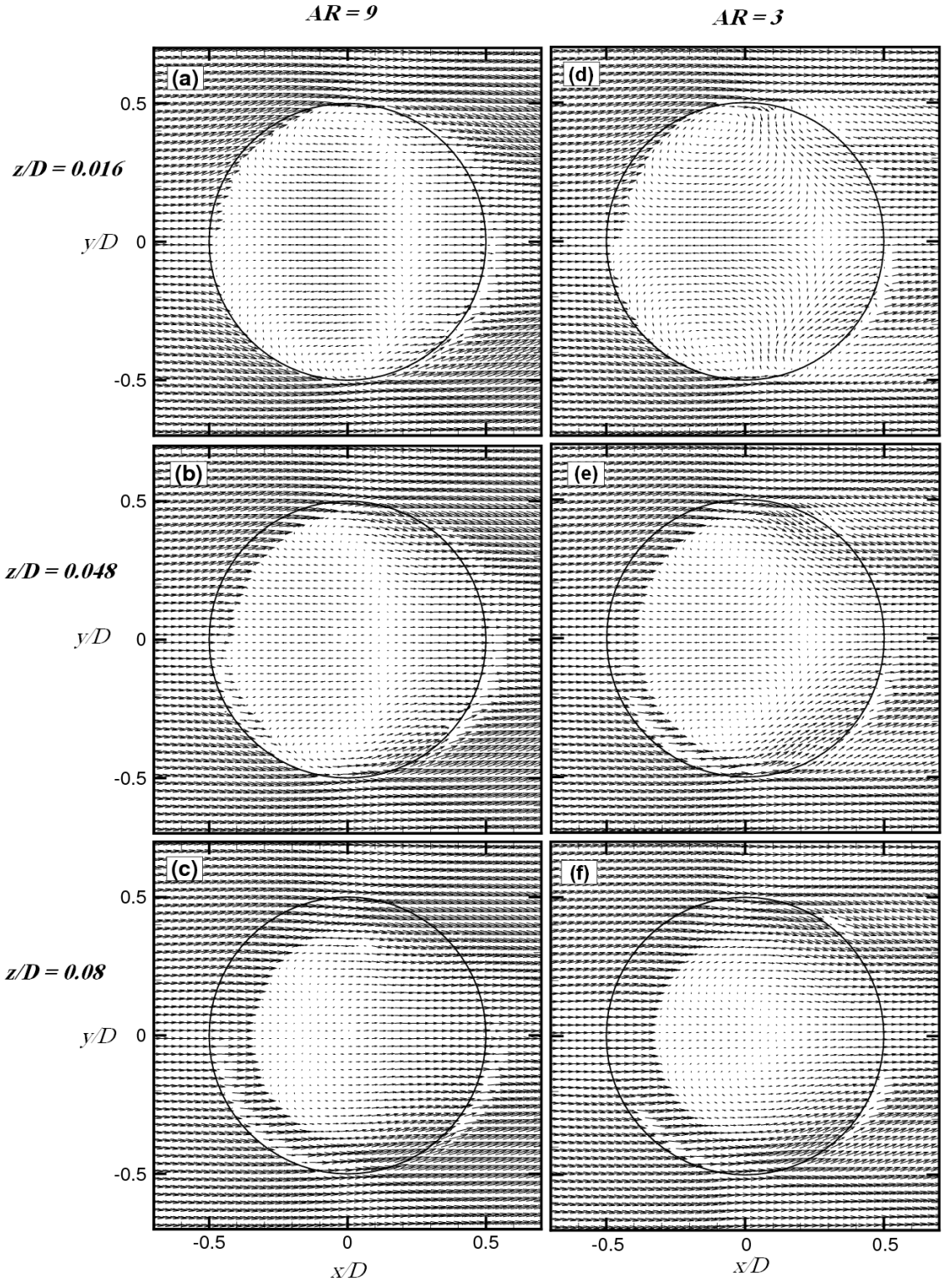

Figure 6.10: Mean velocity vector field for the flow over the free ends of surface-mounted finite-height circular cylinders of AR = 9 and 3; half of all vectors shown.

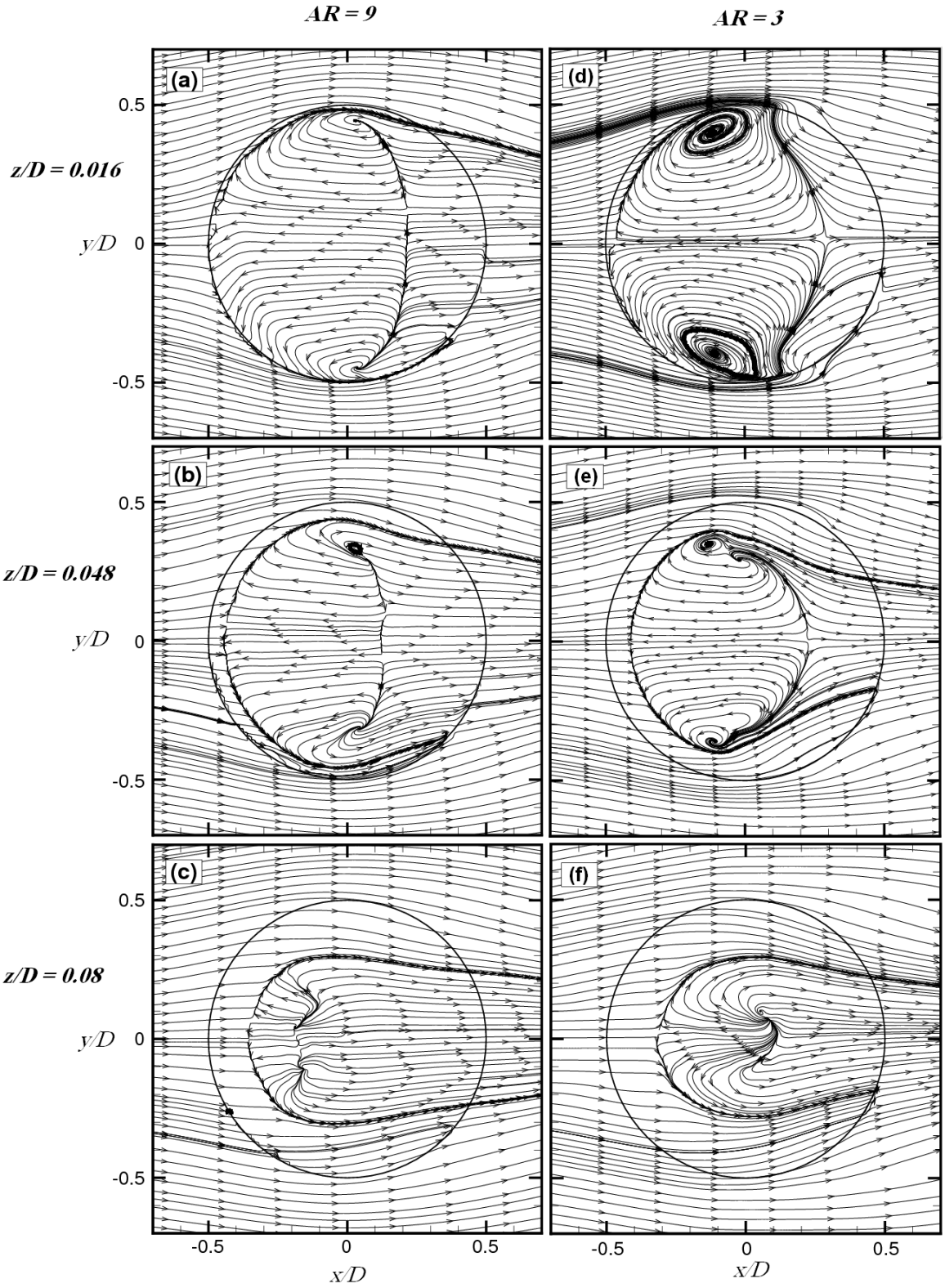

Figure 6.11: Mean streamlines for the flow over the free ends of surface-mounted finite-height circular cylinders of AR = 9 and 3; measurements made in horizontal planes.

According to Figures 6.10(d) and 6.11(d), a strong pair of wall-normal vortices with opposite directions of rotation is seen very close to the free end surface (z/D = 0.016). These vortices are centered at (x/D, y/D) = (-0.1, ±0.4). The centers of these vortices slightly move towards the cylinder center at z/D = 0.048 (Figure 6.11 (e)), while at z/D = 0.08, there is no evidence of a wall-normal vortex (Figure 6.11(f)). At this location and about the free end center, a node is observed which may correspond to the center of the cross-steam vortex seen in Figure 6.8(a).

To show the magnitude of the mean velocity fields for the flow above the free end surface of the cylinders of AR = 9 and 3, contours of the streamwise and cross-stream components of the mean velocity at three wall-normal locations are shown in Figures 6.12 and 6.13, respectively. According to Figure 6.12, for both aspect ratios, the magnitude of the reverse flow over the free end surfaces decreases as the wall-normal distance from the free end increases. The reverse flow with a minimum value of $\overline{U}/U_\infty$= - 0.5 is seen about the cylinder center at z/D = 0.016 for the cylinder of AR = 9 (Figure 6.12(a)), while the reverse flow has a maximum level of $\overline{U}/U_\infty$= - 0.4 for the cylinder of AR = 3 very close to the free end surface and around the cylinder center. According to Figures 6.12(b, c) for AR = 9, the location of the maximum streamwise velocity component moves toward the leading edge of the free end surface as z/D increases, while for the cylinder of AR = 3, the maximum streamwise velocity occurs around the center (Figures 6.12(d, e, f)). Figure 6.12 also shows that for AR = 9 the minimum value of $\overline{U}/U_\infty$ decreases to be approximately -0.3 and -0.1 at the locations of z/D = 0.048 and z/D = 0.08 (Figures 6.12(b, c)), respectively, compared to the value of -0.5 at z/D = 0.016 (Figure 6.12(a)).

For the cylinder of AR = 3 (Figures 6.12(d, e, f)), the maximum level of the magnitude of $\overline{U}/U_{\infty}$ reduces to -0.25 at *z/D* = 0.048, while there is a minimal reverse flow at the location of *z/D* = 0.08 (Figure 6.12(f)).

Figure 6.13 shows the cross-stream component of the mean velocity at three wall-normal locations above the free end surface of a cylinder of AR = 9 and 3. In this figure, regions of positive and negative cross-stream velocity around the leading edge of the free end show that the approaching flow is directed towards the sides of the cylinder, while the regions of positive and negative cross-stream velocity around the trailing edge of the free end indicates the movement of the flow from the sides of the cylinder towards the centerline of the flow. According to Figure 6.13, the magnitude of the cross-stream velocity slightly decreases as the wall-normal distance from the free end surface (*z/D*) increases.

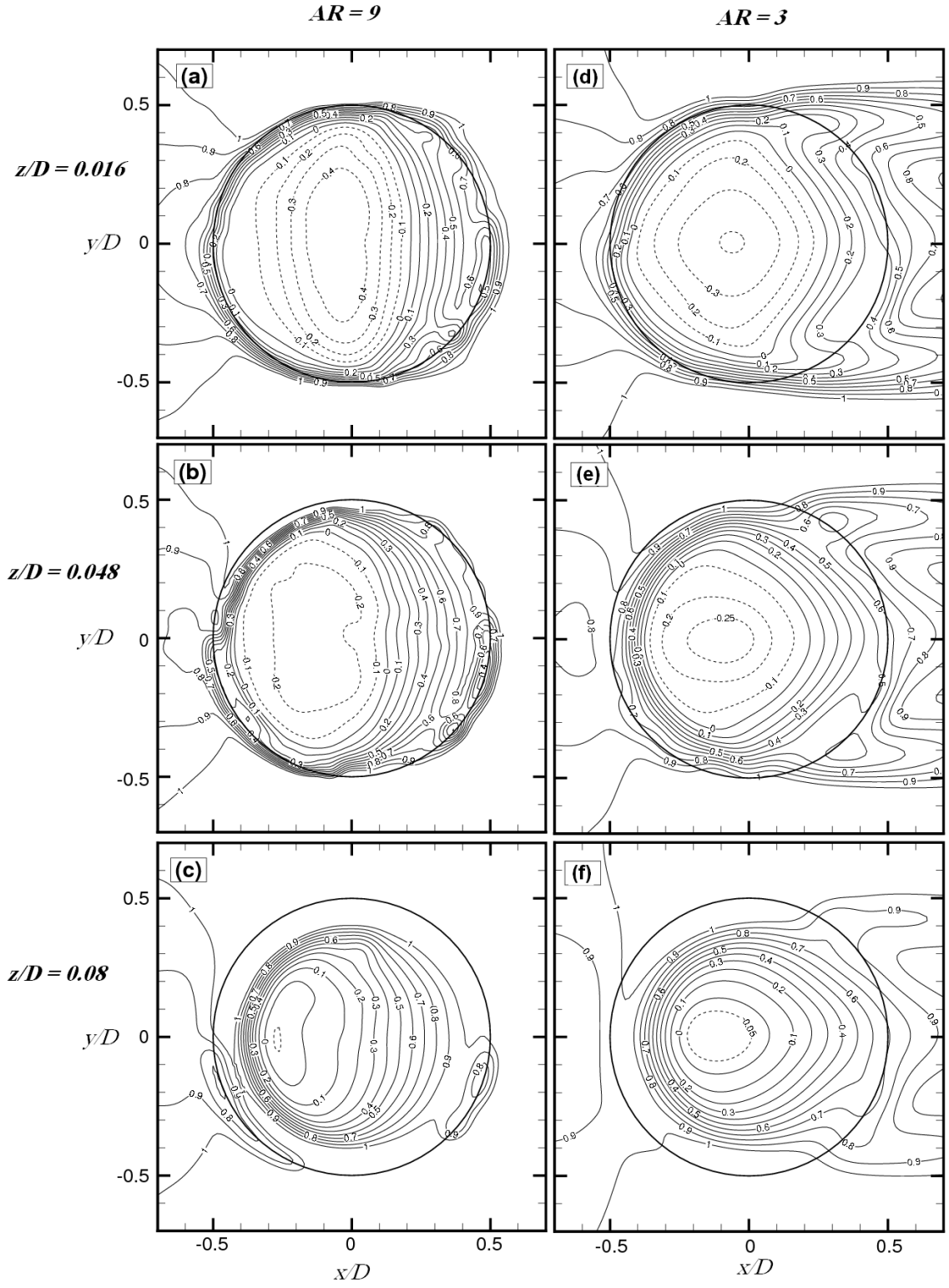

Figure 6.12: Streamwise mean velocity field (contours of $\overline{U}/U_\infty$) for the flow over the free ends of surface-mounted finite-height circular cylinders of AR = 9 and 3.

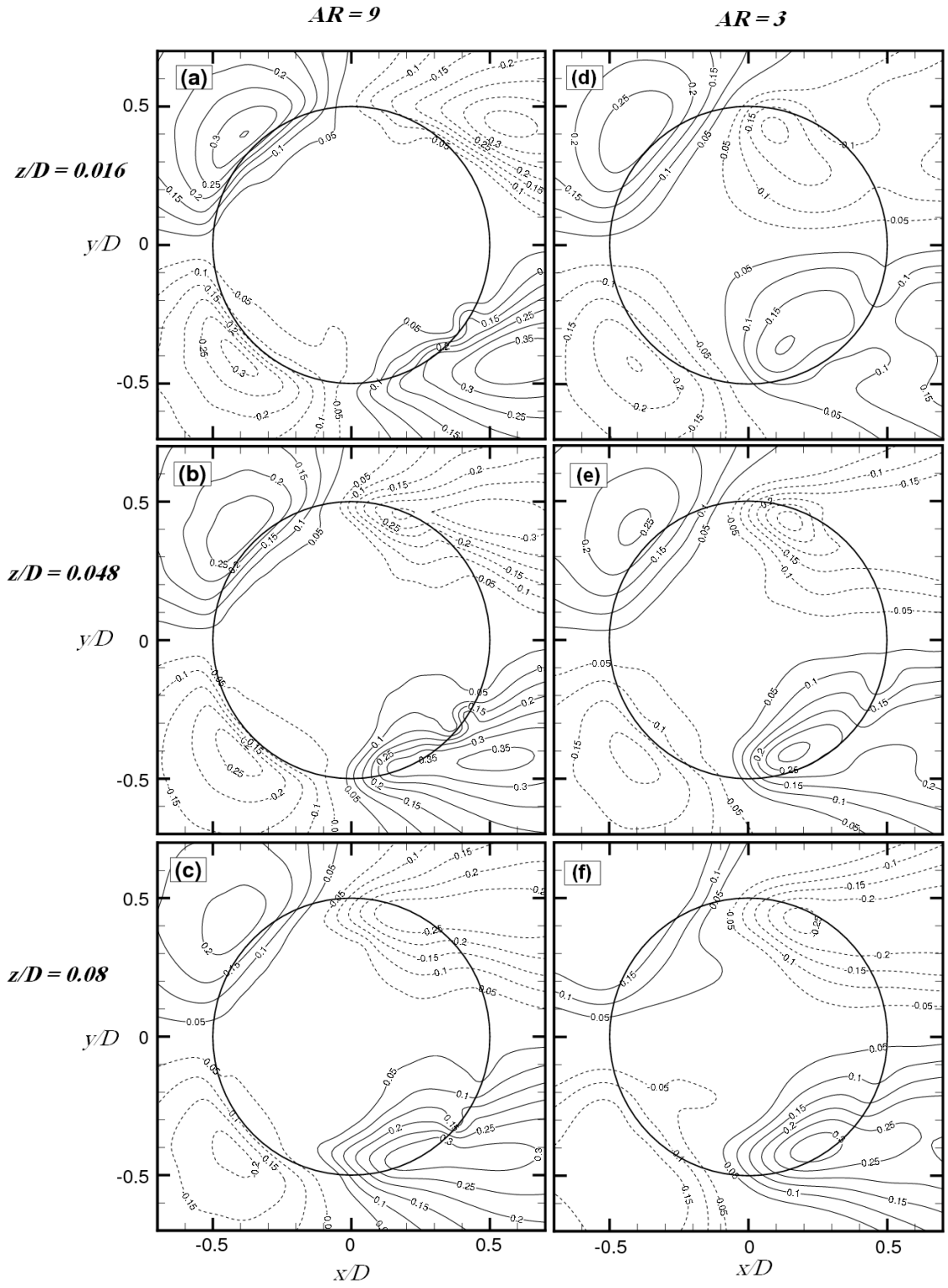

Figure 6.13: Cross-stream mean velocity field (contours of $\overline{V}/U_\infty$) for the flow over the free ends of surface-mounted finite-height circular cylinders of AR = 9 and 3.

Figures 6.14 and 6.15 show, respectively, the streamwise and cross-stream turbulence intensities for the flow above the free end of a circular cylinder of AR = 9 and 3 at three wall-normal distances of z/D = 0.016, 0.048, and 0.08. Note that, the contours shown in these figures are not perfectly symmetric to the cylinder centerline. This may be because of insufficient ensemble size.

According to Figure 6.14(a), the streamwise turbulence intensity has a maximum value of approximately u'/U_∞ = 0.3 occurring close to the outer edge of the free end at the location of x/D = 0.3, while for the cylinder of AR = 3 (Figure 6.14(d)), the maximum u'/U_∞ occurs at $x/D \approx 0.1$. The region of maximum streamwise turbulence intensity moves upstream and towards the cylinder centerline as the wall-normal distance from the free end surface increases (Figures 6.14(c, f)). However, for both aspect ratios, the magnitude of the maximum value of u'/U_∞ does not change significantly as z/D increases.

According to Figure 6.15, a region of maximum cross-stream turbulence intensity with a value of approximately v'/U_∞ = 0.2 is seen over the free end surface of the cylinder of AR = 9 and 3 at all three wall-normal locations of z/D = 0.016, 0.048, and 0.08. For both aspect ratios, the region of maximum cross-stream turbulence intensity (v'/U_∞ = 0.2) slightly moves upstream as the wall-normal distance from the free end surface increases. Similar to the streamwise turbulence intensity, the magnitude of the maximum value of v'/U_∞ does not change dramatically as z/D increases.

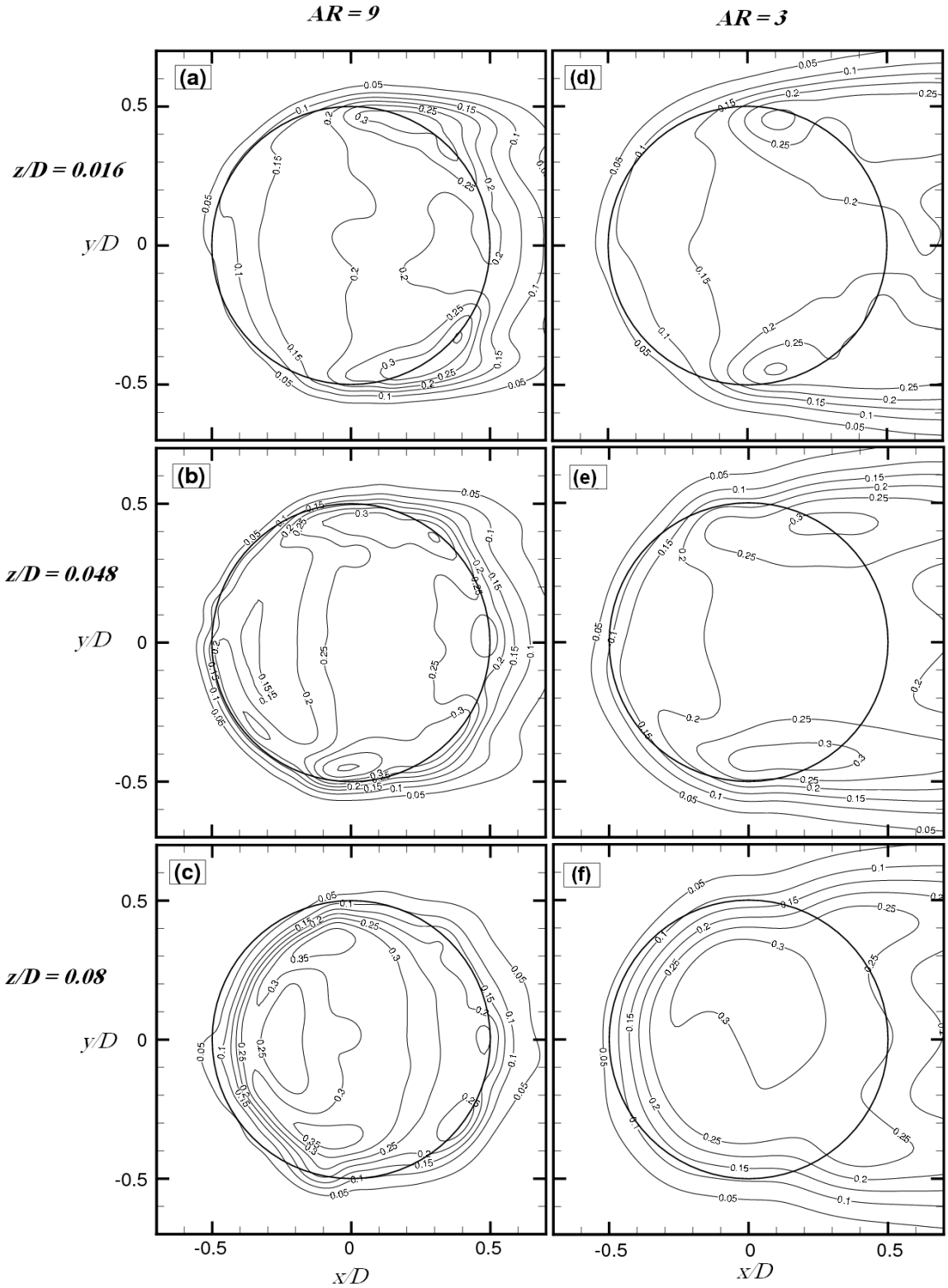

Figure 6.14: Streamwise turbulence intensity (contours of u'/U_∞) for the flow over the free ends of surface-mounted finite-height circular cylinders of AR = 9 and 3.

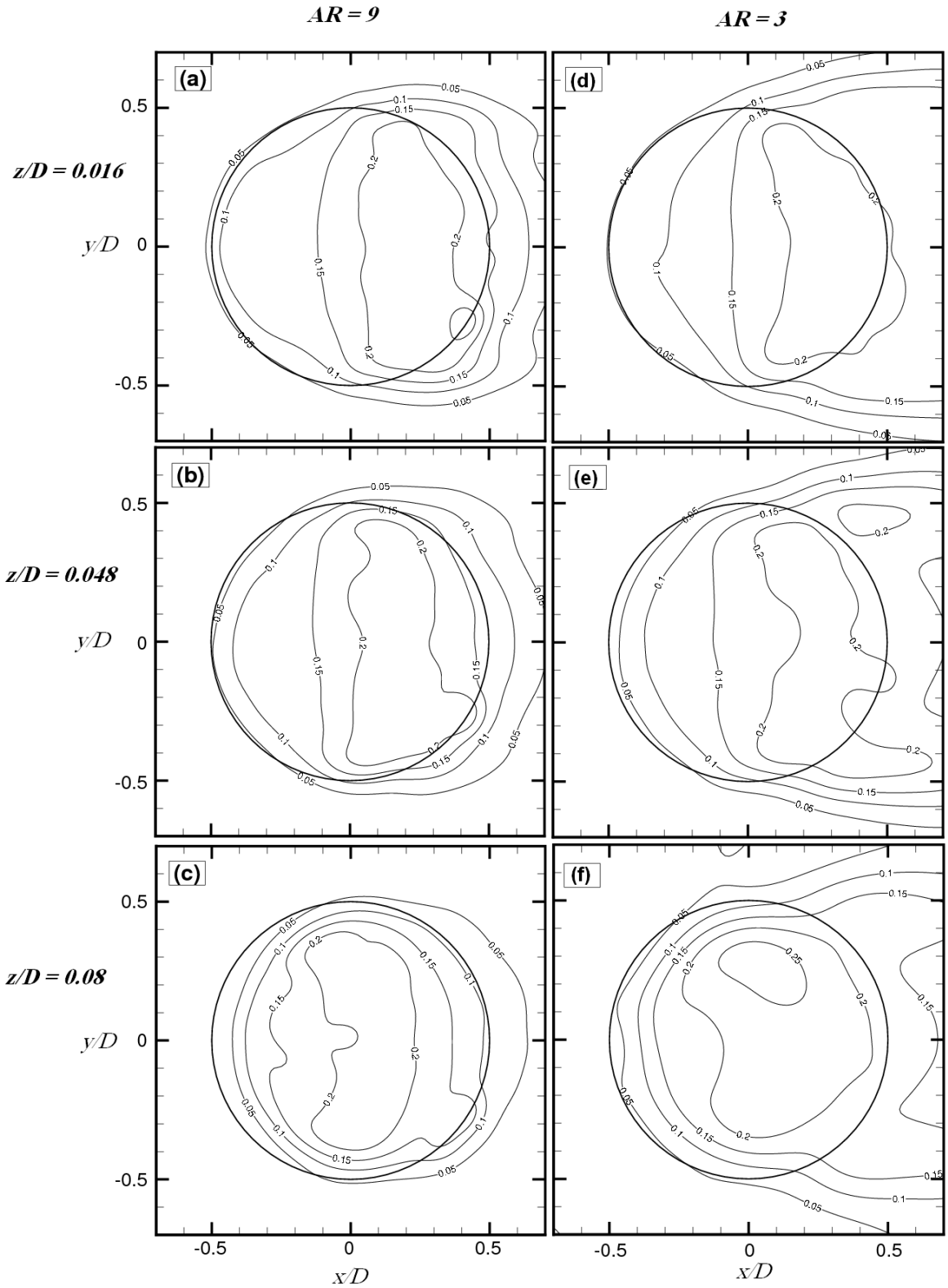

Figure 6.15: Cross-stream turbulence intensity (contours of v'/U_∞) for the flow over the free ends of surface-mounted finite-height circular cylinders of AR = 9 and 3.

Contours of the Reynolds shear stress in horizontal planes above the free end surfaces of surface-mounted finite-height circular cylinders of AR = 9 and 3 are shown in Figure 6.16. According to this figure, the flow above the free end surface of the circular cylinders is characterized by regions of elevated Reynolds shear stress. For the case of AR = 9, regions of positive and negative shear stress are seen around the leading edge of the free end at wall-normal distances of z/D = 0.016 and 0.048 (Figures 6.16(a, b)) due to the separation of the upcoming flow from the leading edge. However, at z/D = 0.08 (Figure 6.16(c)), there is no evidence of the Reynolds shear stress at the leading edge. However, the uncertainty of the PIV results is large in the regions close to the cylinder free end due to the issue of the light sheet reflections from the surfaces. Regions of positive and negative shear stress are also evident at the trailing edge of the cylinder of AR = 9 (Figures 6.16(a, b, c)). These contours are centered on the trailing edge of the free end surface moving upstream and towards the cylinder center as the wall-normal distance increases. Also, according to this figure, the magnitude of the Reynolds shear stress decreases as the wall-normal distance (z/D) increases. According to Figure 6.16, a considerable difference is seen between the Reynolds shear stresses of the cylinders of AR = 9 and 3 in terms of the location of the maximum Reynolds shear stress at the same wall-normal distance. For the cylinder of AR = 3 (Figures 6.16(d, e, f)), the contours of Reynolds shear stress are centered near the trailing edge of the free end surface, while the centers move upstream for the cylinder of AR = 9 (Figures 6.16(a, b, c).

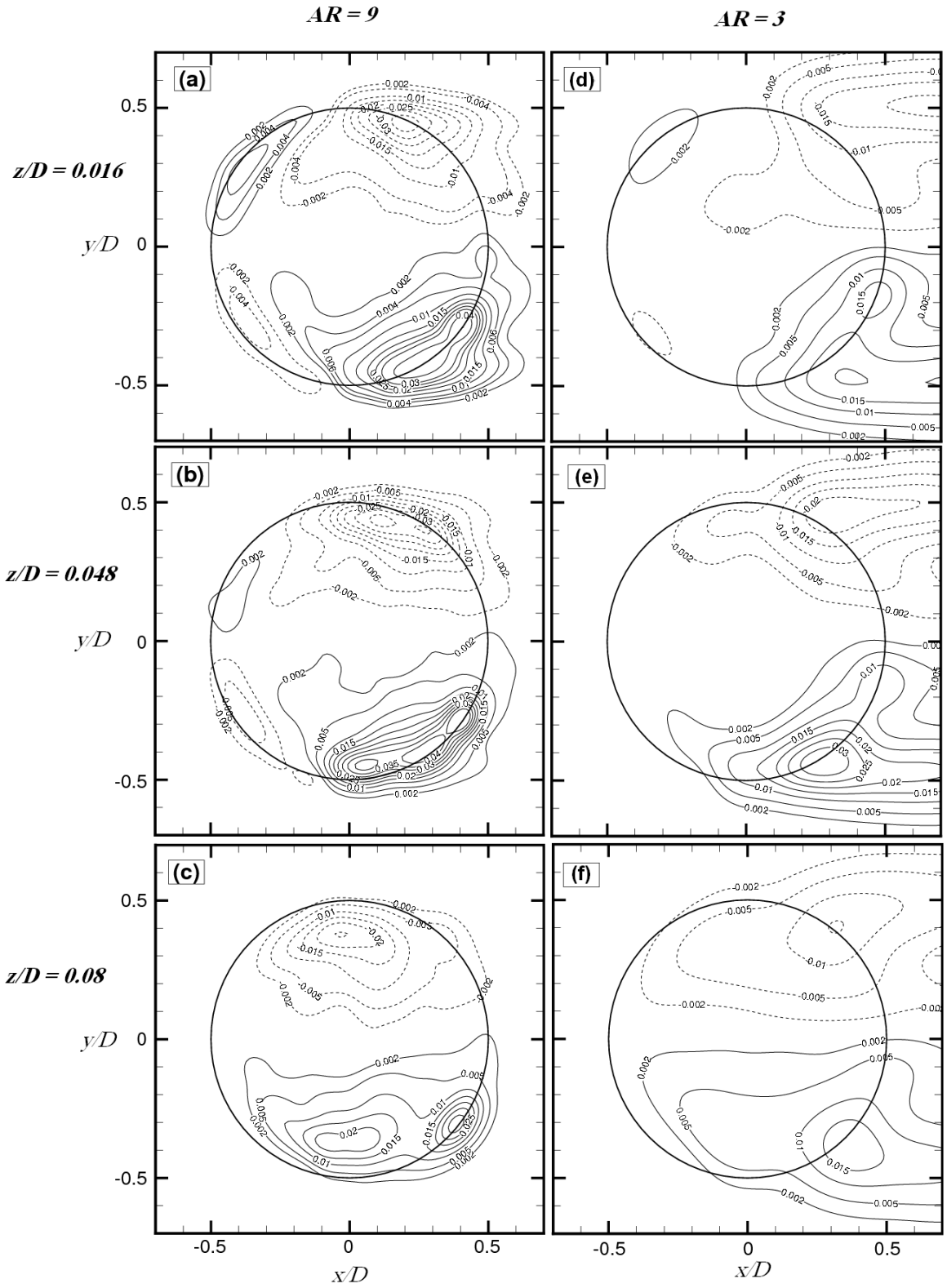

Figure 6.16: Reynolds shear stress field (contours of $-\overline{u'v'}/U_\infty^2$) for the flow over the free ends of surface-mounted finite-height circular cylinders of AR = 9 and 3.

The mean wall-normal vorticity ($\overline{\omega_z} D/U_\infty$) fields above the free end surface of finite circular cylinders of AR = 9 and 3 are shown in Figure 6.17. According to this figure, negative (CW) and positive (CCW) vorticities are generated at the side edges of the free end extending to the leading and trailing edges of the free end surface. Furthermore, Figure 6.17 shows that as the wall-normal distance increases, the strength of the vorticity decreases. The centers of these vorticities move upstream and towards the cylinder center as *z/D* increases, indicating the presence of a wall-normal vortex tube originating from the side edges and bending towards the cylinder center. For the cylinder of AR = 3 (Figures 6.17(d, e, f)), the vorticity contours stretch downstream of the cylinder indicating a different vorticity field for this aspect ratio compared to the more slender cylinder of AR = 9 (Figures 6.17(a, b, c)).

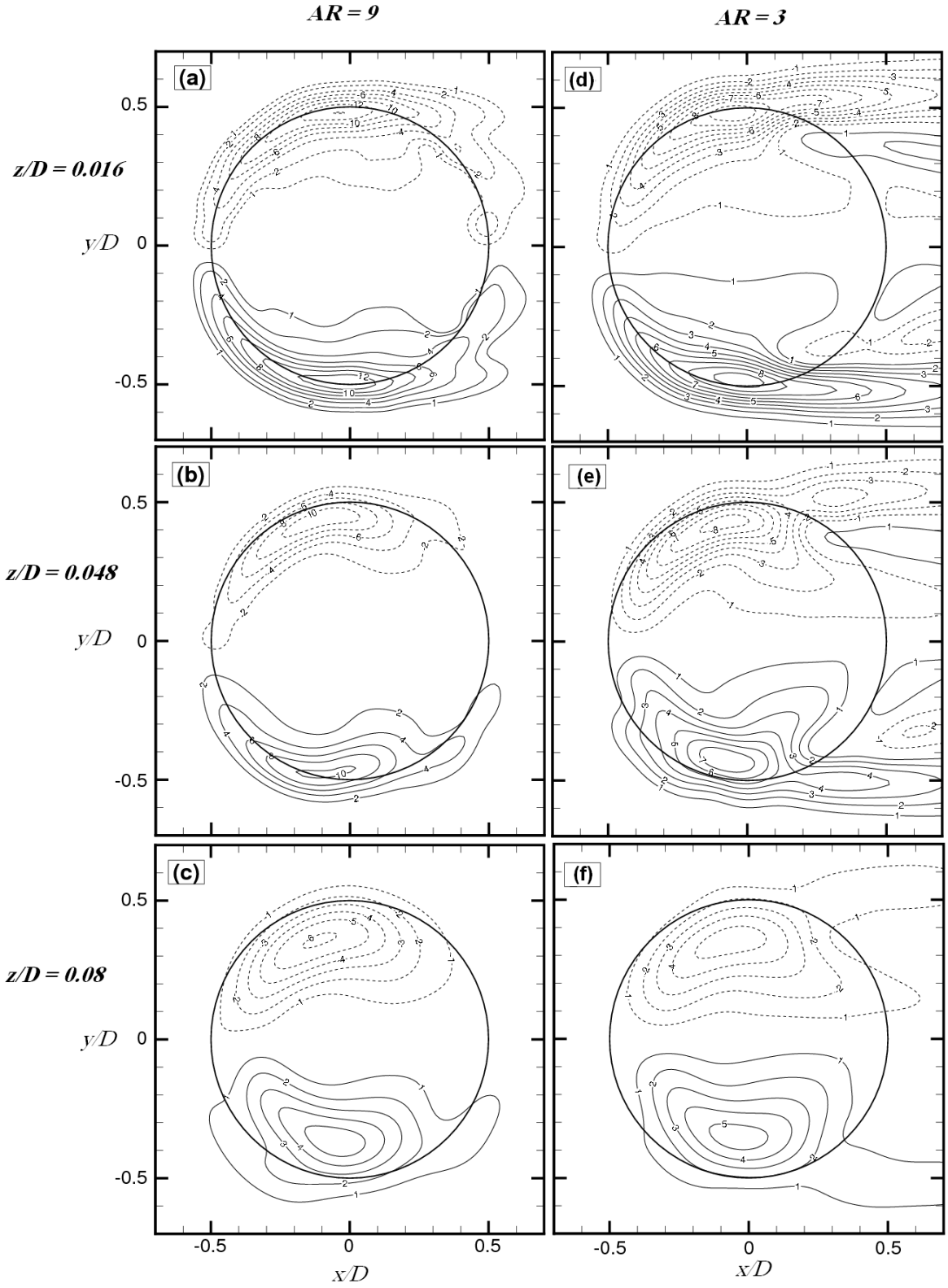

Figure 6.17: Mean in-plane vorticity field (contours of $\overline{\omega_z}D/U_\infty$) for the flow over the free ends of surface-mounted finite-height circular cylinders of AR = 9 and 3.

7. Flow Above the Free End of the Square Prism

7.1 Introduction

Although there are a few studies of the flow above the free ends of finite circular cylinders (Chapter 6), there are virtually no studies in the literature on the flow above the free end of square prisms of different aspect ratios. However, there are a few studies on the flow above the free end surface of cubes (e.g., Martinuzzi and Tropea (1993) and Depardon et al. (2005, 2007)). So, due to the lack of experimental data and numerical simulations on the flow above the free end, further study of this local flow field is of interest in order to obtain a complete understanding of the flow behavior around and above the free end surface of the square prisms.

In this chapter, the mean flow fields above the free end surfaces of surface-mounted, finite-height square prisms in three orthogonal planes were investigated experimentally using PIV. The aim of the present study was to obtain an improved physical description of the flow field above the free end surface of the prisms, as it is directly related to the near-wake flow field of the square prisms. Here, of particular interest were the effects of the aspect ratio of the square prism (AR) on the flow structure above the free end as seen in different measurement planes (for different *x/D*, *y/D*, *z/D* locations). Overall, this chapter presents a unique investigation on the flow above the free end surface of finite square prisms of aspect ratios of AR = 9, 7, 5, and 3.

7.2 Measurements in *x-z* Planes

7.2.1 Free-end Flow Field in the Symmetry Plane (*y/D* = 0)

Figure 7.1 illustrates the flow behavior over the free ends of square prisms of AR = 9, 7, 5, and 3. According to this figure, there is a close relation between the flow separating from the leading edge of the free end surface and the reverse flow caused by the vortices near the trailing edge of the free end. This flow feature is much different than the case of the finite circular cylinder shown in Chapter 6, and studied by Leder (2003), Park and Lee (2004), Hain et al. (2008), Palau-Salvador et al. (2010), Krajnović (2011), and Rostamy et al. (2012). Unlike the case of the finite circular cylinder, the flow separating from the leading edge of the square prism does not reattach onto the upper surface but extends into the near-wake region. In Figure 7.1, an additional small region of locally separated flow can be seen on the upper surface just upstream of the trailing edge. This separated flow is clearer in Figure 7.1(d) for the prism of AR = 3. Similar to the case of the finite circular cylinder, a cross-stream vortex forms above the free end of the square prism, due to interaction between the separated flow from the leading edge of the prism and reverse flow over the trailing edge. According to Figure 7.1, the center of this vortex moves downstream and upwards as the aspect ratio is lowered. Just behind this vortex, a saddle point is observed. As the aspect ratio decreases, the locations of the vortex centre and saddle point are displaced farther away from the free end surface, moving from approximately $z/D = 0.15$ above the surface for AR = 9 (Figure 7.1(a)) to $z/D = 0.25$ for AR = 3 (Figure 7.1(d)). The close relation between the near wake of the square prism and the flow above the free end is obvious from the present experimental results warranting more study on the flow above the free ends of finite-height square prisms.

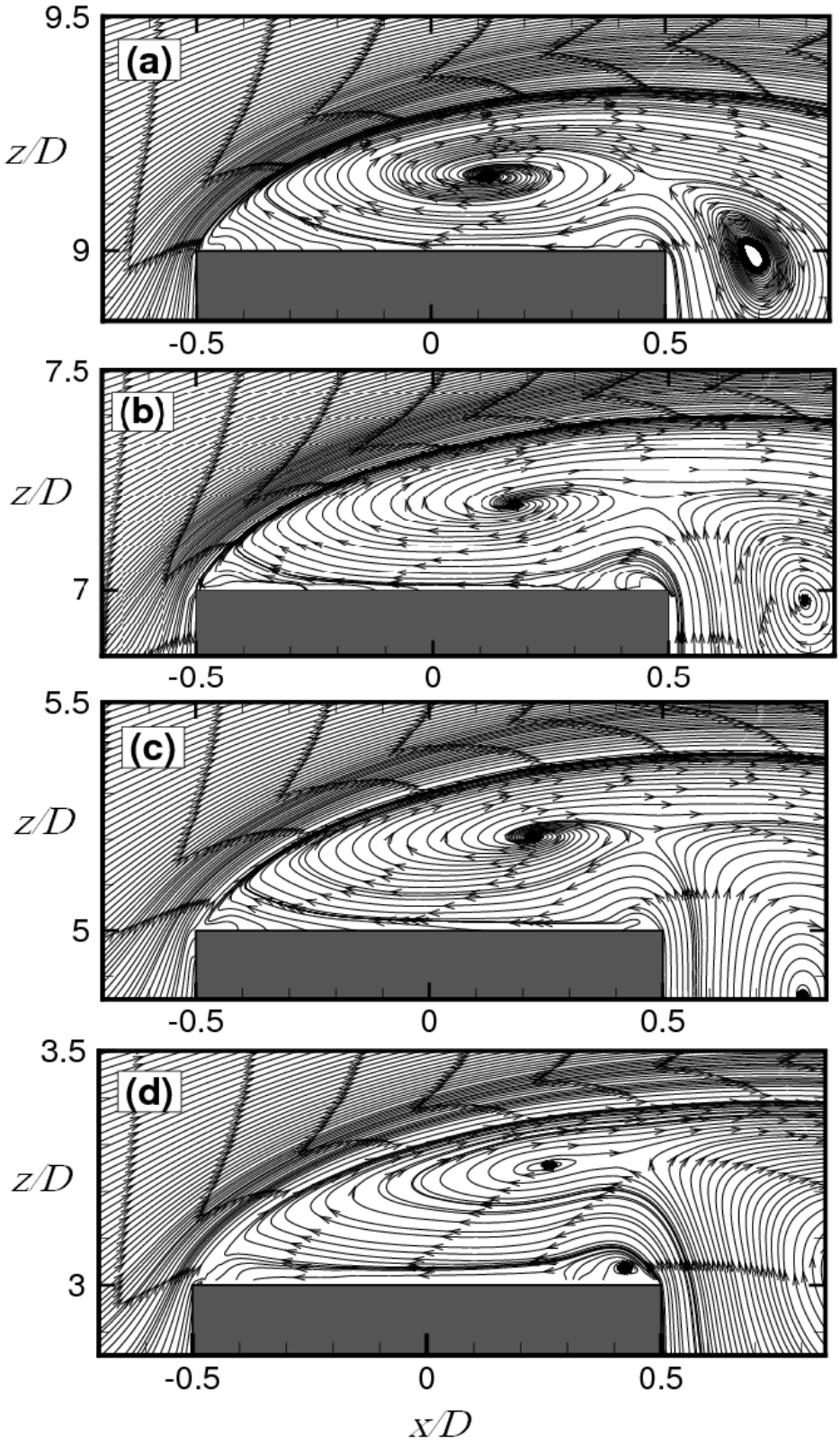

Figure 7.1: Mean streamlines in the symmetry plane (y/D = 0) above the free end surface of finite-height square prisms: (a) AR = 9; (b) AR = 7; (c) AR = 5; (d) AR = 3.

To show the magnitude of the velocity above the free end surface of the prisms, contours of the mean streamwise velocity components are shown in Figure 7.2. According to this figure, the reverse flow with the minimum magnitude of approximately of $\overline{U}/U_\infty$= - 0.1 is seen above the free end surface of the prism of AR = 9, 7, and 5 (Figures 7.2(a, b, c)), while for AR = 3 (Figure 7.2(d)) the reverse flow reaches the value of -0.2 indicating a stronger reverse flow for this AR. Also, the positive streamwise velocity just above the trailing edge for prisms of AR = 3 and 5 (Figures 7.2(c, d)) verifies the presence of a small cross-stream vortex in this region, while there is no evidence of this vortex for the more slender prisms of AR = 9 and 7.

Contour plots of the streamwise turbulence intensity (u'/U_∞) above the free ends of the finite square prisms of AR = 9, 7, 5, and 3 are shown in Figure 7.3. This figure illustrates regions of elevated streamwise turbulence intensity above the free end surfaces that extend significantly downstream of the prisms. According to Figure 7.3, for all aspect ratios, the streamwise turbulence intensity level increases from its minimum value close to the free end surface to its highest level occurring along the shear-layer boundary between the outer flow and the mean recirculation zone. Based on the present experimental data, the maximum level of turbulence intensity of 0.43 occurs for the prism of AR = 9 (Figure 7.3(a)), while it has a lower value of 0.4 for prisms of AR = 7, 5, and 3 (Figures 7.3(b, c, d)). For the circular cylinder case (discussed in Chapter 6), the maximum or peak levels of u'/U_∞ above the free end are almost twice those for square prisms. However, it should be noted that the effect of the light sheet reflections from the free end surface of the circular cylinders in the PIV measurements is larger compared to the square prism cases. According to Figure 7.3, the region of highest level of u' is approximately located 0.2D to 0.3D above the free end surface of the square prisms and in the streamwise distance range of x/D = -0.3 to -0.2.

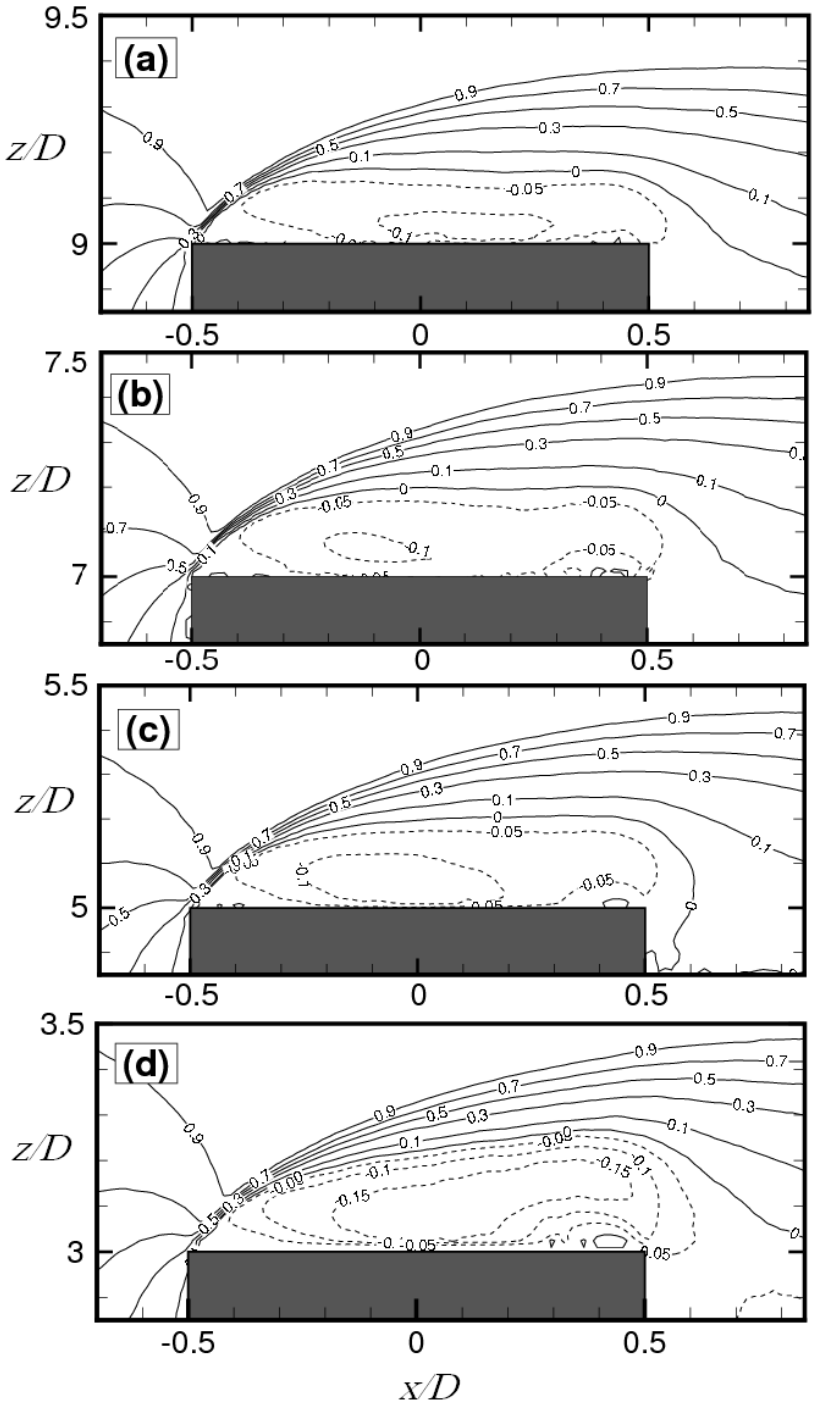

Figure 7.2: Mean streamwise velocity field (contours of $\overline{U}/U_\infty$) in the symmetry plane (y/D = 0) above the free end of square prisms: (a) AR = 9; (b) AR = 7; (c) AR = 5; (d) AR = 3.

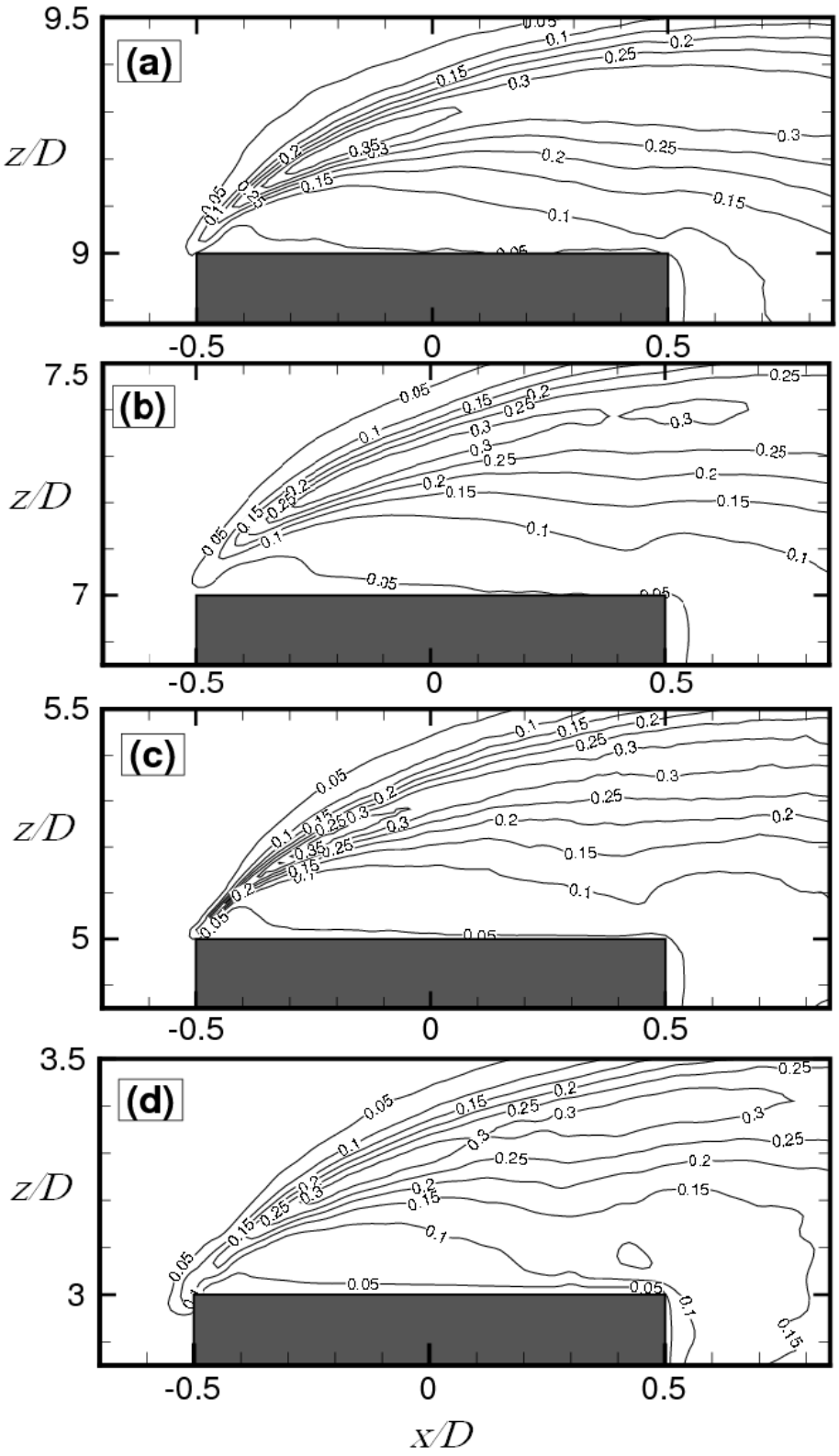

Figure 7.3: Streamwise turbulence intensity field (contours of u'/U_∞) in the symmetry plane (y/D = 0) above the free end of square prisms: (a) AR = 9; (b) AR = 7; (c) AR = 5; (d) AR = 3.

Figure 7.4 shows contours of the in-plane Reynolds shear stress field above the free end surfaces of the finite square prisms. According to this figure, the flow above the free end of the finite square prism is characterized by two regions of elevated Reynolds shear stress: a region of negative shear stress above the free end that extends into the upper part of the near-wake region, and a region of positive shear stress originating from the leading edge and following the separated shear layer bounding the mean recirculation zone.

According to Figure 7.4, the Reynolds shear stress behavior does not change significantly as the aspect ratio of the prism changes. However, as the prism aspect ratio increases, the region of negative Reynolds shear stress becomes wider so that for the prism of AR = 9 (Figure 7.4(a)), the contour of negative Reynolds shear stress extends down to the trailing edge of the free end surface. The present results also show that for all aspect ratios, the level of normalized Reynolds shears stress ($-\overline{u'w'}/U_\infty^2$) varies over the range of -0.035 to 0.12 above the free end of square prism.

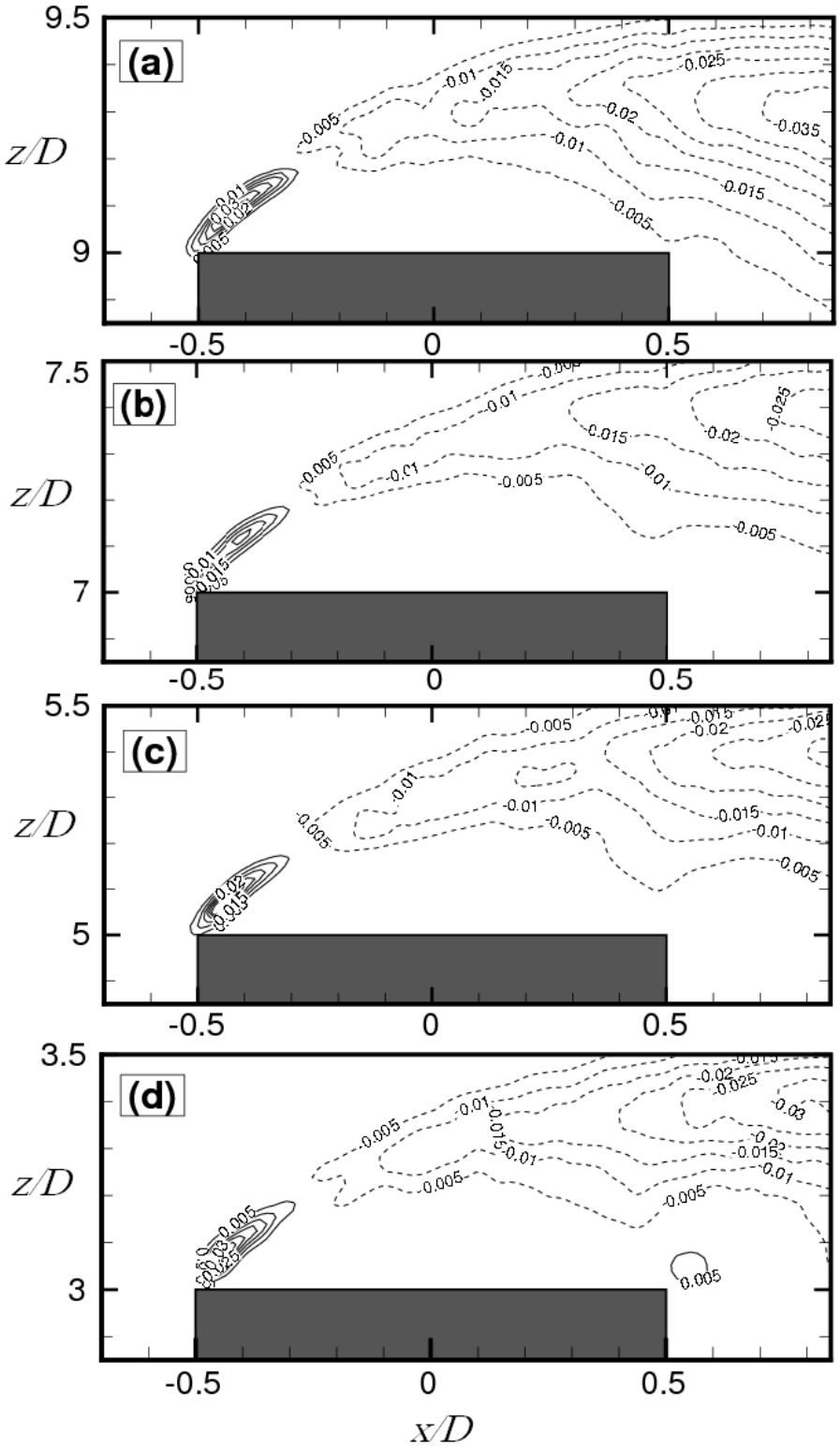

Figure 7.4: Reynolds shear stress field (contours of $-\overline{u'w'}/U_\infty^2$) in a vertical plane on the wake centerline ($y/D = 0$) above the free end of the finite square prism: (a) AR = 9; (b) AR = 7; (c) AR = 5; (d) AR = 3.

7.2.2 Free-end Flow Field Away From the Symmetry Plane

Measurements were carried out in three vertical *x*-*z* planes at cross-stream locations of *y/D* = 0, 0.25, and 0.375. The results in the symmetry plane (*y/D* = 0) for the four prisms of AR = 9, 7, 5, and 3 were discussed in Subsection 7.2.1 to show the flow behavior above the free end surface of the prisms and more specifically to show the effect of the aspect ratio of the prism on the flow structure. In this subsection, the flow behavior in the *x*-*z* planes and at three different cross-stream locations are presented and discussed for the square prisms of AR = 9 and 3 only.

Figures 7.5 and 7.6, respectively, show the mean streamlines in vertical (*x*-*z*) planes above the free ends of square prisms of AR = 9 and 3 for three cross-stream positions of *y/D* = 0, 0.25, and 0.375. According to Figure 7.5, the mean flow pattern above the free end of the square prism changes considerably as *y/D* increases away from the symmetry plane. For the prism of AR = 9, the cross-stream vortex seen at *y/D* = 0 (Figure 7.5(a)) is absent away from the symmetry plane. However, the cross-stream vortex is present at all *y/D* positions for the prism of AR = 3 (Figures 7.6(a, b, c)). Unlike for the flow above the free end of the finite circular cylinders (Subsection 6.2.2), the effect of the cross-stream position (*y/D*) on the flow behavior is more noticeable for the square prism. According to Figure 7.6, the reverse flow and its local separation from the trailing edge of the free end surface is more dominant than the effect of separated shear layer from the leading edge for the prism of AR = 3 at different *y/D* locations, while for the most slender prism (AR = 9), the effect of the shear layer separated from the leading edge is more dominant than the reverse flow as the distance away from the symmetry plane increases (Figure 7.5).

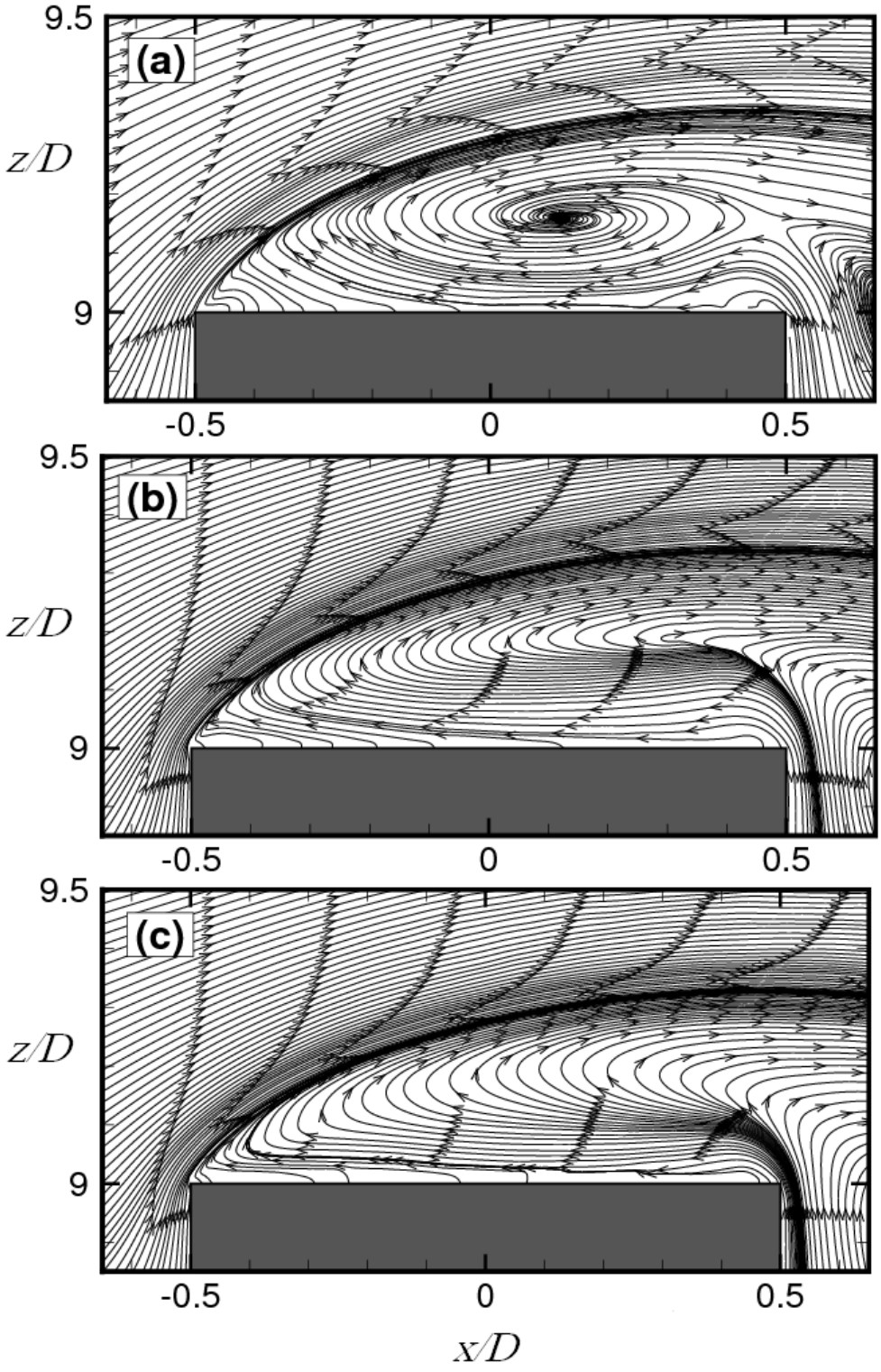

Figure 7.5: Mean streamlines for the flow over the free end of a surface-mounted finite-height square prism of AR = 9, measurements made in vertical planes at: (a) $y/D = 0$; (b) $y/D = 0.25$; (c) $y/D = 0.375$.

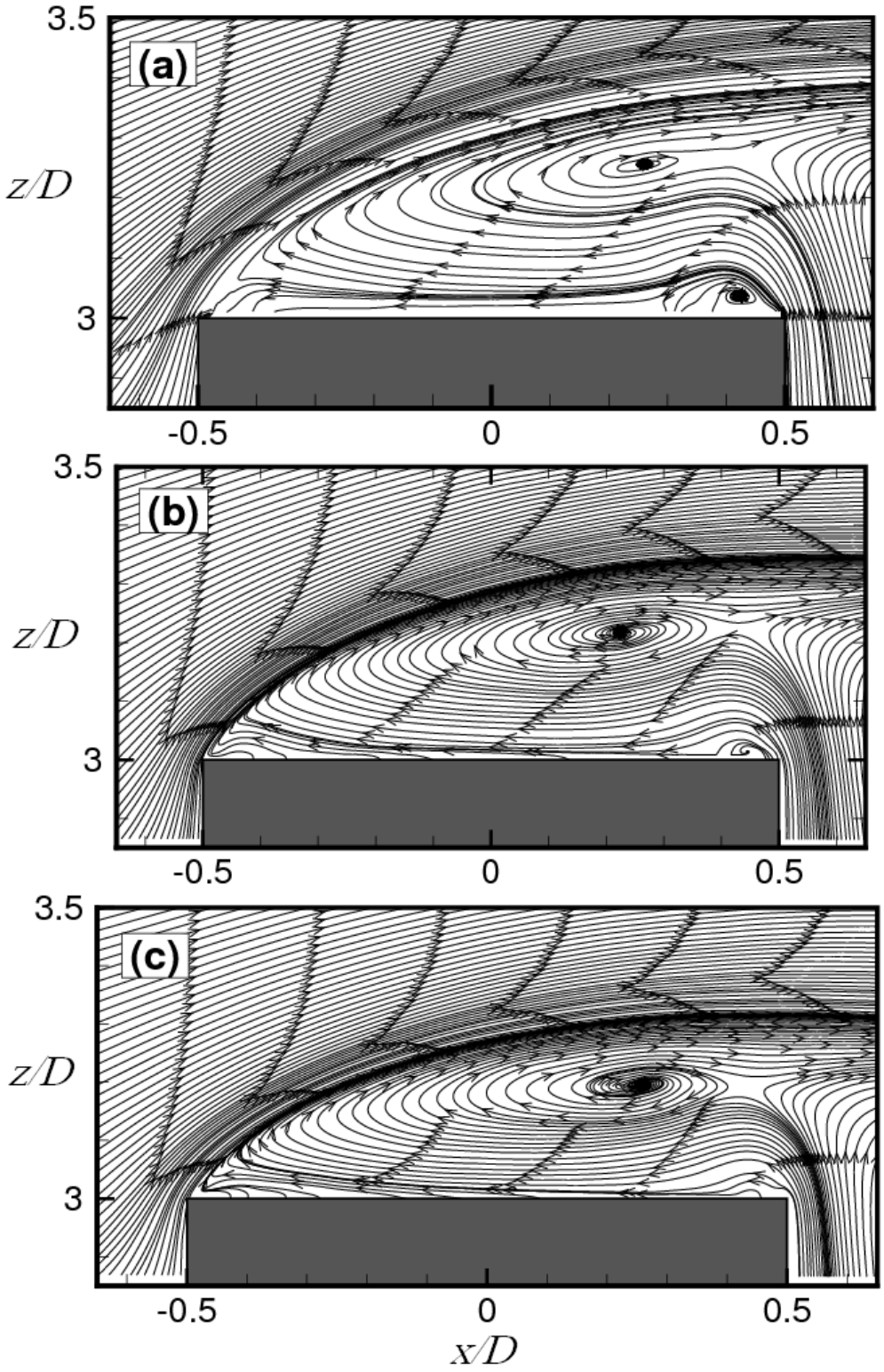

Figure 7.6: Mean streamlines for the flow over the free end of a surface-mounted finite-height square prism of AR = 3, measurements made in vertical planes at: (a) $y/D = 0$; (b) $y/D = 0.25$; (c) $y/D = 0.375$.

Contours of the in-plane Reynolds shear stress above the free end surfaces of the finite square prisms of AR = 9 and 3 at three cross stream locations of y/D = 0, 0.25, and 0.375 are shown in Figures 7.7 and 7.8, respectively. In the symmetry plane (Figures 7.7(a) and 7.8(a)), the flow above the free end of finite square prism is characterized by one region of negative shear stress above the free end extending into the upper part of the near-wake region, and one small region of positive shear stress originating from the leading edge. However, the behavior of the Reynolds shear stress changes significantly as the cross-stream position moves away the centerline. For the prism with the aspect ratio of AR = 9, as y/D increases, the positive Reynolds shear stress originating from the leading edge of the free end surface extends along the shear layer into the upper part of the free end, while the negative Reynolds shear stress located under the positive shear stress extends into the upper part of the near-wake region. For AR = 3 (Figure 7.8(b, c)), two regions of positive Reynolds shear stress are seen in the off-symmetry planes: close to the leading edge of the free end surface, and in the upper part of the free end above the region of negative Reynolds shear stress.

It can also be seen from Figures 7.7 and 7.8, at a given (x/D, z/D) location, the level of negative Reynolds shear stress increases as the cross-stream distance (y/D) increases from the symmetry plane. According to these figures, a different behavior of the Reynolds shear stress is evident for the prism of AR = 3 compared to AR = 9.

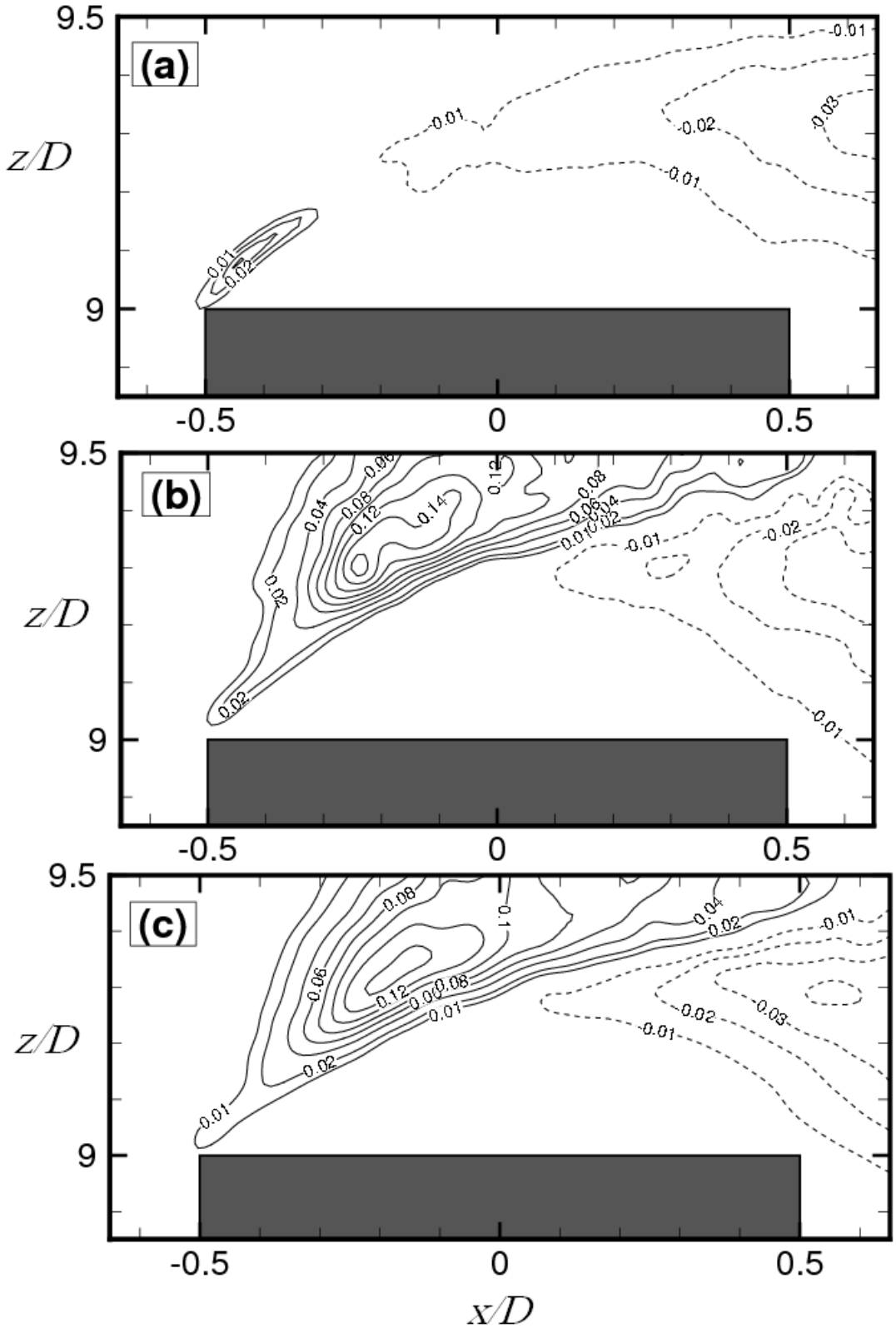

Figure 7.7: Mean Reynolds shear stress ($-\overline{u'w'}/U_\infty^2$) above the free end surface of finite square prisms of AR = 9; (a) *y/D* = 0, (b) *y/D* = 0.25, (c) *y/D* = 0.375.

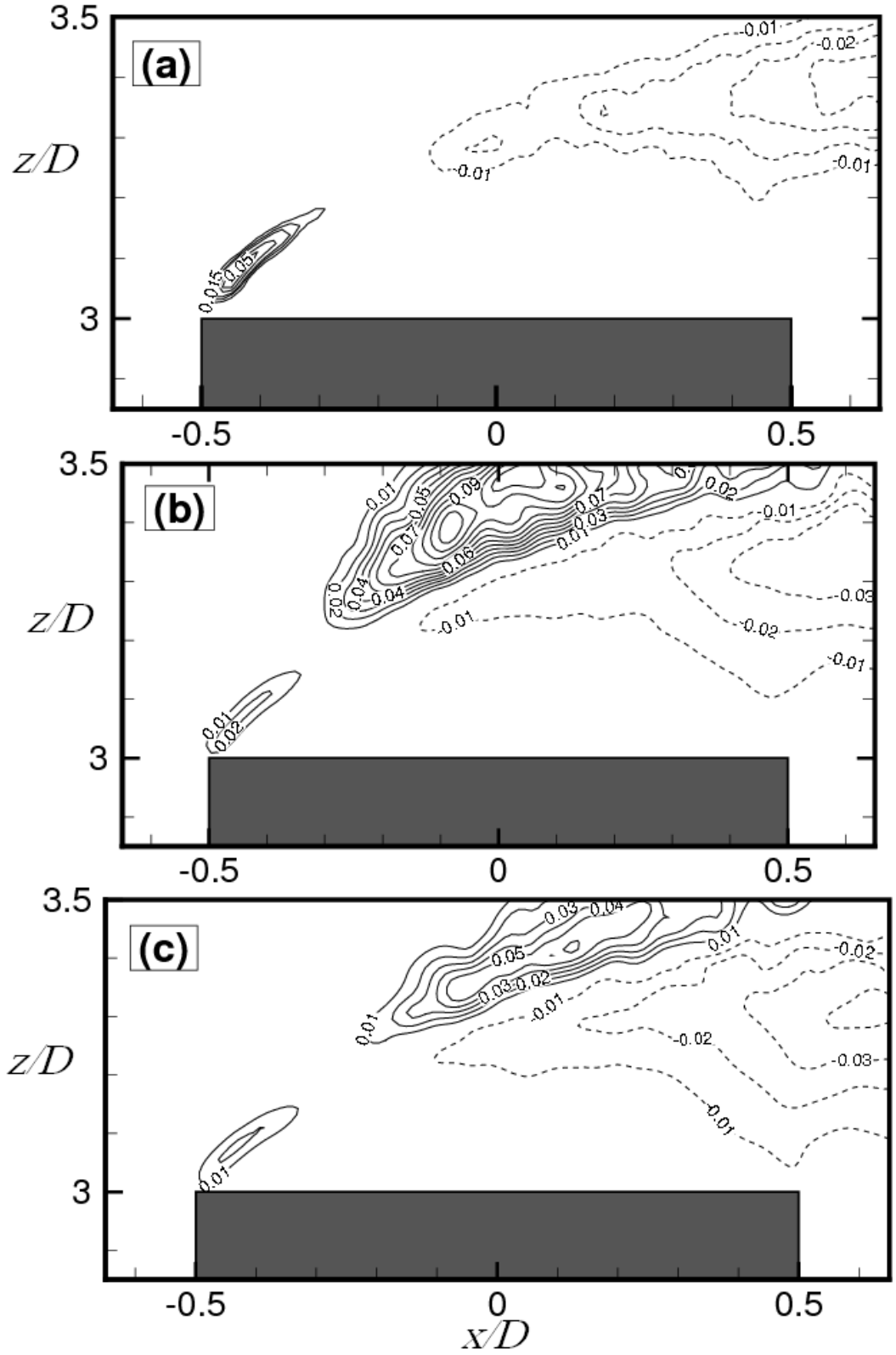

Figure 7.8: Mean Reynolds shear stress ($-\overline{u'w'}/U_\infty^2$) above the free end surface of finite square prisms of AR = 3; (a) y/D = 0, (b) y/D = 0.25, (c) y/D = 0.375.

7.3 Measurements in *x-y* Planes

In this section, the PIV results in a horizontal plane parallel to the free end surface, and a small distance above this surface (z/D = 0.016), for square prisms of AR = 9, 7, 5, and 3 are presented and discussed in order to investigate how the flow structure above the free end is affected by the aspect ratio of the prisms. Also, the results in three horizontal planes at wall-normal distances of z/D = 0.016, 0.08, and 0.16 above the free end surface are presented for two aspect ratios of AR = 9 and 3, to show how the flow behavior changes as the wall-normal distance from the free end surface changes. Figure 7.9 shows a schematic of the free end surface of a square prism identifying the corners and edges of the free end.

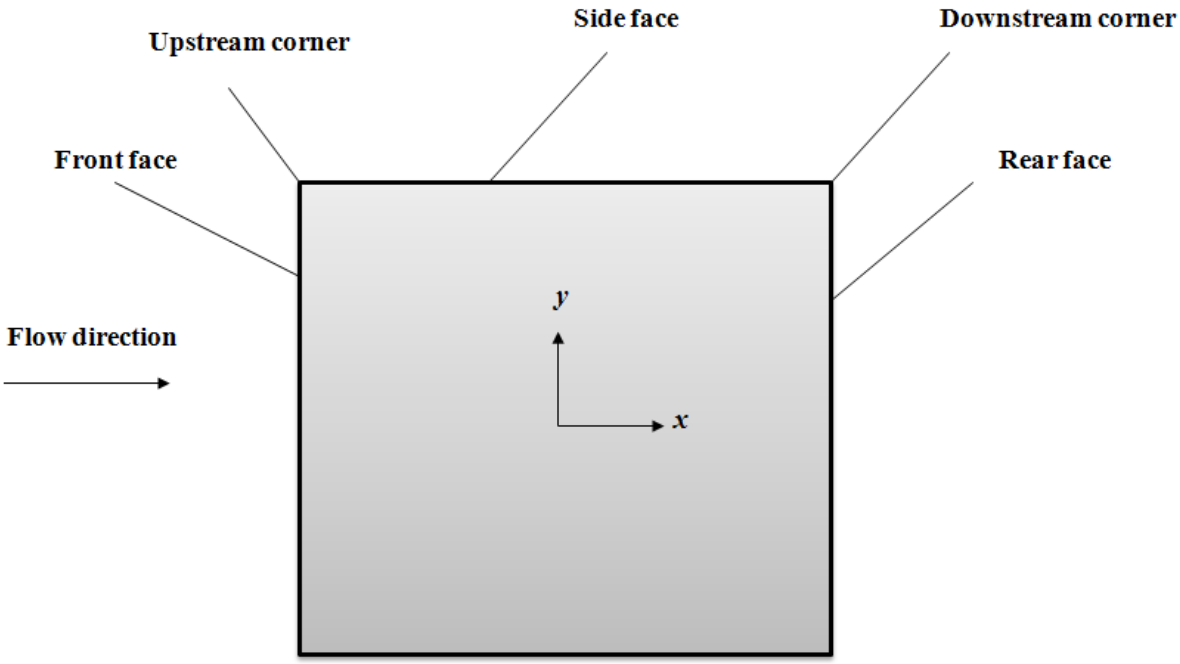

Figure 7.9: Schematic of the top-view of the free end surface of a finite square prism.

Figure 7.10 shows the flow pattern very close to the free end surface of the finite-height square prisms of AR = 9, 7, 5, and 3. According to this figure, a distinct flow behavior is seen for the prism of AR = 3 (Figure 7.10(d)) compared to the other prisms (Figures 7.10(a, b, c)). For the prism of AR = 3 (Figure 7.10(d)), the interaction between the strong reverse flow with the main separated flow forms a pair of vortices (denoted as *V* in Figure 7.10(d)) close to the side edges of the free end, while for the prisms of AR = 9, 7, and 5 (Figures 7.10(a, b, c)) there is no evidence of the wall-normal vortex pair. According to Figure 7.10(d), two saddle points (denoted as *S*) are seen around the downstream corners of the free end surface. Also, one nodal point (denoted as *N*) is evident upstream of the trailing edge for this prism. As the aspect ratio of the prism increases, the saddle points move towards the centerline (Figures 7.10(a, b, c)). The effect of aspect ratio on the flow behavior over the free end surface can be seen in the predominance of the reverse flow from the near-wake region of the prisms and perhaps in the wall-normal flow coming along the prism's sides towards the free end surface. This spanwise flow is affected by the ground plane boundary layer in which the prism is partially immersed.

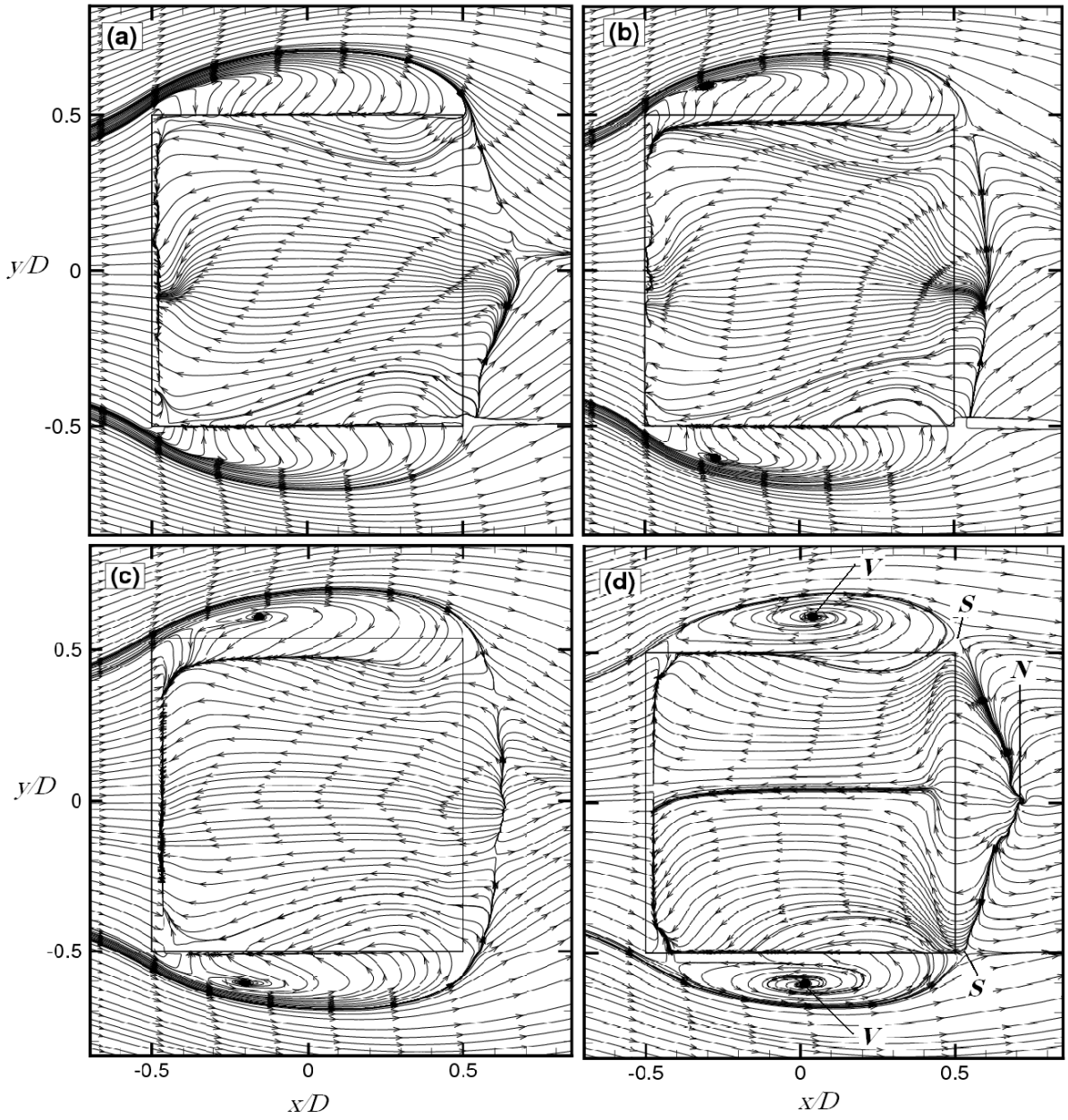

Figure 7.10: Mean velocity fields above the free end surface of a square prism of different aspect ratios of AR = 9, 7, 5 and 3 at the wall-normal location of z/D = 0.016. (a): AR = 9; (b): AR = 7; (c): AR = 5; (d): AR = 3. *N*, *S*, and *V*, respectively, represent the node, saddle points, and vortex.

Figure 7.11 shows the mean velocity field (($\overline{U}/U_\infty$), ($\overline{V}/U_\infty$)) in three horizontal *x*-*y* planes above the free end surface of square prisms of AR = 9 and 3. Very close to the free end surface (*z/D* = 0.016) a nodal point is seen downstream of the trailing edge of the prisms (Figures 7.11(a, d)). This node could be related to the upwash flow behind the prism free end seen in the symmetry *x*-*z* plane (Figure 7.1(a, d)). According to Figure 7.11, the flow pattern changes significantly as the wall-normal distance from the free end surface (*z/D*) increases. Based on the present results, the approach flow separates from the side edges of the prisms. For the prism of AR = 3 (Figures 7.11(d, e, f)), some part of this flow is directed towards the free end surface forming vortices at the two sides of the prism due to a stronger upward flow coming from the near wake, whereas for AR = 9 (Figures 7.11(a, b, c)), there is no evidence of these vortices. According to Figure 7.11, the flow pattern above the prism of AR = 3 is considerably different than that of AR = 9, such that for AR = 3 the vortices observed at *z/D* = 0.016 can be seen at *z/D* = 0.08 (Figure 7.11(e)). The effect of reverse flow on the flow pattern above the free end surface is evident at *z/D* = 0.16 (Figure 7.11(f)). According to this figure, for the prism of AR = 3, the reverse flow moves upstream to the location *x/D* = - 0.2, while for AR = 9, there is no evidence of backward flow at this elevation (Figure 7.11(c)), so that the flow separated from the side edges moves towards the free end surface.

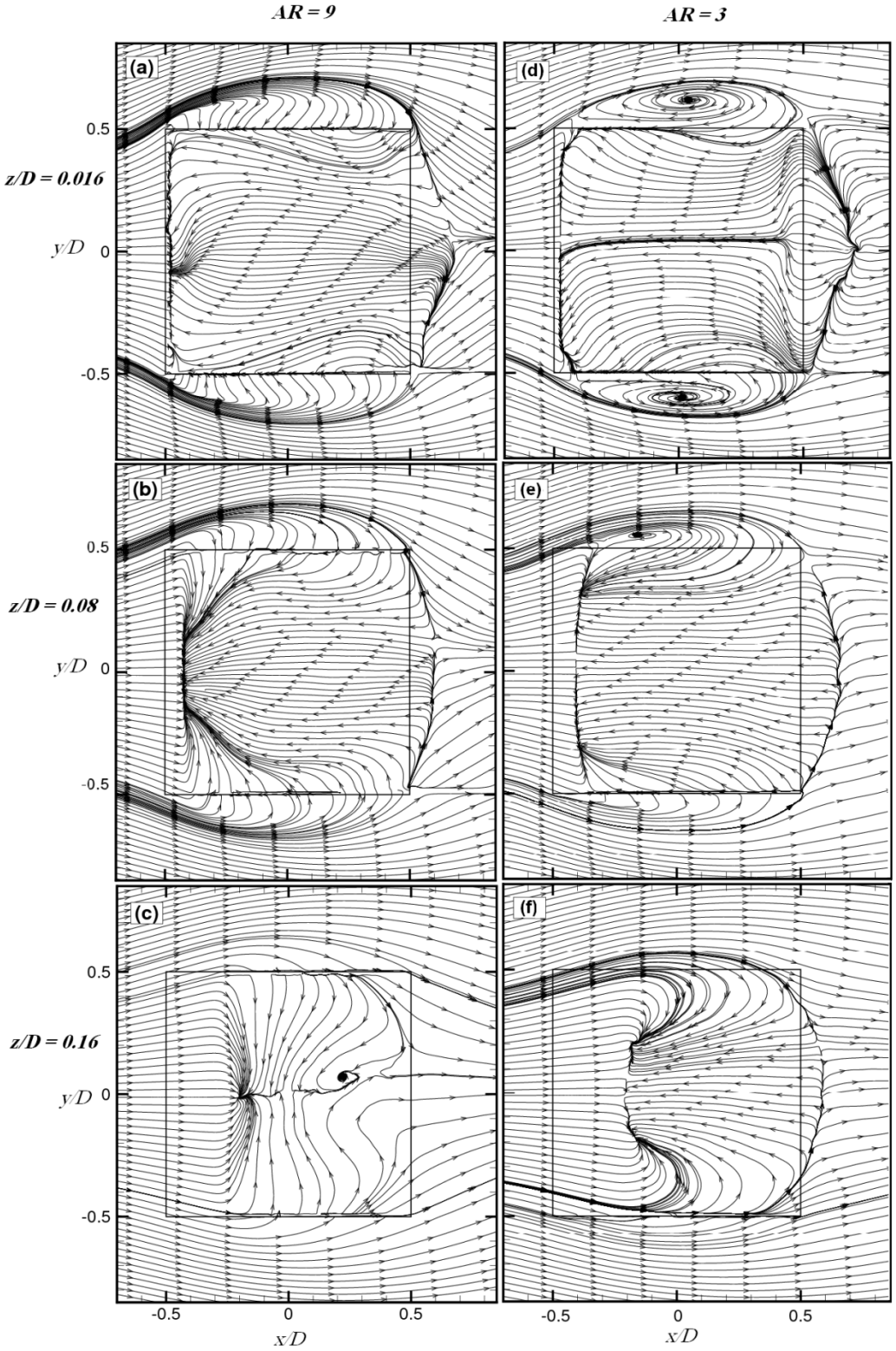

Figure 7.11: Mean velocity fields above the free end surface of a square prism of AR = 9, and 3.

To further illustrate the flow behavior over the free end surface of the finite square prism, contour plots are presented showing the mean streamwise velocity component (Figure 7.12) and the mean cross-stream velocity component (Figure 7.13) for square prisms of AR = 9 and 3. These contour plots show the velocity magnitudes in the *x-y* planes to see how the flow behaves as the wall-normal distance (*z/D*) changes. These figures illustrate regions of positive streamwise mean velocity upstream, downstream, and away from side edges of the free end, while regions of negative streamwise mean velocity are observed over the free end surfaces of the prisms. According to Figure 7.12, for both prisms, the magnitude of negative velocity decreases as the wall normal distance (*z/D*) increases. Furthermore, at a given *z/D*, as the aspect ratio of the prism decreases, the magnitude of negative mean velocity increases. For example, for the prism of AR = 3 at *z/D* = 0.016 and 0.16 (Figures 7.12(d, f)), the mean velocity has the maximum value of $\overline{U}/U_\infty$ = - 0.2 and - 0.15, respectively, on the free end surface, while for the prism of AR = 9, the maximum value of $\overline{U}/U_\infty$ = - 0.1 and -0.05 are observed at *z/D* = 0.016 and 0.16, respectively (Figures 7.12(a, c)).

Contour plots of the mean cross-stream velocity component ($\overline{V}/U_\infty$) above the free ends of finite square prisms of AR = 9 and 3 are shown in Figure 7.13. This figure illustrates regions of flow with opposite direction above the free end surfaces. According to this figure, the flow tends to move away from the prism at the upstream corners of the prisms, and move toward the prism at the downstream corners of the free end. This is consistent with the streamlines shown in Figure 7.11. For the prism of AR = 9 (Figures 7.13(a, b, c)), a stronger mean cross-stream velocity component is clearly evident at larger *z/D* compared to the prism of AR = 3 (Figures 7.13(d, e, f)). This might be related to the stronger mean streamwise velocity component for the flow above the free end of AR = 3 compared to AR = 9. Figure 7.13 also shows that for the

prism of AR = 9, the flow directed towards the prism center extends to the location of x/D = - 0.3 and -0.4 at wall-normal distances of z/D = 0.08 and 0.16, respectively, while for AR = 3 (Figures 7.13(d, e, f)), it extends down to x/D = 0.2 and 0, respectively.

Figure 7.14 shows the streamwise turbulence intensity behavior above the free end of the square prisms of AR = 9 and 3 at three wall-normal locations. According to this figure, the highest values of streamwise turbulence intensity are encountered around the downstream corners of the free end surfaces where regions of flow separated from the side edges of the prisms are located. For both prisms, the magnitude of u'/U_∞ increases with z/D. Figure 7.14 also illustrates that as the prism aspect ratio increases, the magnitude of the streamwise turbulence intensity on the free end surface decreases.

Figure 7.15 shows contour plots of the cross-stream turbulence intensity (v'/U_∞) above the free end surface of prisms of AR = 9 and 3 at three wall-normal positions. According to this figure, the level of v'/U_∞ above the free end surface increases with streamwise distance from the leading edge (x/D). Furthermore, for both prisms of AR = 9 and 3, the location of highest cross-stream turbulence intensity slightly moves toward the leading edge of the prism as the wall-normal distance (z/D) increases. Similar to the streamwise turbulence intensity (shown in Figure 7.14), as the prism aspect ratio increases, the magnitude of the cross-stream turbulence intensity on the free end surface decreases.

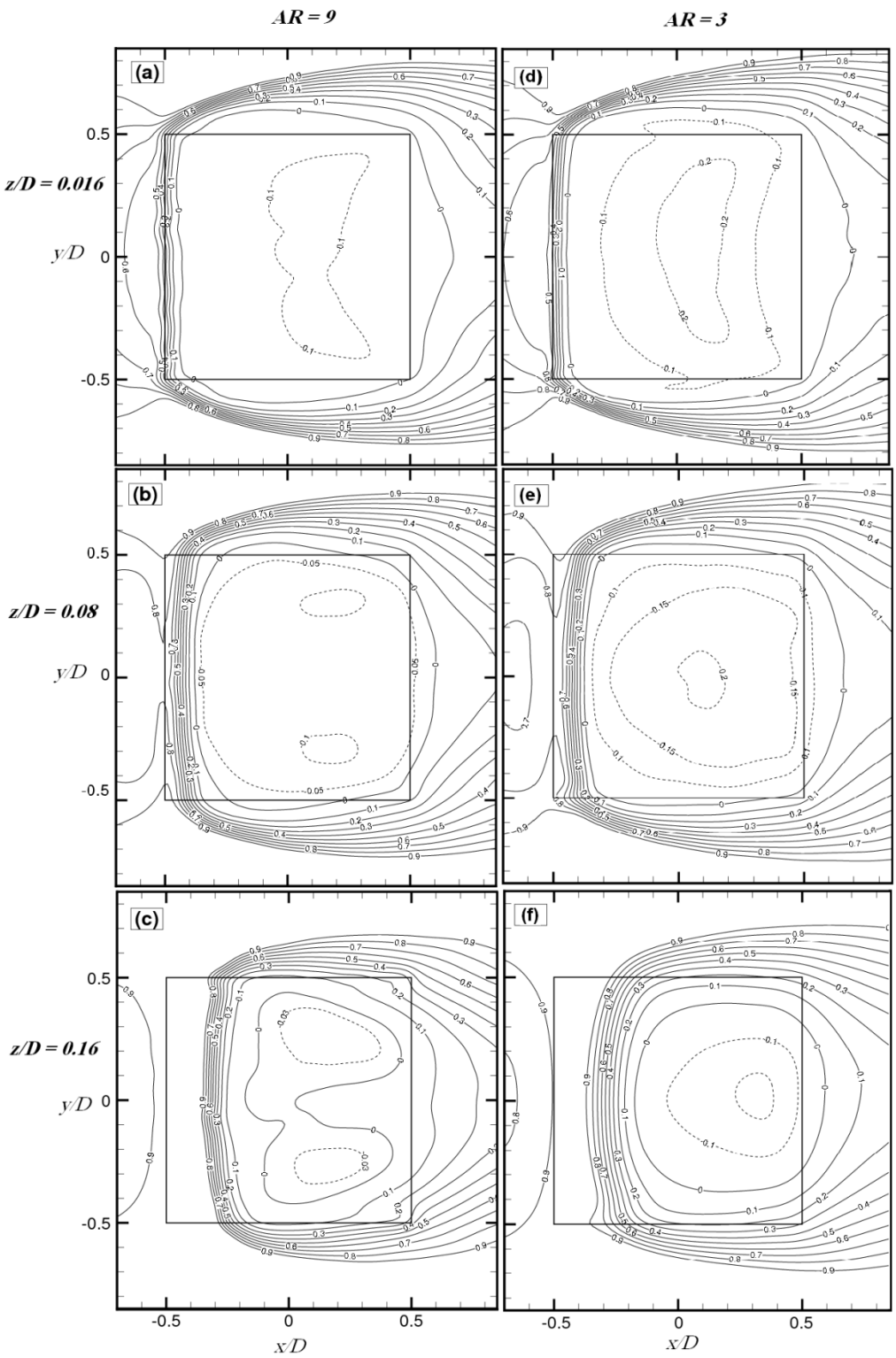

Figure 7.12: Streamwise mean velocity field (contours of $\overline{U}/U_\infty$) in horizontal planes above the free end surface of a square prism of AR = 9 and 3.

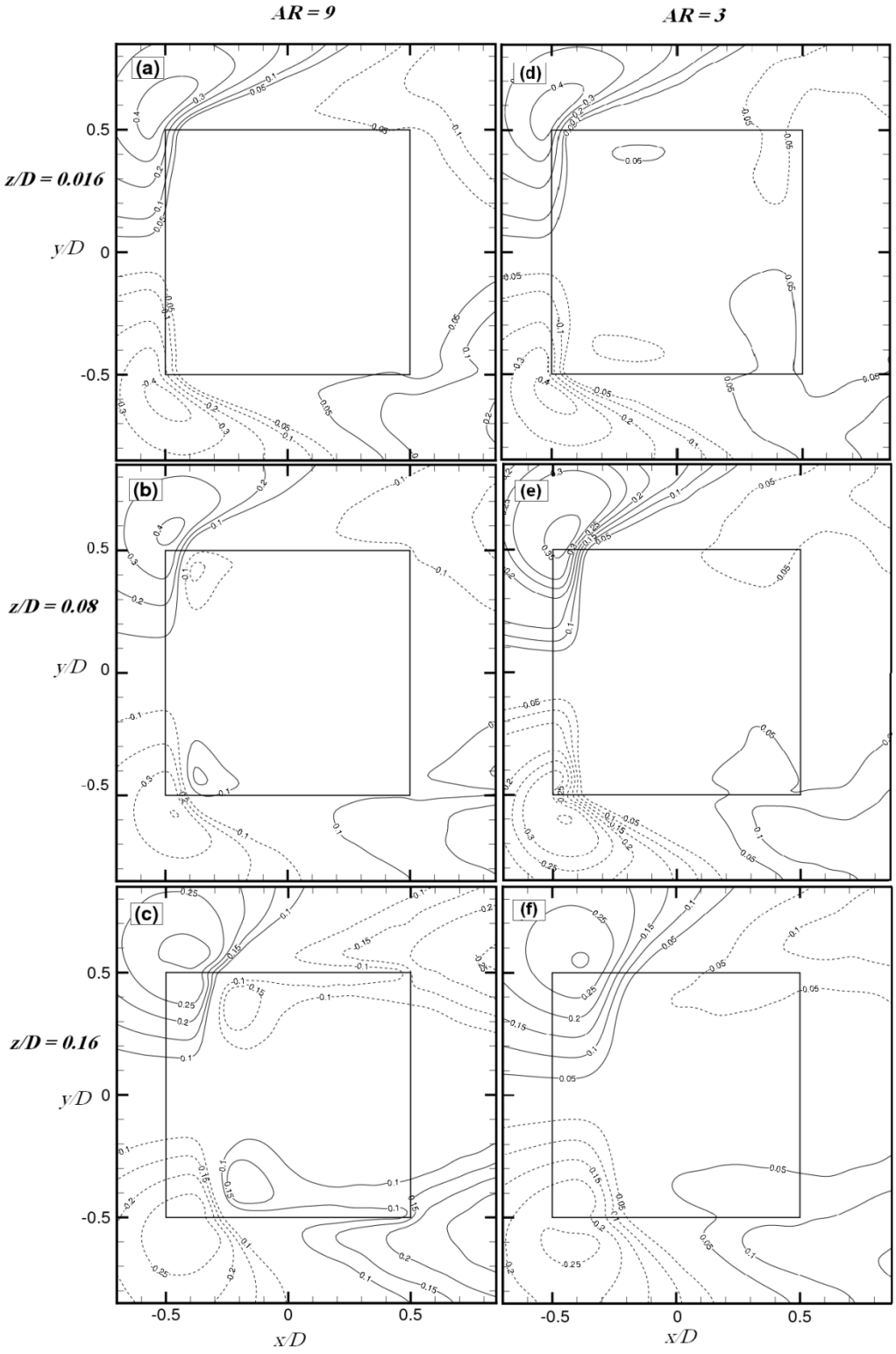

Figure 7.13: Cross-stream mean velocity field (contours of $\overline{V}/U_\infty$) in horizontal planes above the free end surface of a square prism of AR = 9 and 3.

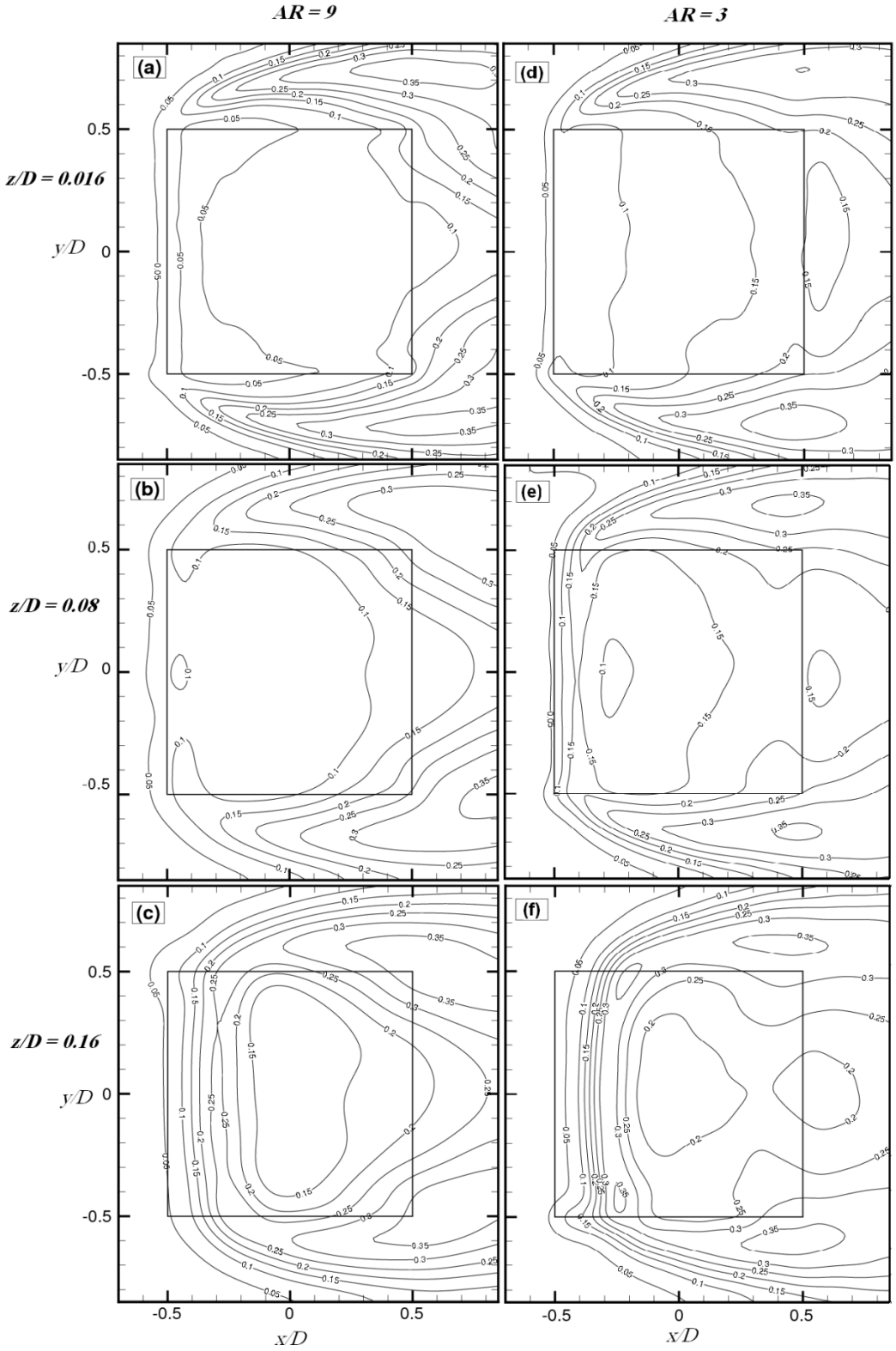

Figure 7.14: Streamwise turbulence intensity (contours of u'/U_∞) for the flow over the free end of a surface-mounted finite-height square prism of AR = 9 and 3.

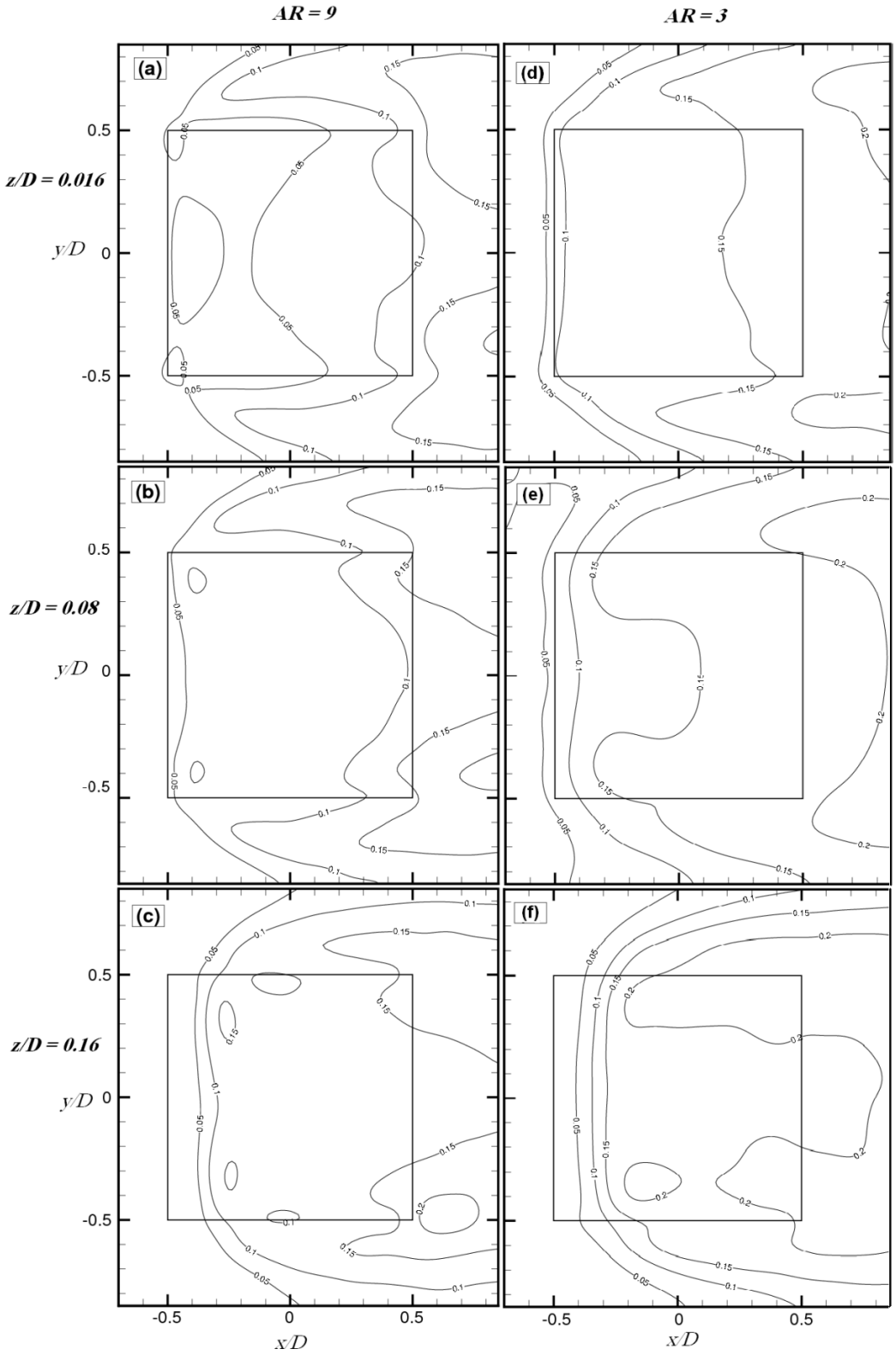

Figure 7.15: Cross-stream turbulence intensity (contours of v'/U_∞) for the flow over the free end of a surface-mounted finite-height square prism of AR = 9 and 3.

Figure 7.16 shows the contour plots of the in-plane Reynolds shear stress ($-\overline{u'v'}/{U_\infty}^2$) above the free end surface of prisms of AR = 9 and 3 in three horizontal planes at elevations of *z/D* = 0.016, 0.08, and 0.16. According to this figure, the flow above the free end surface of the finite prisms is characterized by regions of elevated Reynolds shear stress: two regions of positive and negative shear stress around the upstream corners of the free end originating from the leading edge due to the flow separation from the leading edge, and two broader regions of positive and negative shear stress around the downstream corners of the free end. According to Figure 7.16, for both aspect ratios, the level of Reynolds shear stress decreases as the wall normal distance (*z/D*) increases. It can also be concluded that the Reynolds shear stress does not change significantly as the aspect ratio of the prism changes. However, for the prism of AR = 3 (Figures 7.16(d, e, f)), the level of Reynolds shear stress close to the leading edge is larger than that for AR = 9 (Figures 7.16(a, b, c)). This may be due to the effect of the ground plane boundary layer.

The mean wall-normal vorticity ($\overline{\omega_z}D/U_\infty$) fields above the free end for finite square prisms of AR = 9 and 3 are shown in Figure 7.17. According to this figure, negative (CW) and positive (CCW) vorticities are generated close to the corners of the leading edge extending to the sides of the prisms. The centers of these vorticities move downstream and toward the free end centerline as the wall normal distance (*z/D*) increases. Figures 7.17(a, b, c) also show that for the prism of AR = 9, the vorticities above the free end extend more downstream having a larger magnitude compared to those of AR = 3 (Figures 7.17(d, e, f)).

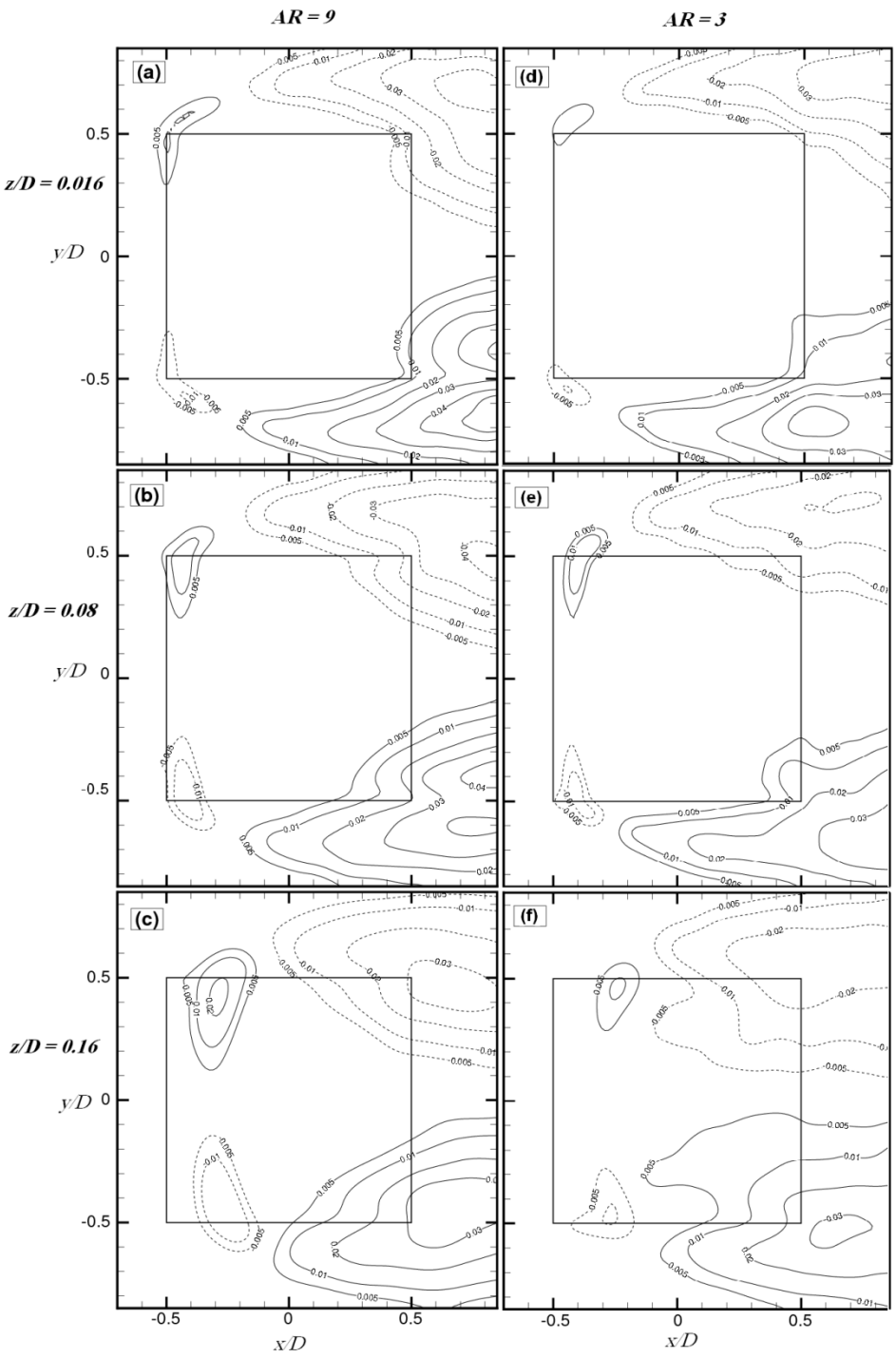

Figure 7.16: Reynolds shear stress field (contours of $-\overline{u'v'}/{U_\infty}^2$) for the flow over the free ends of surface-mounted finite-height square prism of AR = 9 and 3.

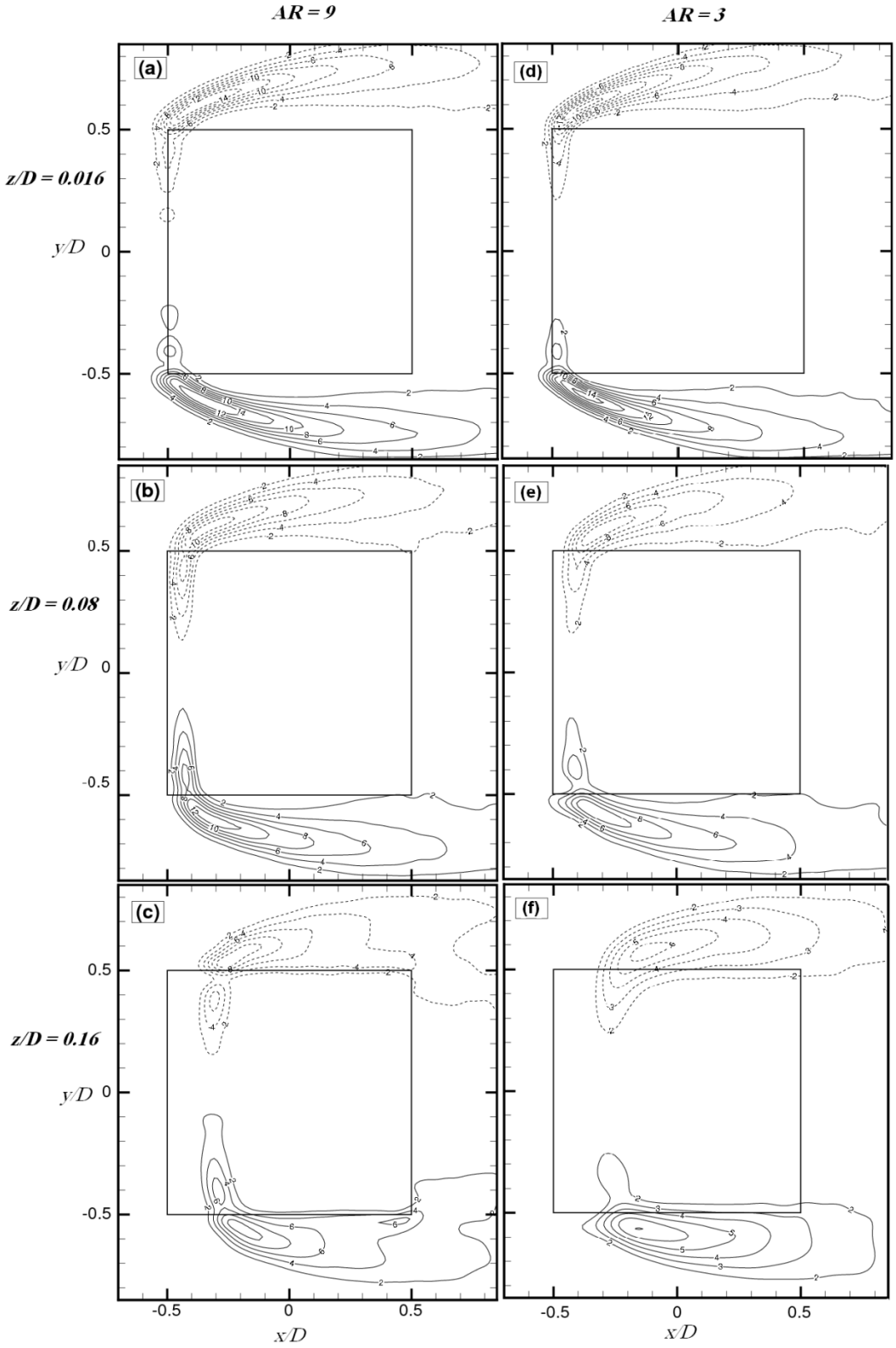

Figure 7.17: Mean in-plane vorticity field (contours of $\overline{\omega_z}D/U_\infty$) for the flow over the free ends of surface-mounted finite-height square prism of AR = 9 and 3.

7.4 Measurements in *y-z* Planes

Flow behavior above the free end surfaces of the finite square prisms of AR = 9 and 3 in *y-z* planes at three different streamwise locations of *x/D* = -0.2, 0.2, and 0.5 are shown through Figures 7.18 to 7.22. In these figures, all dimensions are normalized by the width of the square prism (*D*), while the velocity fields are normalized by the freestream velocity (U_∞). As described in Chapter 3, the measurements in the *y-z* plane are very challenging due to the fact that the dominant velocity component is normal to the light sheet. Also, positioning of the camera inside the test section of the wind tunnel to take images while the wind tunnel is running, is another challenge due to the possible vibration of the camera. However, the frequency of the image acquisition is much larger than the frequency of the vibration of the camera itself inside the test section.

Figure 7.18 shows the mean in-plane velocity field ($\overline{V}/U_\infty$,$\overline{W}/U_\infty$) in three vertical *y-z* planes above the free end surface of finite square prisms of AR = 9 and 3. According to this figure, the flow behavior changes considerably from the leading edge of the prism to the trailing edge. Ahead of the center of the prism at *x/D* = -0.2 (Figure 7.18(d)), the upward flow for the prism of AR = 3 shows the predominance of the flow separated from the leading edge. This flow behavior is also seen for the prism of AR = 9 (Figure 7.18(a)), however, cross-stream velocities are seen closer to the free end surface for the prism of AR = 9, perhaps due to the effect of cross stream flow separated from the side edges of the free end surface (discussed in Section 7.3). Behind the center of the prism at *x/D* = 0.2 (Figure 7.18(b, e)), two vortices with opposite sense of rotation are seen close to the free end surface for the prisms of AR = 9 and 3. These vortices are centered at *y/D* = ±0.45 and ±0.4, respectively for AR = 3, and 9. Figure 7.18 also shows that at the trailing edge of the free end (*x/D* = 0.5), the flow pattern is more complicated than those of

x/D = -0.2 and 0.2 including cross-stream and wall-normal directed flows making some critical points such as nodes and/or saddle points which are difficult to discuss . According to the flow pattern at *x/D* = 0.5, it can be concluded that the streamwise vortices formed at *x/D* = 0.2 for the prisms are no longer streamwise and they may be deflected to other directions as the streamwise distance increases. Hence, these vortices are not considered tip vortices, since they are not evident at the trailing edge of the free end surface.

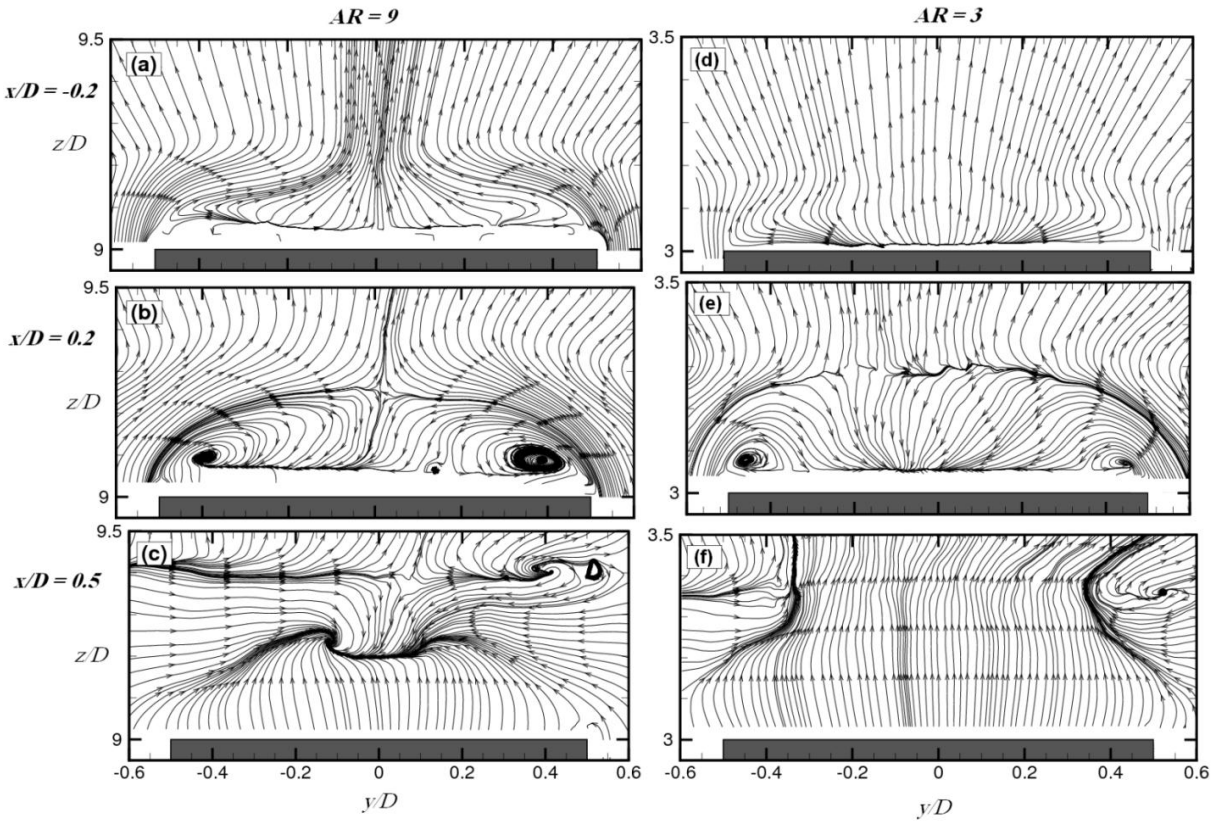

Figure 7.18: Mean velocity fields above the free end surface of square prisms of aspect ratio of AR = 9 and 3.

Contour plots of the cross-stream turbulence intensity (v'/U_∞), wall-normal turbulence intensity (w'/U_∞), and Reynolds shear stress ($-\overline{v'w'}/{U_\infty}^2$), in vertical planes above the free end

surface of square prisms of AR = 9 and 3, at three streamwise locations of x/D = - 0.2, 0.2, and 0.5, are shown in Figures 7.19 to 7.21.

According to Figure 7.19, for both prisms of AR = 9 and 3, the value of the cross-stream turbulence intensity has its lowest value very close to the free end surface increasing to its maximum level (v'/U_∞ = 0.2) and then decreasing to the lowest value at higher elevation. It can be observed from Figure 7.19 that, at a given x/D, the regions of maximum cross-stream turbulence intensity are larger for the prism of AR = 3 (Figures 7.19(d, e, f)) compared to that of AR = 9 (Figures 7.19(a, b, c)).

Figure 7.20 shows contour plots of the wall-normal turbulence intensity (w'/U_∞) above the free end surface of prisms of AR = 9 and 3. According to these figures, for both prisms, the region of highest w'/U_∞ moves away from the free end surface as x/D increases. Similar to the cross-stream turbulence intensity, the value of wall-normal turbulence intensity has its lowest value very close to the free end surface increasing to its maximum level and then decreasing to the lowest value at higher elevation for both aspect ratios.

Figure 7.21 shows the contour plots of the in-plane Reynolds shear stress ($-\overline{v'w'}/{U_\infty}^2$) above the free end surface of prisms of AR = 9 and 3 in vertical planes at streamwise locations of x/D = - 0.2, 0.2, and 0.5. According to this figure, regions of positive and negative shear stresses are observed above the side edges of the free end surface extending upward and towards the center of the prisms. For both prisms, as the distance from the leading edge (x/D) increases, the regions of positive and negative shear stresses increase in size and level. Figure 7.21 also shows that, for prisms of AR = 9 and 3, regions of shear stress with opposite signs are formed above the corners of the free end at the location of the trailing edge (x/D = 0.5). According to this figure,

larger regions of shear stress are seen for the prism of AR = 9 (Figures 7.21(a, b, c)) compared to AR = 3 (Figures 7.21(d, e, f)).

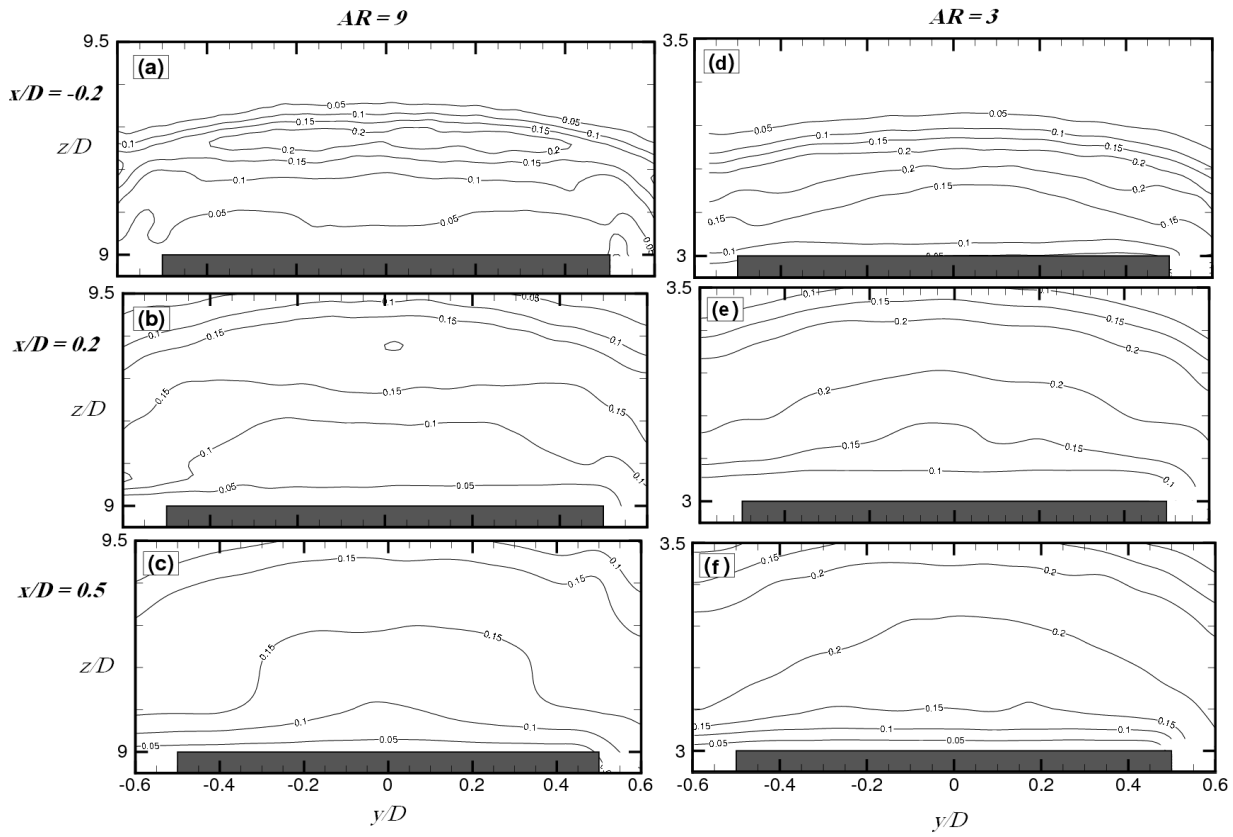

Figure 7.19: Cross-stream turbulence intensity field (v'/U_∞) above the free end of a square prism of AR = 9 and AR = 3.

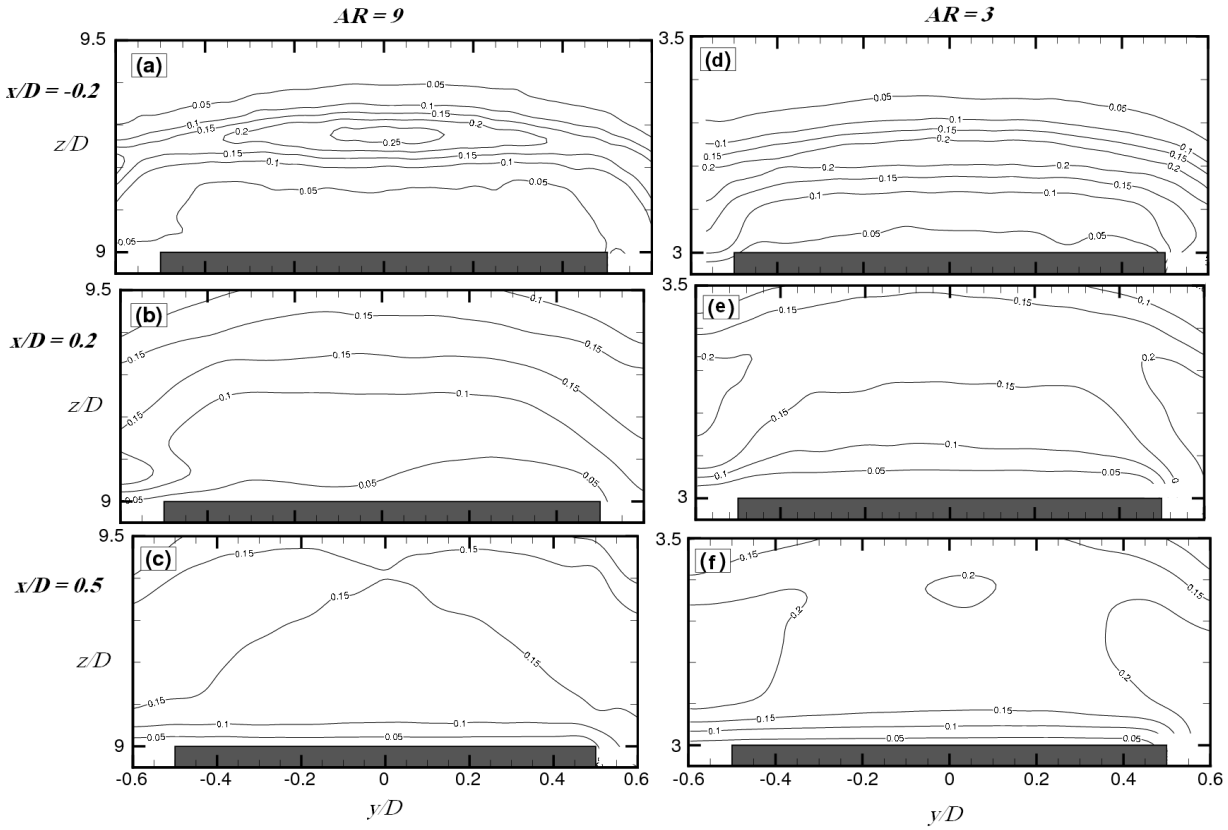

Figure 7.20: Wall-normal turbulence intensity field (w'/U_∞) above the free end of a square prism of AR = 9 and AR = 3.

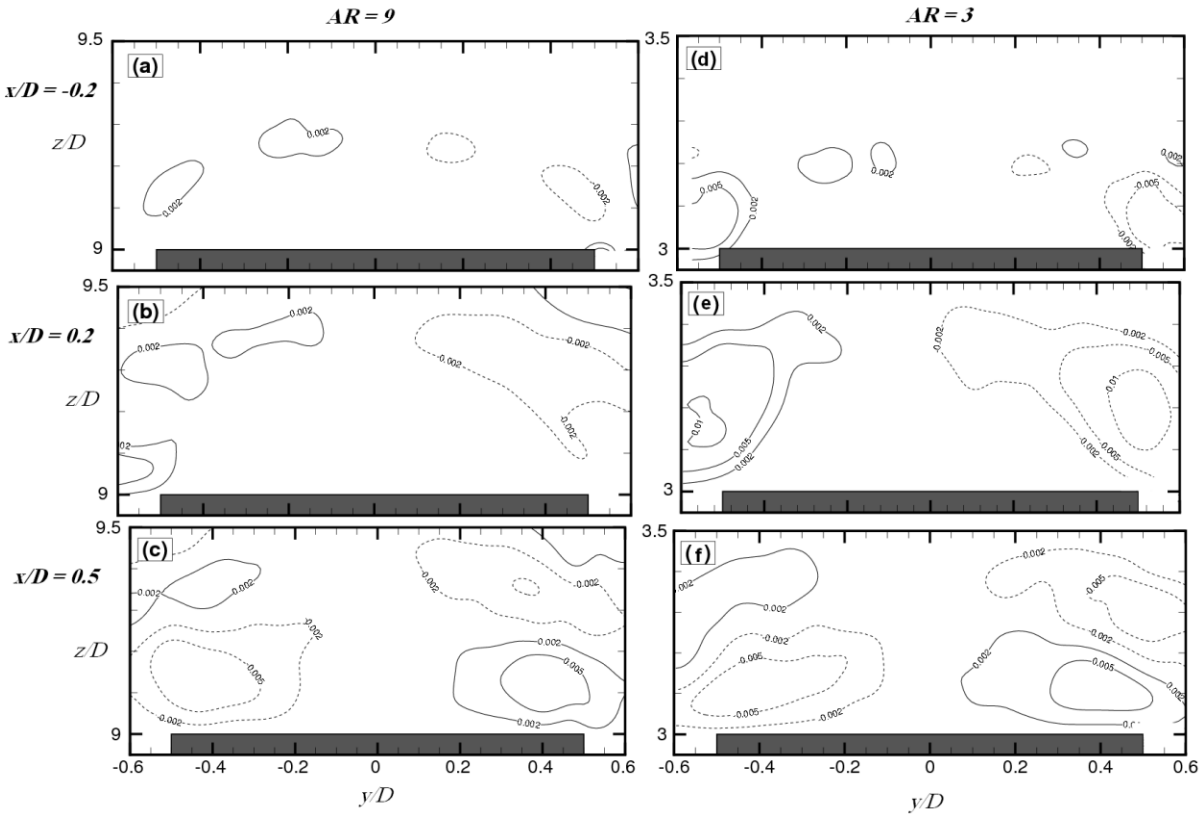

Figure 7.21: Reynolds shear stress field (contours of $(-\overline{v'w'}/{U_\infty}^2)$ above the free end of square prisms of AR = 9 and 3.

The mean streamwise vorticity ($\overline{\omega_x}D/U_\infty$) fields above the free end for two finite square prisms of AR = 9 and 3 are shown in Figure 7.22. According to this figure, two pairs of vorticity with opposite sense of rotation are observed above the side edges of the free end. One pair of vortices is centered close to the free end side edge, while the other pair is located above the first pair. For both prisms, as the streamwise distance increases, the strength of these two pairs of vorticity decreases. From the data in other planes, it is concluded that these vortices originate from the leading edge corners as the upcoming flow separates from the leading edge and the side edges of the free end surfaces of the finite square prisms. It can also be seen from Figure 7.22 that, in all three streamwise locations, as the aspect ratio increases, the vortices become wider and stronger.

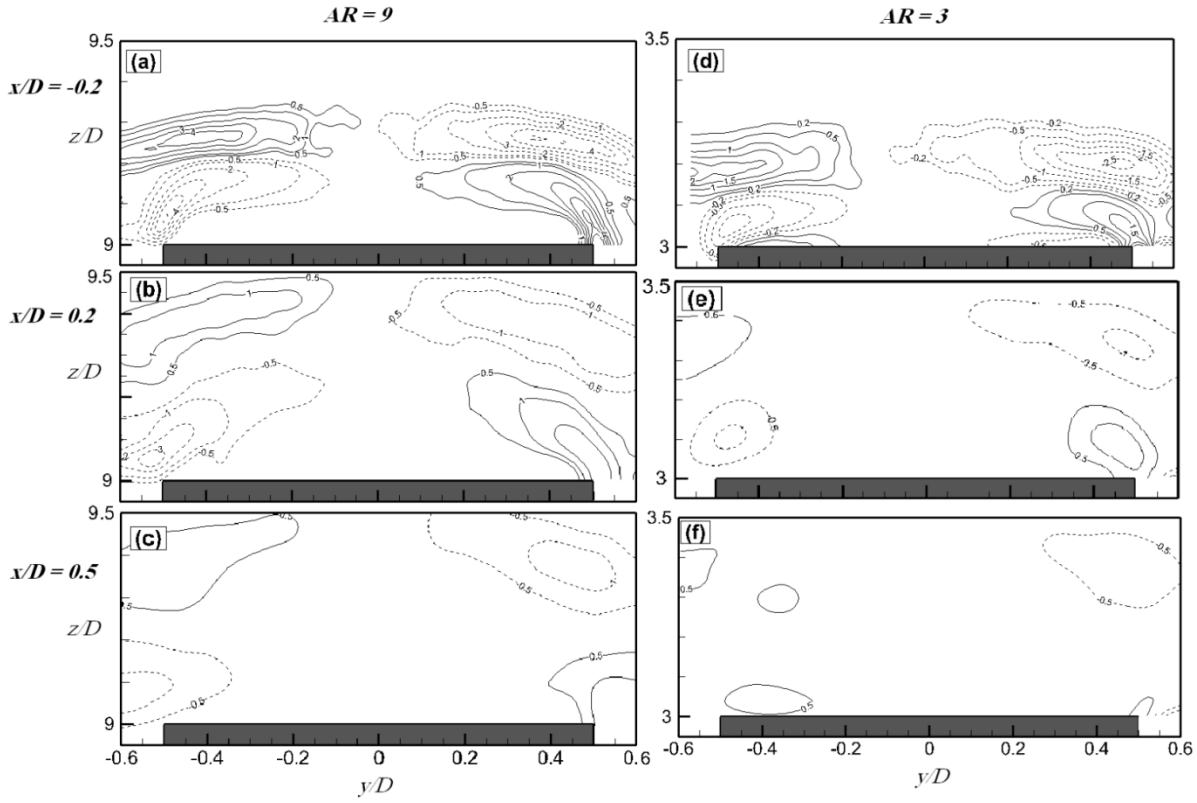

Figure 7.22: Mean streamwise vorticity fields ($\overline{\omega_x}D/U_\infty$) above the free end of finite square prisms of AR = 9 and 3.

To show the effect of the prism's aspect ratio on the flow above the free end surface in the *y*-*z* planes, mean streamlines in vertical planes at a streamwise location of *x/D* = 0.2 are shown for three square prisms of AR = 9, 5, and 3 in Figure 7.23. According to this figure, a counter-rotating vortex pair is seen above the free end for all three aspect ratios. As seen in Figure 7.23, the size and strengths of these vortices are reduced as the aspect ratio decreases. Also, as the aspect ratio of the prism decreases, the centers of these vortices move towards the side edges of the free end, such that for AR = 9 (Figure 7.23(a)) the vortices are centered at approximately *y/D*

= ±0.39, while they are centered at y/D = ±0.42 and ±0.45, respectively, for AR = 5 and 3 (Figures 7.23(b, c)).

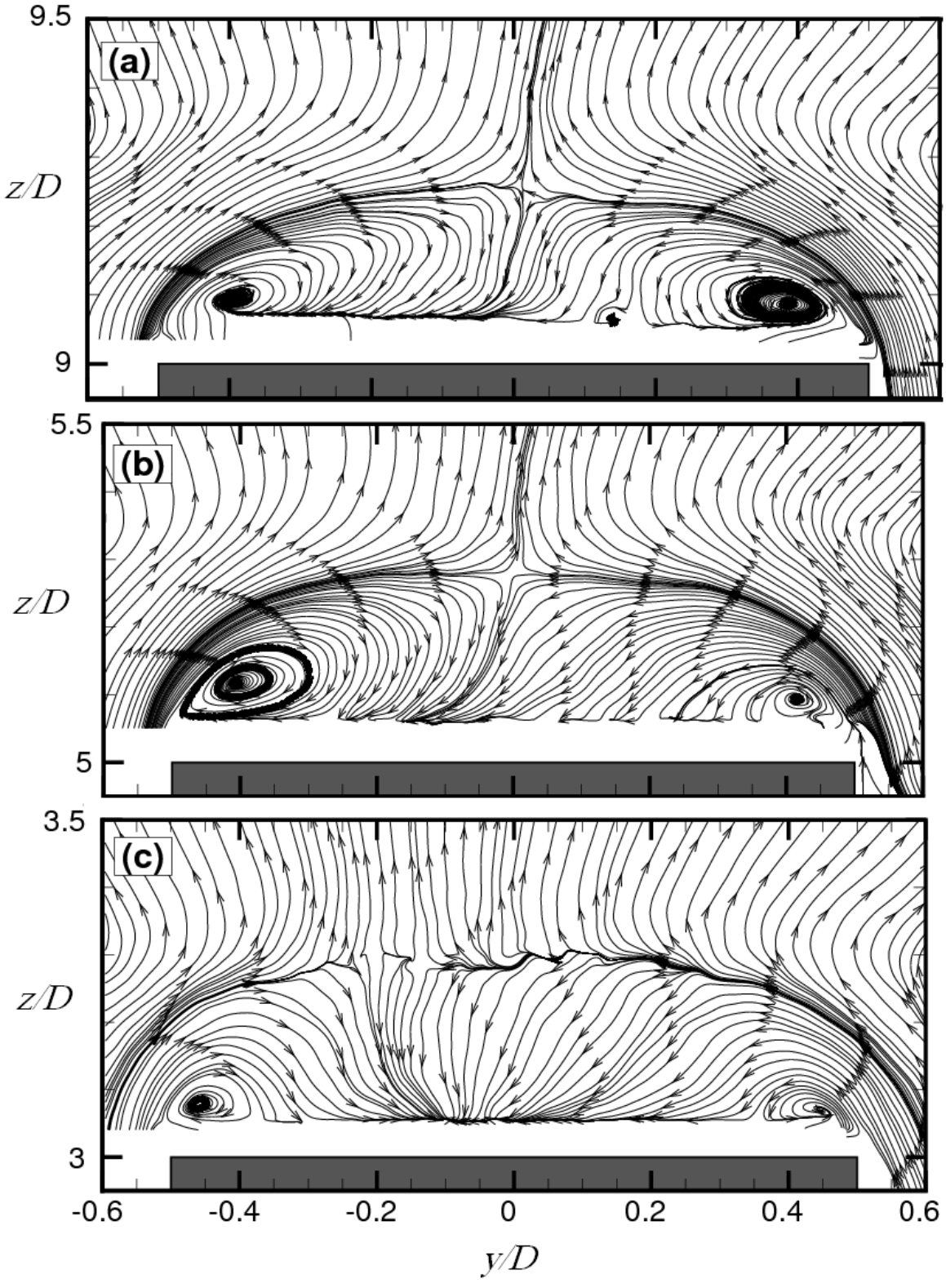

Figure 7.23: Mean streamlines above the free end of square prism in a vertical plane at a streamwise location of x/D = 0.2: (a) AR = 9; (b) AR = 5; (c) AR = 3.

8. Conclusions, Contributions and Recommendations

8.1 Conclusions

The research reported in the thesis is divided into four topics: the near-wake flow field of surface-mounted finite-height circular cylinders, the near-wake flow field of surface-mounted finite-height square prisms, the flow above the free end of finite circular cylinders, and the flow above the free end of finite square prisms. In all of these cases, the flow fields were investigated in a low-speed wind tunnel at $Re_D = 4.2\times10^4$ using PIV. The cylinders and prisms were mounted normal to a ground plane and were partially immersed in a flat-plate turbulent boundary layer with $\delta/D = 1.6$ at the location of the cylinder or prism. Four aspect ratios of AR = 9, 7, 5, and 3 were considered for the cylinder and prism. PIV velocity measurements were made in the vertical symmetry plane on the flow centerline, upstream and downstream of the cylinders and prisms, with a special focus on the near-wake recirculation zone. The PIV measurements were also carried out above the free end surfaces of the cylinders and prisms in three orthogonal planes of *x*-*z*, *x*-*y*, and *y*-*z*.

8.1.1 Finite Circular Cylinder

The results of the present study have provided additional information on the local flow field of a surface-mounted finite circular cylinder and the influence of aspect ratio. In the near-wake region of the circular cylinders, a large recirculation region forms behind the cylinder. Downwash flow enters the central portion of the wake but some flow from the free end reverses and moves toward the base region of the cylinder. A small vortex occurs just downstream of the free end behind the cylinder and below the main downwash flow. This vortex is found for all four aspect

ratios. Near the ground plane and close to the cylinder-wall junction, a second vortex forms; this vortex is absent for the cylinder of AR = 3, an indication of a distinct wake structure for this cylinder, a finding that is consistent with earlier studies of these cylinders by Sumner et al. (2004) and Adaramola et al. (2006). Weak upwash flow occurs from the ground plane directed towards the central region of the wake; this upwash flow is weakest for the cylinder of AR = 3. The maximum length of the recirculation zone increases from 2.09*D* for AR = 3 to 3.76*D* for AR = 7, and then decreases to 2.94*D* for AR = 9. The maximum length of the region of recirculating flow, L_{max}/D, typically occurs at the location close to the saddle points observed in the mean streamlines of the near-wake region. According to the results, the maximum length occurs for an intermediate aspect ratio (AR = 7).

Above the free end of the cylinder, flow separation occurs from the leading edge of the free-end surface and a mean recirculation zone is formed. The present results showed that the reattachment of the separated flow onto the free end of the cylinder depends on AR. The reattachment position for AR = 9 and 7 occurred at approximately *x/D* = 0.21 and 0.25 (measured from the center of the cylinder), respectively, while for AR = 5 and 3 the separated flow reattached onto the upper surface of the cylinder closer to the trailing edge at approximately *x/D* = 0.3 and 0.29, respectively. Elevated levels of turbulence intensity and Reynolds shear stress also occur above the free end. Cross-stream vorticity production also occurs around the free end and into the downwash region behind the cylinder. This region of mean vorticity extends downwards along the base (rear surface) of the cylinder and, as the aspect ratio decreases, extends farther downstream. The region of positive Reynolds shear stress just behind and below the cylinder free end decreases in size and level as the aspect ratio of the cylinder decreases and it disappears for AR = 3. Considering the behavior of the mean recirculation zone

on the free end, and the relationship between cylinder aspect ratio and the reattachment point discussed earlier, it seems that when the reattachment point moves towards the trailing edge there are corresponding changes to the local Reynolds shear stress in the region of downwash flow.

For all aspect ratios, the cross-stream vortex contained within the free end recirculation zone is visible away from the symmetry plane although it is reduced in strength and size. Within the symmetry plane, the streamwise turbulence intensity and in-plane Reynolds shear stress distributions were largely unaffected by aspect ratio.

According to the results in the horizontal *x-y* planes parallel to the free end surface, one of the main characteristics of the flow over the free end surface is the formation of two foci very close to the free end surface representing a pair of wall-normal vortices. As the cylinder aspect ratio increases, the size and strength of the vortices decrease. The center of these vortices moves downstream as the aspect ratio increases. For the cylinder of AR = 9, the centers of the foci are located at (x/D, y/D) = (0, 0.45) at the wall-normal distance of z/D = 0.016, while for the shortest cylinder of AR = 3, those centers are located at (x/D, y/D) = (-0.1, 0.4). Considerable difference is observed between the flow behavior above the free end of the cylinder of AR = 9 and the other aspect ratios.

Regions of positive and negative Reynolds shear stress are seen around the leading edge of the free end at different wall-normal distances close to the free end surface due to the separation of the approaching flow from the leading edge. However, at z/D = 0.08, there is no evidence of the Reynolds shear stress. Regions of positive and negative shear stress are also evident at the trailing edge of the cylinder of AR = 9. These are centered on the trailing edge of

the free end surface moving upstream and towards the cylinder center as the wall-normal distance increases. Also, the level of Reynolds shear stress decreases as the wall-normal distance (*z/D*) increases.

According to the PIV results in the *x*-*z* and *x*-*y* planes, a model for the flow pattern above the free end surface of surface-mounted finite-height circular cylinder of AR = 9 (above the critical AR) and 3 (below the critical AR) is proposed, and is shown in Figures 8.1 and 8.2.

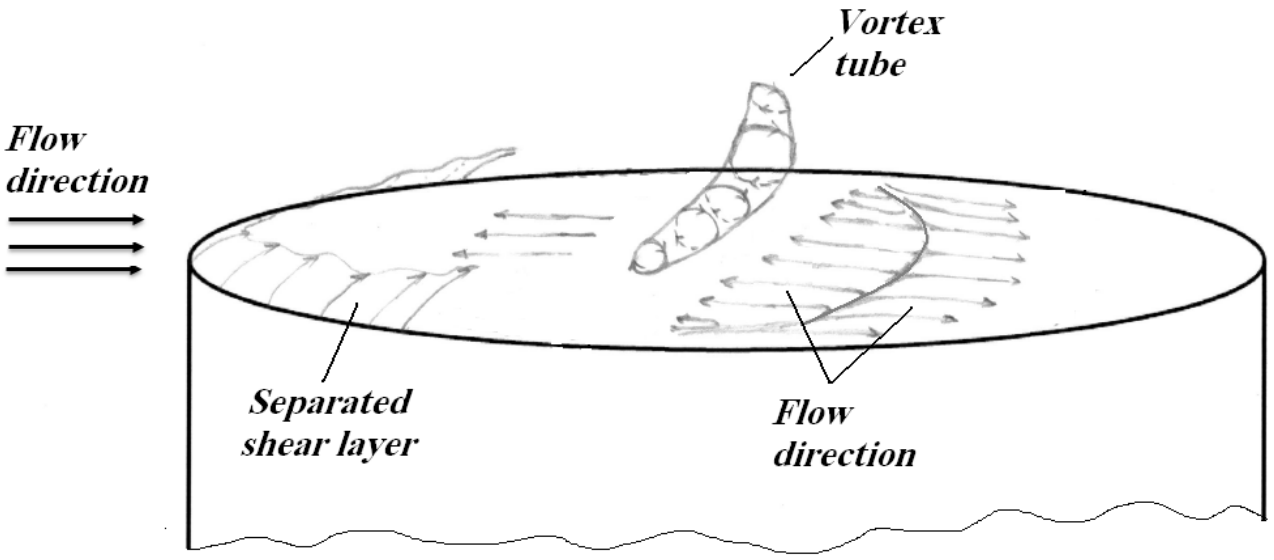

Figure 8.1: Schematic representation of the flow above the free end surface of a surface-mounted finite-height circular cylinder of AR = 9 (above the critical AR).

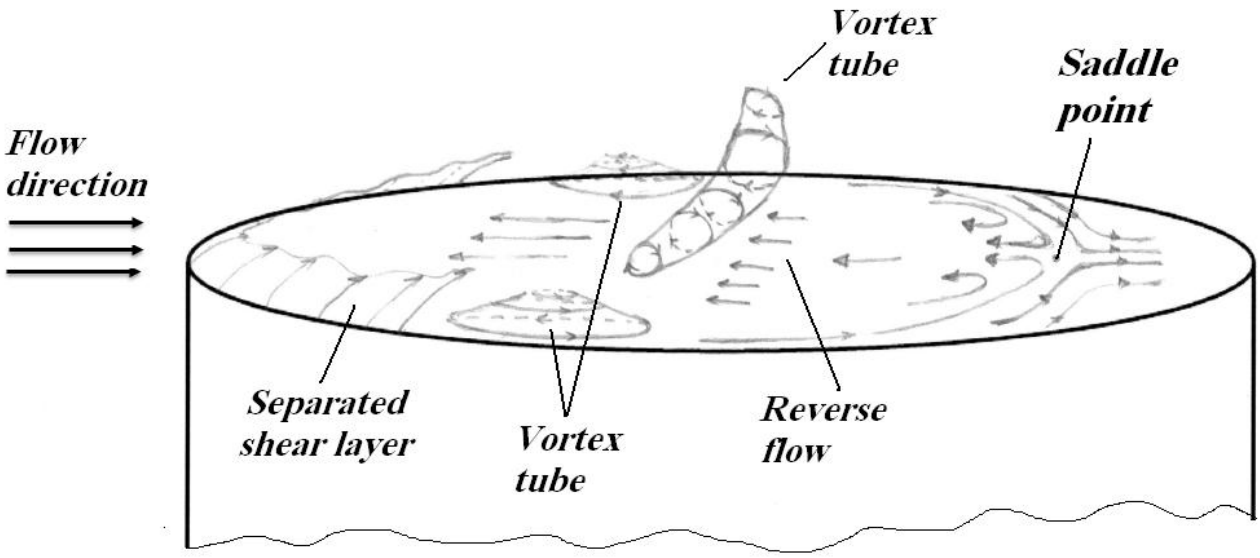

Figure 8.2: Schematic representation of the flow above the free end surface of a surface-mounted finite-height circular cylinder of AR = 3 (below the critical AR).

8.1.2 Finite Square Prism

Similar to the finite-height circular cylinders, PIV velocity measurements were made in a vertical plane on the flow centreline, upstream and downstream of the prism, with a special focus on the near-wake recirculation zone. In the near-wake region, a large recirculation region forms behind the prism. Downwash flow enters the central portion of the wake where some flow from the free end reverses and moves toward the rear surface (base) of the prism. A small vortex is located just downstream of the free end behind the prism and below the main downwash flow. This vortex is found for all four aspect ratios. Near the ground plane and close to the prism-wall junction, a second vortex forms; this vortex is weak or nearly absent for the prisms of AR = 5 and 3. The maximum length of the recirculation zone (L_{max}/D) increases with the prism aspect ratio from 2.3D for AR = 3 to 4.2D for AR = 9. Elevated levels of wall-normal turbulence intensity and Reynolds shear stress also occur above the free end of the square prism. Cross-

stream vorticity production also occurs around the free end and into the downwash region behind the prism. This region of mean vorticity extends farther downstream as the aspect ratio decreases.

PIV velocity measurements were made in three orthogonal planes at different streamwise, cross-stream, and wall-normal locations above the free end of the prism. According to the results in the *x-z* planes, flow separation occurs from the leading edge of the free end and the separated flow extends into the near-wake region. Unlike the circular cylinder case, there is no reattachment of the separated flow on the free end surface of the square prism. Elevated levels of turbulence intensity and Reynolds shear stress also occur above the free end. The highest level of u'/U_∞ for the prism of AR = 9 was reported as 0.43, while for prisms of AR = 7, 5, and 3, it reached a lower value of 0.4. However, for all aspect ratios, the region of highest level of u' is located approximately 0.2*D* to 0.3*D* above the free end surface of the square prisms and in the streamwise range of x/D = -0.3 to -0.2.

The reverse flow and its local separation from the trailing edge of the free end surface was more dominant for the prism of AR = 3 at different cross-stream locations (y/D), while for prisms of AR = 9, 7, and 5, the effect of the shear layer separated from the leading edge was more dominant than the reverse flow as the cross-stream distance (y/D) increases. The results suggest a distinct flow pattern and behavior for the finite square prism of AR = 3, and places the critical aspect ratio between AR = 3 and AR = 5 for these experimental conditions.

According to the results in *x-y* planes, the reverse flow originating from the trailing edge of the free end surface was more dominant for the prism of AR = 3 compared to other aspect ratios. The mean velocity fields in the *x-y* planes showed that for the more slender prism (AR =

9), the separation not only occurs from the leading edge of the free end surface, but also from the side edges of the free end, while for AR = 3, no separation was seen from the side edges of the free end perhaps due to the effect of the strong reverse flow and boundary layer on the flow above the free end for this aspect ratio.

According to the results in the *y-z* planes, the flow pattern above the free end surface of prisms changes dramatically as the distance from the leading edge increases. Above the prism free end at the section of *x/D* = 0.2, two streamwise vortices were observed centered at *y/D* = ±0.4, ±0.45 for the prism of AR = 9 and 3, respectively. These streamwise vortices were also observed for the prisms of AR = 7 and 5 at the distance of *x/D* = 0.2. For both prisms of AR = 9 and 3, one pair of $-\overline{v'w'}$ shear stress with opposite sense of rotation is formed at *x/D* = - 0.2 above the side edges of the free end, while at *x/D* = 0.5, there are three pairs of $-\overline{v'w'}$ shear stress for AR = 9 and two pairs of the shear stress for AR = 3. Larger regions of shear stress were also seen for the prism of AR = 9 compared to AR = 3.

According to the PIV results in the *x-z*, *x-y* and *y-z* planes, a model for the flow pattern above the free end surface of surface-mounted finite-height square prism of AR = 9 (above the critical AR) and 3 (below the critical AR) is proposed, and is shown in Figures 8.3 and 8.4. According to these figures, the present results are in contrast with the results of Wang and Zhou (2009) who showed that the streamwise tip vortices above the free end are part of the arch-type vortex. According to the present results, the tip vortices are generated at the vertices of the free end surface stretching downstream toward the nearwake of the prism.

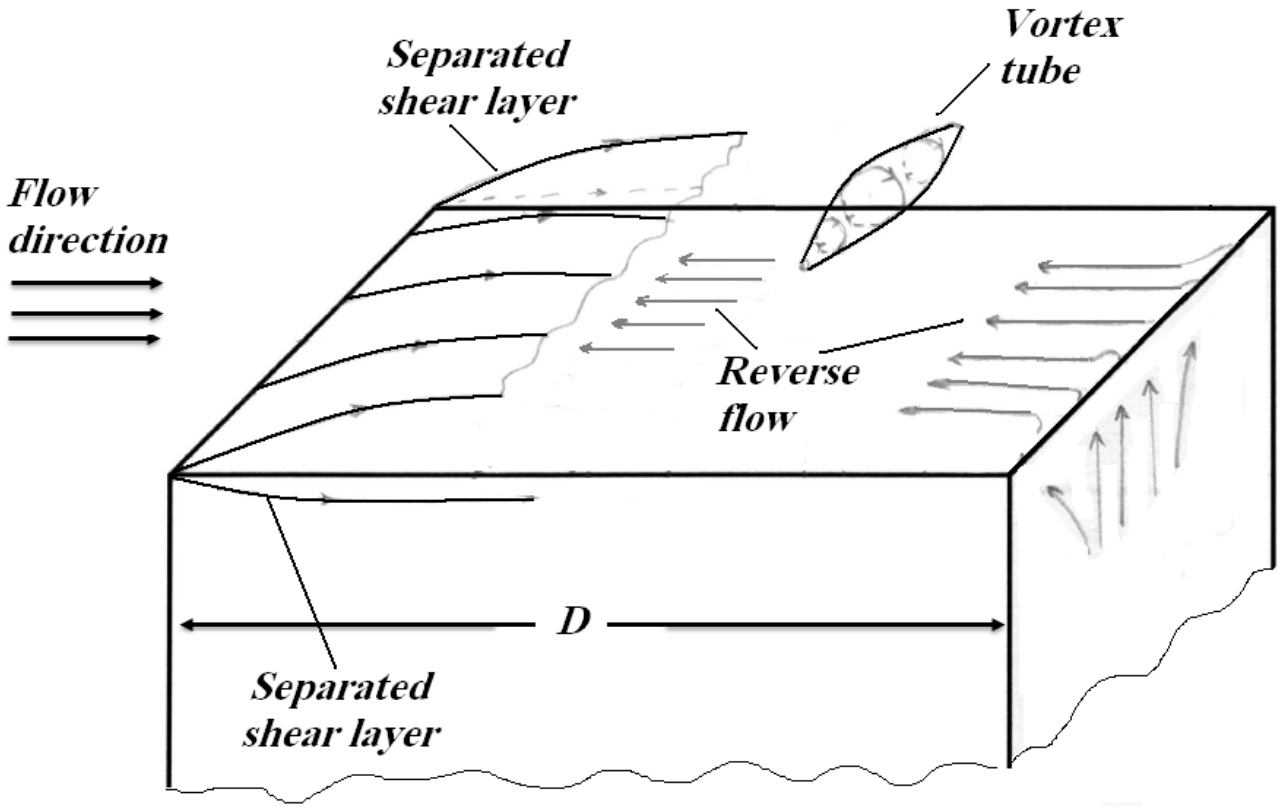

Figure 8.3: Schematic representation of the flow above the free end surface of a surface-mounted finite-height square prism of AR = 9 (above the critical AR).

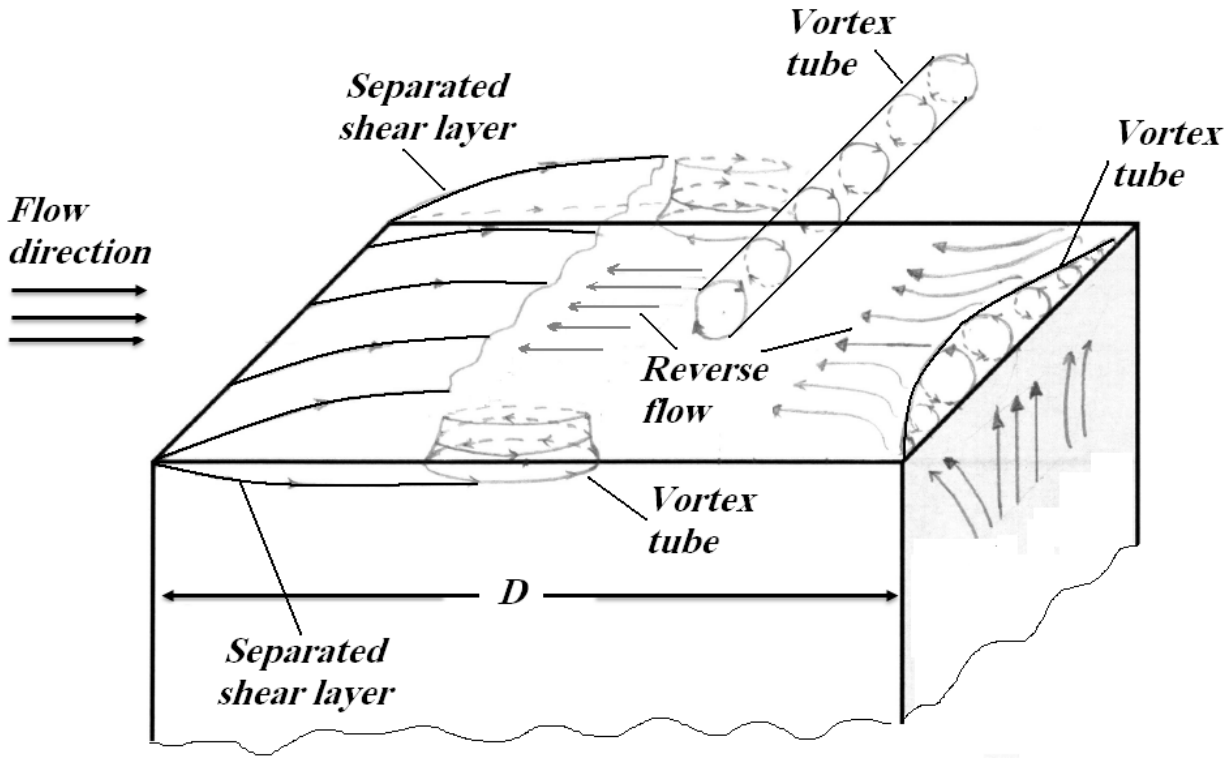

Figure 8.4: Schematic representation of the flow above the free end surface of a surface-mounted finite-height square prism of AR = 3 (below the critical AR).

8.2 Contributions of this Study

The results of this study have provided insight into the turbulent wake characteristics of finite-height surface-mounted circular cylinders and square prisms partially immersed in a turbulent flat-plate boundary layer. Also, the present results have improved the limited state of information on the flow field above the free end surfaces of both circular cylinders and square prisms. The present detailed experimental data collected using the PIV system can be used as validation information for future CFD modeling and simulations.

The effect of cylinder/prism aspect ratio on the flow field in the near-wake region as well as above the free end surfaces was also investigated in this study and makes an important contribution to the literature. The effects of the bluff body shape (circular or square cross-section) on the flow characteristics were also investigated in this thesis. Although, there are a few studies on the flow above the free end surface of circular cylinders, no experimental data or numerical simulations were found for the flow above the free end surface of finite square prism (with the possible exception of flow over a cube). In this thesis, results of mean velocity fields, turbulence intensities, and vorticities in *x*-*z*, *x*-*y*, and *y*-*z* planes are reported. These results make a unique contribution to the literature.

8.3 Recommendations for Future Work

This study has provided detailed and useful information about the flow characteristics in the near-wake region of surface-mounted finite circular cylinders and square prisms. Also the flow behavior above the free end surface of these bodies has been addressed in this thesis. Due to the limitations of the available facilities and also the complex nature of the flow around and above the finite cylinders and prisms, some additional issues still need to be addressed.

The instantaneous velocity field above the free end surface of the cylinders and prisms was investigated and has been documented as a conference paper (Rostamy et al. 2012). However, more analysis of the instantaneous PIV data for the flow above the free end surface of the cylinder or prism can be done using existing techniques such as proper orthogonal decomposition (POD). Also, the instantaneous data in some local regions such as the cylinder/prism-wall junction, or behind and below the free end surface, can be analyzed separately in order to better understand the flow behavior in those regions.

The effect of Reynolds number and the boundary layer thickness on the flow characteristics above the free end surface as well as the near wake of a finite circular cylinder and square prism can be investigated by changing the diameter or width of the bodies, or changing the freestream velocity in the test section.

References

Adaramola, M.S., 2008. The wake of an exhaust stack in a cross flow. Ph.D. Thesis, Department of Mechanical Engineering, University of Saskatchewan, Saskatoon, Canada.

Adaramola, M.S., Akinlade, O.J., Sumner, D., Bergstrom, D.J., Schenstead, A.J., 2006. Turbulent wake of a finite circular cylinder of small aspect ratio. *Journal of Fluids and Structures* **22**, 919-928.

Adaramola, M.S., Sumner, D., Bergstrom, D.J., 2010. Effect of velocity ratio on the streamwise vortex structures in the wake of a stack. *Journal of Fluids and Structures* **26**, 1-18.

Adrian R., and Westerweel J., 2011. *Particle Image Velocimetry*. Cambridge University Press, New York, USA.

Afgan, I., Moulinec, C., Prosser, R., Laurence, D., 2007. Large eddy simulation of turbulent flow for wall mounted cantilever cylinders of aspect ratio 6 and 10. *International Journal of Heat and Fluid Flow* **28**, 561-574.

Agui, J.H., Andreopoulos, J., 1992. Experimental investigation of a three-dimensional boundary layer flow in the vicinity of an upright wall-mounted cylinder. *ASME Journal of Fluids Engineering* **114**, 566-576.

Akon, A. F., 2012. Measurement of axial induction factor for a model wind turbine. M.Sc. Thesis, Department of Mechanical Engineering, University of Saskatchewan, Saskatoon, Canada.

Baker, C.J., 1979. The laminar horseshoe vortex. *Journal of Fluid Mechanics* **95** (Part 2), 347-367.

Baker, C.J., 1980. The turbulent horseshoe vortex. *Journal of Wind Engineering and Industrial Aerodynamics* **6**, 9-23.

Bourgeois, J.A., Sattari, P., Martinuzzi, R.J., 2011 Alternating half-loop shedding in the turbulent wake of a finite surface-mounted square cylinder with a thin boundary layer. *Physics of Fluids* **23** (095101), 15 pages.

Bourgeois, J.A., Sattari, P., Martinuzzi, R.J., 2010. Quasi-periodic structure of vortical flows produced in the wake of finite bluff bodies partially immersed in a boundary layer. In: *Proceedings of the ASME 2010 3rd Joint US-European Fluids Engineering Division Summer Meeting and 8th International Conference on Nanochannels, Microchannels, and Minichannels* (FEDSM-ICNMM2010), August 1-5, 2010, Montreal, Canada, Paper No. FEDSM-ICNMM2010-30804, 10 pages.

Chen J. and Katz J., 2005. Elimination of peak locking error in PIV analysis using the correlation mapping method. *Measurement, Science and Technology* **16**, 1605-1618.

Coutanceau, M., Defaye, J., 1991. Circular cylinder wake configurations: a flow visualization survey. *Applied Mechanics Reviews* **44**, 255-305.

Depardon, S., Lasserre, J.J., Boueilh, J.C., Brizzi, L.E., Boree, J., 2005. Skin friction pattern analysis using near-wall PIV. *Experiments in Fluids* **39**(5), 805-818.

Einian, M., 2012. Large eddy simulation of flow around a finite square cylinder. Ph.D. Thesis, Department of Mechanical Engineering, University of Saskatchewan, Saskatoon, Canada.

Einian, M., Bergstrom, D.J., Sumner, D., 2010. Numerical simulation of the flow around a surface-mounted finite square cylinder. In: *Proceedings of the ASME 2010 3rd Joint US-European Fluids Engineering Division Summer Meeting and 8th International Conference on Nanochannels, Microchannels, and Minichannels* (FEDSM-ICNMM2010), August 1-5, 2010, Montreal, Canada, Paper No. FEDSM-ICNMM2010-30394, 8 pages.

Etzold, F., Fiedler, H., 1976. The near-wake structure of a cantilevered circular cylinder in a cross-flow. *Zeitschrift fuer Flugwissenschaften* **24**, 77-82.

Frederich, O., Scouten, J., Luchtenburg, D.M., Thiele, F., 2011. Large-scale dynamics in the flow around a finite cylinder with a ground plate. *Fluid Dynamics Research* **43** (01554), 22 pages.

Frederich, O., Thiele, F., 2011. Turbulent flow dynamics caused by a truncated cylinder. *International Journal of Heat and Fluid Flow* **32**, 546-557.

Frederich, O., Wassen, E., Thiele, F., Jensch, M., Brede, M., Huttmann, F., Leder, A., 2007. Numerical simulation of the flow around a finite cylinder with ground plate in comparison to experimental measurements. In: Tropea, C., et al. (Eds.), *New Research in Numerical and Experimental Fluid Mechanics*, VI., Springer-Verlag, Berlin Heidelberg, 348-355.

Frohlich, J., Rodi, W., 2004. LES of the flow around a circular cylinder of finite height. *International Journal of Heat and Fluid Flow* **25**, 537-548.

Graf, W.H., Yulistiyanto, B., 1998. Experiments on flow around circular cylinder; the velocity and vorticity fields. *IAHR Journal of Hydraulic Research* **36**, 637-744.

Hart, D., 2000. PIV error correction. *Experiments in Fluids* **29**, 13-22.

Hain, R., Kahler, C.J., Michaelis, D., 2008. Tomographic and time resolved PIV measurements on a finite cylinder mounted on a flat plate. *Experiments in Fluids* **45**, 715-724.

Heseltine, J.L., 2003. Flow around a circular cylinder with a free end. M.Sc. Thesis, Department of Mechanical Engineering, University of Saskatchewan, Saskatoon, Canada.

Igbalajobi, A., 2011. The effect of a splitter plate on the flow around a surface-mounted finite circular cylinder. M.Sc. Thesis, Department of Mechanical Engineering, University of Saskatchewan, Saskatoon, Canada.

Johnston, C.R., Clavelle E.J., Wilson, D.J., Peck, B.J., 1998. Investigation by vorticity generated by flow around a finite cylinder. *In Proceedings of the 6th Conference of the CFD Society of Canada (CFD'98)*, Quebec City, Canada.

Johnston, C.R., Wilson, D.J., 1997. A vortex pair model for plume downwash into stack wakes. *Atmospheric Environment* **31**, 13-20.

Kawamura, T., Hiwada, M., Hibino, T., Mabuchi, T., Kumada, M., 1984. Flow around a finite circular cylinder on a flat plate. *Bulletin of the JSME* **27**, 2142-2150.

Kitagawa, T., Fujino, Y., Kimora, K., 1999. Effects of free-end condition on end-cell induced vibration. *Journal of Fluids and Structures* **13**, 499-518.

Kitagawa, T., Fujino, Y., Kimora, K., Mizuno, Y., 2001. Wind pressures on end-cell-induced vibration of circulat tower. *Journal of Engineering Mechanics* **127**(11). 1135-1143.

Kitagawa, T., Fujino, Y., Kimora, K., Mizuno, Y., 2002. Wind pressures measurement on end-cell-induced vibration of a cantilevered circular cylinder. *Journal of Wind Engineering and Industrial Aerodynamics* **90**, 395-405.

Krajnović, S., 2011. Flow around a tall finite cylinder explored by large eddy simulation. *Journal of Fluid Mechanics* **676**, 294-317.

Leder, A., 2003. 3D-flow structures behind truncated circular cylinders. In*: Proceedings of the FEDSM'03, Fourth ASME-JSME Joint Fluids Engineering Conference*, Honolulu, USA, Paper No. FEDSM2003-45083.

Lee, L.W., 1997. Wake structure behind a circular cylinder with a free end. *Proceedings of the Heat Transfer and Fluid Mechanics Institute,* 241-251.

Lee, T., Lin, C.L., Friehe, C.A., 2007. Large eddy simulation of air flow around a wall-mounted circular cylinder and a tripod tower. *Journal of Turbulence* **8**, 1-28.

Lee, L.W., Wang, Y.L., 1987. Aerodynamics of a circular cylinder of finite length in cross-flow. *Proceedings of ASME Applied Mechanics, Bioengineering, and Fluid Engineering Conference,* Cincinnati, Ohio, 61-65.

Liu, Y., So, R.M.C., Cui, Z.X., 2005. A finite cantilevered cylinder in a cross-flow. *Journal of Fluids and Structures* **20**, 589-609.

Mahjoub Said, N., Mhiri, H., Bournot, H., Le Palec, G., 2008. Experimental and numerical modeling of the three-dimensional incompressible flow behavior in the near wake of circular cylinders. *Journal of Wind Engineering and Industrial Aerodynamics* **96**, 471-502.

Martinuzzi, R.J. Tropea, C., 1993. The flow around surface-mounted, prismatic obstacles placed in a fully developed channel flow. *ASME Journal of Fluids Engineering* **115**, 85-92.

McClean, J.F., Sumner, D., 2012. Aerodynamic forces and vortex shedding for surface-mounted finite square prisms and the effects of aspect ratio and incidence angle. *Proceedings of the ASME*

2012 Fluids Engineering Division Summer Meeting (FEDSM2012), Rio Grande, Puerto Rico, USA, July 8-12, 2012, Paper No. FEDSM2012-72005.

Okamoto, S., 1991. Flow past circular cylinder of finite length placed on ground plane. *Transactions of the Japan Society for Aeronautical and Space Sciences* **33**, 234-246.

Okamoto, S., Sunabashiri, Y., 1992. Vortex shedding from a circular cylinder of finite length placed on a ground plane. *ASME Journal of Fluids Engineering* **144**, 512-521.

Okamoto, T., Yagita, M., 1973. The experimental investigation on the flow past a circular cylinder of finite length placed normal to the plane surface in a uniform stream. *Bulletin of the JSME* **16**, 805-814.

Oster, D., Wygnanski., I., 1982. The forced mixing layer between paralell streams. *Journal of Fluid Mechanics* **123**, 91-130.

Palau-Salvador, G., Stoesser, T., Frohlich, J., Kappler, M., Rodi, W., 2010. Large eddy simulations and experiments of flow around finite-height cylinders. *Flow, Turbulence and Combustion* **84**, 239-275.

Park, C.W., Lee, S.J., 2000. Free end effects on the near wake flow structure behind a finite circular cylinder. *Journal of Wind Engineering and Industrial Aerodynamics* **88**, 231-246.

Park, C.W., Lee, S.J., 2002. Flow structure around a finite circular cylinder embedded in various atmospheric boundary layers. *Fluid Dynamics Research* **30**, 197-215.

Park, C.W., Lee, S.J., 2004. Effects of free-end corner shape on flow structure around a finite cylinder. *Journal of Fluids and Structures* **19**, 141-158.

Pattenden, R.J., Bressloff, N.W., Turnock, S.R., Zhang, X., 2007. Unsteady simulation of the flow around a short surface-mounted cylinder. *International Journal for Numerical Methods in Fluids* **53**, 895-914.

Pattenden, R.J., Turnock, S.R., Zhang, X., 2005. Measurements of the flow over a low-aspect-ratio cylinder mounted on a ground plane. *Experiments in Fluids* **39**, 10-21.

Prasad A.K., Adrian R.J., Landreth C.C., and Offutt P.W., 1992. Effect of resolution on the speed and accuracy of particle image velocimetry interrogation. *Experiments in Fluids* **13**, 105-116.

Raffel M., Willert C., Wereley S., and Kompenhans J., 2006. *Particle Image Velocimetry. A Practical Guide*, Berlin, Springer.

Roh, S.C., Park, S.O., 2003. Vortical flow over the free end surface of a finite circular cylinder mounted on a flat plate. *Experiments in Fluids* **34**, 63-67.

Rostamy, N., Sumner, D., Bergstrom, D.J., Bugg, J.D., 2012. Local flow field of a surface-mounted finite circular cylinder. *Journal of Fluids and Structures* **34**, 105-122.

Rostamy, N., Sumner, D., Bergstrom, D.J., Bugg, J.D., 2012. Instantaneous Flow Field above the Free-end of Finite-height Cylinders and Prisms. *Proceedings of the 7th International Symposium on Turbulence, Heat and Mass Transfer (THMT10)*, September 24-27, Sicily, Italy.

Roth G.I., and Katz J., 2001. Five techniques for increasing the speed and accuracy of PIV interrogation. *Measurement, Science and Technology* **12**, 238-245.

Sakamoto, H., Arie, M., 1983. Vortex shedding from a rectangular prism and a circular cylinder placed vertically in a turbulent boundary layer. *Journal of Fluid Mechanics* **126**, 147-165.

Sattari, P., Bourgeois, J.A., Martinuzzi, R.J., 2010. Turbulent wake of surface-mounted finite aspect ratio bluff bodies: effect of aspect ratio and cross section shape. In: *Proceedings of the ASME 2010 Third Joint US-European Fluids Engineering Division Summer Meeting and Eighth International Conference on Nanochannels, Microchannels, and Minichannels* (FEDSM-ICNMM2010), August 1-5, 2010, Montreal, Canada, Paper No. FEDSM-ICNMM2010- 30811, 9 pages.

Shinneeb, A.M., Bugg, J.D., Balachandar, R., 2004. Variable threshold outlier identification in PIV data. *Measurement Science and Technology* **15**, 1722-1732.

Sumner, D., Heseltine, J.L., Dansereau, O.J.P., 2004. Wake structure of a finite circular cylinder of small aspect ratio. *Experiments in Fluids* **37**, 720-730.

Sumer, B.M., Fredsøe, J., 1997. *Hydrodynamics Around Cylindrical Structures*. World Scientific, London.

Tanaka, S., Murata, S., 1999. An investigation of the wake structure and aerodynamic characteristics of a finite circular cylinder. *JSME International Journal Series B: Fluids and Thermal Engineering* **42**, 178-187.

Wang, H.F., Zhou, Y., 2009. The finite-length square cylinder near wake. *Journal of Fluid Mechanics* **638**, 453-490.

Wang, H.F., Zhou, Y., Chan, C., Lam, K.S., 2006. Effect of initial conditions on interaction between a boundary layer and a wall-mounted finite-length cylinder wake. *Physics of Fluids* **18** (065106), 12 pages.

Wang, H.F., Zhou, Y., Chan, C., Zhou, T., 2009. Momentum and heat transport in a finite-length cylinder wake. *Experiments in Fluids* **46**, 1173-1185.

Wang, H.F., Zhou, Y., Chan, C., Mi, J., 2012. Effects of aspect ratio on the drag of a wall-mounted finite-length cylinder in subcritical and critical regimes. *Experiments in Fluids* **53**, 423-436.

White, F.M., 2003. *Fluid Mechanics*. 5th Edition, McGraw-Hill, New York.

Williamson, C.H.K., 1996. Vortex dynamics in the cylinder wake. *Annual Review of Fluid Mechanics* **28**, 477-539.

Zdravkovich, M.M., 1997. *Flow Around Circular Cylinders*. Vol. 1. Oxford University Press, Oxford, UK.

Appendix

Permission to Reprint Figures

Figure 2.2: Flow pattern on the free end of a circular cylinder

Fwd: Permission to use figures in my PhD thesis

Tadashi KOSHIGE [koshige@jsme.or.jp]

To:
Rostamy, Noorallah

Monday, August 27, 2012 6:22 PM

Dear Noorallah Rostamy

Thank you for your e-mail.

In response to your letter below, we grant you permission to reuse the JSME copyrighted material. Our only requirements are that you credit the original source (author, paper, journal and publication) appears prominently with your paper.

With best regards,

Tadashi Koshige
Publishing Department Manager
The Japan Society of Mechanical Engineers
Shinanomachi-Rengakan Building,

Figure 2.3: Flow pattern on the free end of a circular cylinder

Figure 2.4: Schematic of the flow above the free end surface of a circular cylinder

PERMISSION INVOICE

CAMBRIDGE UNIVERSITY PRESS

Inv. # P03J 21985

August 30, 2012

Noorallah Rostamy
Po Box 473, RPO, University
University of Saskatchewan
Saskatoon S7N 4J8
Canada

32 Avenue of the Americas
New York, NY 10013-2473, USA

www.cambridge.org

Telephone 212 924 3900
Fax 212 691 3239

REFERENCE ISSN: EISSN:

Journal:	Journal of Fluid Mechanics, Volume 676 (2011), pp. 294–317.
Author:	Sinisa Krajnovic
Title:	Flow around a tall finite cylinder explored by large eddy simulation
Selection/pp.:	Fig. 6, p. 302 and Fig. 7, p. 303
Additional	Copyright © 2011 Cambridge University Press.

USE

Reprint Title:	FUNDAMENTAL STUDIES OF THE WAKE STRUCTURE FOR SURFACE-MOUNTED FINITE-HEIGHT CYLINDERS AND PRISMS
Publisher:	University of Saskatchewan
Format:	dissertation / thesis
Quantity (Limit*):	100
Avail. Date:	2012

RIGHTS/ACKNOWLEDGEMENT

Permission is granted for nonexclusive rights throughout the World in the English language for interior text editorial use in the format described above only. Please fully acknowledge our material and indicate the copyright notice as it appears in our publication, followed by the phrase "Reprinted with the permission of Cambridge University Press."

All requests from third parties to reproduce this material must be forwarded to Cambridge University Press.

FEES/RESTRICTIONS

$0.00

*You must re-apply for permission if this print run is exceeded. This permission is restricted to the indicated format and excludes reproduction in any other medium; for additional use, you must apply for permission separately. This permission does not allow reprinting of any material copyrighted by or credited in our publication to another source; Cambridge disclaims all liability in connection with the use of such material without proper consent. A COPY OF THIS INVOICE MUST ACCOMPANY PAYMENT. Payment is due upon publication or within 12 months, whichever is sooner. Make check payable to Cambridge University Press, Attn: Rights and Permissions. (CUP Fed. I.D. #: 13 -1599108.)

This permission does not supersede permission that may be required from the original source indicated in our publication.

This permission requires that you send zero (0) copies of your publication directly to our author and zero (0) copy of your publication to this office upon availability.

Figure 2.5: A schematic model of the flow structure around a surface-mounted finite square prism

PERMISSION INVOICE

Inv. # P03J 21979

August 29, 2012

Noorallah Rostamy
Po Box 473, RPO, University
University of Saskatchewan
Saskatoon S7N 4J8
Canada

CAMBRIDGE UNIVERSITY PRESS

32 Avenue of the Americas
New York, NY 10013-2473, USA

www.cambridge.org

Telephone 212 924 3900
Fax 212 691 3239

REFERENCE ISSN: EISSN:

Journal:	Journal of Fluid Mechanics, Volume 638 (November 2009), pp. 453-490
Author:	H. F. Wang and Y. Zhou
Title:	The finite-length square cylinder near wake
Selection/pp.:	Figure 11, p. 470
Additional	Copyright © 2009 Cambridge University Press.

USE

Reprint Title:	FUNDAMENTAL STUDIES OF THE WAKE STRUCTURE FOR SURFACE-MOUNTED FINITE-HEIGHT CYLINDERS AND PRISMS
Publisher:	University of Saskatchewan
Format:	dissertation / thesis
Quantity (Limit*):	100
Avail. Date:	2012

RIGHTS/ACKNOWLEDGEMENT

Permission is granted for nonexclusive rights throughout the World in the English language for interior text editorial use in the format described above only. Please fully acknowledge our material and indicate the copyright notice as it appears in our publication, followed by the phrase "Reprinted with the permission of Cambridge University Press."

All requests from third parties to reproduce this material must be forwarded to Cambridge University Press.

FEES/RESTRICTIONS

$0.00

*You must re-apply for permission if this print run is exceeded. This permission is restricted to the indicated format and excludes reproduction in any other medium; for additional use, you must apply for permission separately. This permission does not allow reprinting of any material copyrighted by or credited in our publication to another source; Cambridge disclaims all liability in connection with the use of such material without proper consent. A COPY OF THIS INVOICE MUST ACCOMPANY PAYMENT. Payment is due upon publication or within 12 months, whichever is sooner. Make check payable to Cambridge University Press, Attn: Rights and Permissions. (CUP Fed. I.D. #: 13 -1599108.)

This permission does not supersede permission that may be required from the original source indicated in our publication.

This permission requires that you send zero (0) copies of your publication directly to our author and zero (0) copy of your publication to this office upon availability.

Figure 2.6: Model of the educed mean vortex structure proposed by Bourgeois et al. (2011)

Figure 2.7: Model of educed phase-averaged vortex structure (Bourgeois et al., 2011)

AIPRights Permissions [Rights@aip.org]

In response to the message from Physics of Fluids, 8/21/2012

To:
Rostamy, Noorallah

Wednesday, August 29, 2012 12:28 PM

Dear Dr. Rostamy:

Thank you for requesting permission to reproduce material from American Institute of Physics publications.

Permission is granted – subject to the conditions outlined below – for the following:

Figure 9 (page 7) and Figure 16 (page 9)
Alternating half-loop shedding in the turbulent wake of a finite surface-mounted square cylinder with a thin boundary layer.
J.A. Bourgeois, P. Sattari, and R.J. Martinuzzi, Physics of Fluids 23 (095101), 2011.

To be used in the following manner:

Reproduced in your PhD thesis for submission to the University of Saskatchewan.

1. The American Institute of Physics grants you non-exclusive world rights in all languages and media.

2. This permission extends to all subsequent and future editions of the new work.

3. The following copyright notice must appear with the material (please fill in the information indicated by capital letters): "Reprinted with permission from [FULL CITATION]. Copyright [2011], American Institute of Physics."
Full citation format is as follows: Author names, journal title, Vol. #, Page #, (Year of publication).
For an article, the copyright notice must be printed on the first page of the article or book chapter. For figures, photographs, covers, or tables, the notice may appear with the material, in a footnote, or in the reference list.

4. This permission does not apply to any materials credited to sources other than the copyright holder.

5. If you have not already done so, please attempt to obtain permission from at least one of the authors. The author's address can be obtained from the article.

Please let us know if you have any questions.

Sincerely,
Susann Brailey

Manager, Rights and Permissions
American Institute of Physics
Suite 1NO1
2 Huntington Quadrangle
Melville, NY 11747-4502

Phone: 1-516-576-2268
Fax: 1-516-576-2450
Email: sbrailey@aip.org

Figure 3.18: Variation of PIV bias and random errors with d_τ/d_{pix}

SPRINGER LICENSE
TERMS AND CONDITIONS

Sep 16, 2012

This is a License Agreement between Noorallah Rostamy ("You") and Springer ("Springer") provided by Copyright Clearance Center ("CCC"). The license consists of your order details, the terms and conditions provided by Springer, and the payment terms and conditions.

All payments must be made in full to CCC. For payment instructions, please see information listed at the bottom of this form.

License Number	2975490872054
License date	Aug 24, 2012
Licensed content publisher	Springer
Licensed content publication	Experiments in Fluids
Licensed content title	Effect of resolution on the speed and accuracy of particle image velocimetry interrogation
Licensed content author	A. K. Prasad
Licensed content date	Jun 1, 1992
Volume number	13
Issue number	2
Type of Use	Thesis/Dissertation
Portion	Figures
Author of this Springer article	No
Order reference number	
Title of your thesis / dissertation	Fundamental study of the wake structure for surface-mounted finite-height cylinders and prisms
Expected completion date	Sep 2012
Estimated size(pages)	220
Total	0.00 CAD